University of South-Eastern Norway
Faculty of Technology, Natural Sciences and Maritime Studies

Doctoral dissertation no. 103
2021

Martha Nohemi Acosta Montalvo

Intelligent frequency control for the secure operation of modern power system

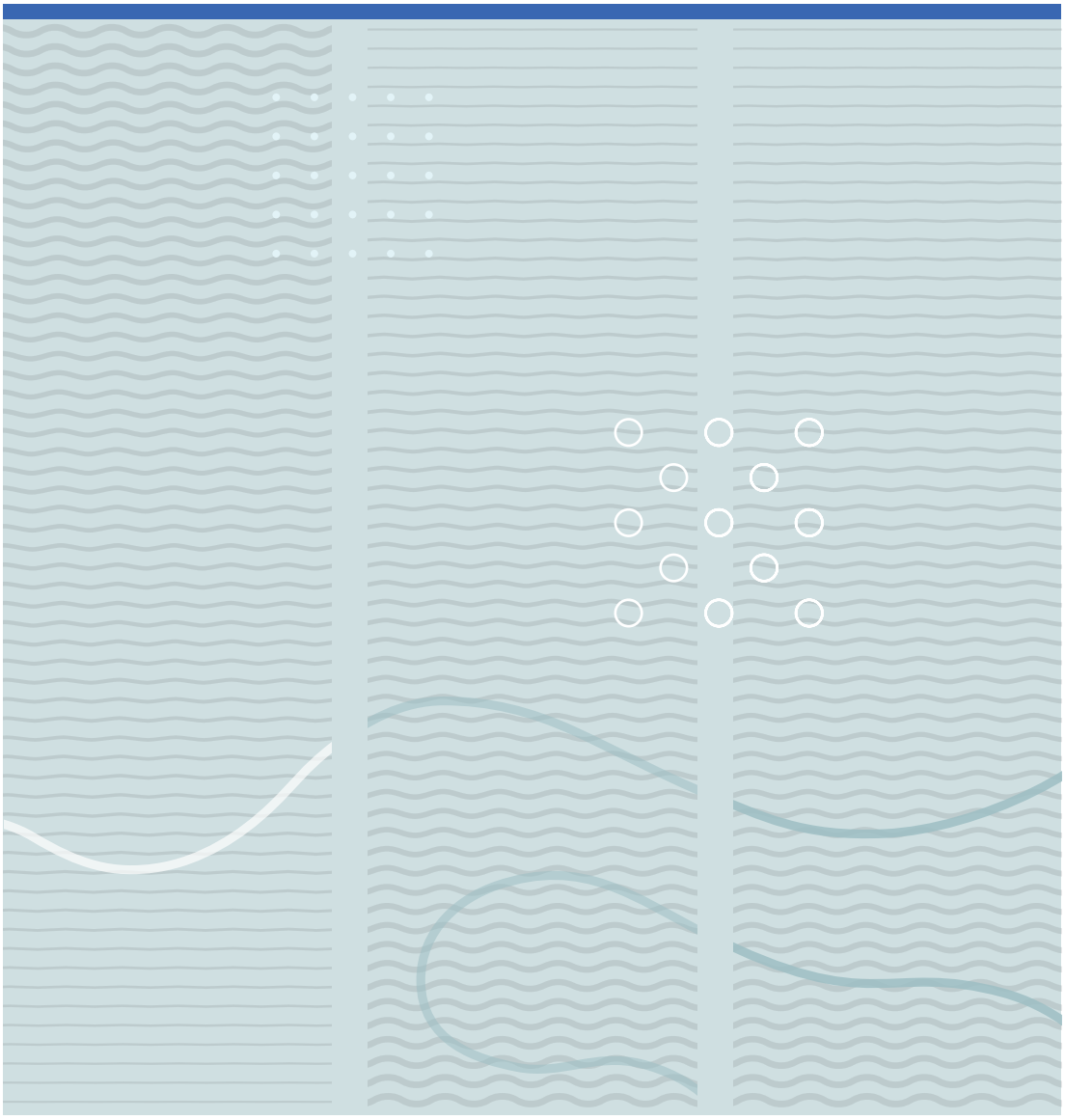

Martha Nohemi Acosta Montalvo

Intelligent frequency control for the secure operation of modern power system

A PhD dissertation in
Process, Energy and Automation Engineering

Faculty of Technology, Natural Sciences and Maritime Studies
University of South-Eastern Norway
Porsgrunn, 2021

Doctoral dissertations at the University of South-Eastern Norway no. 103

ISSN: 2535-5244 (print)
ISSN: 2535-5252 (online)

ISBN: 978-82-7206-621-4 (print)
ISBN: 978-82-7206-622-1 (online)

Print: University of South-Eastern Norway

Acknowledgements

Foremost, I would like to thank my supervisors, Dr Manuel Andrade Soto and Professor Francisco Gonzalez-Longatt, for their advice, support and supervision during these years.

Special thanks to Dr Manuel Andrade Soto for being the first person who gave me the opportunity to work in the research field since my master's degree. For providing me with the bases of knowledge and helping me develop the abilities to initiate my PhD. And most important, to encouraging me to take new challenges.

My deepest gratitude to Professor Francisco Gonzalez-Longatt, for being such a good mentor. I am very grateful for allowing me to be part of his research team, sharing his knowledge and endless support, for always knowing that I could do it better and challenge me every day to improve myself. I really enjoy, as he would say, *"this amazing learning experience".* I will always remember those enriching discussions while we were writing or working at the lab.

I would like to thank Dr Jose Luis Rueda, who has been an incredible support and add invaluable contributions and comments to this thesis. I also want to thank Dr Ernesto Vazquez Martinez for his academic and administrative support.

To my friend Osvaldo Gomez Diaz, for always being there, helping me every time that I need it.

Last but not least, to my family, who all made an effort to help me get here, special thanks to Mama Gloria, Papá Cande, Aida, Lucy, Mary, Mini, Victoria and Marcela. Each of them supported me in different ways, and most importantly, they showed love and care for me. To Samantha, who has always been my support and encouraged me to do the impossible, for her patience and cheer me up when I felt homesick. To Hector and Dalia for always be there, for their advice and good wishes.

Abstract

The modern power system is experiencing several changes to meet the objective to become in a zero CO2 emissions industry. The principal changes are the high penetration of renewable energy sources (RESs) into the power system. As the electrical energy produced by the RESs do not satisfy the technical requirements of the power system (AC and nominal frequency), power electronic converters are used as an interface between RESs and the power system. Therefore, these changes are leading to the power system being dominated by power converter-based technologies. The principal concern of the transmission system operators regarding these changes is the power supply uncertainty coming from RESs affecting the power balance. In addition, the significant reduction of the rotational inertia producing that frequency drop faster and reaches deeper values when a disturbance occurs. These two problems negatively affect the secure operation of the power system.

The integration of energy storage systems (ESSs) to counteract low rotational inertia levels and intermittent power supply of RESs is a reality in several power systems worldwide. Consequently, distributed energy resources (DERs) and ESSs as providers of frequency support services to the power system can enhance frequency stability. Furthermore, enabling DERs and ESSs with fast frequency response (FFR) controls helps counteract the rapid frequency deviation. Therefore, developing novel FFR models and control strategies is one of the most prominent research topics. However, if the action of primary frequency control and FFR are insufficient to re-establish the power balance and limit the frequency deviation, under-frequency load shedding (UFLS) is required to arrest the frequency drop. Therefore, the accurate performance of the UFLS scheme is essential to maintain the continuous operation of the power system and avert possible blackouts.

This thesis aims to create novel control strategies to cope with the challenges created by the reduced rotational inertia in modern power systems and provide frequency support. Therefore, the interest of this research work converges into two main topics— the frequency control provision based on FFR control strategies and frequency control

during emergency conditions considering the UFLS scheme. The developed methodologies were assessed on realistic power system models considering the expected low rotational inertia scenarios in the coming decades. The real power systems were modelled in DIgSILENT® PowerFactory™ using publicly available data, including the dynamic model of battery energy storage system (BESS) and variable-speed pumped-storage hydropower plants (PHPPs). In addition, the Python programming language was used to implement several optimisation algorithms.

This thesis provides a statistical assessment of the time series of frequency, kinetic energy and power demand of the Nordic power system. It unveiled a strong correlation between kinetic energy and power demand during high power consumption hours, opening the door to creating sophisticated prediction models only using the power demand forecast. Furthermore, it demonstrated that the ESSs, particularly variable-speed PHPPs and BESS enabled with FFR control, effectively counteract the reduced rotational inertia. It strengthened the theory of ESSs as reliable technology to provide frequency support services to the transmission and distribution network. Lastly, it highlighted the importance of computing the parameters of each under-frequency relay instead of setting all under-frequency relays with the same set of parameters. The proposed optimal UFLS scheme has proved to be an essential control for power systems with low rotational inertia and high power demand levels.

Keywords: battery energy storage systems, energy storage systems, fast frequency response, frequency control, rotational inertia, under-frequency load shedding, optimisation.

List of publications

The following list shows details of the publications defining the scientific contribution of this thesis, and they have been published during the PhD studies.

[P1] **M. N. Acosta**, D. Pettersen, F. Gonzalez-Longatt, J. Peredo Argos, and M. A. Andrade, "Optimal Frequency Support of Variable-Speed Hydropower Plants at Telemark and Vestfold, Norway: Future Scenarios of Nordic Power System," *Energies*, vol. 13, no. 13, p. 3377, Jul. 2020, doi: 10.3390/en13133377.

[P2] **M. N. Acosta** *et al.*, "Optimal Under-Frequency Load Shedding Setting at Altai-Uliastai Regional Power System, Mongolia," *Energies*, vol. 13, no. 20, p. 5390, Oct. 2020, doi: 10.3390/en13205390.

[P3] **M. N. Acosta**, C. Adiyabazar, F. Gonzalez-Longatt, J. L. Rueda, and P. Palensky, "Optimal UFLS Settings: An Assessment of Frequency System Response Indicators," in *2020 IEEE PES Innovative Smart Grid Technologies Europe (ISGT-Europe)*, Oct. 2020, pp. 1141–1145, doi: 10.1109/ISGT-Europe47291.2020.9248760.

[P4] **M. N. Acosta**, M. A. Andrade, E. Vazquez, F. Sanchez, F. Gonzalez-Longatt, and J. L. Rueda, "Descriptive Statistical Analysis of Frequency control-related variables of Nordic Power System," in *2020 IEEE Power & Energy Society General Meeting (PESGM)*, Aug. 2020, pp. 1–5, doi: 10.1109/PESGM41954.2020.9282021.

[P5] **M. N. Acosta** *et al.*, "Improvement of the Frequency Response Indicators by Optimal UFLS Scheme Settings," in *2020 IEEE 29th International Symposium on Industrial Electronics (ISIE)*, Jun. 2020, vol. 2020-June, pp. 1250–1255, doi: 10.1109/ISIE45063.2020.9152466.

[P6] **M. N. Acosta**, F. Gonzalez-Longatt, S. Denysiuk, and H. Strelkova, "Optimal Settings of Fast Active Power Controller: Nordic Case," in *2020 IEEE 7th International Conference on Energy Smart Systems (ESS)*, May 2020, pp. 63–67, doi: 10.1109/ESS50319.2020.9160281.

The following publications have also been published during the PhD studies as a result of research collaborations. These publications are slightly connected to this thesis. However, they enriched and contributed to developing knowledge and skills applied to this thesis.

[P7] **M. N. Acosta**, F. Gonzalez-Longatt, D. Topić, and M. A. Andrade, "Optimal Microgrid–Interactive Reactive Power Management for Day–Ahead Operation," *Energies*, vol. 14, no. 5, p. 1275, Feb. 2021, doi: 10.3390/en14051275.

[P8] F. Gonzalez-Longatt, **M. N. Acosta**, H. R. Chamorro, and Jose Luis Rueda, "Power Converters Dominated Power Systems," in *Modelling and Simulation of Power Electronic Converter controlled Power Systems in PowerFactory*, First Edit., F. Gonzalez-Longatt and Jose Luis Rueda, Eds. Switzerland: Springer Nature Switzerland AG, 2020.

[P9] C. Adiyabazar, F. Gonzalez-Longatt, **M. N. Acosta**, J. L. Rueda, and P. Palensky, "Assessment of Under-Frequency Load Shedding in Mongolia Considering Inertia Scenarios," in *2020 IEEE PES Innovative Smart Grid Technologies Europe (ISGT-Europe)*, Oct. 2020, pp. 1201–1205, doi: 10.1109/ISGT-Europe47291.2020.9248837.

[P10] A. M. Ersdal, F. Gonzalez-Longatt, **M. N. Acosta**, J. L. Rueda, and P. Palensky, "Frequency Support of Fast-Multi-Energy Storage Systems in Low Rotational Inertia Scenarios," in *2020 IEEE PES Innovative Smart Grid Technologies Europe (ISGT-Europe)*, Oct. 2020, pp. 879–883, doi: 10.1109/ISGT-Europe47291.2020.9248843.

[P11] F. Gonzalez-Longatt, **M. N. Acosta**, H. R. Chamorro, and D. Topic, "Short-term Kinetic Energy Forecast using a Structural Time Series Model: Study Case of Nordic Power System," in *2020 International Conference on Smart Systems and Technologies (SST)*, Oct. 2020, pp. 173–178, doi: 10.1109/SST49455.2020.9264087.

[P12] D. Pettersen, E. Melfald, A. Chowdhury, **M. N. Acosta**, F. Gonzalez-Longatt, and D. Topic, "TSO-DSO Performance Considering Volt-Var Control at Smart-

Inverters: Case of Vestfold and Telemark in Norway," in *2020 International Conference on Smart Systems and Technologies (SST)*, Oct. 2020, pp. 147–152, doi: 10.1109/SST49455.2020.9264097.

[P13] C. Adiyabazar, **M. N. Acosta**, F. Gonzalez-Longatt, J. . Rueda, and P. Palensky, "Under-Frequency Load Shedding in Mongolia: Simulation Assessment Considering Inertia Scenarios," in *2020 IEEE 29th International Symposium on Industrial Electronics (ISIE)*, Jun. 2020, vol. 2020-June, pp. 1256–1261, doi: 10.1109/ISIE45063.2020.9152584.

[P14] J.A. Barrios-Gomez, F. Sanchez, G. Claudio, F. Gonzalez-Longatt, **M.N. Acosta**, S. Denysiuk, H. Strelkova, "Framework for Real-Time Simulation of Hardware in the Loop Applied to Primary Frequency Control," in *2020 IEEE 7th International Conference on Energy Smart Systems (ESS)*, May 2020, pp. 30–35, doi: 10.1109/ESS50319.2020.9160023.

[P15] E. Gómez, E. Vázquez, **N. Acosta**, and M. A. Andrade, "Independent Estimation of Generator Clustering and Islanding Conditions in Power System with Microgrid and Inverter-Based Generation," in *Power Systems*, Springer Science and Business Media Deutschland GmbH, 2021, pp. 523–553.

[P16] J. A. Barrios-Gomez, F. Sanchez, G. Claudio, F. Gonzalez-Longatt, **M. Acosta**, and D. Topic, "RoCoF Calculation Using Low-Cost Hardware in the Loop: Multi-area Nordic Power System," in *2020 International Conference on Smart Systems and Technologies (SST)*, Oct. 2020, pp. 187–192, doi: 10.1109/SST49455.2020.9264119.

List of tables

List of figures

Abbreviations

AC	Alternating Current
AIC	Akaike Information Criterion
ALPS	Altai-Uliastai Local Power System
BESS	Battery Energy Storage System
BIC	Bayesian Information Criterion
CFSG	Converter Fed Synchronous Generator
CO2	Carbon Dioxide
COI	Centre of Inertia
DC	Direct Current
DERs	Distributed Energy Resources
DFFR	Derivative Fast Frequency Response
DFIG	Doubly-fed Induction Generator
DSO	Distribution System Operators
ESS	Energy Storage Systems
FCR	Frequency Containment Reserves
FFCR	Fast Frequency Combined Response
FFR	Fast Frequency Response
GMM	Gaussian Mixture Model
MPS	Mongolian Power System
NAPS	North American Power System
NPS	Nordic Power System
PDF	Probability Density Function
PFC	Primary Frequency Control
PFFR	Proportional Fast Frequency Response
PHPPs	Pumped-storage Hydropower Plants
QP	Quadratic Programming
RESs	Renewable Generation Sources
RMSE	Root Mean Square Error
ROCOF	Rate of Change of Frequency

SERC	South-eastern Electric Reliability Council
SFC	Secondary Frequency Control
SLSQP	Sequential Least-Square Programming
SPI	Smart Power Inverters
TFC	Tertiary Frequency Control
TSOs	Transmission System Operators
TUFLS	Traditional Under-frequency Load Shedding
UF	Under-frequency
UFLS	Under-frequency Load Shedding
WAMS	Wide-area Measurement System

Table of contents

1 Introduction

1.1 Background

The exponential growth of industrialisation and urbanisation worldwide has produced alarming environmental damage. The principal cause of this environmental damage is CO2 emission into the atmosphere produced by fossil fuel combustion. The electrical sector has been identified as one of the sectors that produce the most CO2 emissions [1], [2]. Therefore, the international environmental authorities established strict regulations to encourage replacing fossil fuel-based power generation with renewable energy sources (RESs) and thus reduce CO2 emissions [3], [4].

The installed capacity of RESs worldwide up to the year 2019 was above 2,300 GW. Furthermore, it is projected that by the year 2040, it will increase 1,200 GW, of which 25% will be wind-based technologies and 60% solar-based technologies [5], [6] these two technologies being the most promising power generation sources. Nevertheless, the primary energy source of solar and wind power plants is directly dependent on the weather conditions, causing variability and uncertainty of the power supply coming from them [7], [8]. Consequently, the utilisation of energy storage systems (ESSs) to transform and store excess energy and then use it when needed is an alternative to mitigate the stochastic nature of solar and wind power plants. The battery energy storage system (BESS) and pumped hydro storage are the most popular ESSs used in the power system, representing more than 70% of the ESSs projects worldwide [9].

Decarbonising the electrical sector to make it environmentally friendly have been creating significant changes in the power system, as depicted in Figure 1.1. It is producing the transition from a power system dominated by synchronous generators, high levels of rotational inertia and reliable and straightforward control strategies to a modern power system dominated by power converter-based technologies, low levels of rotational inertia and a lack of control mechanism to cope with the changes produced by these technologies.

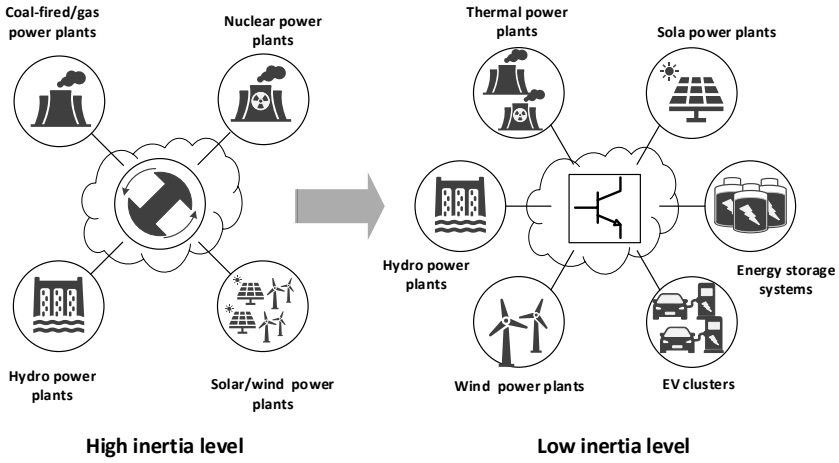

Figure 1.1. Schematic representation of the changes in the power system produced by the decarbonisation process.

1.2 Research motivation

The transition towards a power system of CO2 emissions-free is changing the traditional way to supply energy, i.e., the linear energy design starting at power generation sources, then passing through transmission and distribution systems to the end-user. The integration of distributed energy resources (DERs), mainly formed by RESs, at transmission and distribution levels, enables dynamic power flow iterations with these networks producing a decentralised energy supply landscape, as shown in Figure 1.2.

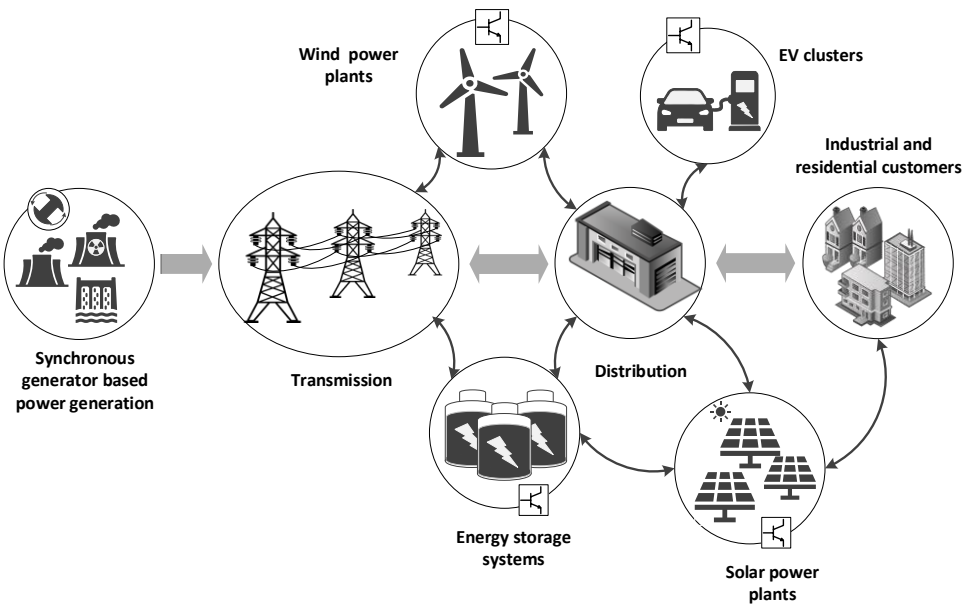

Figure 1.2. Schematic representation of the decentralised modern power system.

The power energy coming from the DERs is not consistent with the rest of the power system. For instance, solar power plants produce DC, whilst wind power plants and variable-speed PHPs produce AC but with a frequency value different from the power system's nominal frequency. Consequently, most DERs and RESs are integrated into the power system using power electronic converters as an interface [10].

The intermittence of the power supply coming from RESs produces an uncertainty of the power balance. Furthermore, the growing integration of technologies based on power electronic converters decouples the power generation sources and the power demand. Moreover, the power electronic converters do not provide features to regulate the frequency as the synchronous generators do naturally. Consequently, they provide low or even zero rotational inertia, directly impacting the safe operation of the power system.

Notwithstanding the significant challenges that represent the increasing integration of DERs and RESs into de power systems, several studies have demonstrated that the transition to a modern power system of CO2 emissions-free can be a reality in the near coming years [11]–[15]. Furthermore, countries worldwide have planned to decommission fossil fuel-based power plants and significantly increase the installation of RESs. For example, the Continental Europe synchronous area has estimated that 62% of its installed capacity will be based on RESs by 2050 [16]. Consequently, the transmission system operators (TSOs) have identified numerous challenges arising from the high penetration of DERs and RESs in the power system that must be tackled to ensure the power system's continuous and safe operation in the coming years. The projected challenges include reducing short circuit levels, forecasting wind and PV power generation, and novel voltage controls. However, the reduction of the rotational inertia is one of the biggest challenges that is concerning to the TSOs.

The reduction of the rotational inertia impacts the frequency deviation and the rate of change of frequency (ROCOF) of the power system directly after a disturbance occurs. The low rotational inertia levels produce the frequency drops faster and more profound, making the primary frequency control (PFC) insufficient to stop the frequency deviation

and limit the ROCOF values. Therefore, incorporating FFR control coming from the DERs and ESSs is required to counteract the rapid frequency deviation. Furthermore, developing novel FFR models and control strategies is one of the most prominent research topics. Nevertheless, when the power system experiences a significant power imbalance, the action of PFC and FFR are probably insufficient to re-establish the power balance and limit the frequency deviation. In such a case, the action of an under-frequency load shedding (UFLS) scheme is required to arrest the frequency drop. Consequently, the correct performance of the UFLS scheme is essential to maintain the continuous operation of the power system and avert possible blackouts.

1.3 Objectives

This thesis aims to create novel intelligent frequency control strategies to cope with the challenges produced by the reduced rotational inertia in modern power systems considering normal operation (FFR control) and emergencies conditions (UFLS scheme). To this aims, powerful computational hardware and novel optimisation algorithms are used. The open-source Python programming language is used to implement several optimisation algorithms. Furthermore, the simulation software DIgSILENT® PowerFactory™ is used to modelling the power system and executing dynamic simulations.

This thesis unfolds three specific objectives:

- Create a method to identify features and patterns of electromechanical time series related to frequency control and stability: datasets of frequency, kinetic energy, and power demand; to create kinetic energy prediction models.
- Create a novel methodology to enable the power converter-based technologies with an FFR controller and provide optimal frequency support into a modern power system considering non-linear dynamic models and reduced rotational inertia.
- Create a novel mechanism to calculate the optimal parameters of under-frequency (UF) relays of the UFLS protection scheme to cope with the challenges

of reduced rotational inertia in the power system and minimise the total load disconnection.

1.4 Scope

A power imbalance produced by the sudden disconnection of a power generation source or a significant unexpected increase of the power demand results in a frequency deviation that can lead it to be outside the permissible operational range. Furthermore, it also causes small or large voltages excursion around its nominal values, depending on the size of disturbance and other factors. Nevertheless, this thesis is centred only on the frequency behaviour and control considering technical aspects and strategies of the frequency response modelling and control. Consequently, the voltage management, economic and market studies are out of the scope of this thesis.

1.5 Research work outline

The research work done during the PhD studies is presented in this thesis. The core of this thesis is based on six scientific publications that are organised and presented throughout different chapters. However, ten more scientific publications that are not part of this thesis also enriched the research work. The rest of the thesis is structured as follows.

1.5.1 Chapter 2

Chapter 2 introduces the fundamental concepts and equation describing frequency control. Besides, it describes the parameters defining the frequency quality and highlights the main frequency requirements of TSOs in Europe and North America. Moreover, it depicts different frequency events that occurred in recent years worldwide. Furthermore, it presents an outline of the different optimisation algorithms used in this thesis.

1.5.2 Chapter 3

Chapter 3 introduce a methodology to identify features and patterns of electromechanical time series related to frequency control and stability: datasets of frequency, kinetic energy, and power demand. Moreover, it uses the features and patterns to represent the relationship between the mentioned electromechanical variables and create kinetic energy prediction models. This chapter introduces the principal statistical methods and models used to study a set of data. Furthermore, a methodology to perform a clustering of the time series using the gaussian mixture model technique and then create a set of prediction models is presented. Afterwards, it provides a statistical analysis of the time series of frequency, kinetic energy, and power demand of the Nordic power system, highlighting the principal features, patterns and trends found. Lastly, the proposed methodology is used to compute the set of linear regression models of the kinetic energy considering the time series of power demand as a predictor variable. The fundamentals of this chapter are based on publication **[P1][P4]**.

1.5.3 Chapter 4

Chapter 4 proposes a novel methodology to enable power converter-based technologies with an FFR control to provide optimal fast frequency support to the power system with low rotational inertia. Furthermore, it assesses the impact of the FFR on the frequency quality indicators following a disturbance. This chapter includes a description of the traditional frequency response model for single and multiple areas. Besides, it provides the fundamental equations and frequency control techniques that govern the FFR model, i.e., proportional, derivative and combined control actions. Then, the combined FFR provided by the variable-speed pumped-storage hydropower plants (PHPPs) and BESS is formulated and written as an optimisation problem, including the frequency quality indicators as inequality constraints, to compute the optimal parameters of FFR control. The single-area model of the Nordic power system (NPS) and a realistic distribution network of the Norwegian power system are implemented and used as testbeds for the developed optimal FFR provision methodology. It is considered the expected changes of the NPS in power demand (increase), power generation

(substituting traditional by power converted based technologies) and kinetic energy (decrease) up to the year 2040. The foundation of this chapter is based on publications **[P1]** and **[P6]**.

1.5.4 Chapter 5

Chapter 5 introduces a novel methodology to calculate the optimal parameters of the UF-relays of the UFLS scheme to minimise the total load shedding. Besides, it provides a detailed description of the traditional UFLS scheme and its parameters. Furthermore, it introduces an optimal UFLS scheme formulation to minimise the total load shedding and enhance the frequency quality indicators by formulating them as inequality constraints. Subsequently, a co-simulation framework based on a programming language and a power system simulation software developed to solve the optimal UFLS scheme is presented. Finally, the New England power systems and the real power system susceptible to low rotational inertia conditions of a region of Mongolia are modelled and utilised as the test systems for assessing the performance of the proposed optimal UFLS scheme. The core of this chapter is based on publications **[P2]**, **[P3]** and **[P5]**.

1.5.5 Chapter 6

Chapter 6 presents the principal finding and conclusion of this thesis. Furthermore, it provides insight into the future work topics derived from the research work done.

2 Frequency control basics

The integration of low and zero-carbon technologies in the power system creates several challenges to achieve the safe operation of the power system. One of the most critical issues is reducing the total power system rotational inertia affecting the frequency control performance directly.

This chapter presents an overview of the fundamental concepts of the frequency control of the power system. It initiates describing the dynamic behaviour of the frequency. Then, it introduces a description of the parameters that define the frequency quality and outlines the principal requirements of the transmission system operator to regulate and control the frequency. Afterwards, various frequency events that occurred in different countries during recent years are presented. Finally, an overview of the optimisation algorithms used in this thesis is presented.

2.1 Introduction

The growing replacement of traditional power generation sources by RESs and the installation of power converted based technologies, knowns a DERs, is creating significant challenges to TSOs [17]. Nevertheless, in the next few years, many more significant transformations will come because it is a doubly-fed induction generator (DFIG) expected that fossil fuels-based technologies would not be used to produce electricity. Consequently, the frequency control of the power system is encountering several challenges, such as the decrease of the power system inertia [18].

The reduction of the power system rotational inertia directly negatively impacts the frequency response and can deteriorate the performance and capability of the frequency control. The high penetration of DERs and the power production variability coming from RES make challenging the balance between the power demand and power generation [19]. The poor frequency control performance can lead to significant frequency deviation, activation of UFLS scheme and at last to frequency instability [20]. Consequently, there is a constant and increasing need to develop methodologies to cope with the power system changes and enhance frequency control.

There are innumerable methodologies in the scientific literature that addresses the problem of frequency control. Recently, several methodologies are focused on emulating the inertial response of the synchronous generators by controlling the active power output coming from the power converter-based technologies. The fast response of power converter based technologies makes this a promising solution because the active power injection into the power system can be done in a short time, providing frequency support [21]–[26]. Furthermore, the control of the demand response is also an attractive solution to the frequency control of the power system. The demand response involves the control of loads and flexible demand-side units. It takes advantages of the monitoring, computing and communication technologies to control the switching of the loads in response to a power imbalance [27]–[30]. Lastly, several methodologies are focused on the local frequency estimation [31]–[33].

2.1.1 Contribution

The principal contributions of this chapter are described below.

1. Provides the mathematical context of the dynamic behaviour of the frequency.
2. Identification of four indicators derived from the parameters that define the frequency quality. These indicators can be used for frequency response assessment purposes.
3. Highlight the principal requirement for frequency regulation and control in Europe and North America.

2.2 Dynamic behaviour of the frequency

The electromechanical dynamics of a synchronous generator motion can be described using Newton's second law by relating the inertia torque to the difference between the driving mechanical torque of the turbine and the opposing electrical torque of the synchronous generator acting on the shaft attached to the rotor:

$$J\frac{d^2\theta_m}{dt^2} = T_m - T_e \tag{2.1}$$

where J is the total moment of inertia of the turbine and synchronous generator attached to the shaft in kg·m^2, θ_m is the angular displacement of the rotor in radians regarding a fixed angular reference. T_m is the driving mechanical torque of the turbine in N·m, T_e is the opposing electrical torque of the synchronous generator in N·m.

Assuming the angular reference is chosen in a synchronous-rotating-reference frame with constant angular speed (ω_0), the angular displacement of the rotor can be written as

$$\theta_m = \omega_0 t + \delta_m \tag{2.2}$$

where δ_m is the initial angular displacement of the rotor measured in the synchronous-rotating-reference frame. Substituting (2.3) in (2.1) and multiplying both sides of the resulting expression by the mechanical angular speed of the shaft (ω_m) yields the so-called swing equation.

$$M\frac{d^2\delta_m}{dt^2} = P_m - P_e \tag{2.3}$$

where $M = J\omega_m$ is the angular momentum in J·s, P_m is the input mechanical power to the synchronous generator coming from the turbine in watts, and P_e is the output electrical power of the synchronous generator in watts. The angular momentum is not rigorously constant. During a disturbance, M experiences small variation due to ω_m does not have large deviations regarding ω_0; as a consequence, M is computed assuming $\omega_m \approx \omega_0$, and it is presumed it remains constant. Moreover, it is related to the kinetic energy stored in the rotating masses and therefore can be computed as

$$M = J\omega_0 = \frac{2E_k}{\omega_0} \tag{2.4}$$

where $E_k = 1/2J\omega_0^2$ is the kinetic energy in Joule. Another quantity related to M is the inertia constant (H). Physically, it represents the number of seconds that the

synchronous generator keeps rotating at nominal speed (ω_0) when a difference between P_m and P_e occurs. H is the ratio between kinetic energy stored in the synchronous generator and its three-phase rated apparent power (S_0). Consequently, the swing equation defined in (2.3) can be rewritten in terms of H as in the subsequent expression.

$$\frac{2HS_0}{\omega_0}\left(\frac{d^2\delta_m}{dt^2}\right) = P_m - P_e \tag{2.5}$$

where H is in s, ω_0 in rad/s, δ_m in rad, P_m and P_e are in watts, S_0 in VA.

The electrical angle (δ) of the rotor is related to its mechanical quantity, δ_m, through the number of pole pairs of the synchronous generator as $\delta=(p/2)\delta_m$. Therefore, the swing equation can be rewritten for synchronous generators with *p* number of pole pairs as

$$\frac{2H}{\omega_0}\left(\frac{d^2\delta}{dt^2}\right) = P_m - P_e \tag{2.6}$$

where H is in s, ω_0 in rad/s, δ_m in rad, P_m, and P_e are in pu. The equation (2.6) is the most common nonlinear expression of swing equation used to describe the dynamics of the motion of the rotor and the interaction of the mechanical and electrical power.

The swing equation stated in (2.6) is a second-order differential equation which can be split into two first-order differential equations as:

$$\frac{d\delta(t)}{dt} = \omega(t) - \omega_0 \tag{2.7}$$

$$\frac{d\omega(t)}{dt} = \frac{\omega_0}{2H}\left(P_m - P_e\right) \tag{2.8}$$

The equation (2.7) outlines the rate of change of the electrical angle, and it is directly proportional to the deviation of the electrical speed (ω) from its nominal value (ω_0). Whilst, the equation (2.8) describes the rate of change of electrical speed, and it is proportional to the power imbalance multiplied by the inverse of the constant of inertia. Given the relationship between the electrical speed and the frequency, i.e., $\omega=2\pi f$, the equation (2.8) can be written as [34]:

$$\frac{df}{dt} = \frac{f_0}{2H}\left(P_m - P_e\right) \tag{2.9}$$

where f_0 is the nominal frequency.

2.2.1 Frequency of the centre of inertia

The frequency response of a power system with a single synchronous generator is unique. However, power systems have multiple generators and are highly meshed. Therefore, the frequency response following a disturbance may be different throughout the power system due to the frequency response of the synchronous generator depends on the location of the disturbance. Therefore, it is helpful to have an indicator that characterises the overall frequency of the power system. The frequency of the centre of inertia (f_{COI}) is defined as the weighted average of the frequencies of all synchronous generators connected to the power system. Mathematically speaking, f_{COI} is written as [35]:

$$f_{\mathrm{COI}} = \frac{\sum_{i=1}^{n_{SG}} H_i f_i}{\sum_{i=1}^{n_{SG}} H_i} \tag{2.10}$$

where H_i and f_i are the inertia constant and frequency of the i-th generator, respectively. n_{SG} is the number of synchronous generators connected to the power system.

2.3 Frequency quality parameters

The frequency is one of the main parameters of the power system providing relevant information about the ratio of power generation (P_G) to power demand (P_d). It can be used as the measure of the instantaneous balance between P_G and P_d. Therefore, the instantaneous imbalance or difference between these two quantities produces a continuous variation of the frequency. The TSOs attempt to correct the power imbalance and limit the frequency variation by considering different stages of frequency management, as shown in Figure 2.1.

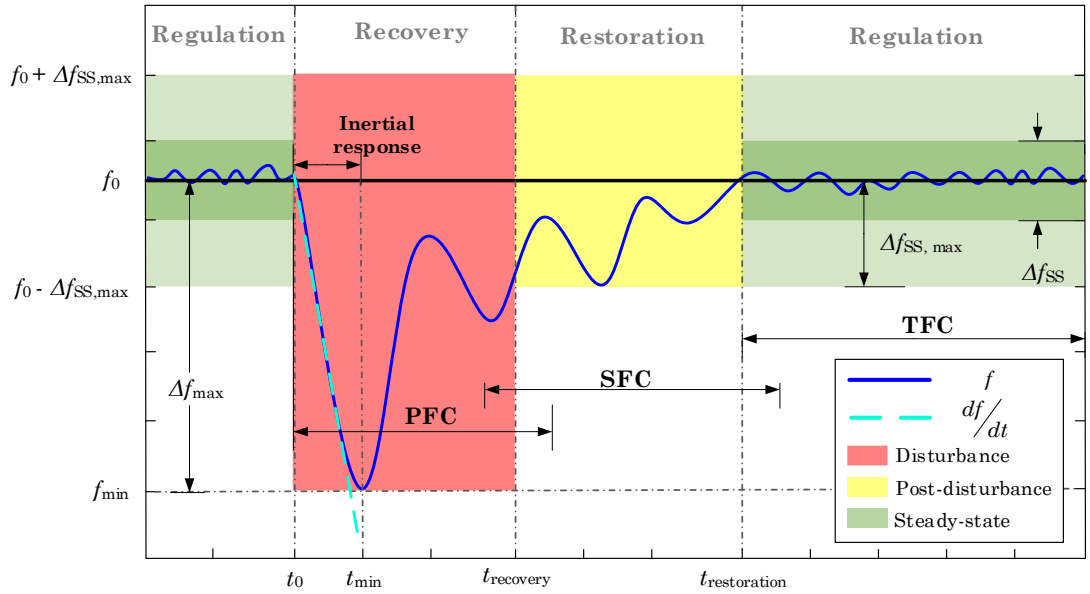

Figure 2.1. Representation of the frequency management stages.

The frequency regulation stage is carried out when the power system is in normal or steady-state operation. The frequency is regulated to be within the standard frequency range (Δf_{SS}) and does not exceed the maximum steady-state frequency range ($\Delta f_{SS,max}$). Meanwhile, following a disturbance, the frequency should not reach values outside the maximum instantaneous frequency deviation (Δf_{max}). Therefore, the frequency recovery stage occurs to return the frequency into the $\Delta f_{SS,max}$ within a specific time recovery range ($t_{recovery}$), measured from the beginning of the disturbance until the frequency is inside $\Delta f_{SS,max}$. In this stage, the PFC takes actions. Finally, the frequency restoration stage is activated to re-establish the frequency close to the nominal value (f_0) inside the Δf_{SS} range within a specific time restoration range ($t_{restoration}$). In this stage, the secondary frequency control (SFC) is activated. The tertiary frequency control (TFC) can be activated if required.

The TSOs of the power system defines a set of frequency quality parameters to ensure the frequency quality in both steady-state operations and after a disturbance. The frequency quality parameters are those involved in the frequency management stages (Δf_{SS}, $\Delta f_{SS,max}$, Δf_{max}, $t_{recovery}$, $t_{restoration}$). Table 2.1 presents the requirements of the TSOs of Europe and North America for the frequency quality parameters.

Table 2.1. Frequency quality parameters in Europe and North America [36], [37].

Frequency quality indicator	Europe synchronous area				North America
	Continental Europe	*Grain Britain*	*Ireland*	*North Europe*	
f_0 (Hz)	50				60
Δf_{SS} (Hz)	±0.05	±0.2	±0.2	±0.1	±0.05
$\Delta f_{SS,max}$ (Hz)	0.2	0.5	0.5	0.5	0.5
Δf_{max} (Hz)	0.8	0.8	1.0	1.0	--
$\Delta f_{recovery}$ (Hz)	not used	$\Delta f_{SS,max}$	$\Delta f_{SS,max}$	not used	$\Delta f_{SS,max}$
$t_{recovery}$ (s)	not used	60	60	60	60
$\Delta f_{restoration}$ (Hz)	not used	Δf_{SS}	Δf_{SS}	Δf_{SS}	Δf_{SS}
$t_{restoration}$ (min)	15	10	20	15	10

2.3.1 Classic frequency control levels

The frequency management stages (regulation, recovery and restoration) described above involve the action of three frequency controls: primary frequency control (PFC), secondary frequency control (SFC) and tertiary frequency control (TFC).

PFC act right after a disturbance is detected; first, it provides a combined response of the kinetic energy stored in rotating masses (known as the inertial response) and load damping to arrest the frequency deviation. This phase acts from the time the disturbance starts until the maximum instantaneous frequency deviation is reached (Δf_{max}). Then, the governors of the synchronous generators in the control area are activated and change the position of the turbine valvule in proportion with the sensed frequency deviation to adjust the power of the synchronous generators and start to stabilise the frequency. Furthermore, SFC consists of activating the automatic generation control and the manual control dispatch. It takes actions within minutes after the disturbance occurs. Lastly, TFC entails the change of the synchronous generators setpoint of power dispatch to replenish the power reserves used at the SFC level. Moreover, it implies the optimal distribution of load to ensure sufficient energy reserves, and the

frequency is inside the standard frequency range. TFC acts in a timescale from few minutes to hours after the disturbance occurs.

2.3.2 Frequency quality indicators

The parameters that define the frequency quality described in Table 2.1 are used to define the frequency quality indicators employed in this thesis to assess the frequency response.

2.3.2.1 Minimum frequency

The minimum frequency ($f_{\min}$) represents the minimum instantaneous value that the frequency reaches during the dynamic frequency response after a disturbance occurs (if the power system is frequency stable). The minimum frequency is related to the maximum instantaneous frequency deviation ($\Delta f_{\max}$) that the frequency attains after a disturbance. Therefore, it is calculated as:

$$f_{\min} = f_0 - \Delta f_{\max} \tag{2.11}$$

where f_0 is the nominal frequency in Hz.

2.3.2.2 Minimum time

The minimum time ($t_{\min}$) is the time at which the frequency reaches its maximum instantaneous deviation ($\Delta f_{\max}$) and, therefore, its minimum instantaneous value $f_{\min}$.

2.3.2.3 Rate of change of frequency

The rate of change of frequency is defined as the speed at which the frequency deviates from its nominal value (f_0) following disturbance. Its unit is given in hertz per second (Hz/s). ROCOF is represented by the equation (2.9).

$$ROCOF = \frac{df(t)}{dt} = \frac{f_0}{2H}\left(P_m - P_e\right) \tag{2.12}$$

ROCOF is a very important variable of the power system. After a disturbance occurs, if the power imbalance is slight and/or the power system has a high level of inertia, it is

expected a low value of ROCOF, meaning slow and minor frequency decaying. In contrast, a very large power imbalance and/or a low level of inertia in the power system results in a high value of ROCOF, indicating the frequency is dropping fast and moving away from the permissible frequency ranges (Δf_{SS} and $\Delta f_{\mathrm{SSmax}}$). Furthermore, if the ROCOF value is too high, the frequency will drop too fast to dangerous values that the controls to arrest the frequency drop will not have time to act. Numerous strategies for frequency control purposes are designed to act based on ROCOF values. Consequently, it is essential to evaluate the methods for computing the ROCOF, considering the noise added to the frequency signals by real measuring devices. It can be done using historical data of frequency or implementing a real-time simulations framework to obtain the frequency measurements, as was done in publication **[P16]**.

2.3.2.4 Steady-state frequency

The steady-state frequency (f_{SS}) is defined as the value at which the frequency settles down after the frequency control actions take place when a disturbance occurs. Theoretically, the frequency deviation is zero when the power system is in steady-state operation, and therefore, the frequency is assumed to be at its nominal value. However, there are continuous frequency variations in a real power system because the power demand fluctuation causes constant power imbalances. Consequently, the frequency is allowed to variate within a range, and the steady-state frequency is defined as

$$f_{\mathrm{SS}} = f_0 \pm \Delta f_{\mathrm{SS,max}}, \text{ when } t \to \infty \tag{2.13}$$

The steady-state frequency as a frequency quality indicator provides a measure of the capability of the power system to restore the frequency following a power imbalance.

2.4 Power system operation states

The definition of the power system operation states in terms of frequency is based on the frequency deviation level and are described in Table 2.2. The European network of transmission system operators for electricity in the operational and security network code defines three power system operation states: normal, alarm and emergency [38].

The power system operates without any disturbance in the normal operation state, and the frequency deviation is allowed to variate inside Δf_{SS}. In this operation state, frequency control actions are not required. Furthermore, the alarm operation state occurs when there is a mismatch between the power demand and power generation, and the frequency deviation is more significant than $\Delta f_{\mathrm{SS,max}}$. In this operation state, frequency control actions are required, PFC is activated, and in this timescale can also provide frequency regulation the power converter-based technologies enabled with fast frequency response (FFR) control. The activation of SFC and TFC may occur if PFC and FFR are not enough to correct the frequency deviation. Finally, the emergency operation state is when a sudden disconnection of a power generation unit or connection of an unscheduled large load occurs. The action of the PFC, SFC, TFC and FFR, are entitled to arrest the frequency deviation. However, if the frequency drops depth during the PFC timescale, the activation of the emergency controls occurs. The emergency controls include all control and protection schemes necessary to re-establish the frequency. The emergency control typically used to stop the frequency deviation is the UFLS scheme. The UFLS is designed to restore the balance between power generation and power demand by performing a controlled load disconnection.

Table 2.2. Summary of the power system operation states.

Operation state	Description	Frequency deviation	Frequency control actions
Normal	Non-contingency: mismatch between power generation and power demand	$\Delta f < \Delta f_{\mathrm{SS}}$	--
Alert		$\Delta f > \Delta f_{\mathrm{SS,max}}$	PFC, FFR, SFC
Emergency	Sudden disconnection of one or multiple power generation units or non-scheduled power demand connection	$\Delta f > \Delta f_{\max}$	PFC, FFR, UFLS, SFC and TFC

2.5 Frequency events in different power systems

This section introduces some frequency events that occurred in different countries. The idea is to illustrate the main challenges that the TSOs cope with when a frequency event

occurs. Furthermore, it is intended to show the frequency response and the frequency control actions the TSOs took to restore the frequency inside permissible limits.

2.5.1 Italian blackout: 28th September 2003

The Italian blackout of 28th September 2003 was mainly caused by the tripping of transmission lines connected the Italian network with the Continental Europe synchronous area through Austria and Switzerland. The transmission lines disconnection produced the Italian network to lose synchronism with the Continental Europe synchronous area and be isolated around 12 seconds. After the Italian network isolation, the primary frequency control and the automatic load shedding acted and stopped the frequency drop at 49 Hz [39]. However, during the last stage of load shedding, additional generation units were tripped due to inappropriate under-voltage load shedding operation. The frequency continued declining until it reached the UF threshold at 47.5 Hz, and the system collapsed in around 150 seconds after the separation of the Continental Europe synchronous area [40]. The measured frequency during the frequency event is depicted in Figure 2.2.

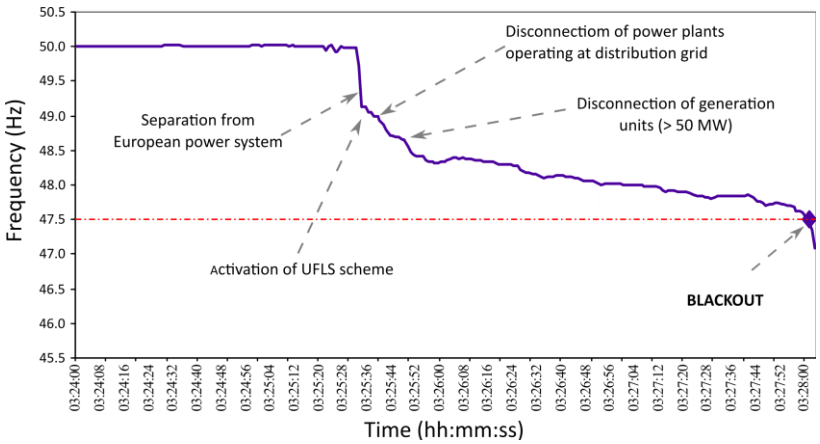

Figure 2.2. Frequency response of the blackout of Italian network on 28th September 2003.

2.5.2 Mongolian under-frequency event: 29th June 2018

The steady-state operation of the Mongolian power system (MPS) has been very close to the stability limits in recent time, which makes it vulnerable when a disturbance occurs. This stressed operation mode mainly contributed to the latest significant UF-event in the Mongolian power system. During the night of 29th June 2018, the MPS had

a power demand of approximately 535 MW and power production of approximately 380 MW coming from coal-fired and wind power plants. During that night, strong wind gusts produced a single phase to ground fault in two transmission lines that interconnect the MPS to the Russian power system. At 23:02, the MPS is separated from the Russian power system causing a power deficit of around 155 MW. Following the isolation of the Mongolian power system, the frequency starts to decline rapidly, reaching a minimum value of 48.4 Hz at 23:03. The low values of the frequency caused the activation of the UFLS scheme, and the frequency was recovered to 49.7 Hz. After a while, the frequency begins to decline again, reaching a value of 48.7 Hz at 23:05. Consequently, the TSOs manually disconnected several loads resulting in an over-frequency condition. The track of the frequency response during the frequency disturbance is depicted in Figure 2.3.

The frequency decline after the activation of UF-relays reveals the poor performance of the current UFLS scheme of the Mongolian system power system, as demonstrated in publications **[P9]** and **[P13]**.

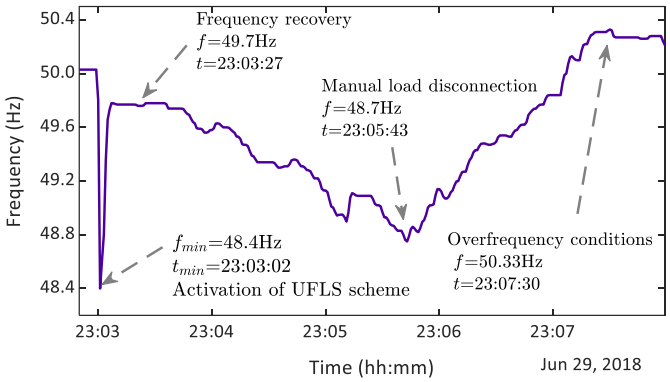

Figure 2.3. Measured frequency in Mongolian power system during the under-frequency event of 9th August 2019.

2.5.3 Great Britain under-frequency event: 9th August 2019

The most recent frequency event in the Great Britain power system occurred on the afternoon of 9th August 2019. The report of the frequency event provided by the National Grid Electricity System Operators indicated that the cause of the frequency declining was the sudden disconnection of two power generation sources. At 16:52, a lightning strike produced the unexpected disconnection of a wind farm and power plant

based on a steam turbine. The total power generation was 1,131 MW and produced a frequency deviation of around 1.3 Hz [41].

The frequency decline caused the disconnection of several DERs due to the activation of its ROCOF protection. These DERs disconnections maximised the frequency deviation, leading the frequency to reaches a minimum frequency of 49.08 Hz. The National Grid Electricity System Operators (NGESO) activated and used most of the power system frequency reserves, including the energy storage system, to recover the frequency to around 49.27 Hz at 16:53. Nevertheless, two power generation units based on a gas turbine of approximately 400 MW were disconnected due to high-pressure conditions. After the disconnection, the frequency starts to drop, reaching a value of 48.7 Hz and activating the UFLS scheme. The total power demand disconnection after the action of the UFLS scheme was around 1.0 GW. Finally, the frequency was recovered inside Δf_{SS} at 15:01. The measured frequency response during the frequency event is shown in Figure 2.4.

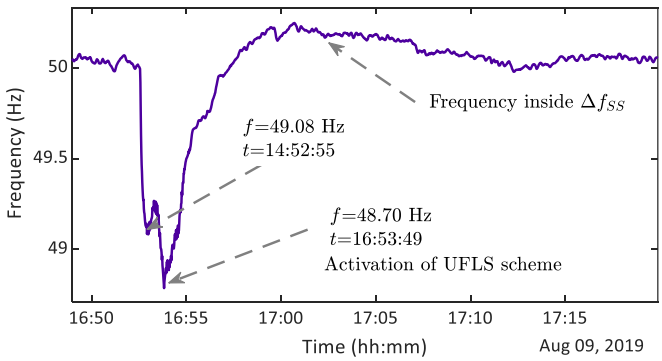

Figure 2.4. Measured frequency in Great Britain power system during the under-frequency event of 9th August 2019.

2.5.4 Continental Europe synchronous area separation: 8th January 2021.

On 8th January 2021, at 14:04:25 CET, the disconnection of several transmission network elements, starting in Croatia and going through Serbia, the border between Romania and Ukraine down to the Mediterranean Sea, place Europe close to a major blackout. The sequence of cascading disconnections causes the Continental Europe synchronous area to separate into two areas: North-West Area and South-East Area. During the event, the control actions were carried out in joint coordination between the frequency

leaders of each area, EMS (Serbia) in the South-East Area and Amprion (Germany) in the North-West Area [42].

In North-West Area, the frequency dropped down to 49.74 Hz within around 15 seconds. Consequently, TSOs initiate the disconnection of around 1.7 GW of the contracted interruptible services in France and Italy to reduce the frequency deviation. Moreover, the automatic supportive power was automatically activated, and the North-West Area received 595 MW from Nordic and Great Britain synchronous areas. These control actions produced a frequency recovering at a steady-state value of around 49.84 Hz. Meanwhile, in South-East Area, the frequency initially increased to a value of up to 50.6 Hz, producing a large over frequency condition. The automatic and manual corrective actions were activated to reduce the power supply of the generation units and return the steady-state frequency between 50.2 Hz and 50.3 Hz. Finally, the contracted interruptible services in North-West Area were reconnected at 14:48 CET, and the separated areas are reconnected at 15:08 CET. The frequency measured during the event is shown in Figure 2.5.

The frequency recovery into safe operational range on both North-West South-East Area was due to the correct performance of frequency control schemes. However, other techniques, like identifying generator clustering and islanding conditions, establish in publication **[P15]**, maybe took place to successfully separate the Continental Europe synchronous area and preserve the continuity of electrical service.

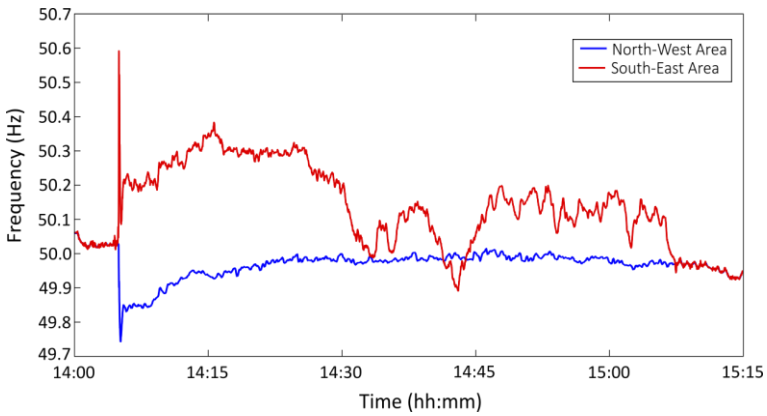

Figure 2.5. Measured frequency in North-west and south-east areas of continental Europe synchronous area during the event of 8th January 2021.

2.6 Optimisation algorithms overview

The optimisation algorithms have been widely used in various disciplines such as economics, biology, medicine, computer science, engineering, among others [43]. In general, an optimisation algorithm performs a search in a feasible solution space to find the optimal value of one or multiple variables of an optimisation problem. The goal of the optimisation problem is to minimise or maximise one or several mathematical equations called objective function [44].

The optimisation algorithms are commonly classified into three groups: deterministic algorithms and heuristic algorithms, and meta-heuristic algorithms. The deterministic algorithms follow a specific sequence of actions that the decision variables and objective function can repeat the same solution path. Whiles the heuristic algorithms are designed for solving specific optimisation problems and are not appropriate for another type of optimisation problem than the ones it is designed for solving. Lastly, the meta-heuristic algorithms are designed as a general problem solver capable of adapting for different categories of optimisation problems. A non-exhaustive classification of the optimisation algorithms is depicted in Figure 2.6.

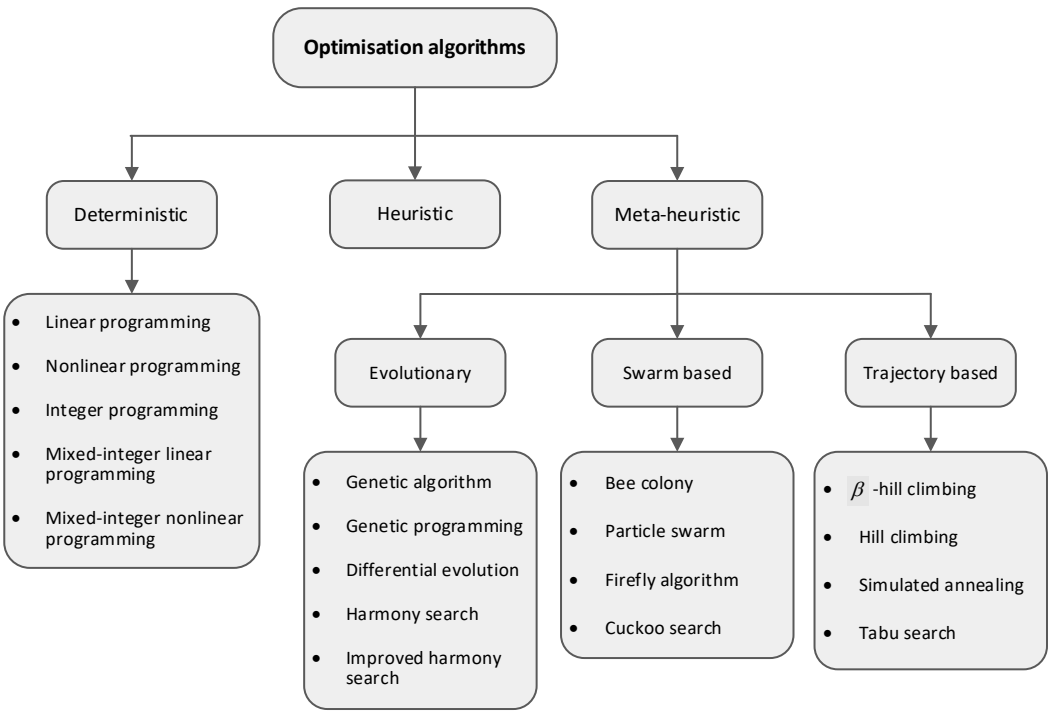

Figure 2.6. Classification of the optimisation algorithms [44], [45].

2.6.1 Optimisation problem definition

The optimisation problems are classified as continuous, discrete and mixed. In this thesis, the problems to be solved are continuous optimisation problem class. The continuous optimisation problem is formulated as a standard constrained nonlinear programming problem as follows:

$$\min_{\mathbf{x}} \left[f(\mathbf{x}) \right] \tag{2.14}$$

subject to:

$$\begin{aligned} g_i(\mathbf{x}) &\le 0 \qquad \forall\ i=1,2,...,n_{\text{ineq}} \\ h_j(\mathbf{x}) &= 0 \qquad \forall\ j=1,2,...,n_{\text{eq}} \\ x_{l,k} \le x_k &\le x_{u,k} \quad \forall\ k=1,2,...,n_x \end{aligned}$$

where $f(\mathbf{x})$ is the function to be minimised, known as the objective function, the vector $\mathbf{x}$ is the vector decision variables. It contains n_x the decision variables of the optimisation problem. $g_i(\mathbf{x})$ represents the i-th inequality constraint and $h_j(\mathbf{x})$ is the j-th equality constraint. Lastly, $x_{u,k}$ and $x_{l,k}$ are the upper and lower boundaries of the k-th decision variable.

2.6.2 Algorithms to solve optimisation problems

In this thesis, three optimisation algorithms are implemented to solve the optimisation problems.

2.6.2.1 Interior-point method

The interior-point method can be used to solve linear and nonlinear optimisation problems. It typically involves the reformulation of the optimisation problem as the minimisation of a linear function with specific constraints [46]. The interior-point method is intended to solve constrained optimisation problems as defined in (2.14) by transforming it into a linear function and solving a sequence of approximate minimisation problems. The nonlinear programming problem defined in (2.14) is transformed into an approximate problem by incorporating slack variables (s) and is written as [47], [48]:

$$\underset{\mathbf{x},s}{\text{minimise}} \qquad f^*(\mathbf{x}), \qquad \text{where} \qquad f^*(\mathbf{x}) = f(\mathbf{x}) - \mu \sum_{i=1}^{n_{\text{ineq}}} \ln(s_i) \tag{2.15}$$

subject to:

$$\begin{aligned} \mathrm{g}_i(\mathbf{x}) + s_i &= 0 \qquad \forall\ i=1,2,...,n_{\text{ineq}} \\ h_j(\mathbf{x}) &= 0 \qquad \forall\ j=1,2,...,n_{\text{eq}} \\ s_i &\geq 0 \end{aligned}$$

where the term $\mu \sum_{i=1}^{n_{\text{ineq}}} \ln(s_i)$ is called a barrier function s_i is the i-th slack variable and μ is the barrier parameter. The number of slack variables is the same as the number of inequalities constraints. It is constrained to be positive to ensure it is inside the feasible region throughout the iterations. This method assumes that as μ tends to zero the minimum of the approximate function, $f^*(\mathbf{x})$ and $f(\mathbf{x})$ tend to be equal.

The equation (2.15) represents an approximated problem with a sequence of equality constraints. Therefore, the equality constraints can be consolidated in a vector as $\mathbf{C}(\mathbf{x})=[\mathbf{h}(\mathbf{x})\ \mathbf{g}(\mathbf{x})+\mathbf{s}]$. The linear combination of the objective function, $f(\mathbf{x})$ and the equality constraint's function, $\mathbf{C}(\mathbf{x})$, can be represented by the Lagrange function as [47], [48]:

$$L(\mathbf{x},\boldsymbol{\lambda}) = f(\mathbf{x}) - \sum_{k=1}^{n_C} \lambda_k c_k(\mathbf{x}) \tag{2.16}$$

where λ is the Lagrange multiplier, $c_k(\mathbf{x})$ is the k-th equality constrain, and n_C is the total number of equality constraints. Assuming the $f(\mathbf{x})$ and $\mathbf{C}(\mathbf{x})$ are twice differentiable functions, $\mathbf{x}^*$ is the first-order point if there is a Lagrange multiplier vector ($\boldsymbol{\lambda}^*$) that satisfies the first order Karush-Kuhn-Tucker (KKT) conditions [47], [48]:

$$\nabla_{\mathbf{x}} L(\mathbf{x}^*,\boldsymbol{\lambda}^*) = 0 \tag{2.17}$$

$$\boldsymbol{\lambda}^* \mathbf{C}(\mathbf{x}^*) = 0 \tag{2.18}$$

$$\mathbf{C}(\mathbf{x}^*) \geq \mathbf{0} \tag{2.19}$$

$$\boldsymbol{\lambda}^* \geq \mathbf{0} \tag{2.20}$$

The interior-point algorithm performs several iterations to solve $f^*(\mathbf{x})$ and stops when the KKT conditions are satisfied. It considers two types of steps at each iteration, the direct step, also known as the Newton step, which uses linear approximations to solve $f^*(\mathbf{x})$. Furthermore, the conjugated gradient step uses a trust region approach [49].

2.6.2.2 Sequential Least-Square Programming

The sequential Least-Square programming (SLSQP) algorithm is a methodology used to solve nonlinear programming problems with the objective function and the constraint functions twice continuously differentiable [50]. If the objective function is quadratic form and the constraint functions are linear, the nonlinear programming is now named quadratic programming problem (QP). The general model of the QP problem can mathematically be written as [51]:

$$\begin{aligned} &\underset{\mathbf{x}}{\text{minimise}} \quad f(\mathbf{x}), \quad \text{where} \quad f(\mathbf{x}) = \frac{1}{2}\mathbf{x}^{\mathrm{T}}\mathbf{H}\mathbf{x} + \mathbf{c}^{\mathrm{T}}\mathbf{x} \\ &\text{subject to:} \\ &\qquad g(\mathbf{x}) = \mathbf{A}_1\mathbf{x} = \mathbf{b} \\ &\qquad h(\mathbf{x}) = \mathbf{A}_2\mathbf{x} \leq \mathbf{b} \\ &\qquad \mathbf{x} \geq \mathbf{0} \end{aligned} \tag{2.21}$$

where $\mathbf{H}$ is the Hessian matrix**,** $g(\mathbf{x})$ is the function containing the equality constraints and $h(\mathbf{x})$ is the function containing the inequality constraints. The QP problem defined in (2.21) can be solved iteratively. The Sequential QP algorithm can be summarised into five steps as following:

Step 1. Set the initial conditions of the decision variables and Hessian matrix, i.e., $\mathbf{x}_0$ and $\mathbf{H}_0$. Furthermore, define the permissible errors ε_1 and ε_2.

Step 2. Construct the QP subproblem to obtain the search direction vector $\mathbf{d}_k$ in the k-th iteration.

Step 3. Evaluate whether the termination criterion is fulfilled. If the equation defined in (2.22) is satisfied, the vector of decision variables $\mathbf{x}_k$ is

considered the solution of the nonlinear programming problem, and the algorithm ends. Otherwise, continue with the next step.

$$\begin{aligned} &\left\|\mathbf{d}_k\right\|_1 \le \varepsilon_1 \\ &\left\|g(\mathbf{x}_k)\right\|_1 + \left\|h_k(\mathbf{x}_k)\right\|_1 \le \varepsilon_2 \end{aligned} \tag{2.22}$$

Step 4. Select a loss function, e.g., L1, smooth L1 test or L2 function, to calculate the search step size (α_k) in the search direction.

Step 5. Update the next iteration (k+1) using the equation defined in (2.23). Furthermore, select the method to update $\mathbf{H}_k$ and go back to Step 2.

$$\mathbf{x}_{k+1} = \mathbf{x}_k + \alpha_k \mathbf{d}_k \tag{2.23}$$

The SLSQP algorithm is based on the SQP algorithm and follows the same five steps to solve the nonlinear programming problem. It adopts the Wilson-Han-Powell method [52] to create the QP subproblem, then it uses loss function L1 to calculate the search step size (α_k). Furthermore, the SLSQP algorithm utilises the BFGS quasi-Newton method to update the matrix $\mathbf{H}$.

2.6.2.3 Improved harmony search

The improved harmony search (IHS) is a metaheuristic algorithm that follows the musical composition process. In the IHS algorithm, the decision variables of the optimisation problem represent the musicians' improvised pitches, and each solution vector is a harmony [53]. The procedure of the IHS is based on five main steps [54]:

Step 1. Initialise the IHS parameters

The IHS requires to initialise five parameters:

1. Harmony memory size (*HMS*) defines the harmony memory matrix (HM) size where the harmony vectors are stored.
2. Harmony memory considering rate (*HMCR*) defines the probability of choosing the new decision variables from the HM or create them randomly.

3. Maximum and minimum pitch adjustment rate ($PAR_{\min}$ and $PAR_{\max}$), these parameters represent the probability of the decision variable to be adjusted.
4. Maximum and minimum bandwidth ($bw_{\min}$ and $bw_{\max}$).

The number of improvisations (n_I) is an integer number that indicates the number of times the objective function will be evaluated.

Step 2. Initialise the HM with a set of random harmony vectors.

Step 3. Improvisation of the new harmony.

The new harmony is selected from HM with probability *HMCR*, using a harmony memory selection procedure. Otherwise, the new harmony is randomly created with probability (1−*HMCR*). If the new harmony is selected from HM, it is adjusted with probability *PAR* and not adjusted with probability (1−*PAR*).

Step 4. Update the HM.

If the new harmony stored in the *HM* is better than the worst harmony, the new harmony is stored in the *HM*, and the worst harmony is removed. Otherwise, the *HM* remains unchanged. After that, the *HM* is sorted by the objective function value.

Step 5. Stop criterion.

The IHS algorithm uses n_I as a stopping criterion. If n_I is satisfied, the computation of the IHS algorithm is stopped. Otherwise, Step 2 and Step 3 are repeated.

The IHS meta-heuristic algorithm has implementations to solve power system problems, mostly applied to the optimal load flow solution. However, publication **[P7]** has been demonstrated that the IHS is an efficient tool to solve the problem of computing the optimal reactive power injection/absorption provided by power converter-based technologies in a microgrid.

2.7 Conclusion

This chapter focused on providing an understanding of the principal concepts involved in frequency control. Furthermore, it describes the optimisation algorithms implemented in this thesis. It was mathematically explained the motion equation of a synchronous generator, known as the swing equation, and how it describes the dynamic behaviour of frequency. Then, the procedure to manage the frequency in a normal operation and after a frequency event occurs was described. Furthermore, the principal parameters defined by the transmission system operators of Europe and North America were. Afterwards, the frequency control levels of the power system were described, highlighting the importance of having high levels of rotational inertia. Furthermore, various frequency event occurred in different countries were presented, the idea was emphasising the actions taken by the transmission system operators to control the frequency.

3 Statistical assessment and linear regression model of kinetic energy using GMM

Technological advances have allowed system operators to monitor and control the power system more effectively. Moreover, digital technologies have enabled the use of more robust monitoring and data acquisition mechanism; consequently, it is possible to gather an essential amount of time-series of power system variables coming from control and monitoring systems. The collected data has very important values for the system operator as the analysis of the historical data can provide relevant information about the main features and trends of the power system variables. This chapter focuses on performing a statistical assessment of historical data of the variables related to frequency control, kinetic energy, frequency and power demand. The main goal is to unveil features and patterns of the main electromechanical variables to create kinetic energy prediction models based on statistical models. This chapter presents a description of the statistical techniques and models used to assess the electromechanical variables of the power system. Then, a discussion of the relationship between the variables related to the frequency control is given. Afterwards, the methodology is used to perform the statistical assessment and implement the gaussian mixture model to clustering the time-series datasets. Subsequently, the description of the historical time series of the kinetic energy, frequency and power demand is provided. Furthermore, the results of the statistical assessment of these variables are presented. Lastly, the clustering of the time series of kinetic energy and power demand is carried out using the Gaussian Mixture Model (GMM) technique. Next, the set of linear regression models is computed and evaluated using a validation dataset. The core of this chapter is based on publication **[P4]**.

3.1 Introduction

The modern power system is inevitably experiencing a less predictable behaviour due to the increasing connection of carbon-free technologies such as RESs [55]. A particular

concern of the TSOs is the low or even absence of inertial response of the RESs compared to that provided by the synchronous generator [56], [57]. The rotational inertia available in the power system, and inherently the kinetic energy, plays a significant role in frequency control and operational security [58]. For instance, a small amount of rotational inertia in the power system directly impacts the frequency, leading to faster and deeper frequency deviations and increasing the vulnerability of the power system. Therefore, to take proper control actions and have more precise operational planning scenarios, it is necessary to have accurate and reliable methodologies that allow estimate and track the power system rotational inertia in real-time [59], [60]. It can be done by taking advantage of the digitalisation of the power system, which is evolving to integrate computing, communication and control capabilities to the real physical processes for energy production, transportation, distribution and consumption [61].

Several methodologies for the estimation of the power system rotational inertia been proposed in the scientific literature. The offline techniques are mainly based on a simplified swing equation model or based on data obtained after a disturbance or over a specific time window [62]–[67]. However, prior rotational inertia estimation is needed to perform a remedial control action. As a consequence, the online rotational inertia estimation methods try to overcome the drawback of posterior rotational inertia estimation by using the phasor measurement units to collect the data coming from the power system and combining it with other methods. For instance, [68] proposes an online rotational inertia estimation using the linearised swing equation and a sliding data window made of four filters. In [69], a methodology based on a statistical procedure employing steady-state and small frequency variations is proposed. In [70], an online-inertia estimation using a closed-loop identification method and a probed multi sine signal. Finally, in [71] and [72], a dynamic regressor and mixing procedure are used to estimate the system rotational inertia. Although inertia estimation is essential for the power system operation and security, taking advantage of the historically available data from the phasor measurement units must be analysed to extract information that allows developing new inertia estimation methods to cope with the

power system needs. For instance, publication **[P11]** uses the historical data of the kinetic energy of the NPS to create a short-term forecast model. It uses a decomposable time series model, including a trend component, a seasonal component, and an irregular component. The cross validation of the short-term forecast model produced an error below of 5% demonstrating its suitability to predict the kinetic energy.

3.1.1 Contribution

The contributions of this chapter are listed below.

1. Statistical assessment of the principal variables related to the frequency control: frequency, power demand and kinetic energy. This assessment unveils the tendency of the frequency to archives values above the nominal value and highlights the level of dependency between kinetic energy and power demand.
2. Identification of the dependence between the power demand and kinetic energy of the Nordic power system, revealing these two variables follow similar shape profiles during the day.
3. Implementation of the gaussian mixture model to cluster the time series and creating a set of linear regression models that explain the dependency between the kinetic energy and power demand.

3.2 Statistical techniques

The statistical analysis of the frequency control-related variables of the power system considers two approaches, the descriptive and inferential analysis. The descriptive statistical assessment is carried out to explain the fundamental features of the time series of each individual variable (electrical frequency, kinetic energy, and power demand). The principal indicators in the descriptive statistic are the measure of central tendency and dispersion of the dataset. Meanwhile, the inferential statistic is intended to extract information beyond the one provided by the descriptive statistics. The objective is to identify existing dependency between the variables using covariance analysis and clustering. Moreover, use prediction models to determine the most suitable model to represent such dependency.

3.2.1 Descriptive statistics

Consider a vector $\mathbf{x}$ representing a random variable of the power system. Assuming $\mathbf{x}$ contains *N* scalar observation in form $\mathbf{x} = [x_1\ x_2 \cdots x_i \cdots x_N]^{\mathrm{T}}$, the central tendency of $\mathbf{x}$ is measured by computing the mean value (μ) of the dataset as following :

$$\mu = \frac{1}{N}\sum_{i=1}^{N} x_i \tag{3.1}$$

where x_i is the i-th observation and N is the total number of observations.

The dispersion provides a measure of how spread out is the observations of a dataset. The standard deviation (σ) is the most widespread technique used to measure data dispersion. A significant value of σ indicates the observed values in the dataset are scattered out over an extensive range of values. Meanwhile, a small value of σ implies that the observed values have a tendency to be close to the mean value. The standard deviation is calculated as follows:

$$\sigma = \sqrt{\frac{1}{N}\sum_{i=1}^{N}(x_i - \mu)^2} \tag{3.2}$$

where x_i is the i-th observation and μ is the mean value of $\mathbf{x}$. Further information on the data can be obtained by computing the dispersion of the data concerning the mean value using three techniques: coefficient of variation, Kurtosis and Skewness.

The coefficient of variation (cv) provides a relative measure of data variability concerning the mean value. It is calculated as the ratio of the standard deviation and the mean value:

$$cv = \frac{\sigma}{\mu}100\% \tag{3.3}$$

The data distribution is prone to outliers. Kurtosis is a technique used to measure the degree of prone to outliers in a distribution and is computed as [73]:

$$Kurtosis = \frac{\frac{1}{N}\sum_{i=1}^{N}(x_i - \mu)^4}{\sigma^4} \tag{3.4}$$

The Kurtosis of a normal distribution is three (*Kurtosis* = 3). This value is used as a reference to determine the degree of prone to outliers in a distribution. Therefore, if the Kurtosis is greater than three (*Kurtosis*>3), the distribution is more likely to outliers. Meanwhile, if the Kurtosis is smaller than three (*Kurtosis*<3), the distribution is less prone to outliers.

The degree of asymmetry of the data around the mean value is measured by computing the *Skewness* as following [73]:

$$Skewness = \frac{\frac{1}{N}\sum_{i=1}^{N}(x_i - \mu)^3}{\sigma^3} \tag{3.5}$$

The Skewness of a perfectly symmetric distribution (normal distribution) is zero. Therefore, if the Skewness is positive, the data is spread out to the right side of the mean value. On the other hand, if the Skewness is negative, the data is more spread out to the left side of the mean value.

3.2.2 Inferential statistic

3.2.2.1 Pearson's linear correlation coefficient

Let assume the vector $\mathbf{y}$ represents a random variable of the power system and contains N scalar observations in the form $\mathbf{y} = [y_1\ y_2 \cdots y_i \cdots y_N]^{\mathrm{T}}$. The measure of linear dependence between two random variables, say $\mathbf{X}$ and $\mathbf{Y}$, is represented by the correlation coefficient (ρ) and is computed as:

$$\rho(\mathbf{x},\mathbf{y}) = \frac{\sum_{i=1}^{N}\left(x_i - \mu_{\mathbf{x}}\right)\left(y_i - \mu_{\mathbf{y}}\right)}{\sqrt{\sum_{i=1}^{N}\left(x_i - \mu_{\mathbf{x}}\right)^2}\sqrt{\sum_{i=1}^{N}\left(y_i - \mu_{\mathbf{y}}\right)^2}} \tag{3.6}$$

where x_i is the i-th observation and $\mu_{\mathbf{x}}$ is the mean value of $\mathbf{x}$. Furthermore, y_i is the i-th observation, $\mu_{\mathbf{y}}$ is the mean value of $\mathbf{y}$.

3.2.2.2 Linear regression model

Linear regression is a technique used to model the relationship between a pair of random variables, $\mathbf{x}$ as a predictor variable and $\mathbf{y}$ as a response variable, by fitting a linear equation to a set of observed data. The simple linear regression model is defined as [74]:

$$\mathbf{y}' = \beta_1 \mathbf{x} + \beta_0 + \varepsilon \tag{3.7}$$

where $\mathbf{y}'$ is a vector containing the predicted values, the vector $\mathbf{x}$ is the predictor variable, and ε is a Gaussian random error with expectation zero and variance σ^2, i.e., $\varepsilon \sim N(0, \sigma^2)$. The linear regression coefficients β_0 and β_1 are the results of solving the least square estimate and are calculated using the following equation [74].

$$\beta_1 = \frac{\sum_{i=1}^{N} (x_i - \mu_{\mathbf{x}})(y_i - \mu_{\mathbf{y}})}{\sum_{i=1}^{N} (x_i - \mu_{\mathbf{x}})^2} \tag{3.8}$$

$$\beta_0 = \mu_{\mathbf{y}} - \beta_1 \mu_{\mathbf{x}}$$

where x_i and y_i are the i-th observation of $\mathbf{x}$ and $\mathbf{y}$, respectively, moreover, $\mu_{\mathbf{x}}$ and $\mu_{\mathbf{y}}$ is the mean value of $\mathbf{x}$ and $\mathbf{y}$, respectively.

The suitability of the linear regression model is assessed by computing the goodness of fit indicators. The sum of square error (SSE) is a measure of the total deviation between the predicted values ($\mathbf{y}'$) and the response variable ($\mathbf{y}$) and is defined as:

$$SSE = \sum_{i=1}^{N} w_i (y_i - y'_i)^2 \tag{3.9}$$

where w_i is a weight applied to the i-th observation.

The R-square (R^2) indicator provide a measure of how effective the linear model is to explain the variation of the data and is calculated as the ratio of the sum of squares of the linear regression (SSR) and the total sum of squares (SST):

$$R^2 = \frac{SSR}{SST} = \frac{\sum_{i=1}^{N} w_i (y'_i - \mu_{\mathbf{y}})^2}{\sum_{i=1}^{N} w_i (y_i - \mu_{\mathbf{y}})^2} \tag{3.10}$$

The root mean square error (RMSE) is an estimation of the standard deviation of the predicted values ($\boldsymbol{y'}$) and the response variable ($\mathbf{y}$) and is defined as

$$RMSE = \sqrt{\frac{\sum_{i=1}^{N} w_i (y_i - y'_i)^2}{N}} \tag{3.11}$$

3.2.3 Gaussian Mixture Model

Assuming $\mathbf{X} \in \mathbb{R}^{N \times D}$ is a continuous-valued data vector with *N* observations and *D* dimension in each observation. The data contained in $\mathbf{X}$ can be characterised by a Gaussian Mixture Model. It is comprised of $k \in \{1, \ldots, \gamma\}$ probability density functions (PDF), where γ is the number of clusters of $\mathbf{X}$. Each PDF mathematically explains the data contained in each cluster. The GMM is a parametric PDF constructed by the weighted sum of γ PDFs as follows [75]:

$$p(\mathbf{X}) = \sum_{k=1}^{\gamma} w_k \Phi(\mathbf{X} \mid \boldsymbol{\mu}_k, \boldsymbol{\Sigma}_k) \tag{3.12}$$

where w_k is the k-th mixture weight satisfying the constraint $\sum_{k=1}^{\gamma} w_k = 1$, i.e., the sum of all weights must be equal to one. Moreover, $\Phi(\mathbf{X} \mid \boldsymbol{\mu}_k, \boldsymbol{\Sigma}_k)$ is the k-th Gaussian density function defined as

$$\Phi(\mathbf{X} \mid \boldsymbol{\mu}_k, \boldsymbol{\Sigma}_k) = \frac{1}{\sqrt{2\pi^D |\boldsymbol{\Sigma}_k|}} e^{\left\{-\frac{1}{2}(\mathbf{X}-\boldsymbol{\mu}_k)^{\mathrm{T}} \boldsymbol{\Sigma}_k^{-1} (\mathbf{X}-\boldsymbol{\mu}_k)\right\}} \tag{3.13}$$

with mean vector $\boldsymbol{\mu}_k$ $(1\times D)$, which centres the distribution all along each dimension, and the covariance matrix $\boldsymbol{\Sigma}_k$ $(D\times D)$ as

$$\boldsymbol{\Sigma}_k = \begin{bmatrix} \sigma_{11} & \sigma_{12} & \cdots & \sigma_{1j} & \cdots & \sigma_{1D} \\ \sigma_{21} & \sigma_{22} & \cdots & \sigma_{2j} & \cdots & \sigma_{2D} \\ \vdots & \vdots & & \vdots & & \vdots \\ \sigma_{i1} & \sigma_{i2} & \cdots & \sigma_{ij} & \cdots & \sigma_{iD} \\ \vdots & \vdots & & \vdots & & \vdots \\ \sigma_{D1} & \sigma_{D2} & \cdots & \sigma_{Dj} & \cdots & \sigma_{DD} \end{bmatrix} \quad \forall\ i,j = 1,2,...,D \tag{3.14}$$

where the diagonal elements represent the variance of the distribution, and the off-diagonal elements contain the correlation between the variables of the distribution. The GMM commonly accept four types of covariance matrices.

The diagonal-uniform covariance matrix assumes the dispersion is the same across all clusters do not exist a correlation between the variables in the cluster. Therefore, the elements of the covariance matrix are:

$$\sigma_{ij} = \begin{cases} \sigma^2 & \text{if } i = j \\ 0 & \text{if } i \neq j \end{cases} \qquad \forall\ k = 1,2,...,\gamma \tag{3.15}$$

The diagonal-non-uniform covariance matrix assumes the correlation between the variables in the cluster is zero, and the dispersion can vary between clusters; therefore, the matrix is diagonal but different for each cluster, and its elements are:

$$\sigma_{ij} = \begin{cases} \sigma_k{}^2 & \text{if } i = j \\ 0 & \text{if } i \neq j \end{cases} \qquad \forall\ k = 1,2,...,\gamma \tag{3.16}$$

The full-uniform covariance matrix considers the dispersion of the clusters is equal and exist a correlation between the variables in each cluster; therefore, its elements are:

$$\sigma_{ij} = \begin{cases} \sigma^2 & \text{if } i = j \\ \rho(\mathbf{x}_i, \mathbf{x}_j) & \text{if } i \neq j \end{cases} \qquad \forall\ k = 1,2,...,\gamma \tag{3.17}$$

The full-non-uniform covariance matrix allows the correlation between the variables, and the dispersion of each cluster is different. The elements of the full-non-uniform covariance matrix are:

$$\sigma_{ij} = \begin{cases} \sigma_k^{\,2} & \text{if } i = j \\ \rho(\mathbf{x}_i, \mathbf{x}_j) & \text{if } i \neq j \end{cases} \qquad \forall\ k = 1,2,...,\gamma \tag{3.18}$$

The GMM uses the expectation maximisation algorithm [76] to estimate its parameters (w_k, $\boldsymbol{\mu}_k$, $\boldsymbol{\Sigma}_k$). Furthermore, the type of covariance matrix and the number of clusters (γ) are user-defined parameters.

3.3 Electromechanical variables related to the frequency control

The steady-state operation of a loss-less synchronous machine requires the mechanical power (P_{m}) must be equal to the electrical power (P_e) to comply with the conservation of energy, i.e., $P_m - P_e = 0$. However, the inherent dynamic of the load is constantly changing the power demand and creating power imbalances between the mechanical power and the electrical power, i.e., $P_{\mathrm{m}} - P_e \neq 0$. As a consequence, an exchange of energy is produced between the kinetic energy stored in the rotating masses and the power system to restore the power imbalance between P_m and P_e. These energy exchanges produce changes in the rotor speed (accelerating/decelerating), producing fluctuations in the power system's frequency. The relation of these electromechanical variables (frequency, power and rotational inertia) is described by the swing equation [77]:

$$\frac{df(t)}{dt} = \frac{f_0}{2H}\left(P_m - P_e\right) \tag{3.19}$$

where f_0 is the nominal electrical frequency in pu, H is the inertia constant in s, P_m and P_e are the mechanical power and electrical power in pu, respectively. The inertia constant provides a measure of the energy stored in the rotating masses and can be calculated as the ratio of the kinetic energy and the apparent nominal power[78]:

$$H = \frac{E_{\mathrm{k}}}{S_0} = \frac{\frac{1}{2} J \omega_0^2}{S_0} \tag{3.20}$$

where E_{k} is the kinetic energy in W·s, J is the moment of inertia in kg·m^2, ω_0 is the nominal speed in rad/s, and S_0 is the apparent nominal power in pu. The swing equation can be rewritten in terms of kinetic energy by substituting (3.20) in (3.19):

$$\frac{df}{dt} = \frac{f_0 S_0}{2E_{\mathrm{k}}}\left(P_m - P_e\right) \tag{3.21}$$

From (3.21) can be deducted that the variability of the electrical frequency depends on the ratio of the size of disturbance ($\Delta P = P_{\mathrm{m}} - P_e$) and the amount of kinetic energy available in the power system. Following an imbalance, if the amount of kinetic energy is greater than the power imbalance, the frequency deviation will be small. On the other hand, if the amount of kinetic energy is smaller than the power imbalance, the frequency deviation will increase, and additional frequency control mechanisms, such as PFC and SFC, are activated to restore the imbalance and stop the frequency deviation. Meanwhile, when the power system is in steady-state operation, the frequency variation is inside the standard frequency range (Δf_{ss}). Therefore, assuming the *df*/*dt* is constant inside Δf_{ss}, and the power demand profile contains all possible imbalances during the steady-state operation, the relationship between the power demand and the kinetic energy can be represented by the linear regression model defined in (3.7). Previous studies have revealed that the power demand has been correctly modelled by using the GMM [79]. Consequently, it is presumed that the GMM can also model the kinetic energy, and, therefore, it can be explained by a mixture of γ linear regression models.

$$E_{\mathrm{k},k}(P_{d,k}) = \beta_{1,k} P_{d,k} + \beta_{0,k} \tag{3.22}$$

3.4 Methodology to implement the GMM

This section describes the procedure used to compute the linear regression mixture to model the dependency between kinetic energy and power demand.

3.4.1 Raw data preparation

The electromechanical variables related to the frequency control are collected from historical data publicly available. The data is stored with a timestamp. Therefore, the data structure consists of one column containing the timestamp (YYYY-MM-DD hh:mm:ss) and another column containing the measured values. The historical data is gathered using real-time measurements coming from supervisory control and data acquisition (SCADA) infrastructure and recently from a wide-area measurement system (WAMS). As a consequence, the time series may have gaps and atypical values due to telecommunication errors. Therefore, the raw time series is assessed to identify and fill the missing data using the linear interpolation method [80].

3.4.2 Resampling

The measurements of the electromechanical variables are generally taken at a sampling frequency that depends on the equipment/application requirements in which it will be used. Consequently, the time series of each variable is resampled to be in the exact time resolution (one-minute resolution, one-hour resolution). In this chapter, the method used to resample is linear interpolation.

3.4.3 GMM setup

GMM requires a prior setup of two parameters, the number of clusters at which the data set will be split and the type of covariance matrix (diagonal-uniform, diagonal-non-uniform, full-uniform or full-non-uniform) to be used. The appropriate number of clusters and type of covariance matrix of the GMM, which best model the dependency between kinetic energy and power demand, are determined by following an interactive procedure due to the fitting procedure of the GMM is no deterministic. The criteria used to select the parameters is based on two techniques: Akaike information criterion (AIC) and Bayesian information criterion (BIC). AIC and BIC are mathematical techniques used to evaluate how well a model fits the data. It can be used to determine the trade-off between the fit and complexity of the model. A lower AIC or BIC value indicates the best fitting of the model [81].

Consequently, the number of clusters and the type of covariance matrix will be selected by evaluating the GMM with several sets of parameters, i.e., considering 1, 2, 3, …, γ clusters and the four types of covariance matrices, to obtain the value of AIC and BIC. The set of parameters that produces the lower value of AIC and BIC will be selected as the best GMM parameters.

3.4.4 Computing GMM parameters and creating linear regression mixture

The GMM parameters are setting with the number of clusters and type of covariance matrix obtained after the GMM setup procedure. Then, the EM algorithm is performed to estimate the parameters of each distribution of the GMM ($w_{k,}$ $\boldsymbol{\mu}_{k,}$ $\boldsymbol{\Sigma}_{k}$). Afterwards, $w_{k,}$ $\boldsymbol{\mu}_{k}$ and $\boldsymbol{\Sigma}_{k}$ are used to compute the linear regression coefficients $\beta_{0,k}$ and $\beta_{1,k}$ of the k-th linear regression model defined in (3.22).

3.5 Data description

The electromechanical variables directly involved in the frequency control, i.e., frequency, kinetic energy and power demand, are considered to perform the statistical analysis and evaluate the methodology proposed in the previous section. Therefore, the historical data publicly accessible of the NPS is used. The three electromechanical variables data is collected consisting of time series of frequency, kinetic energy and power demand from the year 2016 to the year 2020. The time series of the frequency and kinetic energy is gathered from the open database of Finland's TSO company (Fingrid) [82]. Furthermore, the raw time series of the power demand is obtained from the Nord Pool company [83] since Fingrid does not publish the power demand data of the Nordic power system. The principal characteristics of the electromechanical variables are presented in Table 3.1.

Table 3.1. Principal characteristics of the time series of electromechanical variables of the Nordic power system.

Characteristics	Electromechanical variable		
	Frequency, f	***Kinetic energy, E_k***	***Power demand, P_d***
Counts	1,578,528,000	2,630,880	43,848
Time resolution	0.1-second	one-minute	one-hour
Missing values	1.07%	0.67%	2.51%
Outliers	0.5%	0%	0.05%

From Table 3.1, it can be observed that the proportion of missing data and outliers are negligible, and the data set is suitable to perform the statistical analysis.

3.6 Statistics of the time-series

This section is dedicated to carrying out a statistical assessment of the time series of the frequency, kinetic energy and power demand to extract the most important features and patterns that may be useful to develop new prediction models.

3.6.1 Frequency

The time series of the frequency (*f*) from January 2016 to December 2020 with a resolution of 0.1-second is depicted in Figure 3.1.

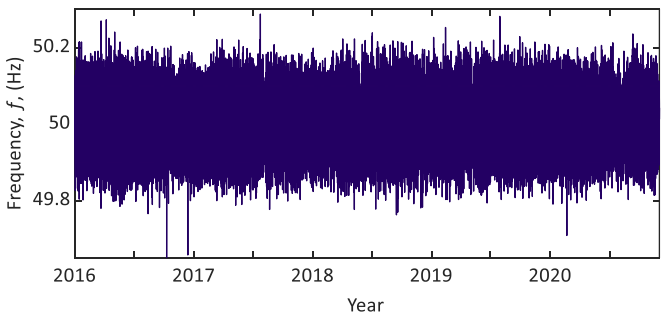

Figure 3.1. Time-series of frequency of five years (2016-2020) of historical data of NPS.

The frequency variation around its nominal value can be easily determined and interpreted by computing the average value and the standard deviation of the frequency. However, other statistical indicators can provide relevant information. The yearly descriptive statistic of the frequency is presented in Table 3.2. The mean value demonstrates the overall yearly frequency is slightly increasing, and the standard

deviation is inside the standard frequency range, Δf_{ss} =±0.1 Hz. However, the maximum and minimum values indicating the frequency has taken values outside $\Delta f_{ss.}$ Furthermore, Skewness of the frequency data around the mean value indicates the frequency values are spread out above the nominal frequency. Kurtosis indicates the frequency is prone to have values above nominal frequency.

Table 3.2. Descriptive statistics of the frequency of the NPS.

Statistical parameters	**Year**				
	2016	***2017***	***2018***	***2019***	***2020***
Mean, μ	50.002	50.002	50.003	50.004	50.006
Std., σ	0.0453	0.0439	0.0437	0.0443	0.0407
Minimum	49.6480	49.7770	49.7630	49.7940	49.7090
Maximum	50.2730	50.2880	50.2390	50.2820	50.2360
Skewness	0.0508	0.0190	0.0412	0.0430	0.0416
Kurtosis	3.1103	3.1168	3.2441	3.1953	3.3987

The NPS frequency's probability density and cumulative distribution function for the years examined reveals a bell-shaped distribution with few peaks around the nominal frequency of 50 Hz, as shown in Figure 3.2. The probability density and cumulative distribution function reveal the asymmetry of the data and the propensity to have values greater than the mean value. It can be attributed to the integration of RESs in the power system, which produces a certain degree of frequency volatility.

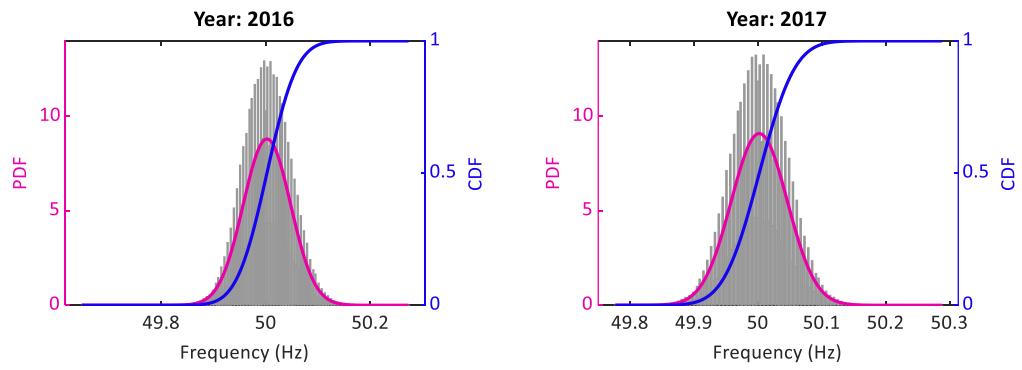

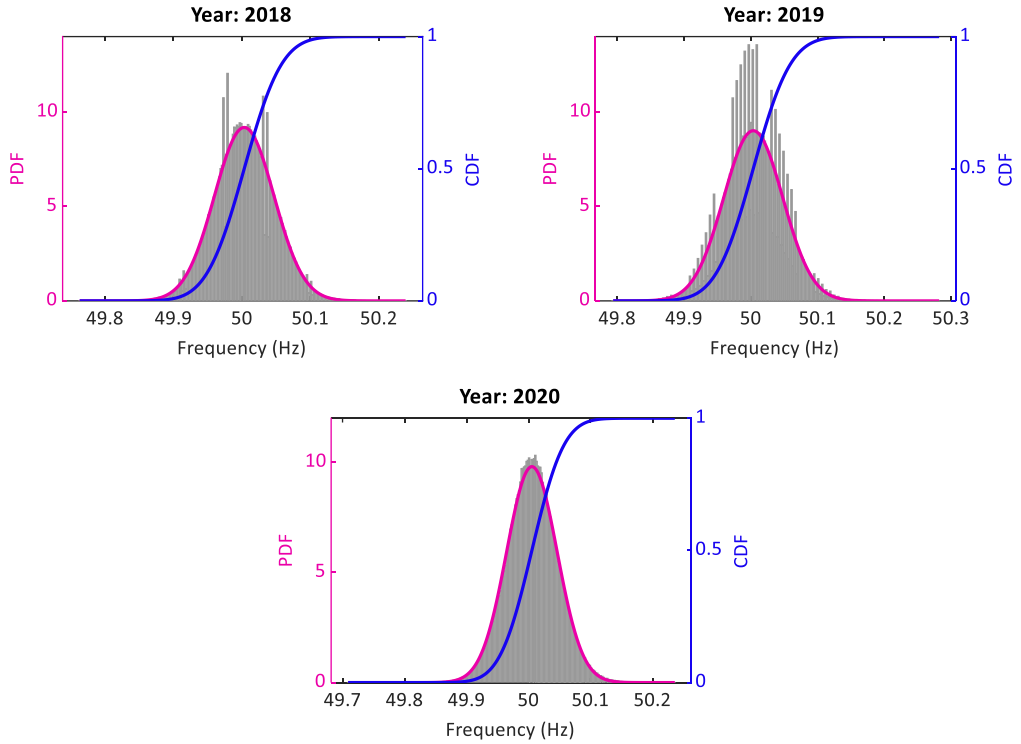

Figure 3.2. Probability density and cumulative distribution function of the frequency in period 2016-2020.

The TSOs of the NPS require the frequency to fulfil several operational requirements, such as the total time per years that the frequency is allowed to be outside the standard frequency range (Δf_{ss}). In the NPS, the yearly time limit is 15,000 minutes [84]. The time series of the frequency was evaluated, and it was found that in 2016 the frequency was outside Δf_{ss} 11,584 minutes, very close to the yearly limit. In contrast, in 2020, the number of minutes the frequency was outside Δf_{ss} is reduced by around 20%. It indicates that the frequency control strategies have been improved. However, the frequency unpredictably caused by the integration of RESs is still an issue to the TSOs. On the other hand, the frequency of the five years assessed was inside the maximum steady-state frequency range ($\Delta f_{\mathrm{ss,max}}$) all the time.

3.6.2 Frequency and kinetic energy dispersion assessment

The equation (3.21) clearly illustrates the relationship between the frequency and the kinetic energy in the power system. The implications of the high/low levels of kinetic energy on the frequency response are for the PFC timescales, where the available kinetic energy acts to re-establish the power balance. When the kinetic energy is not enough

to cope with the frequency deviation, the frequency containment reserves are activated to restore the frequency inside Δf_{ss}. In the NPS, if the mismatch between scheduled power production and power demand produces a frequency deviation more significant than $\Delta f_{\mathrm{ss,max,}}$ FCR is activated within 30 seconds to regulate up and reach a new balance. However, if the frequency deviation continues, the TSOs activate the frequency restoration reserves within 15 minutes [85].

The frequency deviation of the five years of historical data of the NPS does not overcome $\Delta f_{\mathrm{ss,max}}$. As a consequence, the frequency regulation inside the 15-minutes periods relies on the available kinetic energy of the NPS. The main goal of performing a dispersion assessment is to validate the frequency regulation provided by kinetic energy following a power imbalance as described in (3.21). The hypothesis is that within 15 minutes periods, the power dispatch of the synchronous generators remains constant, and the frequency deviation is regulated only by the available kinetic energy stored in the synchronous generators.

The dispersion assessment of the frequency and kinetic energy of the time series is carried out considering 15-minutes periods. The results of mean values, standard deviation and coefficient of variation are depicted in Table 3.3.

Table 3.3. Dispersion results of the frequency and kinetic energy for the period 2016-2020.

Statistics	**Frequency, f (Hz)**		**Kinetic energy, E_K (GW·s)**	
	Min	***Max***	***Min***	***Max***
Mean, μ	49.82	50.18	117.00	287.73
Std., σ	0.00	0.12	0.00	39.06
Coefficient of variation, cv	0.00%	0.23%	0.00%	13.00%

From Table 3.3, it can be observed that the maximum frequency variation concerning the mean is 0.23%, and the maximum coefficient variation of the kinetic energy is 13%. Therefore, it can be concluded the kinetic energy variates to regulated up the frequency and maintain its deviation low within the 15-minutes periods. However, the mean value

of the frequency is outside Δf_{ss}, indicating the available kinetic energy is not sufficient to maintain the frequency inside the standard frequency range.

An illustrative sample of the frequency and kinetic energy variation within 15-minutes periods is shown in Figure 3.3. It depicts the standard deviation of the frequency and kinetic energy of the 1st day of January of the years 2016 to 2020. From Figure 3.3, it can be observed that the standard deviation of the kinetic energy is different from zero most of the time, indicating the kinetic energy of the NPS variates inside the 15-minutes period. However, this should not be the case since the power dispatch of the synchronous generators, if necessary, is made every 15 minutes. Consequently, the intra-15-minutes variation can be attributed to the inertia contribution from other technologies, such as RESs, installed in the power system besides the synchronous generators.

Furthermore, the standard deviation of the frequency has persistent variations from the mean value meaning the kinetic energy is not enough to keep the frequency near to the nominal frequency. The continuous frequency variations are mainly produced by the constant changes in the power demand and/or the load-self regulation.

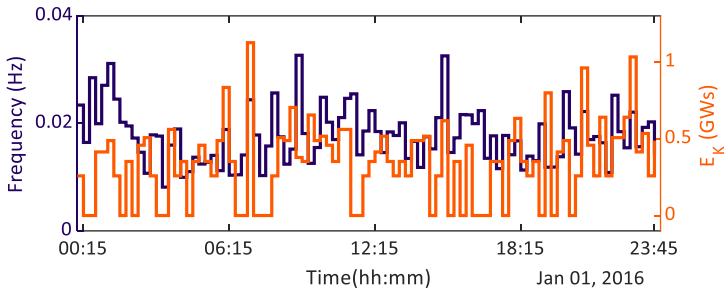

a)

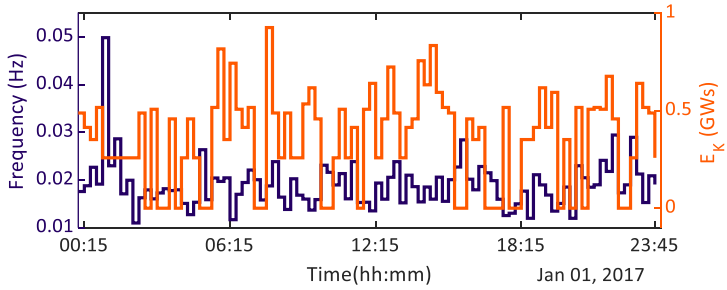

b)

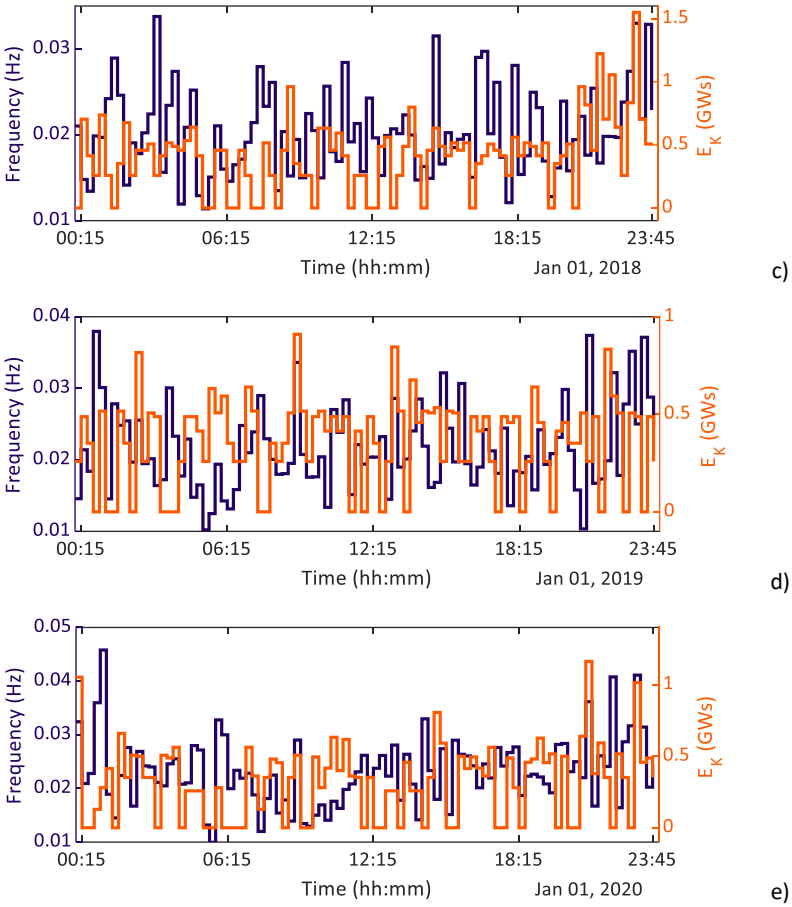

Figure 3.3. Standard deviation of frequency and kinetic energy for 1st January of year: a) 2016; b) 2017; c) 2018; d) 2019; e) 2020.

3.6.3 Reliance between kinetic energy and power demand

The identification of dependency between the kinetic energy and power demand can be a crucial factor to develop prediction models based on the power demand forecast and without relying on the occurrence of a disturbance.

The kinetic energy time series has a time resolution of one-minute sampling, and the power demand time series has a one-hour time resolution. As a result, the kinetic energy time series is resampled using a linear interpolation technique to have both electromechanical variables in the same time resolution.

The level of reliance between kinetic energy and power demand is assessed by computing the Pearson's linear correlation coefficient using (3.6). The correlation

evaluation is performed considering the time series grouped by year, month, day and hour.

3.6.3.1 Yearly and monthly correlation coefficients

The time series of the kinetic energy and power demand for the years 2016 to 2020 is presented in Figure 3.4. It can be seen that kinetic energy and power demand have the same recurrent behaviour over the years. The highest values of kinetic energy and power demand are presented during the first quart of the year, and the lowest values are in the third quarter of the year.

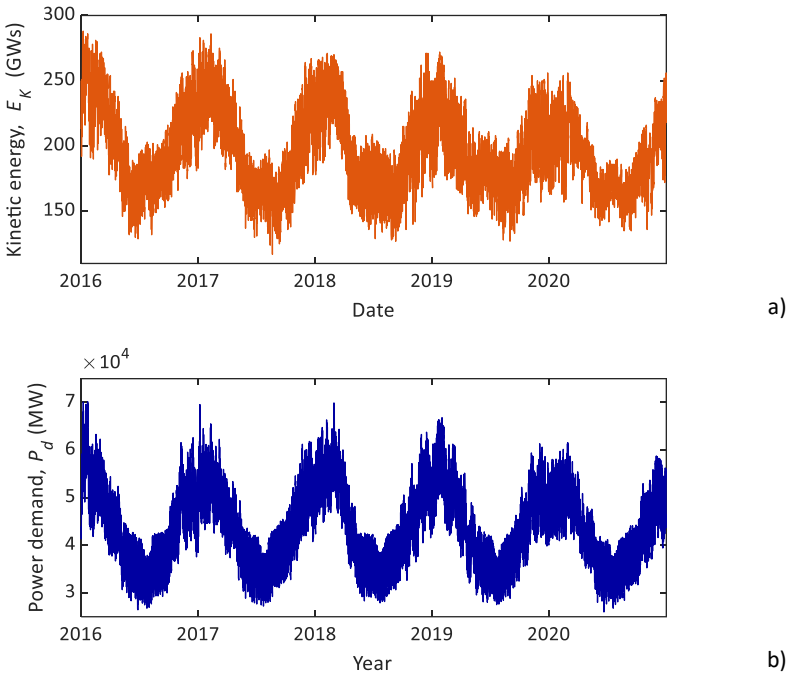

Figure 3.4. Time series of five years of historical data of NPS: a) kinetic energy; b) power demand.

The correlation coefficient of each year is presented in Figure 3.5. The yearly dependency of these two electromechanical variables tends to decrease over the years. The correlation coefficient value drops from around ρ = 0.92 for years 2016 to 2018 to ρ = 0.88 for years 2019 and 2020. The decrease in the yearly correlation can be caused by the constant evolution of the NPS and the inclusion of power converter-based technologies.

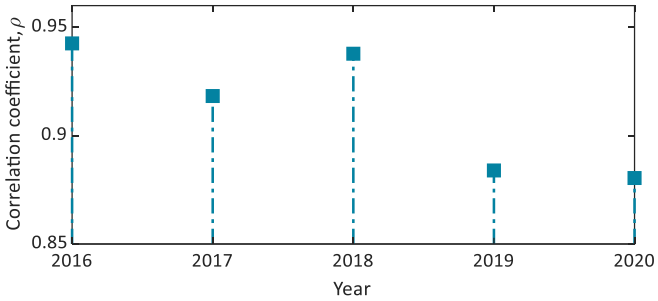

Figure 3.5. Yearly correlation coefficients of kinetic energy and power demand for the 2016 to 2020 period.

From Figure 3.4, the time series shows a seasonal pattern in both kinetic energy and power demand. These electromechanical variables present the highest values in the months belonging to the winter season, and the lowest values are in the months belonging to the summer season. Therefore, dependency of kinetic energy and power demand is assessed considering the time series grouped by months. The correlation coefficients of the time series are presented in Figure 3.6. The months of the winter season presents the highest correlation coefficients, around ρ = 0.87, indicating a strong dependency. This dependency is produced because the season is characterised by low temperatures and days with few hours of light (up to 7 hours). Therefore, the power demand is elevated due to the use of the heating system and more power generation unit on service, which increase the level of kinetic energy in the NPS.

In contrast, the months of summer and part of the fall season have the lowest correlation coefficients, around ρ = 0.68. The weak dependency is caused because, in this season, the power demand decreases due to the pleasant temperatures, and the heating system is turned off. Moreover, the days are with up to 19 hours of light and the holiday season peak.

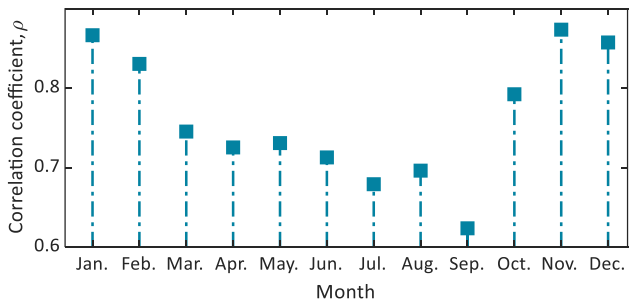

Figure 3.6. Monthly correlation coefficients of kinetic energy and power demand for the 2016 to 2020 period.

3.6.3.2 Daily and hourly correlation coefficients

The time series of the kinetic energy and power demand for the years 2016 to 2020 grouped by day is shown in Figure 3.7. It is evident that on weekdays both kinetic energy and power demand have a clearly defined behaviour in contrast to the weekend days where the behaviour is not well-defined through the hours. On weekdays, the kinetic energy and power demand reach their minimum values between 0:00 and 5:00. Afterwards, their values begin to increase, attaining maximum values around 10:00 and continuing around maximum values up to 21:00. Then their values start to drop until they achieve the minimum value. Furthermore, on weekend days, the kinetic energy and power demand also get their minimum values between 0:00 and 5:00. However, the time at which the kinetic energy and power demand get their maximum values and the time when they start to decrease vary.

Human activities mainly produce the difference between the patterns of weekdays and weekend days. For instance, scheduled duties or tasks such as commercial/industrial hours, work hours, school hours. On the other hand, most of the activities carried out on weekend days does not have a specific plan or are not scheduled [86].

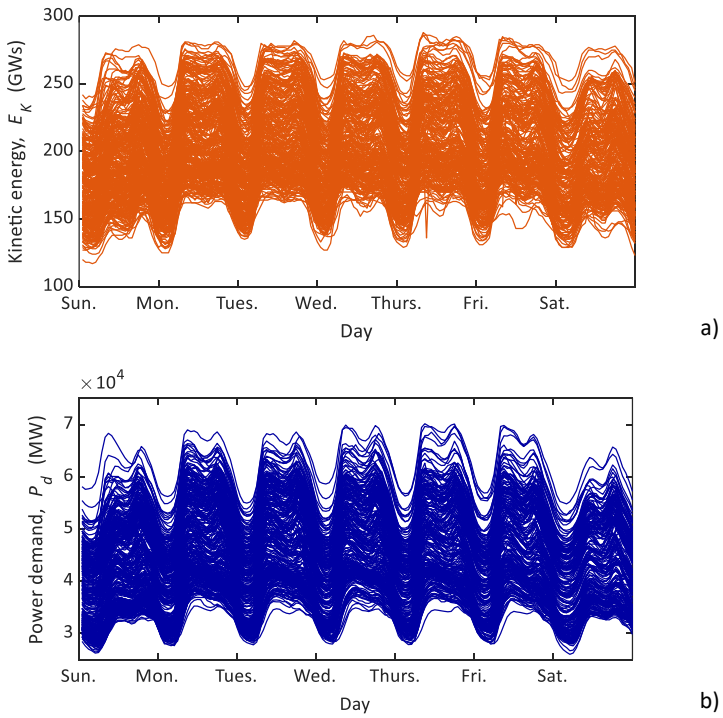

Figure 3.7. Daily time series of period 2016 to 2020 of a) kinetic energy; b) power demand.

The behaviour on weekdays conducts to have a scheduled power production causing the kinetic energy to follow the same pattern as the power demand. On the other hand, on weekend days, the power demand does not have a well-known profile for hours of the day. Consequently, the correlation coefficients are computed to unveil the level of dependency between kinetic energy and power demand, considering data grouped by day and hour.

Figure 3.8 depict the correlation coefficients of the time series grouped by day. The daily correlation coefficients have values around ρ = 0.90, showing a strong dependency between kinetic energy and power demand, even on the weekend days. These variables follow the same pattern during the weeks and have a similar shape profile.

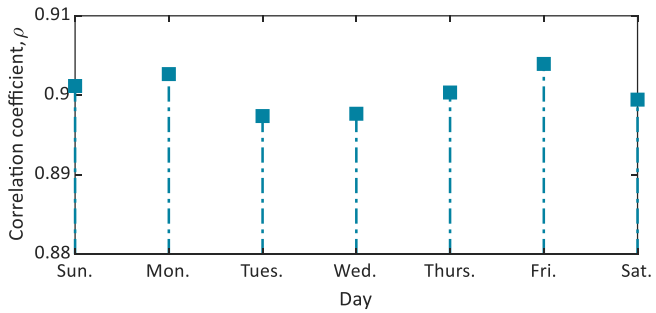

Figure 3.8. Daily correlation coefficients of kinetic energy and power demand for the 2016 to 2020 period.

Furthermore, the hourly correlation coefficients are depicted in Figure 3.9. It can be seen that from midnight to 5:00, the correlation values are decreasing from ρ = 0.88 to ρ = 0.84, corresponding to hours where the human activities are minimum, and both kinetic energy and power demand have their lower level. Then, at 6:00, the correlation value jumps up to ρ = 0.89, and from 7:00 to 19:00 is around the maximum value, which is ρ = 0.92. The strong correlation coincides with the hours in which the power demand and kinetic energy present their highest values. Afterwards, at 20:00, the correlation starts to decrease.

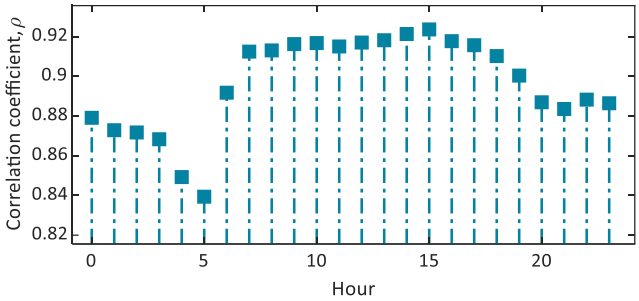

Figure 3.9. Hourly correlation coefficients of kinetic energy and power demand for the 2016 to 2020 period.

3.7 Kinetic energy and power demand dependency model by a mixture of linear regression models

The massive amount of historical data on the electromechanical variables of the NPS represents a significant challenge at the time it is analysed to identifying their main features and patterns. Therefore, partitioning the time series into clusters with similar statistical attributes helps extract and understand the principal characteristic of the data.

The correlation assessment between the kinetic energy and the power demand indicated these two electromechanical variables have a strong association and follow a similar pattern presenting low values during the night hours and high values during the hours of the day. Therefore, the GMM is used to partition the observations into clusters with similar features and then create a linear regression model to represent the dependency of each cluster.

The kinetic energy and power demand clustering is carried out following the procedure to implement the GMM described in Section 3.4. The time series used correspond to the 2016 to 2019 period, and the data of the year 2020 is used to validate the resulting linear regression models.

The continuous-valued data vector, $\mathbf{X}$, contains 35064 two-dimensional observations, i.e., N = 35,064, and D = 2. Each dimension corresponds to the time series of the kinetic energy and power demand. Therefore, $\boldsymbol{\mu}_k$ is 1×2 mean vector, and $\boldsymbol{\Sigma}_k$ is a 2×2 covariance matrix.

The GMM setup is carried out to determine the effectiveness of a different number of clusters and the four types of covariance matrices. The AIC and BIC indicators were computed for $k \in \{1, \ldots, \gamma = 10\}$ clusters and the four types of covariance matrices: diagonal-uniform, diagonal-non-uniform, full-uniform and full-non-uniform and the results are shown in Figure 3.10.

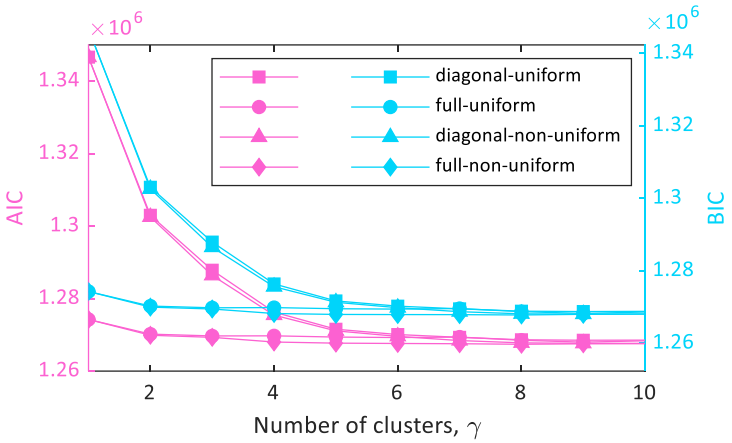

Figure 3.10. AIC and BIC indicators for $k \in \{1,\ldots, \gamma = 10\}$ clusters and the four types of covariance matrices.

The AIC and BIC indicators have the lowest values when eight clusters (γ = 8) and full-non-uniform covariance matrix type are used. Moreover, the AIC and BIC values for γ = 2 with full-non-uniform covariance matrices show a decrease of 1.05% concerning γ = 1. Besides, AIC and BIC values AIC values decrease only 0.23% from γ = 2 to γ = 8. Therefore, the number of clusters was selected as K = 2 with the full-non-uniform covariance matrix assumption. This selection is made to comply with the trade-off between the fit and complexity of the model. Moreover, it was decided to use the full-non-uniform covariance matrix since this type of matrix allows to include the correlation of the variables in the GMM. It is no required that the dispersion of the data be the same in each cluster.

The GMM parameters, which are the parameters of each PDF that explains the data contained in each cluster (w_k, $\boldsymbol{\mu}_k$, $\boldsymbol{\sigma}_k$), are computed using the expectation maximisation algorithm. It considering a clusters number γ = 2 and the assumption of full-non-uniform covariance matrices. The parameters of each PDF describing the data of the kinetic energy and power demand for each cluster are presented in Table 3.4.

Table 3.4. PDF parameters of each cluster explaining the data of kinetic energy and power demand.

Electromechanical variable	Cluster name, γ	Weight, w (p.u.)	Mean, μ	Std., σ
Kinetic energy, E_K (GW·s)	L-L	0.325	237.64	398.52
	H-H	0.675	182.04	431.52
Power demand, P_d (MW)	L-L	0.580	38537	2693.42
	H-H	0.420	52260	3,741.90

Figure 3.11 depicts the GMM PDF and the individual PDF that describes the data of kinetic energy and power demand in each cluster. It can be observed that the clustering based on GMM partitioned the time series of kinetic energy and power demand into two clusters that characterise the levels of kinetic energy and power demand presents in the NPS. The L-L cluster holds low values of kinetic energy and power demand, and the mean values of these electromechanical variables are μ_{EK}=182.04 GWs and μ_{Pd} = 38,537 MW. Meanwhile, the H-H cluster contains high kinetic energy and power demand values, and their mean values are μ_{EK} = 237.64 GWs and μ_{Pd} = 52,260 MW.

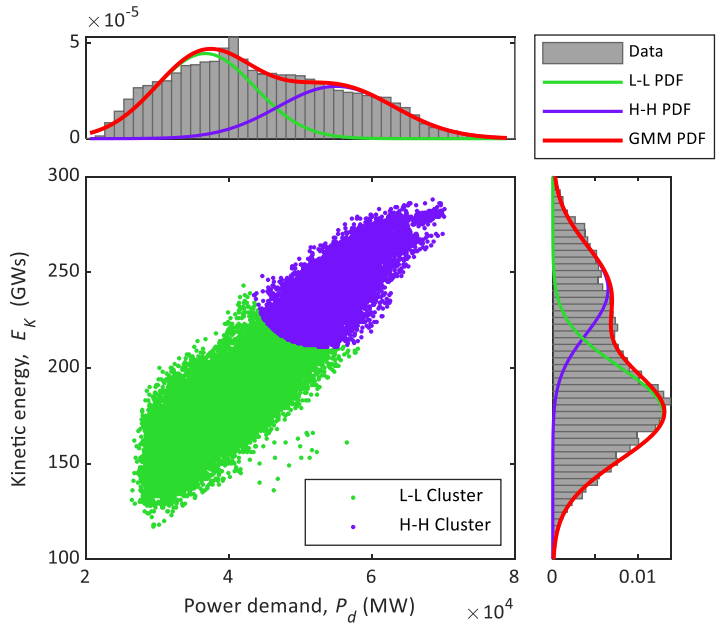

Figure 3.11. Graphical representation of the induvial PDF of each cluster and the GMM PDF.

The clusters defined by the GMM, L-L cluster and H-H cluster, containing low and high levels of kinetic energy and power demand, are used to compute the linear regression

models representing the dependency of the data. The linear regression model of the L-L cluster and the H-H cluster is computed and presented in Table 3.5.

Table 3.5. Linear regression model of L-L cluster and H-H cluster.

Cluster name, γ	**Correlation coefficient, ρ**	**Linear regression model: $E_K = \beta_0 + \beta_1 P_d$**
L-L	0.738	E_K=181.59+ 14.43P_d
H-H	0.749	E_K=240.51+ 12.58P_d

Furthermore, the time series of the year 2020, representing approximately 25% of data from 2016 to 2019, is used to validate the linear regression models. The *goodness of fit* indicators is shown in Table 3.6.

Table 3.6. *Goodness of fit* indicators of linear regression model and validation data.

Cluster name, γ	**Linear regression model**			**Validation with 25% of data**	
	SSE	**R^2**	**RMSE**	**SSE**	**RMSE**
L-L	3.177×10^6	0.545	13.275	1.022×10^6	13.045
H-H	8.727×10^5	0.561	11.132	5.860×10^5	14.58

The linear regression model of the *L-L cluster* and the PDF of the kinetic energy and power demand is presented in Figure 3.12. The correlation between kinetic energy and power demand $\rho_{\text{L-L}}$ = 0.738. This level of correlation indicates that when the NPS has low levels of kinetic energy and power demand, these two variables have a fairly strong relationship. The goodness of fit indicators of the linear regression model indicates that it only can represent 54.5% of the total data variation around the mean value. Furthermore, the SSE and RMSE of the validation dataset have smaller values than those obtained for the linear regression model.

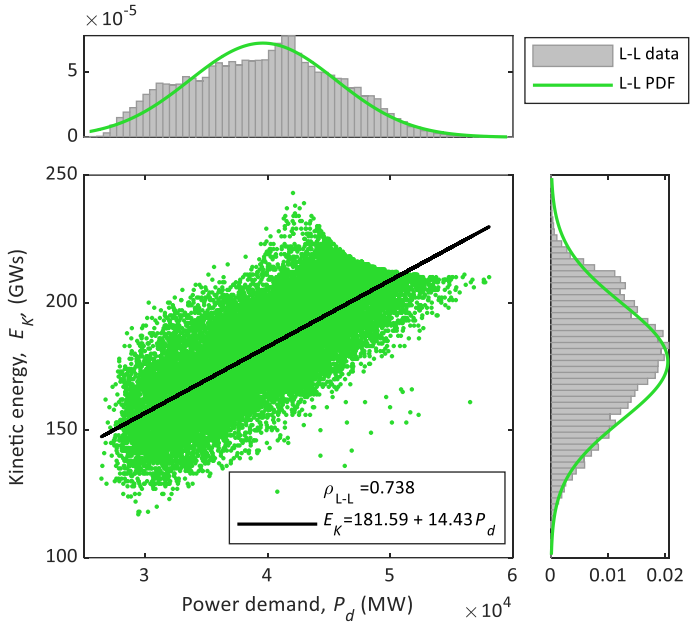

Figure 3.12. Linear regression model and PDF of the L-L cluster.

The histogram of the hours corresponding to the low values of kinetic energy and power demand in the L-L cluster is shown in Figure 3.13. The hours of the day with low levels of kinetic energy and power demand can be easily identified. At the beginning of the day from 0:00 to 5:00 and at the end of the day from 21:00 to 23:00. These hours represent 47% of the total data contained in the L-L cluster. This cluster has a fairly strong correlation between kinetic energy and power demand. Although these variables do not follow the same pattern at all hours of the day when the power demand has low values, the kinetic energy has low values.

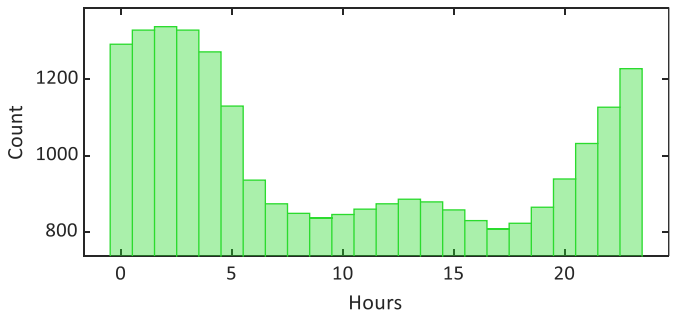

Figure 3.13. Histogram of the hours in the L-L cluster.

The linear regression model of the H-H cluster and the PDF of the kinetic energy and power demand is depicted in Figure 3.14. The linear regression model for this cluster can explain 56.1% of the total variation in the data about the mean value. Moreover,

the correlation between kinetic energy and power demand is ρ = 0.749. This correlation value indicates that the relationship between kinetic energy and power demand when they have high values is strong. Moreover, linear regression validation produces the SSE and RMSE have higher values than those obtained for the linear regression model. The increase in the goodness of fit indicators, SSE and RMSE, is because the kinetic energy values of the year 2020 are lower than the previous years.

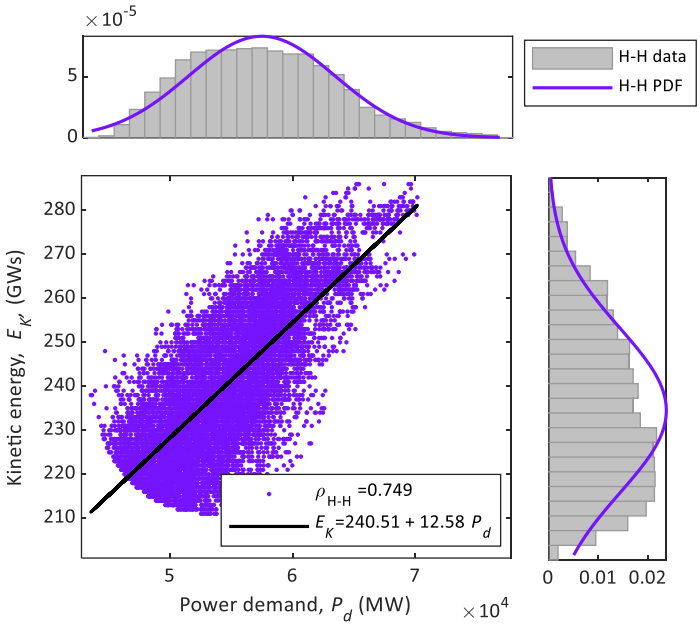

Figure 3.14. Linear regression model and PDF of the H-H cluster.

The distribution of the hours corresponding to the high levels of kinetic energy and power demand in the H-H cluster is depicted in Figure 3.15. The histogram indicates that the hours of the day with high kinetic energy and power demand values are from 6:00 to 20:00, representing 81.2% of the total data contained in the H-H cluster. This cluster has a strong correlation between kinetic energy and power demand. The pattern of the variables is the same over the mentioned hours. Moreover, when the power demand has high values, the kinetic energy also has high values.

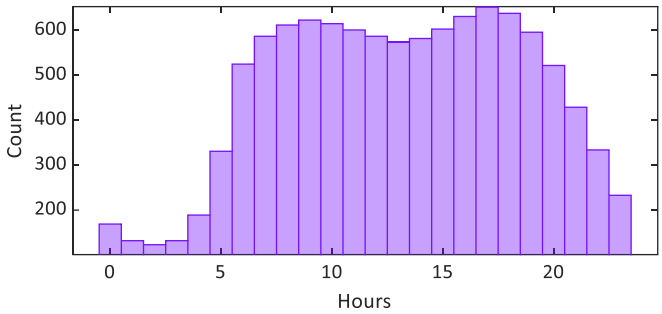

Figure 3.15. Histogram of the hours in the H-H cluster.

3.8 Conclusions

This chapter presents a statistical assessment of three electromechanical variables involved in frequency control: frequency, kinetic energy, and power demand. It is used the historical data of the NPS provided by Nordpool and Fingrid company. The statistics of the frequency demonstrated that the yearly frequency mean value is above the nominal value and tends to continue increasing in the coming year due to the integration of power converter-based technologies. The dispersion assessment of the frequency and kinetic energy considering 15-minute periods was carried out. The assessment results mainly highlighted the kinetic energy variation inside the 15-minute periods, indicating that other inertial response sources provide frequency control besides the PFC.

Furthermore, a correlation analysis between kinetic energy and power demand was performed, unveiling these two electromechanical variables follow the same seasonal pattern considering monthly grouping. Meanwhile, the hourly grouping allowed differentiating between the hours with a strong correlation related to high kinetic energy and power demand values and the hours with week correlation belonging to low kinetic energy and power demand values. The dependency between these two variables was corroborated by computing the gaussian mixture model considering two clusters. The clustering demonstrated that partitioning the time series of kinetic energy and power demand into clusters allowed to split the time series into groups of the same features. It was proved that the GMM correctly grouped the kinetic energy and power demand data into two clusters with the same features. The L-L cluster holds the low

values, and the H-H cluster contains the high values of power demand and kinetic energy. Furthermore, the relationship between the power demand and kinetic energy was model by a set of linear regression models, each representing the dependency of the power demand and kinetic energy variables. The linear regression was validated using the time series of the year 2020, and it was found that for the L-L cluster, the linear regression model can explain the validation data. In contrast, the linear regression model of the H-H cluster cannot explain the validation data because the kinetic energy has a decreasing tendency.

4 Optimal Fast Frequency Support for Low Inertia Conditions: Variable-speed PHHPs and BESS

The replacement of conventional power generation sources, mainly based on synchronous generators, by RESs is causing stress in the modern power system. Furthermore, it makes it less tolerant to disturbances principally because the PFC is deteriorating due to the shortage of inertia in the RESs. Therefore, it is desirable operational flexibility in conventional power plants and the use of new and/or existing smart power inverters-based technologies to provide frequency support and overcomes power imbalances in low inertia scenarios. This chapter focuses on evaluating the variable-speed PHPPs, and BESS technologies as fast frequency support providers and their impact on the frequency response after a disturbance occurs. First, an overview of the frequency response model of synchronous generators is presented. Then, the fundamental concepts and common control models of FFR are described. Subsequently, the description of the variable-speed PHPPs, BESS and its formulation as combined FFR control is defined.

Furthermore, a methodology is developed to compute the optimal FFR parameters. Finally, two models of the NPS are implemented and used to validate the proposed methodology considering the projected changes in power demand, power generation and kinetic energy in the 2020-2040 period. This chapter is based on publications **[P1]** and **[P6]**.

4.1 Introduction

Worldwide electrical power systems are evolving to migrate to an eco-friendly industry, thereby facing significant topological adjustments and operational and control challenges. The trend is to increase the RESs volume connected to the power system, mainly at the distribution level [17]. One of the main challenges is the tendency of inertia to decrease. For instance, the TSOs of the NPS has estimated the total kinetic energy of the NPS will take values between 120 GW·s and 145 GW·s up to 19% of the time,

depending on the clime of the year [87], [88]. Consequently, new methods and device are required to deal with this problem.

The integration of RESs into the power system, such as photovoltaic, wind, hydro variable-speed and ESSs technologies, requires advanced power electronic devices known as smart power inverters (SPI) to act as an interface to the power system. Publication **[P8]** describes the basic concepts and modelling of power electronic converters and their implementation in DIgSILENT® PowerFactory™. Furthermore, it provides a discussion of their applications in the modern power system.

SPI entitles several functionalities, for instance, frequency and voltage regulation, dynamic current injection, ride-through and anti-islanding [89]. For instance, publications **[P7]** and **[P12]** demonstrated that SPI enabled with a reactive power control strategy provides voltage regulation and reduces active power losses. Furthermore, publications **[P7]** determined that a centralised optimal reactive power control allows microgrids to provide ancillary services to the rest of the power system and represent a techno-economic solution to voltage regulation. The SPI controller family contains three types of controllers: proportional, derivative and integral. SPI can use any of the controls mentioned above for frequency regulation purposes and enable the so-called fast frequency response acting inside the PFC timescales to provide fast frequency support.

The implementation of FFR using the derivative approach has shown drawbacks in wind turbines and other SPI based technologies [90], [91]. Therefore, the combination of the proportional and derivative control actions tries to emulate synchronous generators response, i.e., the proportional action can be related to the governor droop constant. In contrast, the derivative action is associated with inertial response (kinetic energy stored in the rotating masses [92]. Consequently, enabling FFR control in the SPI technology-based provides an attractive solution to cope with the inertia reduction problem.

In this chapter, two ESSs are considered to enable FFR control and provide fast frequency support to the power system: variable-speed PHPPs and BESS technologies.

The pumped hydropower plants are considered as RESs. However, unlike other RESs, such as wind or solar power plants, they provide inherent inertia response and excellent controllability features. Furthermore, equipping the PHPPs with variable-speed technologies increases their efficiency and allows to enable FFR control to provide fast frequency support. On the other hand, BESS has been recognised as one of the most suitable technologies in the market to provide services to the power system due to their high efficiency, lifetime and fast response [93]. Besides, several methodologies have implemented BESS to provide frequency regulation [93]–[97].

4.1.1 Contribution

The main contributions of this chapter are unfolding below:

1. Formulate the problem of setting the parameters of FFR control: droop coefficient, synthetic coefficient, or a combination of both, as an optimisation problem. The optimisation problem is formulated in such a way that any SPI technology-based can be included in the optimisation problem.
2. Development of two objective functions to compute the parameters of FFR control, one allows to enhance the minimum frequency as desired, and the other focuses on enhancing the steady-state frequency.
3. To provide optimal fast frequency support by using the combined action of variable-speed PHPPs and BESS.
4. Model the Vestfold and Telemark distribution system, using real publicity information.
5. Assessment the proposed methodology using realistic simulation scenarios based on the projected changes on the Nordic power system.
6. Enhance the frequency quality indicators by implementing the proposed methodology.
7. Provide a realistic outlook of how to mitigate the low inertia challenges by using variable-speed PHPPs and BESS to provide optimal fast frequency support in the Nordic power system.

4.2 Frequency response model

The synchronous generator is considered a fundamental component of frequency regulation in the PFC. It automatically reduces/increases its power value in response to the frequency variation. Therefore, suitable models for studying the frequency response after a disturbance occurs on either an isolated or interconnected power system can be done by linearising, under reasonable considerations, the swing equation given in (2.6).

Considering a slight deviation around the nominal operating point of the synchronous generator equation (2.6) can be expressed as

$$\frac{2H}{\omega_0}\frac{d^2(\delta_0+\Delta\delta)}{dt^2} = (P_{m,0} - P_{e,0}) + (\Delta P_m - \Delta P_e) \tag{4.1}$$

The subscript 0 denotes the nominal operation point of mechanical power, electrical power, and electrical angle. Due to the nominal operation point represents an equilibrium point of the power system, the power difference at the equilibrium point is zero, i.e., $P_{m0} = P_{e0}$, and δ_0 remains constant. Consequently, $d^2\delta_0/dt^2 = 0$ and presuming the angular deviation is related to the speed deviation as $d\Delta\delta/dt = \Delta\omega$, (4.1) becomes

$$2H\frac{d\Delta\omega}{dt} = \Delta P_m - \Delta P_e \tag{4.2}$$

where Δw is in pu. Multiplying both sides of (4.2) by 2π and computing Laplace transformation of (4.2), the frequency deviation for a small perturbation is defined as

$$\Delta f(s) = \frac{1}{2Hs}\left(\Delta P_m(s) - \Delta P_e(s)\right) \tag{4.3}$$

with Δf in pu. The change of the mechanical power depends on the turbine power output, which in turn depends on the governor's response to a frequency variation. Moreover, the electrical power shifts are directly related to the load response to a frequency deviation. Therefore, it is necessary to include the turbine, governor, and load model in the equation (4.3).

4.2.1 Load model

The electrical load consists of various devices commonly categorised into two types: frequency-independent load and frequency-dependent load. The frequency-independent load consists of purely resistive loads such as heating or lighting loads. Whilst the frequency-dependent load is sensitive to the frequency variation, for instance, motor loads. Therefore, total electrical power deviation neglecting losses can be expressed as

$$\Delta P_e(s) = \Delta P_L(s) + D\Delta f(s) \tag{4.4}$$

where ΔP_L is the power deviation of frequency-independent load and D is a damping constant that relates the power deviation of the frequency-dependent load to the frequency deviation and is given in MW/Hz or pu.

4.2.2 Turbine model

The turbine model depends on the prime mover technology, for instance, non-reheat steam, reheating steam and hydro turbine. The simplest turbine model is the non-reheat steam. In this model, the mechanical power output of the turbine depends on the valvule position that regulates the steam input to the turbine. The transfer function of the non-reheat steam turbine is

$$\frac{\Delta P_m(s)}{\Delta P_v(s)} = \frac{1}{T_t s + 1} \tag{4.5}$$

where T_t is a time constant modelling the time delay experienced in the steam container, typically in the range from 0.2 to 2.0 s [98], and ΔP_v represent the valvule position change signal coming from the governor.

4.2.3 Speed governor model

The speed governor is a device sensible to the speed variation of the synchronous generator. It sends out a signal to change the turbine valve position when it senses a speed deviation from its nominal value. Consequently, an increase in the sensed speed

leads to reducing the turbine primary energy input and decreasing the mechanical power. On the other hand, a decrease in the measured speed produces a change in the valvule position to raise the turbine primary energy input and therefore increase the mechanical power. Assuming the steam flow feedback is neglected, the transfer function of the speed governor model is defined as

$$\frac{\Delta P_v(s)}{\Delta P_G(s)} = \frac{1}{T_G s + 1} \tag{4.6}$$

where ΔP_G is the input signal to the governor and T_G is the time constant of the servomotor. ΔP_G is calculated as the difference between a reference power deviation (ΔP_{ref}) and governor steady-state characteristic action:

$$\Delta P_G(s) = \Delta P_{\text{ref}}(s) - \frac{\Delta f(s)}{R} \tag{4.7}$$

The governor steady-state characteristic, known as droop constant (R), is a feedback gain that describes the ratio of relative frequency deviation to the relative mechanical power with units in Hz/MW but typically is expressed in percentage or pu and take values in the range from 4% to 9%. If R is given in percentage, it represents the speed deviation needed to change the valve position from 0% to 100%.

The elemental frequency response model of a power system is obtained by incorporating the load, turbine and speed governor model described in (4.4) - (4.7) into (4.3) and the block diagram representation is depicted in Figure 4.1. The elemental frequency response model is within PFC timescales; consequently, $\Delta P_{\text{ref}}\,\text{is}$ presumed zero since this quantity actuates in timescales beyond the PFC, and the resulting transfer function is written as:

$$\frac{\Delta f(s)}{\Delta P_L(s)} = -\frac{1}{(2Hs + D) - \frac{1}{R}\left(\frac{1}{T_G s + 1}\right)\left(\frac{1}{T_t s + 1}\right)} \tag{4.8}$$

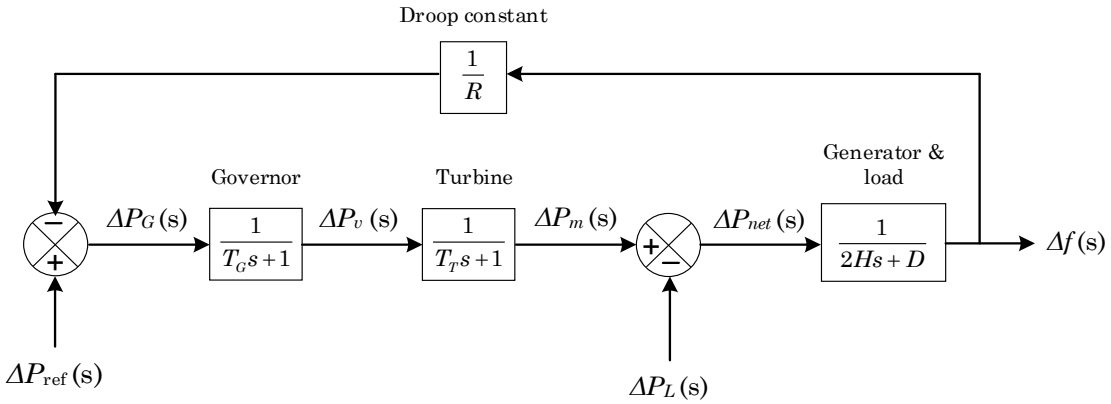

Figure 4.1. Block diagram of the elemental frequency response model of a power system.

4.2.4 Single-area frequency response model

The single-area frequency response model is used to represents the power system without power exchanges with neighbouring areas. This model undertakes that all synchronous generators maintain the synchronism of each other after a disturbance. Therefore, they can be represented by a single synchronous generator with an equivalent inertia constant computed as the sum of inertia constants of all synchronous generators as

$$H_{\text{equiv}} = \sum_{i=1}^{N_g} \frac{H_i S_i}{S_{0,i}} \tag{4.9}$$

where H_i is the constant inertia, S_i is the apparent power and $S_{0,i}$ is the nominal apparent power of the i-th synchronous generator. N_g is the total number of synchronous generators. Moreover, it considers a single damping constant, D.

The single area frequency response model is helpful to perform PFC studies representing the frequency response of large power systems. For instance, in publication **[P14]**, the (NPS) is represented by the single-area model and implemented in a real-time simulation framework considering hardware in the loop to assess the frequency support provided by the battery energy storage system.

4.2.5 Multi-area frequency response model

The multi-area frequency response model represents an interconnected power system with power exchanges with neighbouring areas. It consists of *N* single-area models connected through tie-lines assuming the frequency inside every single area is identical. The block diagram of the frequency response of the k-th single-area is shown in Figure 4.2.

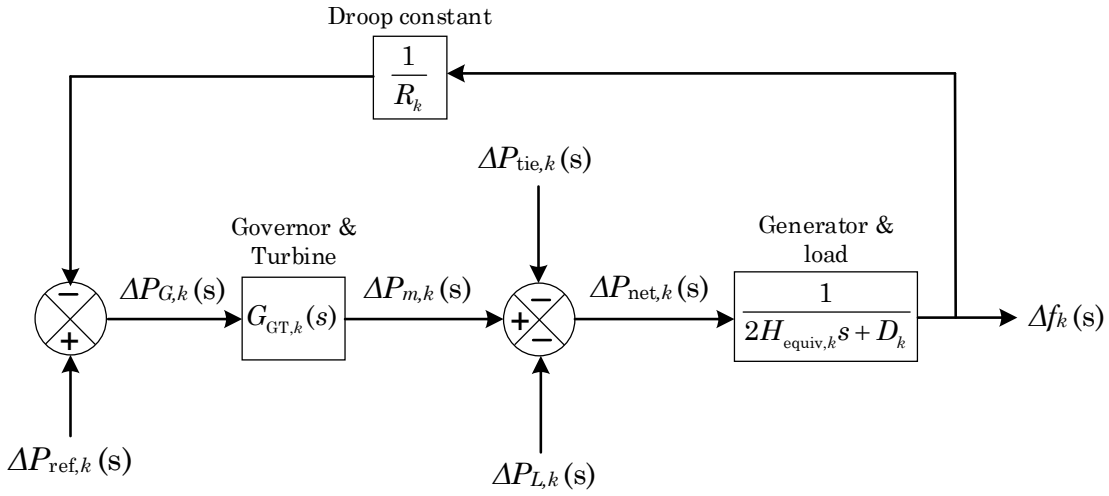

Figure 4.2. Block diagram representation of the k-th single area of the multi-area frequency response model.

The frequency deviation of the k-th area represented in Figure 4.2 after a disturbance is calculated as

$$\Delta f_k(s) = \frac{\Delta P_{\text{net},k}(s)}{\left(2H_{\text{equiv},k}s + D_k\right)} \tag{4.10}$$

where $\Delta P_{\text{net},k}$ *is* the difference between the change of the turbine mechanical power ($\Delta P_{m,k}$) and the joint deviation of the power imbalance ($\Delta P_{L,k}$) and tie-line power interchange ($\Delta P_{\text{tie},k}$) computed as

$$\Delta P_{\text{net},k}(s) = \Delta P_{m,k}(s) - \Delta P_{L,k}(s) - \Delta P_{\text{tie},k}(s) \tag{4.11}$$

Moreover, the tie-line power interchange is computed as [99]:

$$\Delta P_{\text{tie},k}(s) = \frac{2\pi}{s}\left[\sum_{\substack{j=1 \\ j\neq k}}^{N} T_{kj}\Delta f_k(s) - \sum_{\substack{j=1 \\ j\neq k}}^{N} T_{kj}\Delta f_j(s)\right] \tag{4.12}$$

where $T_{k,j}$ is the synchronising torque coefficient between area k and j.

4.3 Fast frequency response

The PFC as a mechanism to arrest the frequency deviation following a disturbance is becoming insufficient, particularly in the inertial response stage due to the inertia decreasing caused by the growing installation of RESs in the power system. The low inertia levels impact the first few seconds of frequency excursions, experiencing high ROCOF values and violating the frequency quality requirements and/or reaching dangerously low values. Consequently, FFR provides an alternative to replace the lack of inertia by mimicking the inertial response of the synchronous generator. It enables the exchanges of active power between non-synchronous technologies and the power system in response to the frequency deviation within a high-speed response in the range of 10 to 20 milliseconds [100]. The energy available at the DC side of the SPI determines its maximum active power exchange [101]. The primary purpose of FFR is contributing to arrest the frequency deviation by injecting/absorbing active power in scenarios of under or over frequency. FFR scheme can be modelled considering different control models. In this thesis, the proportional, derivative, and combination control models are used and described below.

4.3.1 Proportional fast frequency response (PFFR)

PFFR represent a traditional linear feedback control. It changes the active power (ΔP_{PFFR}) in proportion to the frequency deviation Δf. The transfer function of the PFFR control is defined as

$$\frac{\Delta P_{PFFR}(s)}{\Delta f(s)} = K_P \tag{4.13}$$

where K_P is a proportional gain, named in this thesis as droop coefficient. Considering a deadband, the transfer function of the PFFR is rewritten by a piecewise power-frequency characteristic as

$$\frac{\Delta P_{\text{PFFR}}(s)}{\Delta f(s)} = \begin{cases} 0 & \text{if } \Delta f_{db,\min} \le \Delta f \le \Delta f_{db,\max} \\ K_P & \text{if } \Delta f > \Delta f_{db,\max} \\ -K_P & \text{if } \Delta f < \Delta f_{db,\min} \end{cases} \tag{4.14}$$

where K_P represent the slope. Assuming the SPI have limited energy capacity, its active power output can be represented by the following expression.

$$\Delta P_{\text{PFFR}}(s) = \begin{cases} \Delta P_{\text{PFFR,max}} & \text{if } \Delta P_{\text{PFFR}} \ge \Delta P_{\text{PFFR,max}} \\ \Delta P_{\text{PFFR,min}} & \text{if } \Delta P_{\text{PFFR}} \le -\Delta P_{\text{PFFR,max}} \end{cases} \tag{4.15}$$

Considering the K_P can variate within a given range, i.e., $K_P \in [K_{P,\min}, K_{P,\max}]$, the slope of the power-frequency characteristic changes and it is shown in Figure 4.3a. Furthermore, if K_P is beyond $K_{P,\min}$, $K_{P,\max}$, the active power output is saturated, as illustrated in the power-time characteristic depicted in Figure 4.3b.

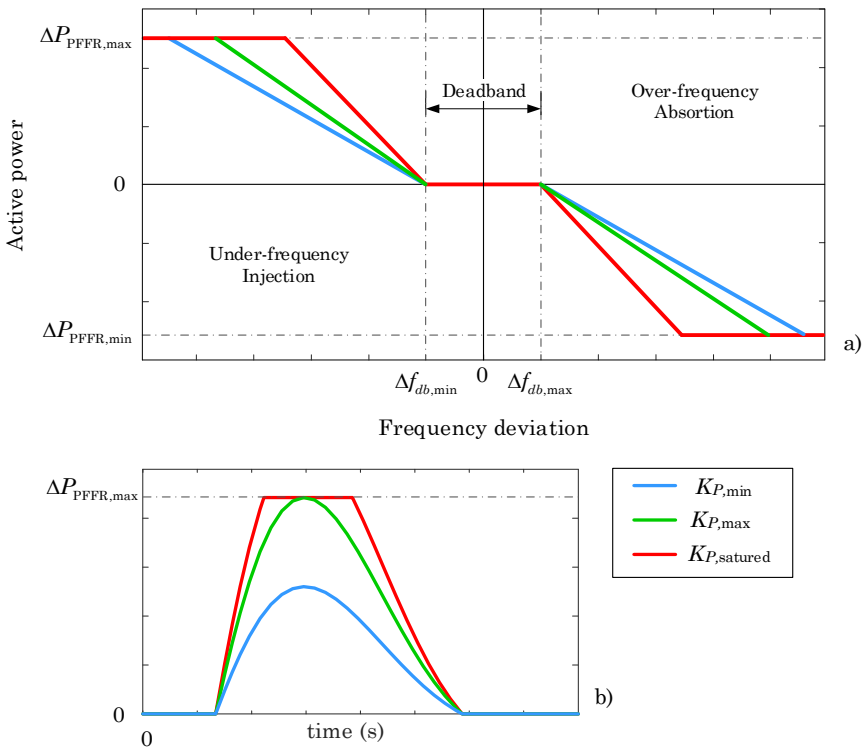

Figure 4.3. Proportional fast frequency controller considering deadband and KP variating in a range [$K_{P,\min}$, $K_{P,\max}$]: a) Power-frequency characteristic; b) Powe-time characteristic.

4.3.2 Derivative fast frequency response (DFFR)

DFFR provides an active power response (injection/absorption) in proportion to the speed of frequency deviation, i.e., based on the ROCOF value. Moreover, due to the ROCOF is practically zero during the steady-state operation, DFFR control only acts during the dynamic frequency response after a disturbance occurs. Consequently, this control enables the SPI to emulate the behaviour of the synchronous generator in the transient period. The transfer function of DFFR control is defined as

$$\frac{\Delta P_{\mathrm{DFFR}}(s)}{\Delta f(s)} = sK_D \tag{4.16}$$

where K_D is the gain of the DFFR controller, also known as synthetic inertia, and ΔP_{DFFR} is the active power injected/absorbed by the SPI.

4.3.3 Fast frequency combined response (FFCR)

The DFFR controller substantially impacts the ROCOF after a disturbance; it emulates an increase in kinetic energy and reduces the ROCOF value. Meanwhile, the PFFR controller mainly influences the steady-state frequency. Therefore, these controllers enhance the frequency response, and further advantages can be obtained by combining their dynamic response into a single FFCR control whose transfer function can be mathematically expressed as

$$\frac{\Delta P_{DFFR}(s)}{\Delta f(s)} = K_P + sK_D \tag{4.17}$$

The integration of the FFCR controller into the elemental frequency response model is presented in Figure 4.4, and the resulting transfers function is written in (4.18).

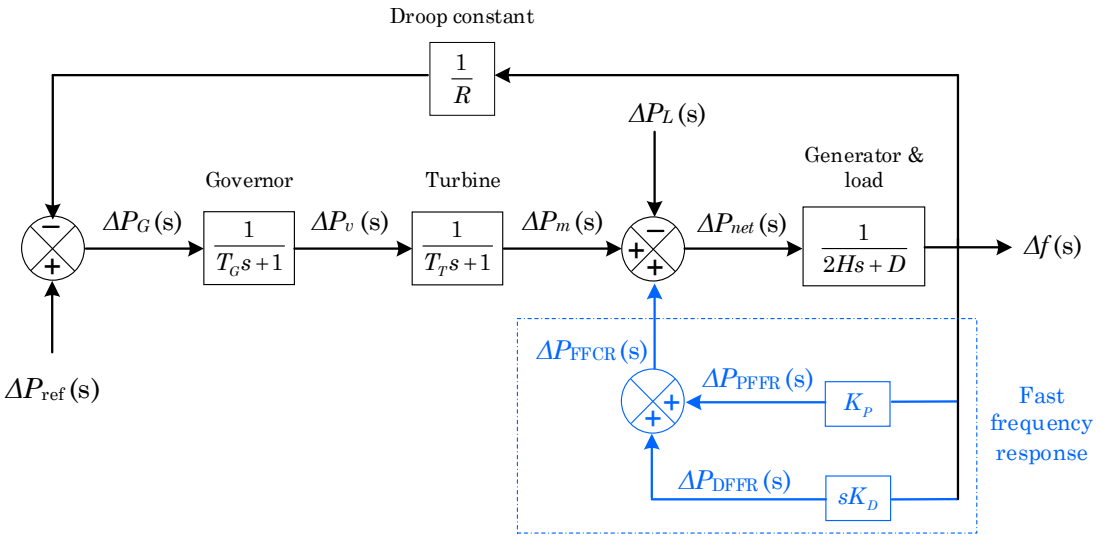

Figure 4.4. Block diagram of the elemental frequency response model, including the fast frequency combined response (FFCR) control.

$$\frac{\Delta f(s)}{\Delta P_L(s)} = -\frac{1}{(2Hs+D)-\frac{1}{R}\left(\frac{1}{T_G s+1}\right)\left(\frac{1}{T_t s+1}\right)-(K_P+sK_D)} \tag{4.18}$$

4.4 Energy storage systems

The controlled storing of energy as an alternative to mitigate the power imbalance in the power system has gained massive relevance in recent years. The process to transform the excess of power, store it as energy and then transform it back when needed can be done through the energy storage system (ESSs) [102]. Therefore, the provision of FFR can be made by employing ESSs. However, the successful implementation depends on features like energy density, power density and discharge duration. The energy density indicates the amount of energy that the ESSs can deliver, whilst the power density is the rate at which the ESSs delivers the energy. Lastly, the discharge duration is defined as the amount of time the ESSs can operate at their nominal power. The utilisation of the different ESSs technologies depends on the features mentioned above and categorised based on their timescale response as short-term, long-term, and long-term [103]. The ESSs classified into the short-term group are characterised by having a high power density and are appropriate for FFR and PFC applications. Meanwhile, the ESSs classified into the long term group are suitable for

SFC and TFC applications since this kind of ESSs exchanges energy in timescales between some minutes to several hours [104]. Finally, the ESSs into the very-long term group exchanges energy all-around 24 hours or above and are appropriate for balancing demand purposes [103], [105].

According to the department of energy based in the United States of America, up to February 2020, 1,697 ESSs projects have been registered worldwide, of which around 80% are in operation. The projects are classified depending on the technology to use, 964 BESS projects, 351 pumped hydro storage projects, 220 thermal projects, 53 flywheel projects, 29 supercapacitor projects, 13 hydrogen projects and 67 miscellaneous ESS projects. [9]. More than 70% of the ESSs projects are based on BESS and pumped hydro storage. Therefore, it provides an insight into what technologies are used in the decarbonisation process of the power system. In this research work, the pumped hydro storage and BESS are considered to provide FFR services to the power system. However, other technologies can be included in the frequency response model to provide frequency support. For instance, publication **[P10]** introduces the mathematical development of a frequency response model consisting of a fast-multi-energy storage system: flywheel and supercapacitor.

4.4.1 Pumped-storage hydropower plants.

From the variety of low-carbon technologies, the hydropower plants have a promising future in the decarbonisation plans of the power system since they are classified as renewable resources, and their turbines provide a natural inertial response. Moreover, HPPs offer higher control capabilities than others RESs, such as wind and solar power plants.

Most of the HPPs in operation in the present are built of classical damping. They are connected to the power system through a conventional fixed-speed synchronous generator, which is continuously regulated to fit the system frequency. Moreover, this kind of HPPs is equipped with Francis turbines designed for a wide range of heads and flows. Meanwhile, the traditional PHPPs are the eldest technology for large-scale energy

storage. The PHPPs are constituted of reversible pump turbines to have a fixed-geometry runner and two water reservoirs (high-reservoir and low-reservoir). The PHPPs produce electricity by releasing water flow from the high-reservoir to the low-reservoir. The water flow gets certain kinetic energy due to the difference in altitudes. When water flow passes through the turbine creates a torque that is transmitted to the generator and produces electricity. The high reservoir can be refilled by setting the turbine to pump operation mode and using electricity from the power system.

For different operational regimen, the control of the rotational speed and efficiency of HPPs and PHPPs is not always feasible due to the efficiency decreases when the operating point is shifted to reaches a fixed speed. Consequently, the operation of the hydro turbine at variable speed seems to be a solution since it enhances the efficiency at operating points other than the operating-design- point. Moreover, it provides several benefits, such as flexibility to deal with the balancing issues produced by integrating RESs into the power system, prolongs the turbine lifetime by reducing the number of starts/stop and increase the capability to control active power in pumping mode [106].

4.4.1.1 Variable-speed PHPPs

The conventional PHPPs are connected to the power system through a synchronous generator rotating at a constant speed to maintain the system frequency at nominal values. Moreover, the hydraulic turbine's energy conversion, cavitation, and vibration-free operation can achieve maximum efficiency values when the hydraulic turbine operates at its best operating point, i.e., at rotating speed, head, and discharge nominal design values. Therefore, the hydraulic efficiency curve is created to reach maximum efficiency when the hydraulic turbine operates at its best operating point. In this approach, the synchronous generator is restricted to maintain a constant speed, which may be not the same as the hydraulic turbine moving the operating point away from the best operating point and leading to efficiency drops.

The use of DC-link instead of AC-link to interconnect the PHPPs to the power system allows the synchronous generator to adopt rotational speeds different from the synchronous speed. Therefore, the speed of the hydraulic turbine can freely be regulated to satisfy the power demand and reaches its maximum efficiency value [107]. Moreover, the efficiency of the PHPPs using the variable speed approach increases in a ranger from 3% to 10% in contrast to the conventional PHPPs [106], [107].

The variable-speed PHPPs are typically based on two technologies, a DFIG and converter fed synchronous generator (CFSG). Moreover, it includes a power converter that enables the frequency variation of the generators [108].

The DFIG technology is commonly used in variable-speed PHPPs with power output levels greater than 100 MW [109]. The variable-speed PHPPs scheme based on DFIG technology shown in Figure 4.5. In this model, the hydro turbine is coupled to the shaft of the DFIG. The DFIG rotor winding is connected to the power system through a back-to-back power converter, which links the rotor to the DC-link using a power converter (rotor side converter). Whilst the DC-link is connected to the power system using a power inverter (network side inverter). Meanwhile, the DFIG stator is directly connected to the power system. This decoupling between the DFIG rotor and the power system enables DFIG speed variation.

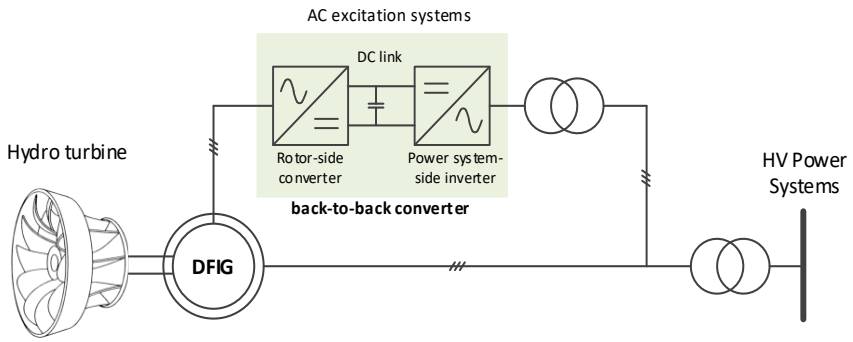

Figure 4.5. Schematic representation of variable-speed PHPPs scheme based on DFIG technology.

The CFSG technology uses a conventional synchronous generator which is coupled to the hydro turbine, and its stator is connected to the power system through a back-to-back power converter. The frequency of the synchronous generator is decoupled from the power system thanks to the DC-link of the power converter allowing the

synchronous generator to rotate at a wide range of speeds. The CFSG technology is used in variable-speed PHPPs with power output levels up to 100 MW [110]. The variable-speed PHPPs scheme based on CFSG technology is shown in Figure 4.6.

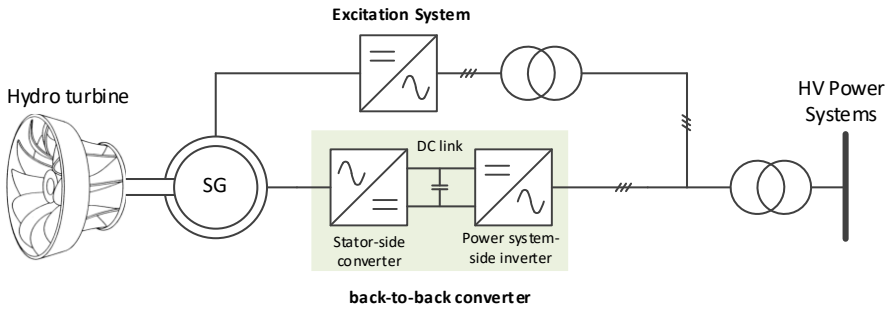

Figure 4.6. Schematic representation of variable-speed PHPPs scheme based on CFSG technology.

4.4.2 Battery energy storage system

The battery energy storage system is one of the ESSs technologies in the market with high energy density and long-time life, providing superior efficiency (up to 80%) and fast response (within 20 microseconds) for FFR and PFC applications [111]. BESS is constituted of three main subsystems, shown in Figure 4.7, that enable the energy exchange with the power system. The power conversion subsystem takes care of the energy transformation, for instance, electrical energy to chemical energy and vice versa, using an electrical or electromechanical device. The storing energy subsystem uses an electromechanical energy storage technology known as a battery to store the transformed energy for a time period. Lately, the BESS control subsystem consists of two types of controllers: fast internal controller and slow external outside controllers. The fast internal controller is associated with the *dq*-axis currents control at the AC side of the SPI. It is directly connected to the power conversion subsystem. Meanwhile, the slow external controller involves *P*-*Q* controller and battery charge controller [35]. Inside the slow external controller can be included the FFR control, which acts to modify the active power reference (P'_{AC}) of the power inverter.

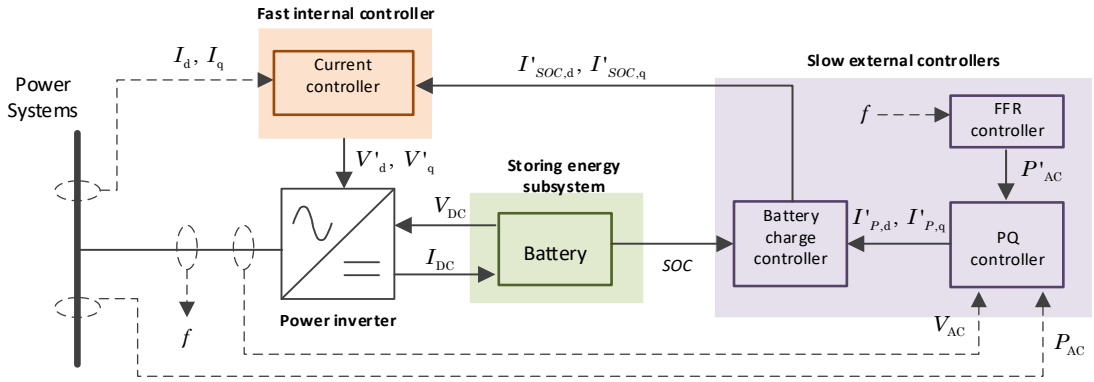

Figure 4.7. Diagram representation of battery energy storage system [35].

4.5 FFR provision using variable-speed PHPPs and BESS

The growing integration of RESs in the power system creates uncertainty concerning the power balance since intermittent power sources such as wind, and solar power plants do not have deterministic power production. In addition, the construction of the RESs is such that they can provide limited or even null inertia. Therefore, the control and operation capabilities of the TSOs are affected, leading them to interact with the distribution system operators (DSOs) and use ESSs technologies to counteract the power balance and control issues [112]. The ESSs are mainly used to provide FFR services by exchanging active power with the power system when is needed.

The variable-speed PHPPs are enabled to operates in two modes: pump mode and turbine mode. The operation in pump mode allows controlling the power thanks to the variable speed. Meanwhile, the operation in turbine mode enables the mechanical power to be controlled by the rotational speed and the gate position [113]. For purposes of FFR services, in this thesis, the variable-speed PHPPs are considered to operate in turbine mode, and the FFR is enabled at the power system inverter side.

Considering a power transmission system consisting of synchronous generators, transformers, and protection equipment at which several distribution systems are connected to it through the sub-transmission system, it can be defined as the TSO-DSO interaction. Therefore, the frequency response following a disturbance can be obtained by the swing equation defined in (2.6) if the automatic voltage regulation and power system stabiliser are overlooked in the PFC period [78]. Moreover, the FFR support

provided by the DSO to the TSO is considered as the total active power provided by the ESSs installed in the DSO network. In this thesis, the FFR service provided by the PHPPs and BESS.

$$\Delta P_{FFR} = \sum_{i=1}^{n_{ESS}} \Delta P_{ESS,i} = \sum_{j=1}^{n_{PHPP}} \Delta P_{PHPP,i} + \sum_{k=1}^{n_{BESS}} P_{BESS,k} \tag{4.19}$$

where $\Delta P_{ESS,i}$ is the active power of the i-th ESS technology connected in the DSO network. The active power of the j-th PHPP and k-th BESS are $\Delta P_{PHPP,j}$ and $\Delta P_{,BESS,k}$, respectively. Moreover, n_{PHPP} and n_{BESS} are the total number of PHPP and BESS, respectively and $n_{ESS} = n_{PHPP} + n_{BESS}$.

4.6 Optimisation of the FFR parameters

The installation of power inverter-based technologies, such as PHPP and BESS, raises the need to analyse their implications on the frequency response. Due to FFR can be enabled in PHPP and BESS, the appropriate amount of power exchange between the PHPP, BESS, and the power system can substantially improve the frequency response. Therefore, it is of paramount significance to determine the optimal parameter of the FFR to provide adequate frequency support by ensuring the frequency quality metrics are within their permissible values and avoiding the activation of emergency frequency controls such as UFLS.

The computation of the FFR parameters is formulated as an optimisation problem in the form described in Section 2.6.1, and it is fully described below.

4.6.1 Control variables

The active power injection/absorption of the FFR is strongly dependent on the droop coefficient (K_P) when PFFR is used, synthetic inertia (K_D) when DFFR is used or both when FFCR is implemented. Therefore, the decision variables are selected to be K_P and K_D, and the decision variable vector ($\mathbf{K}$) is comprised of the droop coefficient and synthetic inertia of all ESS equipped with the FFR controller (i.e., PHPP and BESS), and it is written as:

$$\mathbf{K} = \begin{bmatrix} \mathbf{k}_P & \mathbf{k}_D \end{bmatrix} \tag{4.20}$$

with

$$\mathbf{k}_P = \begin{bmatrix} K_{P,1} & K_{P,2} & \cdots & K_{P,i} & \cdots & K_{P,n_{ESS}} \end{bmatrix}$$
$$\mathbf{k}_D = \begin{bmatrix} K_{D,1} & K_{D,2} & \cdots & K_{D,j} & \cdots & K_{D,n_{ESS^*}} \end{bmatrix}$$

where $K_{P,i}$ is the droop coefficient of the i-th ESS with PFFR control enabled and $K_{D,j}$ is the synthetic inertia coefficient of the j-th ESS with DFFR control enabled. Moreover, n_{ESS} *and* n_{ESS^*} are the total number of ESS with PFFR and DFFR control enabled, respectively. Note that this approach allows to implement either PFFR, DFFR or FFCR as desired at each ESS, and the formulation does not need to be modified.

The droop coefficient and synthetic inertia coefficient can acquire values in a range that ensures the FFR controller settings are inside realistic physical values. Therefore, the decision variables are restricted to be within their minimum and maximum permissible values as

$$\mathbf{k}_{P,\min} \leq \mathbf{k}_P \leq \mathbf{k}_{P,\max}$$
$$\mathbf{k}_{D,\min} \leq \mathbf{k}_D \leq \mathbf{k}_{D,\min} \tag{4.21}$$

where $\mathbf{k}_{P,\min}$ and $\mathbf{k}_{P,\max}$ are the minimum and maximum limit of droop coefficients whilst $\mathbf{k}_{P,\min}$ and $\mathbf{k}_{P,\max}$ are the minimum and maximum limit of synthetic inertia coefficient.

4.6.2 Objective function

The goal of the frequency control strategies is to maintain the frequency within the Δf_{SS} and does not exceed the $\Delta f_{\mathrm{SS,max}}$ when the power system is in normal operation. If a disturbance occurs, it is no desirable the instantaneous frequency does not reach the activation zone of emergency control schemes (e.g., UFLS). Therefore, $\Delta f_{\max}$ must be limited. The mentioned frequency quality metrics are essential in frequency control. Consequently, two objective functions are studied: minimisation of the steady-state error and minimisation of the instantaneous frequency deviation. Moreover, the

objective functions are intended to minimise regardless of the disturbance location. Thus, the frequency of the power system is represented by f_{COI}.

4.6.2.1 Objective function 1:

The steady-state frequency should ideally back to its nominal value, f_0, after the action of PFC, and as a consequence, the steady-state frequency deviation $\Delta f_{\mathrm{COI,SS}}$ should be zero. Nevertheless, driving the $\Delta f_{\mathrm{COI,SS}}$ to zero in the PFC period will be an unsatisfactory approach since the FFR will overlap the SFC, and it is not the purpose of this controller. Accordingly, the FFR control can be used to drive the $\Delta f_{\mathrm{COI,SS}}$ into a pre-set value (Δf^*_{SS}) inside the frequency quality indicator $\Delta f_{\mathrm{SS,max}}$. The objective function to minimise the $\Delta f_{\mathrm{COI,SS}}$ concerning $\Delta f^*\mathrm{SS}$ is written as

$$f_1(\mathbf{K}) = \min\left|\Delta f^*_{\mathrm{SS}} - \Delta f_{\mathrm{COI,SS}}\right| \tag{4.22}$$

4.6.2.2 Objective function 2:

The frequency response in the transient period after a disturbance can reach dangerous low values that may lead to activating the UFLS scheme, UF generator protection or even produce worse damage. Therefore, it is desired to reduce as much as possible the maximum instantaneous frequency deviation ($\Delta f_{\mathrm{COI,max}}$).

The objective function to minimise $\Delta f_{\mathrm{COI,max}}$ is defined as

$$f_2(\mathbf{K}) = \min \Delta f_{\mathrm{COI,max}} = \min\left|f_0 - f_{\mathrm{COI,min}}\right| \tag{4.23}$$

4.7 Future of the Nordic power system

The Nordic power system is constantly evolving, mainly due to the increasing replacement of conventional power plants by RESs. The principal changes are installing wind power plants, decommissioning thermal and nuclear power plants, and increasing interconnectors between NPS and neighbouring power systems by about 50% [114], [92]. Moreover, Nordic countries are collaborating to encourage the increase of power production coming from RESs. For instance, a project between Norway and Denmark is

planned to export the excess of power produced by wind power plants from Denmark to Norway. Then, when wind power plants have low power production importing power produced by HPP from Norway to Denmark. Furthermore, some Nordic countries have projects to exchange energy with others countries like the Netherlands, Germany and the United Kingdom [115].

The mentioned changes in the NPS are creating several challenges, mainly impacting the TSO strategies for frequency control. For instance, reducing the total inertia constant of the NPS [116], [117]. Therefore, the different TSO in the NPS investigated the future situation of NPS until the year 2040.

The NPS is expected to have significant changes regarding the amount of power production sources installed or decommissioned in the coming 20 years, except the HPPs [118]. Table 4.1 shows the expected changes in power production; the wind power plants will replace the decommissioned nuclear and thermal plants by 2040. It will produce a change in the power system layout and increase the increase its sensibility to disturbances.

Table 4.1. Expected shift of the power production sources in the NPS considering 20 years.

Power production source	**Power production per year (GW)**			**Shift in 2020-2040 period**	
	2020	***2030***	***2040***	***%***	***Type***
Nuclear	12	10.5	2.5	79 ↓	Decommissioning
Thermal	8	5	3.5	56 ↓	Decommissioning
Wind	20	30	45	125 ↑	Installation

Furthermore, the power demand is projected to increase and reaches a maximum value of 79 GW in 2040. Figure 4.8 present the predicted power demand and power production in the 2020-2040 period. It shows that by 2040 the NPS will depend on intermittent power sources.

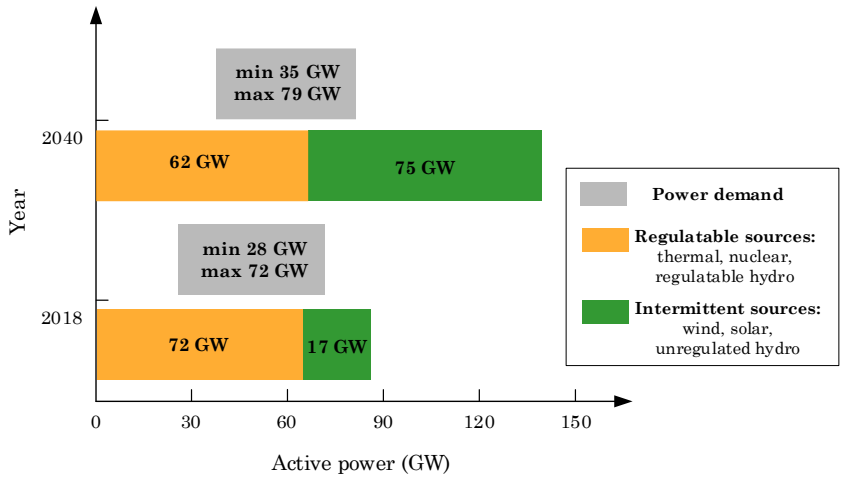

Figure 4.8. Power demand and power production of the NPS in 2018 and predicted by 2040 [119].

The forecasted power demand for the 2020-2040 period is presented in Table 4.2.

Table 4.2. Power demand forecast for the period 2020-2040.

Year	Power demand (GW)	
	Low	***High***
2020	28.6	72.6
2030	31.8	75.8
2040	35	79.0

The predicted kinetic energy of the NPS is presented in Table 4.3. It shows the kinetic energy, and as a consequence, the inertia will decrease, reaching minimum values between 150 GW·s and 190 GW·s in the year 2040. This is due to the projected decommissioning of high inertia power production sources presented in Table 4.1.

Table 4.3. Kinetic energy forecast for the period 2020-2040.

Year	Kinetic energy (GW·s)	
	Low	***High***
2020	174	260
2030	159	255
2040	105	190

4.8 Demonstrative examples and results

The proposed methodology to compute the optimal settings of the FFR control and provide frequency support within the PFC period after a disturbance occurs is assessed considering two test system: the simplified three-area model of NPS and a distribution network of the Norwegian power system. The simplified three-area model of NPS is used to demonstrate the impact of the optimal FFR control on the frequency response quality indicator and evaluate the proposed objective functions. Meanwhile, the distribution network of the Norwegian power system is considered to represent the TSO-DSO interactions and evaluate the proposed methodology in a dynamic model equipped with two ESS technologies (PHPP and BESS) at which the FFR control is enabled. Single-area NPS model

The NPS is constituted of the interconnect the power system of four countries, Denmark, Finland, Norway and Sweden, and three control areas commonly represent its simplified model. Area1 represents the Swedish power system, Area 2 consists of the Norwegian power system, and Area 3 represents the Finnish power system. The NPS simplified model considers the interconnection between the three Areas by two transmission lines. $\mathrm{TL}_{12,}$ interconnecting Sweden (Area 1) and Norway (Area 2), and its power exchange is ΔP_{12}. Moreover, TL_{13} interconnecting Sweden (Area 1) and Finland (Area 3), and its power exchange is ΔP_{13}. The graphical representation of the NPS simplified model is depicted in Figure 4.9.

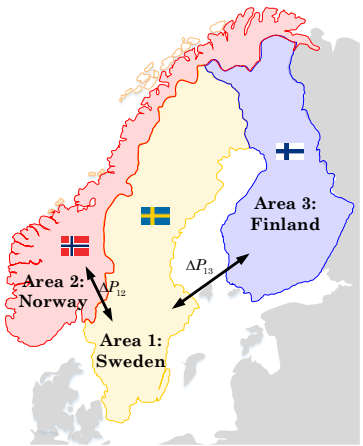

Figure 4.9. Three areas NPS simplified model.

The NPS does not have automatic control of tie-line power flow deviation between the areas. Therefore, it can be shaped as the single-area frequency response model described in section 4.2.4. The NPS is mainly constituted of hydropower plants. Consequently, the transfer function of the frequency response defined in (4.8) is slightly modified to consider the model of a hydro turbine and speed governor.

The transfer function of the hydro turbine is defined as

$$G_{\mathrm{T}}(s) = \frac{1 - T_w s}{1 + \frac{1}{2} T_w s} \tag{4.24}$$

where T_w is a time constant, typically between 0.5 to 4.0 s [120]. T_w is determined in function of the pipe length (l), initial water velocity (v), gravity acceleration constant (g) and headwater (h) as $T_w = lv/gh$.

The speed governor model is considered to be a proportional-integral governor, and its transfer function is used [88]:

$$G_{\mathrm{G}}(s) = \frac{G_P s + G_I}{T_G s^2 + \left(R_P G_P + 1\right) s + R_P G_I} \tag{4.25}$$

where T_G is the servo time constant, G_P is the proportional gain, G_I is the integral gain, and R_P is the droop.

The frequency response of the single-area NPS model, including the hydro turbine, governor and FFR model, is written as

$$\Delta f\left(s\right) = -\frac{\Delta P_L\left(s\right)}{\left(2Hs + D\right) - \left(G_G(s) G_T(s) + \left(K_P + sK_D\right)\right)} \tag{4.26}$$

The parameters of the single-area NPS model were taken from [88] and are defined in Table 4.4.

Table 4.4. Parameters of the single-area NPS model.

Element	Parameter	Units	Value
Governor	G_P	--	1.6
	G_I	--	1.175
	R_P	pu	0.133
	T_G	s	0.2
Turbine	*Tw*	s	1.01
Synchronous generator	*H*	s	9.68
Load	D	pu/pu	0.517

4.8.1.1 Simulations and results

The implemented single-area NPS model is used to evaluate the effect of the FFR control on the frequency response. First, a sensitivity study is carried out to determine the impact of low inertia situation on three frequency response quality indicators. Then, the proposed objective functions described in (4.22) and (4.23) are evaluated. The frequency disturbance is considered to be a sudden change in the power demand (ΔP_L).

4.8.1.1.1 Sensitivity study

The frequency response of the single-area NPS model is assessed considering three frequency response quality indicators: $f_{\min}$, f_{SS} and maximum ROCOF *(*$ROCOF_{\max}$). ΔP_L represent the sudden increase in the demand of 0.0280 pu, i.e., $\Delta P_L = 0.0280$ pu. The low inertia situation is represented by progressively reducing the nominal inertia (H_0), defined in Table 4.4.

The frequency response considering the same disturbance for the progressive reduction of inertia is presented in Figure 4.10. It can be observed that as the inertia is reduced, the frequency response is less damped, and it requires more time to the frequency settle at f_{ss}. Therefore, the capability of the NPS to recover the frequency after the disturbance occurs is increasingly deteriorates as the inertia decreases.

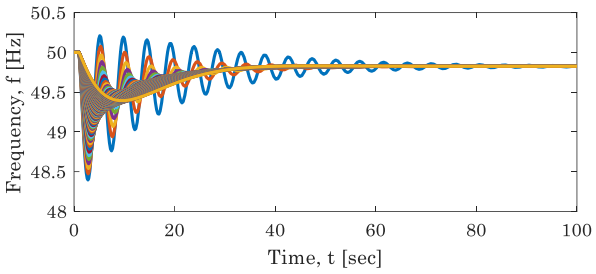

Figure 4.10. Frequency response of single-area NPS model considering the gradual inertia reduction.

The effect of the inertia decreasing is mainly producing high ROCOF values, as shown in Figure 4.11a. Consequently, the high ROCOF values lead to $f_{\min}$ reaches deeper values (see Figure 4.10b). Furthermore, the NPS can tolerate a minimum inertia value of 0.6776 s, meaning the NPS with an inertia reduction of 84% from H_0 can recover the frequency near its nominal value.

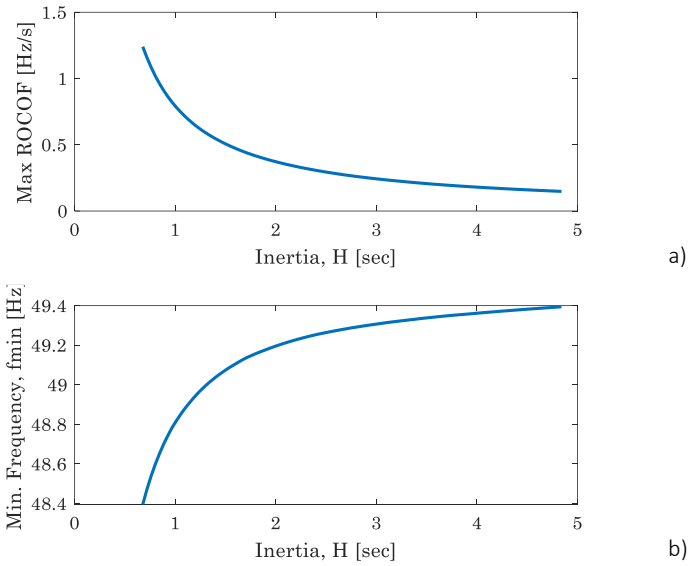

Figure 4.11. Effect of the inertia reduction on a) maximum ROCOF ($ROCOF_{\max}$) and b) minimum frequency ($f_{\min}$).

The sensitivity study demonstrates that there is a minimum limit of inertia that the power system can tolerate. The minimum inertia value at which the power system can restore the frequency after a disturbance happens. Moreover, it underlines that having a low level of inertia in the power system deteriorates the power system stability in case of a disturbance.

4.8.1.1.2 Optimal FFR parameters

The proposed methodology to compute the optimal FFR parameters described in Section 4.6 is evaluated considering the FFCR control is enabled in the single-area NPS model. Therefore, the decision variables are the droop coefficient (K_P) and the synthetic inertia coefficient (K_D). Moreover, it is considered the single-area NPS model operates in a low inertia scenario, assuming a reduction in the inertia of 50% of H_0; therefore, H= 2.42 s. The frequency disturbance is considered the same as the sensitivity study, i.e., an unexpected increase in the power demand of $\Delta P_L = 0.0280$ pu.

The optimisation problem is solved using the interior-point optimisation algorithm, which is described in Section 2.6.2.1 [121], [122].

For illustrative purposes, objective function 1 described in (4.22), intended to minimise the steady-state frequency deviation, is solved considering Δf^*_{ss} = 49.9 Hz. Meanwhile, objective function 2 described in (4.23), which is formulated to minimise the maximum frequency deviation, considers that desired $\Delta f_{\text{COI,max}}$ is 49.5 Hz.

The convergence curve of $f_1(\mathbf{K})$ and $f_2(\mathbf{K})$ is presented in Figure 4.12. $f_1(\mathbf{K})$ is evaluated over 35 iterations and reaches the minimum at iteration six, whilst $f_2(\mathbf{K})$ is calculated across 35 iterations and takes five iterations to reaches the minimum value.

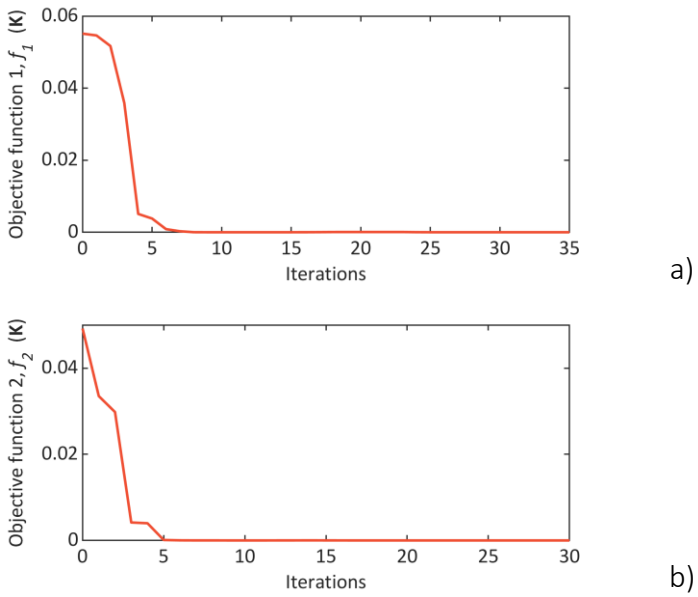

Figure 4.12. Convergence curve of a) objective function 1 ($f_1(\mathbf{K})$) and b) objective function 2 ($f_2(\mathbf{K})$).

The optimal solution of the FFR parameters and the resulting frequency response quality indicators for those optimal parameters are described in Table 4.5. Moreover, the frequency response of the single-area NPS model for the solution of both objective functions is depicted in Figure 4.13.

From Table 4.5, it is determined the optimal FFCR parameters does not impact the maximum ROCOF behaviour since it maintains the same value for both objective function solutions. In contrast, $f_{\min}$ and f_{SS} values reaches the desired values solving objective function 1 (see Figure 4.13a) and objective function 2 (see Figure 4.13b), respectively. Consequently, the objective functions satisfy the optimal solution of (4.22) ,(4.23).

Table 4.5. Optimal solution of FFR parameters and frequency response quality indicators of the single-area NPS model.

Objective function	FFR parameters		Frequency response quality indicators		
	K_P	K_D	$f_{\min}$ (Hz)	f_{SS} (Hz)	$ROCOF_{max}$ (Hz/s)
1	2.5172	2.2628	49.836	49.9	-0.144
2	0.7166	0.6927	49.5	49.836	-0.144

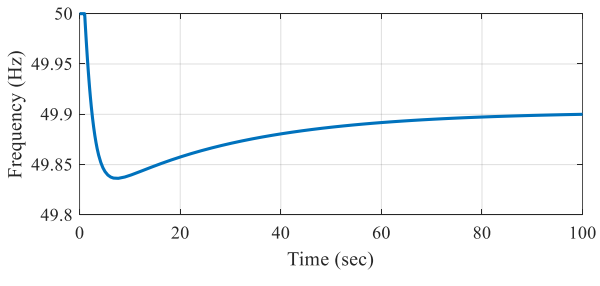

a)

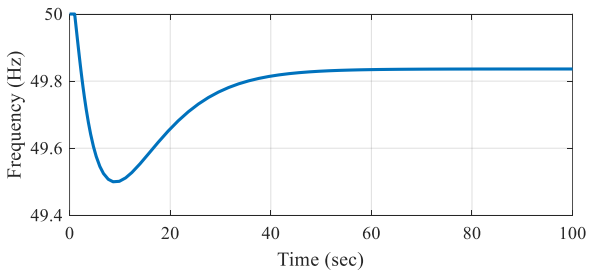

b)

Figure 4.13. Frequency response of single-area NPS model considering the optimal parameters of a) objective function 1 ($f_1(\mathbf{K})$) and b) objective function 2 ($f_2(\mathbf{K})$).

4.8.2 A Norwegian distribution system

The Vestfold-Telemark distribution system (VDS) of the Norwegian power system is modelled using data publicly available. VDS is a 132 kV distribution network of the southeast area of Norway, and it is interconnected to the Norwegian power system through 300 kV and 420 kV transmission lines. It consists of 109 buses, 20 HPP of size from 2.3 MVA up to 190 MVA and 58 lumped loads of power level between 16 MW and up to 62 MW. The total installed power generation (P_G) is 1083 MVA, and the total power demand (P_d) is 1643 MW. To cover P_d, VDS imports 560 MW from the Norwegian power system. The schematic representation of the interconnection of VDS is depicted in Figure 4.14; meanwhile, Figure 4.15 shows the distribution of power generation sources and power demand in the VDS.

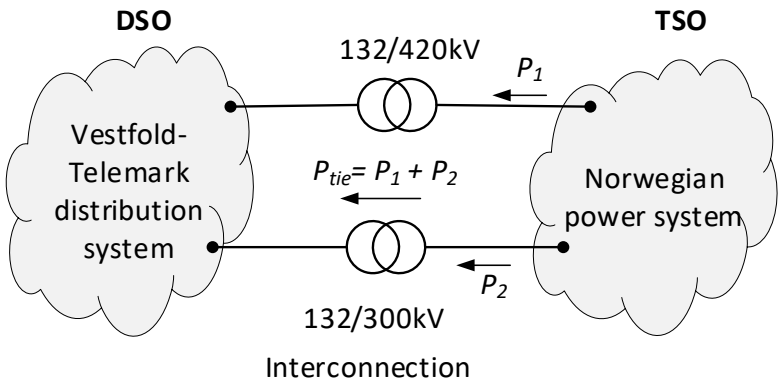

Figure 4.14. Schematic representation of the interconnection of the Vestfold-Telemark distribution system and the Norwegian power system.

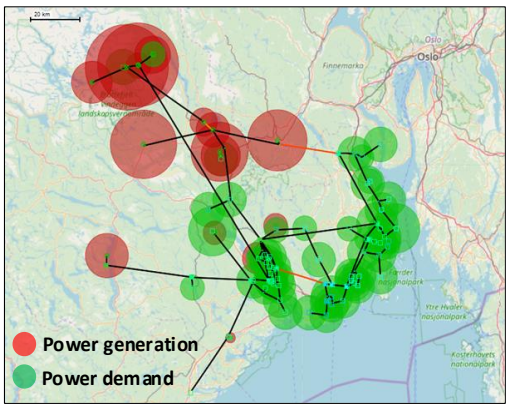

Figure 4.15. Geographical representation of the Vestfold-Telemark distribution system specifying the location of power generation sources (red) and power demand (green).

As mentioned in Section 4.7, the existing HPPs in the NPS are not expected to be decommissioned or planning to build new ones. Consequently, the most significant projected change may be the modernisation and renovation of them to increase efficiency by replacing conventional control and hydro turbine devices with state-of-the-art technologies. Therefore, it is assumed that the retrofitting of the conventional PHPPs, for the coming 20 years will include the installation of CFSG and DFIG to enable the variable-speed functionality on PHPPs. Moreover, the installation of BESS is considered to cope with the projected kinetic energy reduction and growing power demand. The full description of these assumptions is depicted in Table 4.6, which are classified into three cases. Case 0: baseline, Case 1: PHPPs retrofitting and Case 2: BESS installation.

Table 4.6. Definition of the cases of study considered to evaluate the proposed optimisation methodology.

Case	Description	Purpose
0	The VDS remains as it is; not new technologies are integrated. It considers the expected kinetic energy reduction in the coming 20 years.	Used as the baseline case. To observe the performance of the VDS considering the influence of the low kinetic energy in the frequency response. Assuming the frequency support only comes from synchronous generators, any other technology is assumed to be no frequency sensible.
1	Medium PHPPs with nominal power lower than 100 MW will be retrofitted with CFSG units. Large PHPP with nominal power greater than 100 MW will be retrofitted with DFIG units.	Identify the implication on the frequency response of retrofitting the conventional PHPP by integration of variable-speed technologies.
2	BESS installation.	Demonstrate the benefit of integrating BESS technologies to enhance the frequency response.

Furthermore, three scenarios for ten-year intervals in 2020, 2030 and 2040 are considered. Each scenario considers the expected kinetic energy reduction and integrating variable-speed technologies and BESS into the VDS. Details of the defined scenarios are in Table 4.7

Table 4.7. Definition of scenarios that describe the projected changes in the VDS.

Scenario	Kinetic energy (GW·s)	Number of ESSs		
		CFSG	*DFIG*	BESS
2020	174	0	0	0
2030	159	1	2	1
2040	105	4	3	5

Finally, Table 4.8provide the PHPPs of VDS, which are considered that will be modernised with variable-speed technologies and/or equipped with BESS. In this thesis, PHPPs with nominal power equal to or less than 100 MW are considered medium-size, and PHPPs with nominal power greater than 100 MW are considered large-size.

Table 4.8. Plan of PHPPs modernisation with variable-speed and BESS technologies.

PHPP name	Installed capacity (MVA)	PHPPs modernisation		Installation BESS	
		Variable-speed technology	*Year*	*Capacity (MVAh)*	*Year*
Fritzøe	7	--	---	7	2040
Mæl	38	CFSG	2040	38	2040
Fjone	55	CFSG	2030	55	2030
Svelgfoss	93	CFSG	2040	93	2040
Skollenborg	99	CFSG	2040	99	2040
Hjartdøla	130	DFIG	2030	--	--
Såheim	189	DFIG	2030	--	--
Mår	190	DFIG	2040	--	--

4.8.2.1 Simulation and results

The NPS requires the emergency controls to actuate when the maximum instantaneous frequency deviation ($\Delta f_{\max}$) reaches values equal to or greater than 1.2 Hz [123]. Thus, the optimisation methodology proposed in section 4.6 is implemented to compute the optimal droop coefficient of PFFR control. The optimisation goal is to compute the

optimal droop coefficients of all ESSs installed in the VDS while the maximum instantaneous frequency deviation ($\Delta f_{\mathrm{COI,max}}$) is minimised. The objective function to be solved is (4.23) to avoid $f_{\mathrm{COI,\ min}}$ attains values lower than 48.8 Hz and the activation of the UFLS scheme.

The cases described in Table 4.6 are performed for each scenario defined in Table 4.7 to assess the enhancement of the frequency quality indicators produced by integrating ESSs into the VDS. It is assumed that all ESSs technologies (CFSG, DFIG and BESS) are equipped with PFFR control. Moreover, the frequency disturbance is presumed to be an abrupt power demand increase of 1,300 MW.

The dynamic model of VDS is implemented in DIgSILENT® PowerFactory™ version 2020, and the SLSQP algorithm described in Section 2.6.2.2 [124] is implemented in Python programming language and used to solve the optimisation problem. Furthermore, Python is used as an interface between DIgSILENT® PowerFactory™ and the SLSQP algorithm. In general, the decision variables computed by the SLSQP algorithm are set in the PFFR control, and DIgSILENT® PowerFactory™ runs a dynamic simulation considering a frequency disturbance to obtain the frequency response in RMS values and sends it to the SLSQP algorithm to evaluate the objective function. This procedure is repeated until the stopping criteria of the SLSQP algorithm is fulfilled.

4.8.2.1.1 Inertia reduction

Case 0 assumes there will be no changes in the VDS during the 2020–2040 period. However, the rest of the NPS is expected to face several changes regarding the inertia levels. Therefore, the frequency quality indicators are assessed by considering the projected kinetic energy reduction defined in Table 4.7. The frequency response of Scenario 1, Scenario 2 and Scenario 3 following the disturbance are depicted in Figure 4.16.

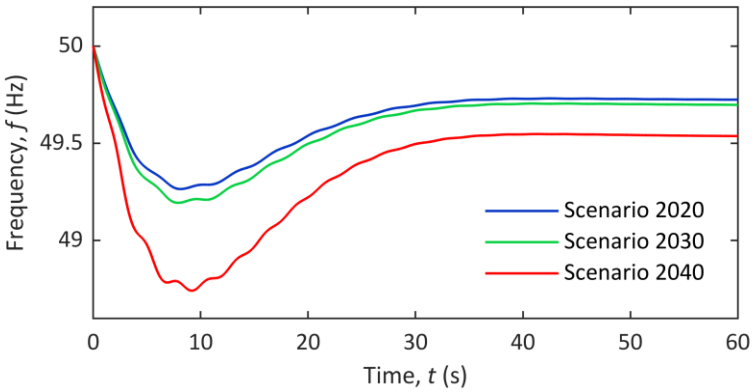

Figure 4.16. Frequency response following an unexpected power rise of 1300 MW considering kinetic energy reduction scenarios up to 105 GW·s

From Figure 4.16, it can be observed for the three scenarios that the frequency is retrieved at different steady-state values. However, it is evident the minimum frequency ($f_{\mathrm{COI,min}}$) achieves deeper values as the kinetic energy decreases, indicating the $ROCOF_{\mathrm{COI,max}}$ values are increasing.

A summary of the frequency quality indicators is presented in Table 4.9, highlighting the frequency response deteriorating for low kinetic energy levels due to the synchronous generators do not have sufficient kinetic energy to cope with the power imbalance and stop the frequency from decaying in the PFC period.

Table 4.9. Results of the frequency quality indicators considering the assessment of Case 0.

Scenarios	Kinetic energy reduction (%)	Frequency quality indicators				
		$\Delta f_{\mathrm{COI,\,max}}$ (Hz)	$f_{\mathrm{COI,\,min}}$ (Hz)	$f_{\mathrm{COI,\,SS}}$ (Hz)	t_{min} (s)	$ROCOF_{\mathrm{COI,\,max}}$ (Hz/s)
2020	0	0.738	49.265	49.723	8.132	−0.186
2030	8.62	0.806	49.194	49.697	7.912	−0.204
2040	39.66	1.258	48.742	49.536	9.182	−0.318

From Table 4.9, Scenario 2040 is the most critical outlook since the kinetic energy is reduced by almost 40%, causing the frequency to reach values below 48.8 Hz and probably activate the UFLS scheme, which is not desired. As a result, Scenario 2040 emphasises the necessity of the NPS to incorporate technologies capable of providing frequency support services or use the existing ones installed at the distribution level.

4.8.2.1.2 Scenario 2030

Scenario 2030 is dedicated to evaluating the frequency response when PHPPs of the VDS are modernised with CFSG, and DFIG technologies and BESS are installed. The PFFR control is enabled in the CFSG, DFIG and BESS technologies and its optimal parameters are computed by minimising the objective function defined in (4.23). In this scenario, Case 0 only considers the kinetic energy of the NPS is decreased by 8.62% due to the decommissioning of thermal power plants. Meanwhile, Case 1 denotes the modernisation of one medium and two large PHPPs by CFSG and DFIG technologies, respectively. Case 2 contemplate the changes in Case 1 and, in addition, the installation of one BESS at a medium-size PHPP (details are depicted in Table 4.8).

The optimal droop coefficient of CFSG, DFIG and BESS for Case 1 and Case 2 are shown in Table 4.10. The optimal droop coefficients are set into the PFFR control of each ESS technology, and the frequency quality indicators are assessed by simulating a power imbalance of 1300 MW.

Table 4.10. Result of the optimal droop coefficients for Case 1 and Case 2 in Scenario 2030.

PHPP name	**ESS technology**	**Droop coefficient (K_P)**	
		Case 1	***Case 2***
Fjone	CFSG	0.052	0.0001
Fjone	BESS	---	0.0001
Hjartdøla	DFIG	0.0072	0.0001
Såheim	DFIG	0.0001	0.0001

The frequency response for Case 0, Case 1 and Case 2 is depicted in Figure 4.17. It shows the frequency response is enhanced by integrating variable-speed technologies (CFSG and DFIG) in Case 1 and the installation of BESS in Case 2 regarding Case 0, where only synchronous generators provide frequency support.

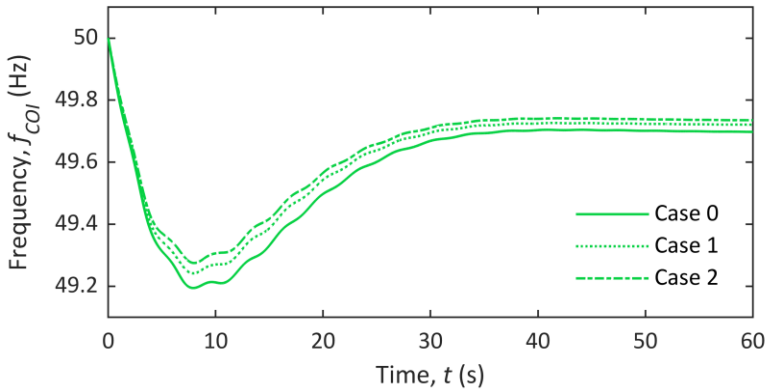

Figure 4.17. Frequency response of Case 0, Case 1 and Case 2 in Scenario 2030 following a power imbalance of 1300 MW.

The frequency enhancement in Case 1 is mainly attributed to the action of the PFFR control in CFSG and DFIG to increase the active power contribution and stop the frequency drop. Furthermore, in Case 2, the installation of BESSs provide active power in proportion to the frequency deviation leading to a reduction in $\Delta f_{\mathrm{COI,\ max}}$. The total active power contribution of Case 0, Case 1 and Case 2 to counter the power imbalance is presented in Figure 4.18.

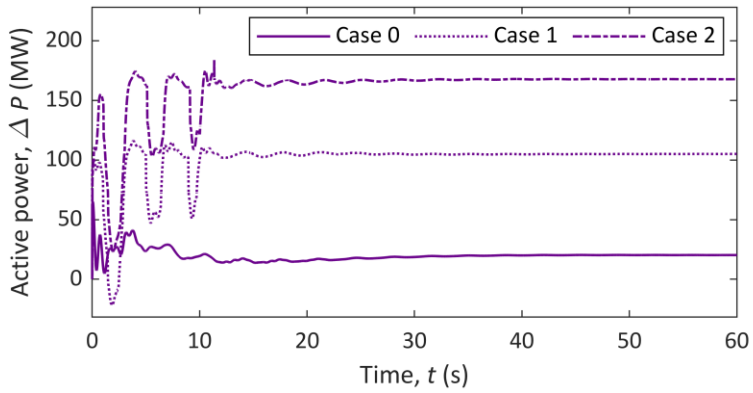

Figure 4.18. Active power contribution of VDS by assessing Case 0 (synchronous generators), Case 1 (synchronous generators+CFSG+DFIG) and Case 2 (synchronous generators+CFSG+DFIG+BESS) in Scenario 2030.

Table 4.11 depicts the frequency response indicator of Case 0, Case 1 and Case 2. It demonstrates that the action of the optimal PFFR control contributes to the enhancement of the frequency indicators. For instance, regarding Case 0, $\Delta f_{\mathrm{COI,\ max}}$ is reduced by about 10% and $ROCOF_{\mathrm{COI,max}}$ by around 4%, preventing frequency response reaches low dangerous values.

Table 4.11. Results of the frequency quality indicators considering the assessment of Case 0, Case 1 and Case 2 in Scenario 2030.

Case	Frequency quality indicators				
	$\Delta f_{\mathrm{COI,\,max}}$ (Hz)	$f_{\mathrm{COI,\,min}}$ (Hz)	$f_{\mathrm{COI,\,SS}}$ (Hz)	t_{min} (s)	$ROCOF_{\mathrm{COI,\,max}}$ (Hz/s)
0	0.806	49.194	49.697	7.912	−0.204
1	0.759	49.241	49.720	7.912	−0.195
2	0.725	49.275	49.734	7.995	−0.196

4.8.2.1.3 Scenario 2040

In the year 2040, several nuclear and thermal power plant will be dismantled, causing a considerable inertia reduction and, as a consequence, a significant reduction of kinetic energy, around 40% concerning Scenario 2020, in the NPS will be experienced, revealing a critical situation in the future years. Therefore, this scenario evaluated the positive influence of technologies that provide FFR to counteract the critical low kinetic energy scenario. Case 1 considers the modernisation of seven PHPPs in the VDS by integrating CFSG and DFIG technologies. Case 2, in addition to the seven PHPPs modernisation, includes the installation of five BESS.

The new integrated technologies (CFSG, DFIG and BESS) are equipped with PFFR control, and its optimal droop coefficients are computed considering the minimisation of the objective function described in (4.23). The frequency disturbance is the same used in Scenario 2030, i.e., a power imbalance of 1,300 MW. The optimal droop coefficients of CFSG, DFIG and BESS for Case 1 and Case 2 are summarised in Table 4.12.

The frequency response considering the optimal droop coefficients for Case 1 and Case 2 is shown in Figure 4.19. It can observe a significant improvement in $f_{\mathrm{COI,min}}$, especially in Case 2, demonstrating that the BESS are suitable for providing inertia support in critical scenarios which have reduced kinetic energy levels. In Case 2, the slight frequency drops several second after the frequency settles. The BESS produces this frequency behaviour, i.e., once the BESS have delivered all their available active power, they begin to charge by absorbing active power and consequently, slightly reducing the

frequency. This behaviour is also clearly presented in the active power response shown in Figure 4.20.

Table 4.12. Result of the optimal droop coefficients for Case 1 and Case 2 in Scenario 2040.

PHPP name	ESS technology	Droop coefficient (K_P)	
		Case 1	*Case 2*
Fritzøe	BESS	---	0.0001
Mæl	CFSG	0.0001	0.0001
	BESS	---	0.0001
Fjone	CFSG	0.0126	0.0001
	BESS	---	0.0001
Svelgfoss	CFSG	0.0298	0.0001
	BESS	---	0.0001
Skollenborg	CFSG	0.0152	0.0001
	BESS	---	0.0001
Hjartdøla	DFIG	0.0975	0.0001
Såheim	DFIG	0.0001	0.0001
Mår	DFIG	0.0001	0.0001

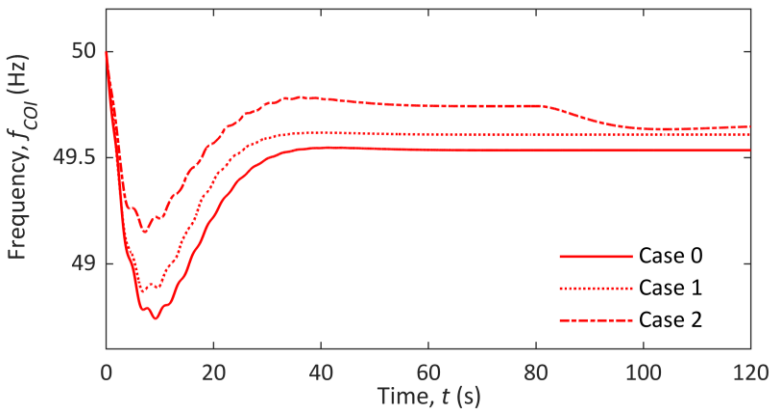

Figure 4.19. Frequency response of Case 0, Case 1 and Case 2 in Scenario 2040 after a power imbalance of 1300 MW.

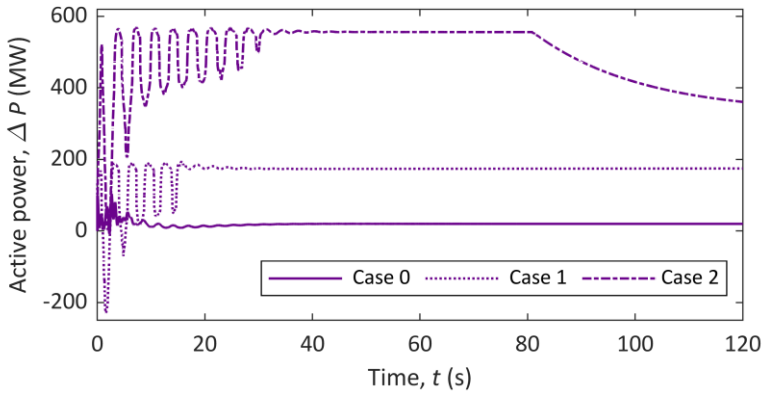

Figure 4.20. Active power contribution of VDS by assessing Case 0 (synchronous generators), Case 1 (synchronous generators+CFSG+DFIG) and Case 2 (synchronous generators+CFSG+DFIG+BESS) in Scenario 2040.

Table 4.13 shows a summary of the frequency response indicators obtained by assessing Case 0, Case 1 and Case 2. From the results, it can be observed that the frequency quality indicators of Case 1 and Case 2 are significatively enhanced concerning Case 0, which is a sensitive case since $f_{\mathrm{COI,min}}$ is inside the activation zone of the UFLS schemes. The integration of variable-speed and BESS technologies helps to reduce $\Delta f_{\mathrm{COI,\,max}}$ value by 10% in Case 1 and around 32% in Case 2, representing a significant contribution to the frequency recovery. Moreover, $f_{\mathrm{COI,min}}$ is above the activation zone of the UFLS schemes.

Table 4.13. Results of the frequency quality indicators considering the assessment of Case 0, Case 1 and Case 2 in Scenario 2040.

Case	Frequency quality indicators				
	$\Delta f_{\mathrm{COI,\,max}}$ (Hz)	$f_{\mathrm{COI,\,min}}$ (Hz)	$f_{\mathrm{COI,\,ss}}$ (Hz)	t_{min} (s)	$ROCOF_{\mathrm{COI,\,max}}$ (Hz/s)
0	1.258	48.742	49.536	9.182	−0.318
1	1.131	48.869	49.609	6.905	−0.282
2	0.850	49.150	49.660	7.223	−0.274

4.9 Conclusions

In this chapter, an evaluation of the impact of using variable-speed PHPPs and BESS technologies to provide fast frequency support to the NPS was carried out. The variable-speed PHPPs and BESS technologies were enabled with FFR control. It was developed a

dedicated methodology to compute the optimal parameters of FFR control. Two objective functions were formulated, one focusing on the minimisation of steady-state frequency and the other concentrating on minimising the minimum frequency. The assessment of the proposed methodology was carried out using two representative models of the NPS. First, the NPS was modelled as a single-area frequency response model. The frequency quality indicators were assessed considering the gradual decrease of the inertia; the simulation results demonstrate that the frequency response is for low inertia levels dangerously deteriorated and, as a consequence, its frequency quality parameters. Then, the combination of the proportional and derivative control of the FFR was implemented, and the proposed objective functions were evaluated. The primary outcome is demonstrating that FFR control can mitigate the low inertia levels and provides fast frequency support by injecting/absorbing the optimal amount of active power to enhance the frequency response. Afterwards, the Vestfold and Telemark distribution system model was used to assess the impact in the frequency response by the integration of variable-speed PHPPs and BESS technologies equipped with proportional FFR control. The use of the realistic dynamic model allowed considering scenarios of real expected changes on the NPS. The simulation results demonstrated that the integration of variable-speed PHPPs considering scenarios of minor inertia decrease is effective for frequency quality indicators enhancement. However, the integration of BESS significantly enhances the frequency quality indicators, especially in critical scenarios where the inertia is critically low. The fast frequency support provided by BESS effectively prevents the activation of emergency control schemes by keeping the minimum frequency above the operating zone of the UFLS schemes.

5 Optimal UFLS scheme for frequency control in low inertia scenarios

The under-frequency load shedding (UFLS) scheme has been used as the last resource to deal with severe UF disturbances to restore the frequency within operational requirements. The computation of the traditional UFLS scheme parameters is a vast problem due to the non-linear frequency response and the number of UF-relays installed across the power system. Therefore, the incorrect estimation of UF-relays parameters can cause further over/under frequency conditions or even a blackout. This chapter presents a novel methodology to calculate the UF-relays parameters of the optimal UFLS scheme. First, a description of the traditional UFLS scheme and the principal UF-relays parameters is presented. Then, the formulation of the proposed optimal UFLS scheme consisting of the control variables definition, formulation of the objective function to minimise the total load disconnected and the formulation of the frequency operational requirements as inequality constraints is presented. Afterwards, a dedicated co-simulation outline to solve the optimisation problem is developed. Lastly, the proposed optimal UFLS scheme is assessed using two test system models. One of them represents a real power system susceptible to low rotational inertia conditions. The foundation of this chapter is based on publications **[P2]**, **[P3]** and **[P5]**.

5.1 Introduction

The stochastic nature of the power demand creates continuous power deviations regarding the power generation leading to the power system constantly trying to reach a balance and maintain the frequency within operational levels. These imbalances are handled by adopting frequency control strategies such as PFC and, recently, FFR, as demonstrated in Chapter 4. In contrast, when a significant power imbalance occurs, for instance, the abrupt disconnection of one or more power generation units or the unscheduled connection of a large block of power demand, the synchronous generators will attempt to stop the frequency deviation by allowing the exchanges of its available kinetic energy. Moreover, the SPI based technologies will provide fast frequency support

restricted by its available energy. Nevertheless, suppose those actions do not provide enough energy to cope with the imbalance. In that case, the frequency deviation will continue increasing, and the power system will enter an emergency state at which emergency frequency control must act to stop the frequency deviation. The emergency frequency control has to take remedial action almost immediately after the frequency reaches a pre-established limit; therefore, the activation of SFC is not attained.

The classical emergency control used to arrest the frequency deviation is the traditional under-frequency load shedding (TUFLS) scheme [125]. It consists of a set of UF-relays installed throughout the power system. The main goal of the TUFLS scheme is to restore the power balance and arrest the frequency deviation by performing a controlled disconnection of load in one or multiple steps at fixed frequency thresholds [126].

The scientific literature presents a large number of approaches based on the TUFLS scheme, such as in [127]–[130]. However, variants of the TUFLS scheme have been proposed. The semi-adaptative strategies are based on the ROCOF; they activate the UF-relays when a frequency deviation exceeds a predefined threshold value, and the size of load to be disconnected is in proportion to the measured frequency deviation [131]. Meanwhile, the adaptative schemes involve three approaches: event-based, response-based and frequency-prediction-based. The event-based approach takes measurements of the tripped generator capacity using WAMS and calculates the load shedding size [132]. The response-based method uses the swing equation to calculate the amount of load to be disconnected [133]. Frequency-prediction-based approaches use the forecast minimum frequency or the distance to the frequency threshold to activated the UF-relays [134]. The semi-adaptative and adaptative offer advantages against the TUFLS scheme: However, they may inaccurately estimate the amount of load shedding due to noise and/or delay in measurements, wrong disturbance estimation, predictions errors.

Recently, the adaptation of computational intelligence techniques to solve the UFLS problem has played an important role. Several approaches have been proposed to compute the optimal UF-relays parameters using artificial intelligence methods in combination with WAMS [135], applications at the industrial level [136] or creating an

adaptative UFLS scheme by using an artificial neural network to estimate the power imbalance and then defining the optimal parameters of UF-relays [137]. Despite the popularity of metaheuristic algorithms nowadays, only a few have been adapted to address the UFLS problem. The trajectory sensitivity is used to minimise the total load shedding of the power system in [138], where also an emergency load shedding model-based is presented. In [139], the particle swarm optimisation algorithm is implemented to compute the optimal amount of load shedding in an islanded operation scenario. [140] uses the combination of the augmented ε-constraint method and the particle swarm optimisation algorithm to solve a multi-objective function and determine optimal load shedding. The imperialist competitive algorithm is used to optimise the UFLS scheme parameters of a WAMS-based model [141]. Further information regarding the various methodologies available in the literature to address the UFLS problem can be found in [142].

5.1.1 Contribution

1. The procedure of setting the UF-relays of the UFLS scheme is formulated as a constrained optimisation problem. The optimal UFLS problem is formulated in such a way that a set of parameters (load shedding size per step, frequency threshold and the time delay) is computed for each UF-relay installed in the power system to minimise the total amount of load shedding.
2. The optimal UFLS problem is defined as a constrained problem and solved by using the IHS algorithm.
3. A co-simulation outline using DIgSILENT® PowerFactoy™ and Python has developed to solve the optimal UFLS problem by implementing the IHS algorithm in Python to solve the optimisation problem and using DIgSILENT® PowerFactoy™ to execute the dynamic simulations and discrete events.
4. Modelling a real power system using realistic data and use the model to test the proposed methodology.

5.2 Traditional under-frequency load shedding scheme

TUFLS scheme consists of several UF-relays installed on specific loads across the power system. The UF-relays are devices intended to perform loads disconnection based on local frequency measurements in one or multiple steps. If the instantaneous frequency drop below a fixed threshold, the UF-relay triggers the load shedding, and it is done at the exact location where the frequency is measured [143]. In general, setting the TUFLS scheme mainly consists of defining the fixed parameters of UF-relays [144]. First, the possible power loss that may cause the worst power imbalance ($\Delta P_{\mathrm{imbalance}}$) is identified. Then, the total load to be disconnected (ΔP_{TLS}) by the UF-relays is estimated. This is done to ensure the power balance will restore and the frequency will recover within a permissible range. Finally, the UF-relays parameters are adjusted. The ΔP_{TLS} and parameters of UF-relays were usually determined based on the power system operator knowledge of the power system and experience [143]. However, this approach to define the UF-relays parameters is prone to errors since the number of parameters to adjust rises as the number of the UF-relays installed across the power system increase.

In general, four parameters can describe an UF-relay. The number of steps (n_{s}) at which the UF-relay will perform the load disconnection, the size of load shedding (ΔP_{LS}) that will be completed at each step, the frequency threshold (f_{t}) at which the load shedding must be activated, and the time delay (t_{d}) is the time the UF-relay must wait before triggers the load shedding [145]. Commonly, the electricity companies establish the minimum and the maximum number of steps at which the load shedding should be done and the frequency range at which the TUFLS scheme must act. However, these vary depending on the electricity companies and countries [146][147].

Considering a power system with n_{R} UF-relay of n_{S} steps, the parameters of the k-th UF-relay are depicted in Figure 5.1. Moreover, the parameters of the k-th UF-relay can be written in a vector form as

$$\begin{aligned}\mathbf{\Delta P}_{\mathrm{LS},k} &= \begin{bmatrix} \Delta P_{\mathrm{LS},k,1} & \Delta P_{\mathrm{LS},k,2} & \cdots & \Delta P_{\mathrm{LS},k,i} & \cdots & \Delta P_{\mathrm{LS},k,n_{\mathrm{S}}} \end{bmatrix} \\ \mathbf{F}_{\mathrm{t},k} &= \begin{bmatrix} f_{\mathrm{t},k,1} & f_{\mathrm{t},k,2} & \cdots & f_{\mathrm{t},k,i} & \cdots & f_{\mathrm{t},k,n_{\mathrm{S}}} \end{bmatrix} \\ \mathbf{T}_{\mathrm{d},k} &= \begin{bmatrix} t_{\mathrm{d},k,1} & t_{\mathrm{d},k,2} & \cdots & t_{\mathrm{d},k,i} & \cdots & t_{\mathrm{d},k,n_{\mathrm{S}}} \end{bmatrix}\end{aligned} \tag{5.1}$$

where the subscript i represent the i-th load shedding step in the k-th UF-relay.

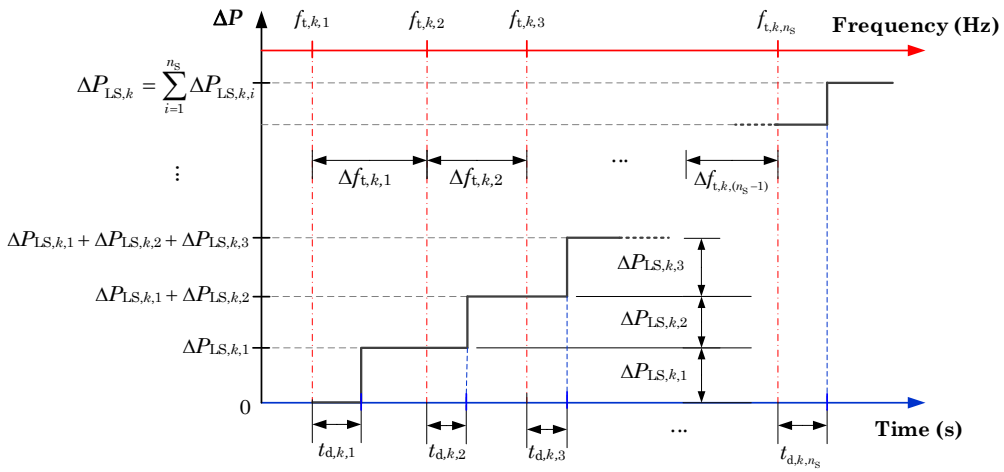

Figure 5.1. Schematic representation of the four parameters of the k-th UF-relay in a power-frequency-time characteristic.

The proper operation of the UFLS scheme highly depends on the accurate estimation of ΔP_{TLS} and the appropriate settings of the UF-relay parameters. Consequently, if the UF-relay parameters are incorrectly set, an over-frequency condition can occur due to the activation of load shedding at an early stage and/or the excess of load shedding, i.e., $\Delta P_{\mathrm{TLS}} > \Delta P_{\mathrm{imbalance}}$. In contrast, an underestimation of load shedding ($\Delta P_{\mathrm{TLS}} \ll \Delta P_{\mathrm{imbalance}}$) leads to setting the ΔP_{LS} with small values that will not be capable of recovering the power balance. Therefore the frequency declining will not be stopped leading to undesirable conditions such as synchronous generators outages or power system blackout [148].

The frequency quality indicators must be deemed when setting the UF-relays. The most important indicator is the maximum instantaneous frequency deviation, Δf_{max}. It must be limited to prevent the instantaneous minimum frequency, f_{min}, drops too low for an extended time to protect the turbine-generator components from UF conditions and further disconnection by activating the UF protection of the synchronous generators.

Furthermore, the frequency threshold at the first step ($f_{t,1}$) must be adjusted outside the maximum steady-state frequency range, $\Delta f_{SS,max}$, to avert the UF-relays activation when frequency varies in non-emergency situations. Moreover, to ensure steady-state frequency, f_{SS}, will be settled inside the $\Delta f_{SS,max}$, it must be considered that, in addition to the UF-relays operation, the TSOs may take other control actions to recover the frequency.

5.2.1 TUFLS scheme in different power systems

5.2.1.1 Mongolian power system

The unbundled MPS consist of five local power systems (LPS): Central (CLPS), Western (WLPS), Altai-Uliastai (ALPS), Eastern (ELPS) and Southern (SLPS). The power demand is supplied by 20 power plants, of which nine are coal-fired, three wind, five solar and three hydro and 85% of the total power generation comes from coal-fired power plants and the residual 15% is provided by RESs. The five LPS are interconnected through overhead transmission lines of 110 kV and 220 kV [149]. Moreover, the CLPS interconnects the MPS with the Russian power system through a double-circuit transmission line of 220 kV. The representation of the five LPS of the MPS is depicted in Figure 5.2.

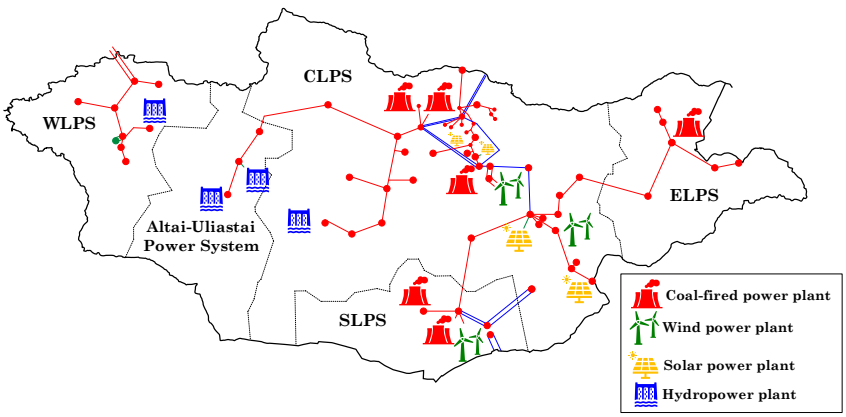

Figure 5.2. Graphic representation of the five local power systems of the Mongolian power system, including the power generation resources and the interconnection.

The power demand of the MPS is strongly influenced by the weather of the country. The winter season is characterised by temperatures below −35 °C, and the use of central heating systems produce a large power consumption. It requires the large power plants to be in service, and therefore, the MPS has high rotational inertia levels. In contrast, the power consumption reaches its minimum values in the summer season due to the central heating systems not being utilised. Moreover, maintenance of large power plants is scheduled for this season, and the rotational inertia levels of the MPS significantly reduces. Therefore, the TSOs of the MPS considers two operational scenarios: winter operational scenario and summer operational scenario. The winter operational scenario starts in the second half of September and ends in the first half of May. Meanwhile, the summer operational scenario begins the second half of May and finishes the first half of September [149].

The TUFLS scheme of the MPS is designed to prevent frequency drops below 47 Hz and avoid the activation of UF-protections of the synchronous generators, which are setting at 46 Hz. Moreover, the synchronous generators continuous operating must kept in a range from 49.8 Hz to 50.2 Hz; thus, $\Delta f_{\mathrm{SS,max}}$ = ±0.2 Hz. Usually, the maximum load disconnection is 55% of the total power demand (P_d), i.e., $\Delta P_{\mathrm{TLS}} = 0.5 P_d$, in a maximum of nine steps. The frequency thresholds (f_{t}) must be in the range of 49.4 Hz to 47.2 Hz, and the time delay (t_{d}) is adjusted between 6 and 18 cycles [149].

5.2.1.1.1 Altai-Uliastai local power system

ALPS is interconnected to the rest of the MPS via the Murun-Telmen transmission line of 110 kV, which connects the ALPS and CLPS. It consists of six HPPs, of which the larges HPP is Taishir, with a power capacity of 11 MW. However, the total power generation depends on the water levels and supply an average power between 3.5 and 4.1 MW. ALPS provides energy to 31 regions and two towns. Figure 5.3 shows an illustrative representation of ALPS, including the location of the HPPs.

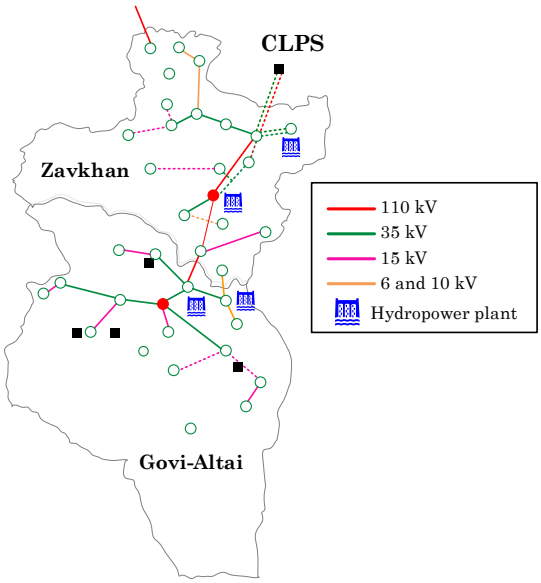

Figure 5.3.Illustrative representation of Altai-Uliastai local power system.

The total power generation of ALPS covers between 49% to 55% of its total power demand in the summer season. Meanwhile, in the winter season, small size HPPs are out of services due to the low temperatures causing rivers to freeze and, therefore, total power generation is decreased. The remaining power demand for both seasons is covered by importing energy from CLPS through the Murun-Telmen transmission line. Therefore, the power balance of ALPS is critically dependent on the power importation from CLPS. Table 5.1 present the power balance of the ALPS in the summer and winter seasons [149].

Table 5.1. Summary of power balance of ALPS during summer and winter season.

Season	Power demand, P_d (MW)	Power generation, P_G (MW)	Power import, P_{tie} (MW)	Demand/inertia level
Summer	6.25	4.60	2.4	Low/High
Winter	11.99	3.00	10.0	High/Low

Murun-Telmen transmission line is extremely vulnerable to outages due to its very long length and the weather conditions. Consequently, when the Murun-Telmen transmission line is tripped, ALPS is isolated, and a critical power loss is experienced, especially in the winter season. Therefore, the existing TUFLS scheme of ALPS acts to ensure the safe operation of the isolated power system. However, it disconnects unnecessary load affecting the local population, especially in the winters season. Table

5.2 presents the settings of the TUFLS scheme currently used in the ALPS for both the summer and winter season, where lines Guulin, and Bigger garaa are out of service in the winter season.

Table 5.2. Parameters of the UF-relays of the current TUFLS scheme in ALPS.

UF-relay location		ΔP_{LS} **(%)**	f_{t} **(Hz)**	t_{d} **(s)**
Element	***Name***			
Load	Baynshand	28	48.0	0.15
Load	Baynhairhan	55	47.8	0.15
Load	Jargalant	50	47.8	0.15
Load	Uildwer	87	47.8	0.15
Load	Harzat	55	47.8	0.15
Line	Uliastai	Open	48.8	0.10
Line	Guulin	Open	48.0	0.15
Line	Biger garaa	Open	48.0	0.10

5.2.1.2 North American power system

The North American power system (NAPS) consist of four interconnected regional power systems: Easter interconnection, Western interconnection, Texas interconnection and Quebec interconnection. The four interconnections operate at a synchronised frequency of 60 Hz [150]. NAPS has an installed capacity of 1200 GW, of which around 72% is thermal power plants (natural gas and coal-fired), 22 % is wind, solar and hydropower plants, and the remaining 6% belongs to other types of power generation [151]. The North American Electric Reliability Council (NERC) is the corporation that regulates the reliability and security of the NAPS and comprises six regional organisations. NERC establish the design and requirements of the automatic UFLS scheme in the Reliability Standard PRC-006-2, which variate depending on the different regional organisations [152]. In this thesis, the UFLS scheme of the South-eastern Electric Reliability Council (SERC) is considered [153].

The SERC UFLS Standard (PRC-006-SERC-02) provide the guidelines and requirements to implement the UFLS scheme [154]:

1. The frequency threshold at the first step ($f_{\mathrm{t},1}$) shall be not greater than 59.5 Hz and not be smaller than 59.3 Hz, i.e., 59.3 Hz ≤ $f_{\mathrm{t},1}$ ≤ 59.5 Hz.
2. The frequency threshold at the last step ($f_{\mathrm{t},n\mathrm{S}}$) shall not be smaller than 58.4 Hz.
3. The frequency difference between two subsequent f_{t} (Δf_{t}) shall be smaller or equal to 0.5 Hz and greater or equal to 0.2 Hz, i.e., 0.2 Hz ≤ Δf_{t} ≤ 0.5 Hz.
4. The time delay shall be greater or equal to six cycles or 0.1 seconds.
5. After the UF-relays action, f_{SS} shall be settled within $\Delta f_{\mathrm{SS,max}}$ = ±0.5 Hz.

5.3 Proposed optimal UFLS scheme formulation

The optimisation-based approaches presented in the literature to address the problem of computing the UF-relays parameters of the UFLS scheme try to simplify the complexity of the problem by presuming the set of parameters of all UF-relays are the same or only including $\Delta P\mathrm{LS}$ as a control variable. However, those assumptions may produce a sub-estimation of the optimal settings since the space of the solution is limited only to the parameters included in the optimisation. Therefore, including all parameters of the UF-relays at the moment to formulate the optimisation problem is the significant importance to determinate the optimal solution.

The proposed formulation first defines the set of control variables based on UF-relays parameters which directly impact the frequency response. Then, the objective function is written to minimise the total amount of load disconnection and simultaneously arrest the frequency decline. Lastly, the frequency requirements are included in the optimisation as inequality constraints.

5.3.1 Control variables

The activation of the UF-relays after a disturbance occurs will immediately impact the frequency quality metrics. The total amount of load shedding principally impacts the point at which the frequency will be recovered. Moreover, in addition to the amount of load shedding, the frequency threshold and time delay influence the maximum

frequency deviation. Therefore, in addition to the four parameters of the UF-relays (n_{S}, ΔP_{LS}, f_{t} and t_{d}), Δf_{t} and the location of the UF-relays can be used as control variables.

The proposed optimal UFLS scheme approach considers the parameters of each UF-relays defined in (5.1) and Δf_{t}. The control variables vector of the k-th UF-relay is expressed as

$$\mathbf{x}'_k = \begin{bmatrix} \mathbf{\Delta P}_{\mathrm{LS},k} & f_{\mathrm{t},k,1} & \mathbf{\Delta F}_{\mathrm{t},k} & \mathbf{T}_{\mathrm{d},k} \end{bmatrix} \tag{5.2}$$

where $f_{\mathrm{t},k,1}$ is the frequency threshold at the first step, $\Delta\mathbf{P}_{\mathrm{LS},k}$ and $\mathbf{T}_{\mathrm{d},k}$ are defined in (5.1) and the vector $\Delta\mathbf{F}_{\mathrm{t},k}$ is defined as

$$\mathbf{\Delta F}_{\mathrm{t},k} = \begin{bmatrix} \Delta f_{t,k,1} & \Delta f_{t,k,2} & \cdots & \Delta f_{t,k,(n_{\mathrm{S}}-1)} \end{bmatrix} \tag{5.3}$$

where n_{S} is the number of load shedding steps. Due to in the vector of decision variables is only considered the frequency threshold at the first step ($f_{\mathrm{t},k,1}$), the remainder frequency thresholds of the k-th UF-relay are calculated as follows

$$f_{\mathrm{t},k,(i+1)} = f_{\mathrm{t},k,i} + \Delta f_{t,k,i} \quad \forall\ i = 1,2,...,(n_{\mathrm{S}}-1) \tag{5.4}$$

The control variables are bounded contemplating the frequency requirements of the electricity companies as follows:

$$\begin{aligned} \mathbf{\Delta P}_{\mathrm{LS}}^{\mathrm{L}} < \mathbf{\Delta P}_{\mathrm{LS},k} < \mathbf{\Delta P}_{\mathrm{LS}}^{\mathrm{U}} \\ f_{\mathrm{t1},k}^{\mathrm{L}} < f_{\mathrm{t1},k} < f_{\mathrm{t1},k}^{\mathrm{U}} \\ \mathbf{\Delta F}_{\mathrm{t},k}^{\mathrm{L}} < \mathbf{\Delta F}_{\mathrm{t},k} < \mathbf{\Delta F}_{\mathrm{t},k}^{\mathrm{U}} \\ \mathbf{T}_{\mathrm{d},k}^{\mathrm{L}} < \mathbf{T}_{\mathrm{d},k} < \mathbf{T}_{\mathrm{d},k}^{\mathrm{U}} \end{aligned} \tag{5.5}$$

where the superscripts L and U indicate the lower and upper bound of the size of load shedding ($\Delta\mathbf{P}_{\mathrm{LS},k}$), the frequency threshold ($f_{\mathrm{t},1,k}$) at the first step, the frequency interval between two subsequent frequency thresholds ($\Delta\mathbf{F}_{\mathrm{t},k}$) and time delay ($\mathbf{T}_{\mathrm{d},k}$), respectively.

The control variables vector considering n_{R} UF-relays is written as

$$\mathbf{X} = \begin{bmatrix} \mathbf{x}'_1 & \mathbf{x}'_2 & \cdots & \mathbf{x}'_k & \cdots & \mathbf{x}'_{n_R} \end{bmatrix} \tag{5.6}$$

5.3.2 Objective function

The purpose of solving the optimal UFLS scheme is to determine the minimum amount of load shedding required to restore the frequency inside the maximum steady-state frequency range ($\Delta f_{SS,max}$) and avoid over or under-frequency conditions. The objective function is written as the sum of all activated load shedding (given in percentage) in each UF-relay multiplied by the power of its respective load.

$$\min_{\mathbf{X}} \left[f(\mathbf{X}) \right] = \min_{\mathbf{X}} \left[\Delta P_{TLS}(\mathbf{X}) \right] = \sum_{k=1}^{n_R} \sum_{i=1}^{n_{S*}} \Delta P_{LS,k,i} P_{load,k} \tag{5.7}$$

where $P_{load,k}$ is the total power of the load equipped with the k-th UF-relay, $\Delta P_{LS,k,i}$ is the size of load shedding in percentage at the i-th activated step of the k-th UF-relay and n_{S*} is the number of activated steps during the frequency disturbance (note that $n_{S*} \leq n_{S)}$.

5.3.3 Frequency constraints

The main goal of computing the optimal parameters of the UF-relays is to minimise $\Delta P_{TLS}(\mathbf{X})$. However, the frequency response and, therefore, the frequency quality indicators must comply with the frequency requirement of the electric companies. The most significant frequency requirements are the minimum frequency (f_{min}) and the steady-state frequency (f_{SS}) and are included in the optimisation as inequality constraints.

5.3.3.1 Constraint 1: minimum frequency

The frequency deviation must be arrested immediately after a disturbance has occurred to protect the turbine-generator module and avoid the UF-protection of the synchronous generator activation. Consequently, the optimal UFLS scheme must be coordinated with the UF-protection of synchronous generators. The coordination is

created by ensuring that $f_{\min}$ does not reach the activation zone of the UF-protection of synchronous generators during the UFLS scheme performing.

Since it is intended to ensure $f_{\min}$ does not reach the activation zone of the UF-protection of synchronous generators, the overall frequency of the power system is represented by f_{COI}. $f_{\min}$ constraint is mathematically written as

$$g_1(\mathbf{X}) = f_{\text{limit}} - f_{COI,\min} \leq 0 \tag{5.8}$$

where f_{limit} is the minimum frequency limit before the activation zone of UF-protection of the synchronous generators.

5.3.3.2 Constraint 2: Steady-state frequency

The turbine-generator units have to be protected from continued operation in abnormal frequency conditions to prevent turbine blades' stress and increase their lifetime [33,34]. Therefore, turbine-generator units require f_{SS} to be inside the maximum steady-state frequency range, $\Delta f_{\mathrm{SS,max}}$, i.e., $f_0 - \Delta f_{\mathrm{SS,max}} \leq f_{\mathrm{SS}} \leq f_0 + \Delta f_{\mathrm{SS,max}}$. The steady-state frequency restriction is included in the optimisation problem as two inequality constraints as:

$$\begin{aligned} g_2(\mathbf{X}) &= f_{\mathrm{COI,SS}} - \left(f_0 + \Delta f_{\mathrm{SS,max}}\right) \leq 0 \\ g_3(\mathbf{X}) &= \left(f_0 - \Delta f_{\mathrm{SS,max}}\right) - f_{\mathrm{COI,SS}} \leq 0 \end{aligned} \tag{5.9}$$

The inequality constraints vector $\mathbf{G}(\mathbf{X})$ containing the minimum frequency and steady-state frequency constraints defined in (5.8) and (5.9) is written as follows:

$$\mathbf{G}(\mathbf{X}) = \begin{bmatrix} g_1(\mathbf{X}) & g_2(\mathbf{X}) & g_3(\mathbf{X}) \end{bmatrix} \leq 0 \tag{5.10}$$

5.4 Methodology to implement the optimal UFLS scheme

The proposed approach to compute the optimal UF-relays parameters and minimise the total load shedding requires an algorithm dedicated to solving the numerical optimisation problem and a simulation environment to model the power system

dynamics and obtain the RMS values of the electrical variables. Therefore, a co-simulation outline has been developed to solve the optimal UFLS scheme problem.

The co-simulation outline involves the Python programming language containing a scientific library (PyGMO) designed to provide a massive parallel optimisation interface [157] and DIgSILENT® PowerFactory™ to perform dynamic simulations and obtain RMS values of frequency and power. Furthermore, including discrete events such as inserting a disturbance and the activation of the UF-relays.

The optimal UFLS scheme problem described in Section 5.3 is solved by the IHS metaheuristic algorithm implemented in Python. Furthermore, Python serves as an interface between the optimisation algorithm and the power system model in DIgSILENT® PowerFactory™. Therefore, the procedure to solve the optimal UFLS scheme is done in an automatised in a close-loop, as shown in Figure 5.4. First, the boundaries of the control variables described in (5.5) and the IHS parameters are defined. Then, the IHS algorithm is initialised with a random set of control variables which are set as UF-relays parameters in the dynamic model inside DIgSILENT® PowerFactory™. Afterwards, DIgSILENT® PowerFactory™ performs a time-domain simulation considering the insertion of a disturbance and the subsequent action of the UFLS scheme if it is activated. The resulting frequency response and UF-relays activation signals are interpreted by Python and used by the IHS algorithm to evaluate the objective function and frequency constraints. Lastly, the optimisation algorithm creates a new set of control variables, and the procedure is repeated until the stopping criterion of the IHS algorithm is fulfilled.

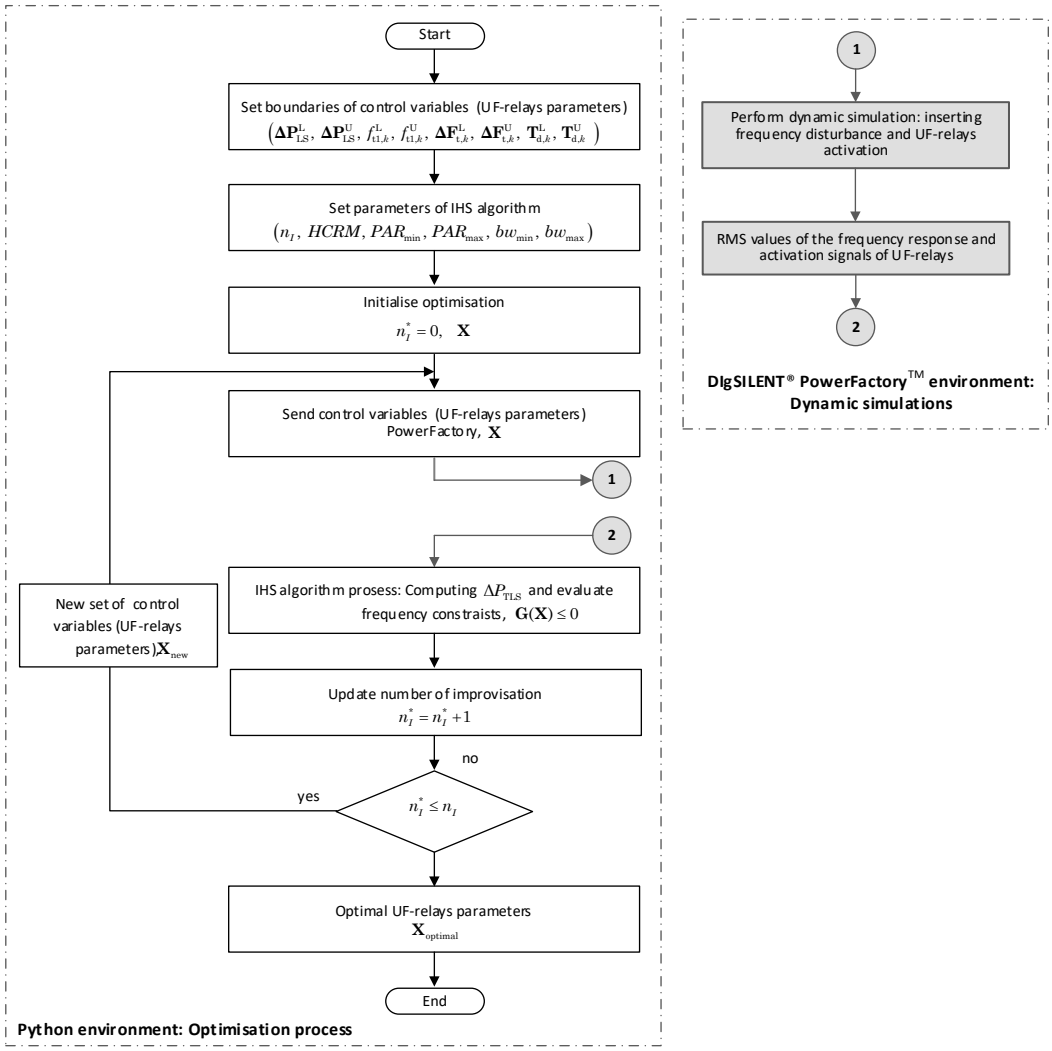

Figure 5.4. Flowchart of the co-simulation outline developed to solve the optimal UFLS scheme.

5.5 Demonstrative examples and results

The proposed optimal UFLS scheme is evaluated using two test systems: the 10-machine New England power system and Altai-Uliastai local power system belonging to the MPS. The 10-machine-New England power system is used to illustrate the performance of the proposed methodology described in Section 5.3 and the positive improvements on the frequency quality indicators. It considers the UFLS scheme requirements of the South-eastern Electric Reliability Council of the North American power system. Furthermore, the Altai-Uliastai local power system is implemented to demonstrate the outstanding performance of the proposed optimal UFLS scheme in a real power system susceptible to frequency disturbances and low rotational inertia scenarios.

5.5.1 10-machine New England power system

The 10-machine New England power system, also known as IEEE 39 bus system, is a well-known test system representative of a portion of the NAPS. It operates at 345 kV, 60 Hz and consists of ten synchronous generators. The synchronous generator G1 represents the aggregation of a large number of synchronous generators [158]. Furthermore, the 10-machine New England power system has 39 busbars, 12 power transformers, 34 transmission lines and 19 loads. The total power demand is 6097.10 MW, and the total power generation is 6,140.81 MW [159].

The 10-machine New England power system has been implemented in DIgSILENT® PowerFactory™ version 2020 and equipped with UF-relays in the 19 loads. The single line diagram of the 10-machine New England power system is depicted in Figure 5.5.

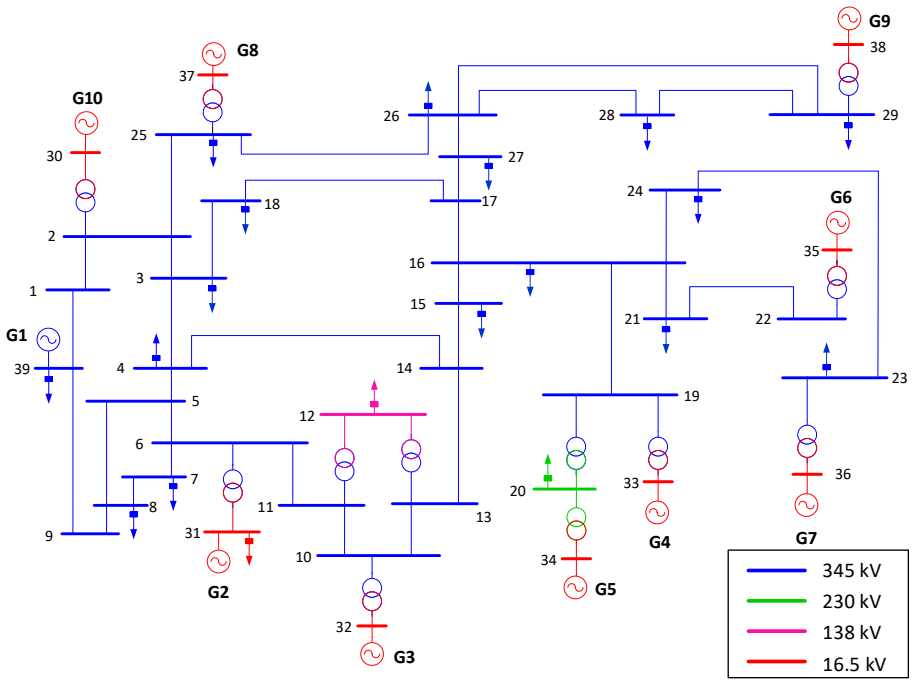

Figure 5.5. Single-line diagram of the 10-machine New England power system equipped with UF-relays.

5.5.1.1 Simulation and results

The worst power imbalance is considered to be the abrupt disconnection of the synchronous generators G1 and G9 at t = 1.0 s. Therefore, the total power imbalance is the power loss of G1 and G9, i.e., $\Delta P_{\text{imbalance}} = P_{\text{G1}}+P_{\text{G9}}$ = 1,830 MW, representing 29.8% of the total power generation. The frequency quality indicators ($f_{\min}$, $t_{\min}$,

$ROCOF_{\max}$ and f_{SS}) are assessed contemplating three simulation scenarios described in Table 5.3.

Table 5.3. Description of the three simulation scenarios defined to evaluate the frequency quality indicators.

Scenario	Description	Purpose
1	The 10-machine New England power system is not considering any emergency control. Therefore, it does not have implemented a UFLS scheme.	Observe the frequency response of the 10-machine New England power system after a frequency disturbance occurs.
2	The TUFLS scheme is implemented in the 10-machine New England power system.	Analyse the frequency response and its quality indicators when the UF-relays are setting with fixed parameters.
3	The proposed optimal UFLS scheme is implemented in the 10-machine New England power system.	Analyse the impact of the optimal UF-relays parameters on the frequency response and its quality indicators.

5.5.1.1.1 Scenario 1: Not UFLS scheme

Scenario considers the 10-machine New England power system does not have UF-relays installed. Therefore, after the frequency disturbance occurs, only the PFC acts to restore the power imbalance caused by the sudden disconnection of G1 and G2. The frequency response measured in all buses of the power system is depicted in Figure 5.6a. It can be observed that the PFC action is not enough to restore the power balance. Therefore, the frequency decline is not counteracted. It activates the UF protection of the synchronous generators, set to operate when the frequency is inside the range 58.4 Hz to 57.9 Hz or below, and it does not re-establish within 30 seconds [160]. The activation of UF protection of the synchronous generators leads to further UF conditions causing the instability of the power system.

Furthermore, Figure 5.6b depicts the ROCOF measured in all buses after the power imbalance. The maximum ROCOF, which was produced in bus 29, is $ROCOF_{\max}$ = 32.88 Hz/s at 1.012s. The significant value of $ROCOF_{\max}$ is produced due to the considerable power generation loss and the response of the remaining synchronous generators to the power imbalance.

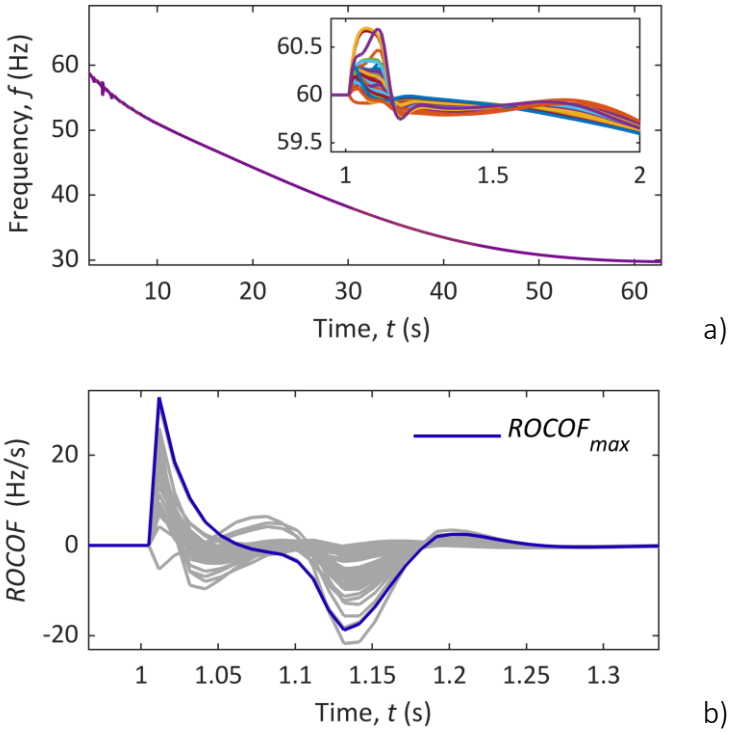

Figure 5.6. a) Frequency and b) ROCOF measured in the 39 buses after the outage of G1 and G9 when no UFLS scheme is implemented.

The frequency response evidence is required an emergency control scheme to cope with the power imbalance and the inability of the PFC to restore the frequency. Moreover, it is necessary to ensure the frequency quality indicators will fulfil the operational requirements.

5.5.1.1.2 Scenario 2: TUFLS scheme

Scenario 2 considers the implementation of the TUFLS scheme in the 10-machine New England power system. The UF-relays of the TUFLS scheme are setting following the standard PRC-006-SERC-02 for UFLS scheme implementation described in Section 5.2.1.2. As a result, the UF-relays are deemed to have four load shedding steps, i.e., n_{S} = 4, and ΔP_{LS}, f_{t}, Δf_{t} and t_{d} of each step are defined in Table 5.4.

Table 5.4. Fixed settings of UF-relays in the TUFLS scheme.

Step	ΔP_{LS} (%)	f_{t} (Hz)	Δf_{t} (Hz)	t_{d} (s)
1	15	59.3	0.3	0.2
2	10	59.0	0.3	0.2
3	10	58.7	0.3	0.2
4	5	58.4	0.3	0.2

The TUFLS scheme consists of 19 UF-relays installed at each load, and it is assumed to have the same fixed set of parameters defined in Table 5.4. The frequency disturbance is assumed the same as Scenario 1, i.e., sudden outage of G1 and G2.

The frequency response of the 10-machine New England power system after the performance of the TUFLS scheme is depicted in Figure 5.7. The activation of the UF-relays arrests the frequency drop, f_{min} take a value of 58.09 Hz, which is barely above f_{limit}, and avoids the operation of the UF-protection of the synchronous generators. The activation of the four load shedding steps defined in Table 5.4 produces a total load disconnection of ΔP_{TLS} = 2,438.84 MW, and the f_{SS} is settled at 60.36 Hz being inside the permissible variation range, $\Delta f_{\mathrm{SS,max}}$.

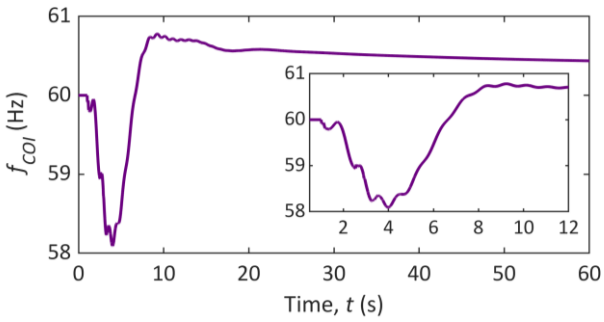

Figure 5.7. Frequency response for a power imbalance.

Implementing the TUFLS scheme has proven the importance of emergency controls to counteract the power system's large power imbalances and ensure its safety and continuous operation. Even though the TUFLS scheme significantly enhances the frequency response, f_{min} is dangerously close to f_{limit} and is susceptible to activate the UF-protections of the synchronous generators, which is not desirable. Furthermore, f_{SS} is near the maximum steady-state limit, and it may cause over-frequency conditions if manual UF control actions are taken.

5.5.1.1.3 Scenario 3: optimal UFLS scheme

Scenario 3 implements the optimal UFLS scheme proposed in Section 5.3, assuming 19 UF-relays installed in the 10-machine New England power system. The power imbalance is the same as Scenario 1 and Scenario 2.

The computation of the optimal UF-relays parameters is intended to minimise the total amount of load shedding and restore the frequency within $\Delta f_{\mathrm{SS,max}}$ range, which is ±0.5 Hz in the NAPS. Thus, the optimal UFLS problem is solved using ΔP_{LS}, f_{t} and inherently n_{S} as control variables. The time delay is assumed to be a fixed parameter set as t_{d} = 0.20s. Furthermore, the control variables are bounded based on the standard PRC-006-SERC-02 (Section 5.2.1.2): $\mathbf{\Delta P}_{\mathrm{LS}}^{\mathrm{L}} = 0 \cdot \mathbf{1}$ and $\mathbf{\Delta P}_{\mathrm{LS}}^{\mathrm{L}} = 100 \cdot \mathbf{1}$ in percentage, $f_{\mathrm{t1},k}^{\mathrm{L}} = 59.3$ Hz, $f_{\mathrm{t1},k}^{\mathrm{U}} = 59.5$ Hz, $\mathbf{\Delta F}_{\mathrm{t},k}^{\mathrm{L}} = 0.2 \cdot \mathbf{1}$ and $\mathbf{\Delta F}_{\mathrm{t},k}^{\mathrm{U}} = 0.5 \cdot \mathbf{1}$ in Hz, where **1** is a pure diagonal vector. The frequency constraints defined in (5.8)-(5.9) are evaluated considering f_{limit} = 58 Hz and $\Delta f_{\mathrm{SS,max}}$ = ±0.5 Hz. Lastly, the parameters of the IHS algorithm are established as HMS=3, $HMCR$=0.85, PAR_{min}=0.35, PAR_{max}=0.99, bw_{min}= 1×10^{-5} and bw_{max}= 1 and n_I=3000 [161].

The optimisation process is illustrated by the plot of the objective function evaluated at each improvisation, also known as the convergence curve, as shown in Figure 5.8. The IHS algorithm finds the optimal at improvisation 2,351, at which the total load disconnection is $\Delta P_{\mathrm{TLS}} =$ 1,768.79 MW, and the frequency constraints are fulfilled.

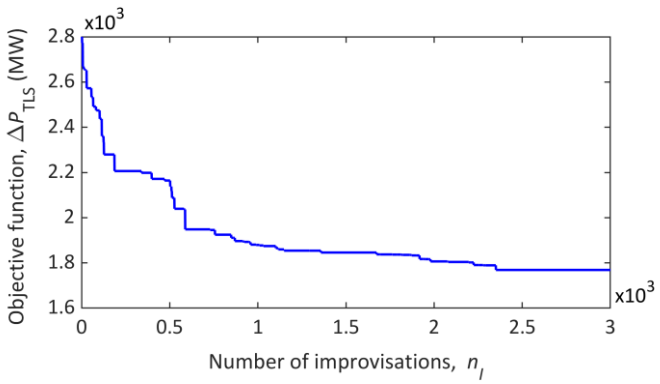

Figure 5.8. Optimisation process illustrated by the convergence curve of the objective function.

The optimal UF-relays parameters obtained from the solution of the optimal UFLS scheme are described in Table 5.5. The optimal number of load shedding steps is two for all UF-relays except UF-relays installed at Load 24 and Load 29, which uses one and three load shedding steps. The frequency measured at busbar 24 reaches values below 58.99 Hz. Therefore, it is required that the UF-relay activate three stages of load shedding to disconnect 100% of Load 24 and stop the frequency decline.

Table 5.5. Optimal UF-relays parameters for the 10-machine New England power system.

UF-relay location	ΔP_{LS} (%)			f_{t} (Hz)		
	Step 1	***Step 2***	***Step 3***	***Step 1***	***Step 2***	***Step 3***
Load 03	22.02	3.35	––	59.40	58.93	––
Load 04	0.19	11.78	––	59.43	59.10	––
Load 07	4.68	4.75	––	59.31	58.91	––
Load 08	6.40	0.09	––	59.44	59.06	––
Load 12	13.23	2.27	––	59.31	58.89	––
Load 15	19.69	11.25	––	59.44	59.00	––
Load 16	53.51	11.25	––	59.38	59.01	––
Load 18	48.85	5.38	––	59.45	59.01	––
Load 20	32.56	0.05	––	59.34	59.02	––
Load 21	16.02	19.09	––	59.49	59.13	––
Load 23	18.81	1.69	––	59.41	59.15	––
Load 24	48.72	46.60	4.68	59.42	59.20	58.99
Load 25	44.51	48.25	––	59.47	59.06	––
Load 26	36.82	48.59	––	59.45	59.07	––
Load 27	15.94	2.38	––	59.39	58.90	––
Load 28	26.05	3.20	––	59.46	59.01	––
Load 29	17.21	––	––	59.37	––	––
Load 31	36.81	18.87	––	59.35	59.00	––
Load 39	0.01	0.29	––	59.45	59.04	––

The optimal UF-relays parameters described in Table 5.5 are set in the UF-relays installed in the 10-machine New England power system model and are evaluated by

inserting the frequency disturbance used in Scenario 1 and Scenario 2 (outage of generators G1 and G9). The frequency response after the action of the optimal UFLS scheme is compared with the frequency response obtained by implementing the TUFLS scheme and is shown in Figure 5.9.

The action of the UF-relays in the optimal UFLS scheme improves the frequency response concerning Scenario 2. The maximum frequency deviation is reduced, moving the instantaneous minimum frequency away from the operation zone of UF-protections of synchronous generators. The UF-relays only requires the activation of two steps, except UF-relays installed at Load 24 and Load 29 (see Table 5.5) to restore the frequency. Furthermore, the total amount of load shedding is ΔP_{TLS} = 1,768.79 MW, decreasing about 27.5% concerning Scenario 2. It prevents an unnecessary load disconnection of 670.05 MW.

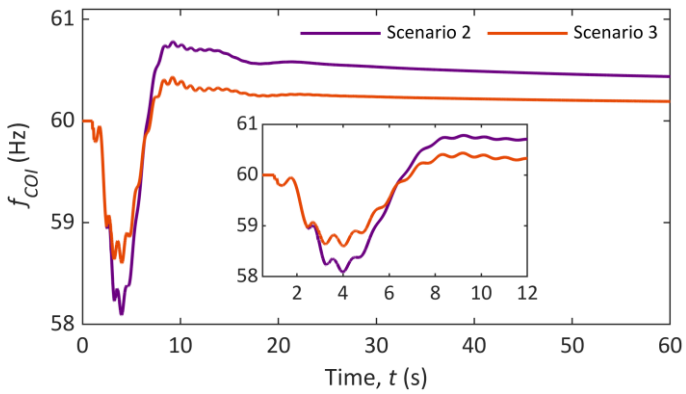

Figure 5.9. Frequency response of the traditional and the optimal UFLS scheme considering the power imbalance produced by the outage of generators G1 and G9.

Table 5.6 presents the frequency quality indicators of the three assessed scenarios. Also, the table highlights the positive impact on the frequency response by computing the optimal parameters of the UF-relays. It arrests the frequency drop and avoids frequency instability in contrast to Scenario 2. Furthermore, it ensures the steady-state frequency is inside $\Delta f_{\mathrm{SS,max}}$ range.

Table 5.6. Frequency quality indicators and total load shedding for Scenario 1, Scenario 2 and Scenario 3.

Scenario	$f_{\min}$ (Hz)	$t_{\min}$ (s)	$ROCOF_{\max}$ (Hz/s)	f_{SS} (Hz)	ΔP_{TLS} (MW)
1	values below 58.4 Hz at 3.062s		-32.88	Frequency instability	---
2	58.09	3.99	-32.88	60.36	2438.84
3	58.60	4.02	-32.88	60.16	1768.79

5.5.2 Altai-Uliastai local power system of the MPS

The real Altai-Uliastai local power system described in Section 0 is modelled and implemented in DIgSILENT® PowerFactory™ version 2021 using real available data to illustrate the performance of the optimal UFLS scheme in a realistic network. The ALPS consist of 13 synchronous generators, six three-winding power transformers, 25 two-winding power transformers, 39 lines and 46 loads. It operates at different voltage levels, and its nominal frequency is 50 Hz. The single-line diagram of the AL representing the different voltages levels and the main interconnection with the rest of the MPS is shown in Figure 5.10.

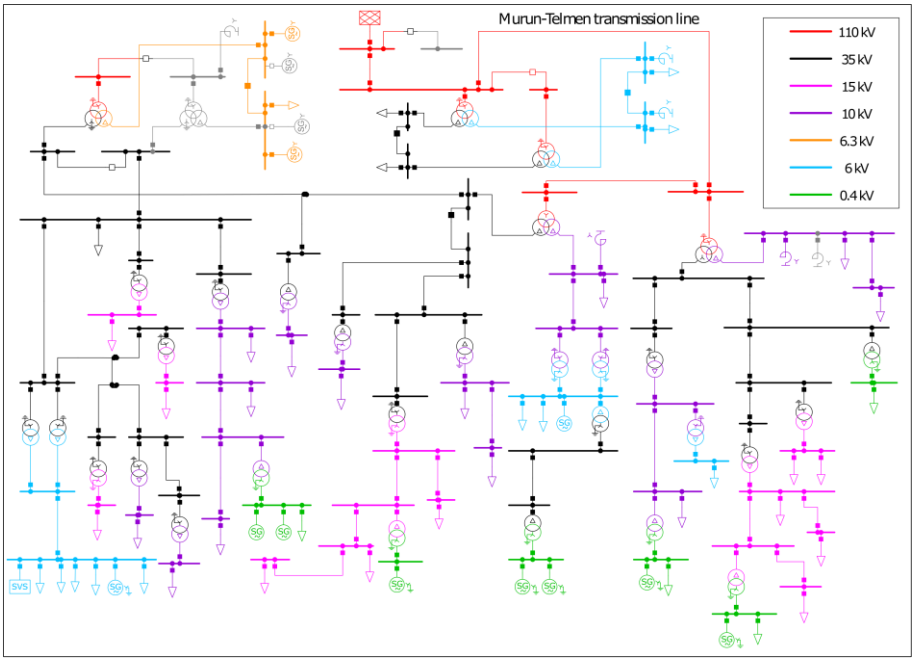

Figure 5.10. Single-line diagram of Altai-Uliastai local power system, indicating the interconnection with rest of MPS through Murun-Telmen transmission line.

The power balance in the ALPS is highly dependent on the power import from the CLPS, and the Murun-Telmen interconnector becomes crucial to keep the power balance and continuous operation of the ALPS. However, the Murun-Telmen transmission line is exceptionally vulnerable to weather conditions and experiences recurrent outages. Therefore, following the disconnection of the Murun-Telmen transmission line, ALPS is isolated, suffering a significant power imbalance, and the UFLS scheme must act to try to regain the power balance. Therefore, the parameters of the UF-relays must be calculated accurately to guarantee the frequency restoration. Furthermore, when calculating the parameters of the UF-relays, it must be considered that the severity of the power imbalance depends on the season (summer or winter) because the power demand and power generation levels change significantly, as stated in Table 5.1. As a result, two sets of optimal UF-relays parameters are computed, one for the summer operational scenario and another for the summer operational scenario.

5.5.2.1 Simulation and results

The worst power imbalance in the ALPS is produced when the Murun-Telmen transmission line is disconnected. Therefore, the sudden outage of the Murun-Telmen transmission line is used as a frequency disturbance. The ALPS frequency indicators

($f_{\min}$, $t_{\min}$ and f_{SS}) are evaluated considering two study cases defined in Table 5.7 for both summer and winter operational scenarios.

Table 5.7. Description of the study cases considered to evaluate the frequency quality indicators in summer and winter operational scenarios.

Case	Description	Purpose
1	The existing TUFLS scheme in the ALPS is implemented in the model created in DIgSILENT PowerFactory. The UF-relays parameters used are those described in Table 5.1, and it is assumed they are the same for summer and winter operational scenarios.	Determinate the frequency response of the ALPS with the existing TUFLS scheme after the outage of the transmission line.
2	The proposed optimal UFLS scheme is implemented in ALPS for each operational scenario.	Evaluate the influence of the optimal UF-relays parameters on the frequency response and its quality indicators.

The ALPS modelled in DIgSILENT® PowerFactory™ is equipped with eight UF-relay at different loads and lines, as indicated in Table 5.2. The five UF- relays installed in the loads are type ANSI 81 and have one load shedding step (n_S = 1) as in the real power system. Furthermore, the three UF-relays installed in lines are type SEL751A.

The optimal UFLS problem is solved using ΔP_{LS}, f_t and t_d as control variables, and they are bounded considering the frequency requirements of the MPS [149]. The control variables ΔP_{LS} are continuous UF-relays ANSI 81 and discrete for UF-relays SEL751A. Therefore the boundaries are set as $\mathbf{\Delta P}_{LS}^{L} = 0 \cdot \mathbf{1}$ and $\mathbf{\Delta P}_{LS}^{L} = 100 \cdot \mathbf{1}$ in percentage for UF-relays ANSI 81, $\mathbf{\Delta P}_{LS}^{L} = 0 \cdot 1$ and $\mathbf{\Delta P}_{LS}^{L} = 1 \cdot \mathbf{1}$ for UF-relays SEL751A. Furthermore, $f_{t1,k}^{L} = 47.6$ Hz, $f_{t1,k}^{U} = 49.4$ Hz, $\mathbf{T}_{d}^{L} = 0.1 \cdot \mathbf{1}$ and $\mathbf{T}_{d}^{U} = 0.3 \cdot \mathbf{1}$ in s. The frequency constraints defined in (5.8)-(5.9) considers f_{limit} = 47 Hz and $\Delta f_{SS,max}$ = ±0.2 Hz. Lastly, the parameters of the IHS algorithm are established as HMS=3, $HMCR$=0.85, PAR_{min}=0.35, PAR_{max}=0.99, bw_{min}= 1×10^{-5} and bw_{max}= 1 and n_I=500[161].

5.5.2.1.1 Summer operational scenario

The summer operational scenario is characterised by high rotational inertia and low power demand levels. The optimal UF-relay parameters are obtained by solving the optimal UFLS problem formulated in Section 5.3 and are shown in Table 5.8.

Table 5.8. Optimal UF-relays parameters for summer operational scenario (high-inertia) in ALPS.

UF-relay location		**ΔP_{LS} (%)**	**f_t (Hz)**	**t_d (s)**
Element	***Name***			
Load	Baynshand	17.845	48.124	0.248
Load	Baynhairhan	43.595	48.644	0.244
Load	Jargalant	12.477	48.401	0.219
Load	Uildwer	29.740	48.784	0.210
Load	Harzat	9.733	47.986	0.188
Line	Uliastai	Open	49.317	0.220
Line	Guulin	Open	48.720	0.105
Line	Biger garaa	Open	48.661	0.126

The convergence curve of the objective function defined in (5.7) is shown in Figure 5.11. The IHS algorithm finds the optimal UF-relays parameters in the improvisation 303. Therefore, the minimum load disconnection that fulfil the frequency constraints described in (5.8)-(5.9) is $\Delta P_{\mathrm{TLS}} = 3.144$ MW.

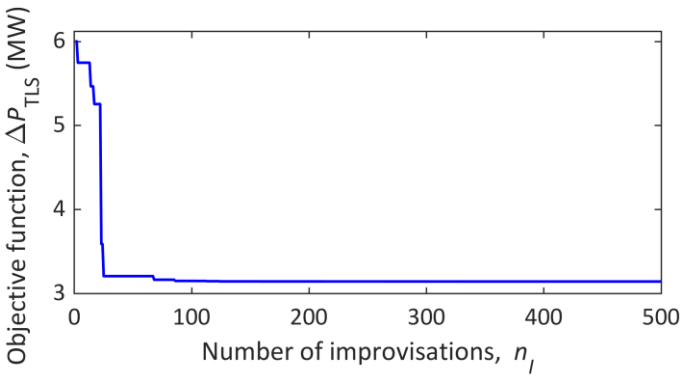

Figure 5.11. Evaluation of the objective function over 500 improvisations for the summer operational scenario.

The optimal UFLS scheme is implemented in the ALPS, and the frequency response after the outage of the Murun-Telmen transmission line is obtained. The frequency response of Case 1 and Case 2 (defined in Table 5.7) following the outage of the Murun-Telmen

transmission line is depicted in Figure 5.12. The frequency response of Case 1 (TUFLS scheme) reaches a maximum instantaneous value of 53.3 Hz crossing the operation zone of the over-frequency protection of synchronous generators, which is usually set at 53 Hz. In contrast, in Case 2 (optimal UFLS scheme), $f_{\min}$ is improved concerning Case 1 and does not produce over-frequency conditions.

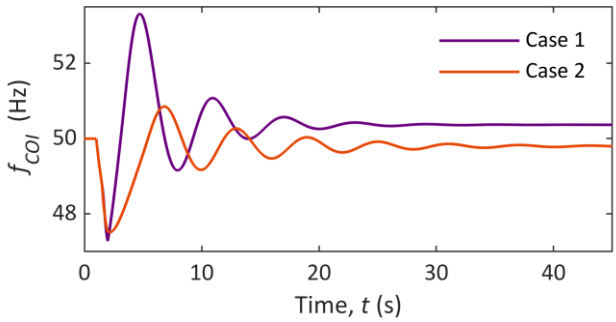

Figure 5.12. Frequency response of ALPS after the outage of the Murun-Telmen transmission line for summer operational scenario.

The frequency quality indicators of the Case 1 and Case 2 are computed and presented in Table 5.9. Case 2 enhance the frequency response of the ALPS. It reduces the value of $f_{\min}$ by 0.232 Hz and prevents an unnecessary load disconnection of 1.056 MW concerning Case 1. Moreover, Case 2 restore the frequency within the range $\Delta f_{\mathrm{SS,max}}$ = ±0.2 Hz and reduces the possibility of over-frequency conditions.

Table 5.9. Summary of frequency quality indicator for the summer operational scenario.

Case	UFLS type	$f_{\min}$ (Hz)	f_{SS} (Hz)	$t_{\min}$ (s)	ΔP_{TLS} (MW)
1	Traditional	47.28	50.37	1.99	4.20
2	Optimal	47.51	49.80	2.16	3.14

5.5.2.1.2 Winter season: Low inertia

The winter operational scenario is challenging for the TSOs of MPS because, in this operational scenario, the local power generation decreases by approximately 35%. Furthermore, the power demand increases about 95% concerning the summer operational scenario. Therefore, the outage of the Murun-Telmen transmission line represents a precarious situation for the ALPS, primarily because of the low rotational inertia conditions. Consequently, it is essential to compute the optimal UF-relay

parameters that ensure the frequency will be re-established within its permissible values.

The optimal UF-relays parameters obtained by solving the proposed optimal UFLS scheme are presented in Table 5.10. Furthermore, the convergence curve of the objective function defined in (5.7) evaluated over 500 improvisations is shown in Figure 5.13. The optimisation algorithm reaches the optimal minimum in improvisation 348; at this point, the minimum load disconnection is ΔP_{TLS} = 4.803 MW, and the frequency constraints are fulfilled.

Table 5.10. Optimal UF-relays parameters for winter operational scenario (low-inertia) in ALPS.

UF-relay location		ΔP_{LS} **(%)**	f_{t} **(Hz)**	t_{d} **(s)**
Element	***Name***			
Load	Baynshand	84.818	49.003	0.264
Load	Baynhairhan	5.049	47.661	0.275
Load	Jargalant	72.712	48.816	0.108
Load	Uildwer	5.001	48.382	0.161
Load	Harzat	74.248	49.108	0.150
Line	Uliastai	Open	49.120	0.187

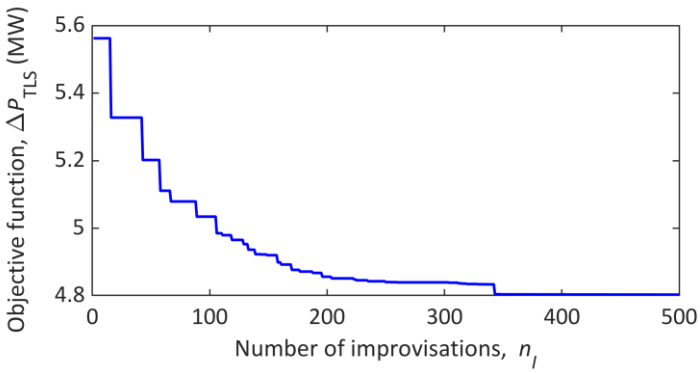

Figure 5.13. Evaluation of the objective function over 500 improvisations for the winter operational scenario.

The optimal UF-relays parameters are implemented in the ALPS model and assessed by inserting a frequency disturbance consisting of the disconnection of the Murun-Telmen. The frequency response after the action of the optimal UFLS scheme (Case 2) is compared against the frequency response obtained by implementing the TUFLS scheme

(Case 1) and is depicted in Figure 5.14. In Case 1, the frequency drop reaches deeper values compared to the summer operational scenario due to the rotational inertia reduction and increase of power demand. Furthermore, $f_{\min}$ exceeds the frequency limit ($f_{\min} < f_{\text{limit}}$) and may cause the disconnection of synchronous generators. Otherwise, Case 2 enhances the frequency response by reducing $f_{\min,}$ moving it out of the operation zone of UF-protection of synchronous generators.

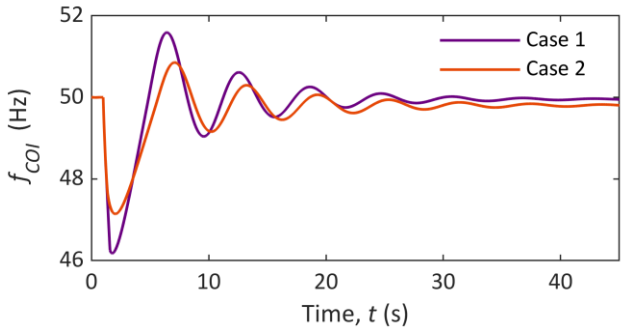

Figure 5.14. Frequency response of ALPS after the outage of the Murun-Telmen transmission line for winter operational scenario.

Table 5.11 presents the frequency quality indicators and the total load disconnection after the performance of the UFLS schemes of Case 1 and Case 2. From the results presented in Table 5.11, it can be concluded Case 2 (optimal UFLS scheme) enhance the frequency quality indicators by reducing the frequency deviation and restrict $f_{\min}$ to values above f_{limit}. Furthermore, the optimal UF-relay parameters prevent excessive load disconnection and reduce ΔP_{TLS} by 0.29 MW concerning Case 1.

Table 5.11. Summary of frequency quality indicator for the winter operational scenario.

Case	UFLS type	$f_{\min}$ (Hz)	f_{SS} (Hz)	$t_{\min}$ (s)	ΔP_{TLS} (MW)
1	Traditional	46.164	49.955	1.775	5.093
2	Optimal	47.142	49.804	2.038	4.803

The optimal UFLS scheme has demonstrated outstanding performance in both summer and winter operational scenarios against the existing TUFLS in ALPS. The optimal UFLS scheme is particularly important in the low rotational inertia condition of the winter operational scenario. It prevents the activation of the UF-protection of the synchronous

generators and ensures the frequency quality indicators achieve the requirements of the MPS.

5.5.2.1.3 Sensitivity assessment

The optimal UFLS scheme has proven excellent results to compute the UF-relays parameters and improve the frequency quality indicator. Therefore, a sensitivity assessment of UF-relays parameters is conducted to verify the IHS algorithm computed the optimal solution. The sensitivity assessment is intended to demonstrate that does not exist another set of UF-relays parameters (ΔP^*_{LS}, f^*_{t} and t^*_{d}) that would produce the minimum load shedding and satisfy the frequency constraints defined in (5.8)-(5.9).

The sensitivity analysis was carried out considering the variation of the size of load shedding in a range from 1% to 5% of the optimal ΔP_{LS} value for both summer and winter operational scenarios. The frequency response after the variation of ΔP_{LS} is depicted in Figure 5.15.

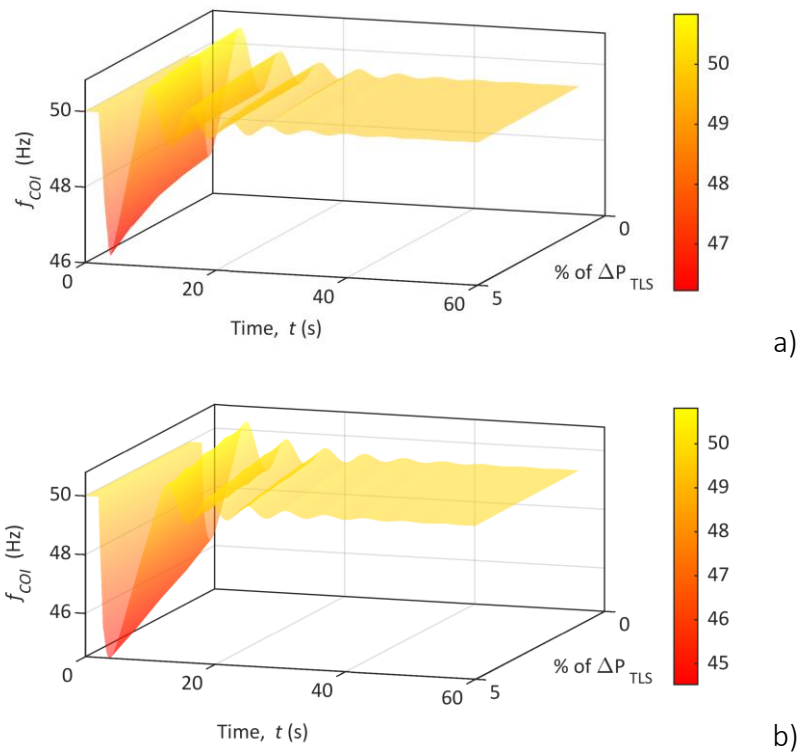

Figure 5.15. Sensitivity assessment of ΔP_{TLS} considering variation in a range of 1% to 5%. Frequency response: a) Summer operational scenario; b) Winter operational scenario.

After the sensitivity assessment for the summer operational scenario, the frequency response depicted in Figure 5.15a shows that $f_{\min}$ take values of 47.38 Hz and 46.22 Hz for 1% and 5% of ΔP_{LS} variation, respectively. It indicates the ΔP_{LS} variation produces violation of the minimum frequency constraint defined in (5.8). Furthermore, f_{SS} is settled in a range between 49.79 Hz and 49.77 Hz for the 1% to 5% of ΔP_{LS} variation. Consequently, the steady-state frequency constraint defined in (5.9) is not fulfilled for values above 1% of ΔP_{LS} since f_{SS} is settled outside the range $\Delta f_{\mathrm{SS,max}}$ = ±0.2 Hz.

On the other hand, the sensitivity assessment for the winter operational scenario demonstrated that the frequency response does not satisfy the frequency constraints defined in (5.8)-(5.9) (see Figure 5.15b). $f_{\min}$ reaches values below the frequency limit, f_{limit} = 47 Hz, and f_{SS} is beyond the range $\Delta f_{\mathrm{SS,max}}$ = ±0.2 Hz.

The results of sensitivity assessment have demonstrated that the UF-relays parameters of summer and winter operational scenarios are the optimal solution of the proposed optimal UFLS formulation.

5.6 Conclusion

This chapter presented a novel formulation to compute the UF-relays parameters of the optimal UFLS scheme. The goal of the proposed optimal UFLS scheme is to minimise the total amount of load disconnection and guarantee that the maximum frequency deviation does not activate the over/under frequency protection of the synchronous generator. In addition, the proposed methodology ensures the frequency indicators meet the operational requirements of the utility companies.

The optimal UFLS scheme was formulated in a general approach by considering each individual UF-relays parameter as a control variable instead of assuming a set of parameters are the same for all UF-relays installed in the power system. Consequently, the optimal UFLS scheme formulation can be used to compute the optimal UF-relay parameters for any power system independently of the number of UF-relays installed or the frequency requirements of the utility company. Moreover, the proposed

formulation is adjustable and allows the user to define which parameters consider as control variables as desired. Furthermore, the minimum frequency and steady-state frequency were included in the optimisation formulation as a set of inequality constraints to ensure the frequency response after the action of the optimal UFLS scheme will fulfil the frequency operational requirements.

A co-simulation outline was developed to solve the optimal UFLS scheme considering the IHS algorithm to solve the optimisation problem and DIgSILENT® PowerFactory™ to evaluate the UF-relays parameters and obtain the frequency response.

The assessment of the proposed optimal UFLS scheme was conducted using the 10-machine New England power system and the real Altai-Uliastai power system. The simulation results showed that implementing the optimal UFLS scheme significantly improves the frequency response. Particularly in vulnerable power systems with low rotational inertia and high power demand, as demonstrated in the real Altai-Uliastai power system.

The most crucial enhancement provided by the optimal UFLS schemes is in the minimum frequency; it limits the frequency drop and avoids subsequent over/under frequency situations. Furthermore, it ensures that the steady-state frequency is re-established inside the maximum steady-state range. Finally, and not less important, it counteracts excessive load disconnection.

6 Conclusions and future work

This thesis focused on creating novel intelligent frequency control methods to deal with the reduced rotational inertia in the modern power system. The integration of FFR controls and the UFLS scheme was considered to mitigate frequency deviation in normal and emergency conditions. It was demonstrated that enabling FFR control in the DERs and ESSs provides fast frequency support to the power system. Moreover, computing the optimal parameters of FFR control reduces the minimum frequency and prevent the activation of the UFLS scheme. It was proved the variable-speed HPPs, and BESS are a realistic alternative to the NPS to cope with the traditional power plants decommission and rotational inertia reduction. Whilst the optimal UFLS schemes provided significant enhancements to the frequency response. It limits the frequency decline, avoids subsequent over/under frequency situations, ensures the steady-state frequency is inside the maximum steady-state range and counteracts excessive load disconnection.

Chapter 2 was dedicated to describing the fundamental concepts related to frequency control, including the dynamic behaviour of frequency and the principal stages used by the TSOs to manage the frequency. It was highlighted the principal requirements and parameters of the frequency quality and the importance of the rotational inertia to limit the frequency deviation. Furthermore, several frequency disturbances were analysed to underline the importance of the appropriate control actions to recovering the frequency.

In Chapter 3, a methodology was created based on a statistical assessment to unveil features and patter of time series of frequency, kinetic energy and power demand of the Nordic power system. It was demonstrated that the yearly mean value of frequency is above the nominal frequency and tends to increase in the following years. Furthermore, a dispersion assessment considering 15-minute periods foregrounded that other elements of the power system besides synchronous generators can provide an inertial response. The correlation assessment between kinetic energy and power demand unveiled they follow the same seasonal pattern and have a strong correlation during high power demand and kinetic energy hours. The dependency between power

demand and kinetic energy was validated by clustering the data using the GMM. Then, it was computed a set of linear regression model that represent the data of each cluster. The clusters well classified the time series of power demand and kinetic energy with the same statistical features, i.e., the L-L cluster holds the low values, and the H-H cluster contains the high values of power demand and kinetic energy. The validation of the linear regression models determined that the linear regression model of the H-H cluster is not capable of explaining the validation data due to its tendency to decrease.

Furthermore, in Chapter 4, a novel methodology to enable power converter-based technologies (DERs and ESSs) with FFR control to deliver optimal fast frequency support and cope with reduced rotational inertia in the modern power system was developed. The methodology was formulated to compute the optimal parameters of FFR control considering two objective functions, one to minimise the steady-state frequency and the other to minimise the minimum frequency. It was demonstrated that the frequency support provided by the combination of the proportional and derivative control of the FFR, considering a gradual decreasing of rotational inertia, is capable of enhancing the frequency response by limiting either the minimum frequency or the steady-state frequency variation. Furthermore, it was found that the variable-speed PHPPs and BESS technologies equipped with proportional FFR control can improve the frequency quality indicators of a realistic dynamic model under low rotational inertia scenarios. Moreover, the proposed methodology to compute the optimal parameters of FFR control effectively limit the frequency deviation and avoid the activation of the UFLS scheme.

Lastly, Chapter 5 introduced a novel approach to compute the optimally UF-relays parameters of the proposed optimal UFLS scheme. The main goal of this approach was to minimise the total amount of load shedding and limit the maximum frequency deviation to avers the activation of the UF protection of synchronous generators. The minimum frequency and permissible steady-state variation were formulated as inequality constraints to guarantees compliance with the frequency quality indicators. It was demonstrated that this methodology computes the optimal UF-relay parameters for any power system and is adjustable so that the user can define which parameters

use as control variables as desired. The optimal UFLS scheme showed to be particularly important for vulnerable power systems with low rotational inertia and high levels of power demand, as demonstrated in the real Altai-Uliastai power system.

6.1 Future work

The outcomes and findings presented in this thesis provide the following potential topics for future research:

- Given the dependency of the kinetic energy and power demand, the use of historical data to develop more sophisticated prediction models of kinetic energy relying solely on the forecast of power demand could be helpful to the system operator to ensure a secure operation. It could provide knowledge of kinetic energy level in the power system and enables more effective controls.
- The frequency support provided by the FFR control has proven to be an effective solution to cope with low rotational inertia in the power systems. However, further work must explore more features that enable DERs and RESs to behave as synchronous generator. The first steps can be implementing the proposed methodology to compute the optimal FFR parameters in a real-time simulation environment to identify and solve possible implementation issues in a real power system. Develop and evaluate a synchronise frequency-voltage control provided by DERs.
- Incorporate the prediction model of kinetic energy to estimate the size of power imbalance and create an adaptative UFLS scheme using artificial intelligence techniques.

References

[1] Organisation for economic co-opreation and developement, “Greenhouse gas emissions.” https://stats.oecd.org/Index.aspx?DataSetCode=AIR_GHG (accessed May 12, 2021).

[2] United States Environmental Protection Agency, “Sources of Greenhouse Gas Emissions.” https://www.epa.gov/ghgemissions/sources-greenhouse-gas-emissions (accessed May 12, 2021).

[3] United States climate alliance, “STATE CLIMATE & ENERGY POLICIES.” https://www.usclimatealliance.org/state-climate-energy-policies (accessed Apr. 18, 2021).

[4] “2020 climate & energy package.” https://ec.europa.eu/clima/policies/strategies/2020_en (accessed Feb. 18, 2021).

[5] *Renewables 2019 Global Status Report*. Paris: REN21 Secretariat, 2019.

[6] International Energy Agency, *Renewables 2019: Analysis and forecast to 2024*. IEA Publications, 2019.

[7] S. Tabatabaee, S. S. Mortazavi, and T. Niknam, “Stochastic scheduling of local distribution systems considering high penetration of plug-in electric vehicles and renewable energy sources,” *Energy*, vol. 121, pp. 480–490, Feb. 2017, doi: 10.1016/j.energy.2016.12.115.

[8] R. Hemmati, H. Saboori, and M. A. Jirdehi, “Stochastic planning and scheduling of energy storage systems for congestion management in electric power systems including renewable energy resources,” *Energy*, vol. 133, pp. 380–387, Aug. 2017, doi: 10.1016/j.energy.2017.05.167.

[9] U.S. Department of Energy, “DOE OE Global Storage Database,” *U.S. Department of Energy*, 2020. https://www.sandia.gov/ess-ssl/global-energy-storage-database-home/ (accessed Mar. 16, 2020).

[10] K. Shi, H. Ye, W. Song, and G. Zhou, “Virtual Inertia Control Strategy in Microgrid Based on Virtual Synchronous Generator Technology,” *IEEE Access*, vol. 6, pp. 27949–27957, 2018, doi: 10.1109/ACCESS.2018.2839737.

[11] D. Connolly and B. V. Mathiesen, “A technical and economic analysis of one potential pathway to a 100% renewable energy system,” *Int. J. Sustain. Energy Plan. Manag.*, vol. 1, pp. 7–28, 2014, doi: 10.5278/ijsepm.2014.1.2.

[12] B. Elliston, M. Diesendorf, and I. MacGill, “Simulations of scenarios with 100% renewable electricity in the Australian National Electricity Market,” *Energy Policy*, vol. 45, pp. 606–613, Jun. 2012, doi: 10.1016/j.enpol.2012.03.011.

[13] B. V. Mathiesen, H. Lund, and K. Karlsson, “100% Renewable energy systems, climate

mitigation and economic growth," *Appl. Energy*, vol. 88, no. 2, pp. 488–501, Feb. 2011, doi: 10.1016/j.apenergy.2010.03.001.

[14] H. Lund and B. V. Mathiesen, "Energy system analysis of 100% renewable energy systems—The case of Denmark in years 2030 and 2050," *Energy*, vol. 34, no. 5, pp. 524–531, May 2009, doi: 10.1016/j.energy.2008.04.003.

[15] G. Pleßmann, M. Erdmann, M. Hlusiak, and C. Breyer, "Global Energy Storage Demand for a 100% Renewable Electricity Supply," *Energy Procedia*, vol. 46, pp. 22–31, 2014, doi: 10.1016/j.egypro.2014.01.154.

[16] P. Capros *et al.*, "EU Reference Scenario 2016-Energy, transport and GHG emissions Trends to 2050," 2016. doi: 10.2833/001137.

[17] F. Gonzalez-Longatt, M. N. Acosta, H. R. Chamorro, and Jose Luis Rueda, "Power Converters Dominated Power Systems," in *Modelling and Simulation of Power Electronic Converter controlled Power Systems in PowerFactory*, First Edit., F. Gonzalez-Longatt and Jose Luis Rueda, Eds. Switzerland: Springer Nature Switzerland AG, 2020.

[18] N. Hatziargyriou, T. Van Cutsem, J. Milanović, P. Pourbeik, C. Vournas, and O. Vlachokyriakou, "Contribution to Bulk System Control and Stability by Distributed Energy Resources connected at Distribution Network," 2017.

[19] H. Bevrani and J. Raisch, "On Virtual inertia Application in Power Grid Frequency Control," *Energy Procedia*, vol. 141, pp. 681–688, Dec. 2017, doi: 10.1016/j.egypro.2017.11.093.

[20] H. Golpira, A. R. Messina, and H. Bevrani, "Emulation of Virtual Inertia to Accommodate Higher Penetration Levels of Distributed Generation in Power Grids," *IEEE Trans. Power Syst.*, vol. 34, no. 5, pp. 3384–3394, Sep. 2019, doi: 10.1109/TPWRS.2019.2908935.

[21] T. Liu, W. Pan, R. Quan, and M. Liu, "A Variable Droop Frequency Control Strategy for Wind Farms that Considers Optimal Rotor Kinetic Energy," *IEEE Access*, vol. 7, pp. 68636–68645, 2019, doi: 10.1109/ACCESS.2019.2914496.

[22] U. Datta, A. Kalam, and J. Shi, "Frequency performance analysis of multi-gain droop controlled DFIG in an isolated microgrid using real-time digital simulator," *Eng. Sci. Technol. an Int. J.*, vol. 23, no. 5, pp. 1028–1041, Oct. 2020, doi: 10.1016/j.jestch.2019.11.008.

[23] A. B. T. Attya and J. L. Dominguez-Garcia, "Insights on the Provision of Frequency Support by Wind Power and the Impact on Energy Systems," *IEEE Trans. Sustain. Energy*, vol. 9, no. 2, pp. 719–728, Apr. 2018, doi: 10.1109/TSTE.2017.2759503.

[24] F. M. Gonzalez-Longatt, "Effects of Fast Acting Power Controller of BESS in the System Frequency Response of a Multi-Machine System: Probabilistic Approach," in *2018 IEEE Innovative Smart Grid Technologies - Asia (ISGT Asia)*, May 2018, pp. 798–803,

doi: 10.1109/ISGT-Asia.2018.8467909.

[25] F. Sanchez and F. Gonzalez-Longatt, “Optimization of Frequency Controller Parameters of a BESS by considering Rate of Change Constraints,” in *2019 IEEE Milan PowerTech*, Jun. 2019, pp. 1–6, doi: 10.1109/PTC.2019.8810730.

[26] F. Sanchez, F. Gonzalez-Longatt, A. Rodriguez, and J. L. Rueda, “Dynamic Data-Driven SoC Control of BESS for Provision of Fast Frequency Response Services,” in *2019 IEEE Power & Energy Society General Meeting (PESGM)*, Aug. 2019, pp. 1–5, doi: 10.1109/PESGM40551.2019.8973551.

[27] H. Zhao, Q. Wu, S. Huang, H. Zhang, Y. Liu, and Y. Xue, “Hierarchical Control of Thermostatically Controlled Loads for Primary Frequency Support,” *IEEE Trans. Smart Grid*, vol. 9, no. 4, pp. 2986–2998, Jul. 2018, doi: 10.1109/TSG.2016.2624509.

[28] P. Babahajiani, Q. Shafiee, and H. Bevrani, “Intelligent Demand Response Contribution in Frequency Control of Multi-Area Power Systems,” *IEEE Trans. Smart Grid*, vol. 9, no. 2, pp. 1282–1291, Mar. 2018, doi: 10.1109/TSG.2016.2582804.

[29] A. Delavari and I. Kamwa, “Improved Optimal Decentralized Load Modulation for Power System Primary Frequency Regulation,” *IEEE Trans. Power Syst.*, vol. 33, no. 1, pp. 1013–1025, Jan. 2018, doi: 10.1109/TPWRS.2017.2708058.

[30] G. Benysek, J. Bojarski, R. Smolenski, M. Jarnut, and S. Werminski, “Application of Stochastic Decentralized Active Demand Response (DADR) System for Load Frequency Control,” *IEEE Trans. Smart Grid*, vol. 9, no. 2, pp. 1055–1062, Mar. 2018, doi: 10.1109/TSG.2016.2574891.

[31] F. Milano, A. Ortega, and A. J. Conejo, “Model-Agnostic Linear Estimation of Generator Rotor Speeds Based on Phasor Measurement Units,” *IEEE Trans. Power Syst.*, vol. 33, no. 6, pp. 7258–7268, Nov. 2018, doi: 10.1109/TPWRS.2018.2846737.

[32] H. Golpira and A. R. Messina, “A Center-of-Gravity-Based Approach to Estimate Slow Power and Frequency Variations,” *IEEE Trans. Power Syst.*, vol. 33, no. 1, pp. 1026–1035, Jan. 2018, doi: 10.1109/TPWRS.2017.2710187.

[33] J. Zhao, L. Mili, and F. Milano, “Robust Frequency Divider for Power System Online Monitoring and Control,” *IEEE Trans. Power Syst.*, vol. 33, no. 4, pp. 4414–4423, Jul. 2018, doi: 10.1109/TPWRS.2017.2785348.

[34] J. C. M. Vieira, W. Freitas, Z. Huang, W. Xu, and A. Morelato, “Formulas for predicting the dynamic performance of ROCOF relays for embedded generation applications,” *IEE Proc. - Gener. Transm. Distrib.*, vol. 153, no. 4, p. 399, 2006, doi: 10.1049/ip-gtd:20045205.

[35] F. M. Gonzalez-Longatt, “Effects of Fast Acting Power Controller of BESS in the System Frequency Response of a Multi-Machine System: Probabilistic Approach,” in *2018 IEEE Innovative Smart Grid Technologies - Asia (ISGT Asia)*, May 2018, pp. 804–809, doi: 10.1109/ISGT-Asia.2018.8467855.

[36] North American Electric Reliability Corporation, “Balancing and Frequency Control,” 2011.

[37] “Network Code on Load-Frequency Control and Reserves in line with the ACER Framework Guidelines on Electricity System Operation,” 2013.

[38] A. H. Kuisti -MLahtinen MNilsson -KEketorp -EØrum DWhitley -A Slotsvik -AJansson, “FREQUENCY QUALITY REPORT-NAG i Nordic Analysis Group NAG-FREQUENCY QUALITY REPORT Title Final report Circulation RGN-Internal TSO Version 2.0,” 2015.

[39] UCTE, *Final Report of the Investigation Committee on the 28 September 2003 Blackout in Italy*, no. 1. 2004.

[40] S. Corsi and C. Sabelli, “General blackout in Italy sunday September 28, 2003, h. 03:28:00,” in *2004 IEEE Power Engineering Society General Meeting*, 2004, vol. 2, pp. 1691–1701, doi: 10.1109/pes.2004.1373162.

[41] National Grid ESO, “Technical Report on the events of 9 August,” no. September, pp. 2–38, 2019.

[42] “ENTSO-E Interim Report – Continental Europe Synchronous Area Separation on 8 January 2021.”

[43] M.-H. Lin, J.-F. Tsai, and C.-S. Yu, “A Review of Deterministic Optimization Methods in Engineering and Management,” *Math. Probl. Eng.*, vol. 2012, pp. 1–15, 2012, doi: 10.1155/2012/756023.

[44] M. Shehab, A. T. Khader, and M. A. Al-Betar, “A survey on applications and variants of the cuckoo search algorithm,” *Appl. Soft Comput.*, vol. 61, pp. 1041–1059, Dec. 2017, doi: 10.1016/j.asoc.2017.02.034.

[45] J. Lin, F. Magnago, and J. M. Alemany, “Optimization Methods Applied to Power Systems: Current Practices and Challenges,” in *Classical and Recent Aspects of Power System Optimization*, Elsevier, 2018, pp. 1–18.

[46] J. Bleyer, “Advances in the simulation of viscoplastic fluid flows using interior-point methods,” *Comput. Methods Appl. Mech. Eng.*, vol. 330, pp. 368–394, Mar. 2018, doi: 10.1016/j.cma.2017.11.006.

[47] R. H. Byrd, M. E. Hribar, and J. Nocedal, “An Interior Point Algorithm for Large-Scale Nonlinear Programming,” *SIAM J. Optim.*, vol. 9, no. 4, pp. 877–900, Jan. 1999, doi: 10.1137/S1052623497325107.

[48] R. H. Byrd, J. C. Gilbert, and J. Nocedal, “A trust region method based on interior point techniques for nonlinear programming,” *Math. Program.*, vol. 89, no. 1, pp. 149–185, Nov. 2000, doi: 10.1007/PL00011391.

[49] T. Steihaug, “The Conjugate Gradient Method and Trust Regions in Large Scale Optimization,” *SIAM J. Numer. Anal.*, vol. 20, no. 3, pp. 626–637, Jun. 1983, doi:

10.1137/0720042.

[50] D. Kraf, “A software package for sequential quadratic programming,” Technical Report DFVLR-FB, 1988.

[51] J. Xie, H. Zhang, Y. Shen, and M. Li, “Energy consumption optimization of central air-conditioning based on sequential-least-square-programming,” in *2020 Chinese Control And Decision Conference (CCDC)*, Aug. 2020, pp. 5147–5152, doi: 10.1109/CCDC49329.2020.9164009.

[52] W. Sun and Y.-X. Yuan, *Optimization Theory and Methods: Nonlinear Programming*. New York, NY: Springer Science+Business Media, LCCc, 2006.

[53] Zong Woo Geem, Joong Hoon Kim, and G. V. Loganathan, “A New Heuristic Optimization Algorithm: Harmony Search,” *Simulation*, vol. 76, no. 2, pp. 60–68, Feb. 2001, doi: 10.1177/003754970107600201.

[54] M. Mahdavi, M. Fesanghary, and E. Damangir, “An improved harmony search algorithm for solving optimization problems,” *Appl. Math. Comput.*, vol. 188, no. 2, pp. 1567–1579, May 2007, doi: 10.1016/j.amc.2006.11.033.

[55] F. Gonzalez-Longatt, J. Rueda, and E. Vázquez Martínez, “Effect of Fast Acting Power Controller of Battery Energy Storage Systems in the Under-frequency Load Shedding Scheme,” 2018.

[56] H. R. Chamorro *et al.*, “Nadir Frequency Estimation in Low-Inertia Power Systems,” in *2020 IEEE 29th International Symposium on Industrial Electronics (ISIE)*, Jun. 2020, pp. 918–922, doi: 10.1109/ISIE45063.2020.9152296.

[57] A. Perilla, S. Papadakis, J. L. Rueda Torres, M. van der Meijden, P. Palensky, and F. Gonzalez-Longatt, “Transient Stability Performance of Power Systems with High Share of Wind Generators Equipped with Power-Angle Modulation Controllers or Fast Local Voltage Controllers,” *Energies*, vol. 13, no. 16, p. 4205, Aug. 2020, doi: 10.3390/en13164205.

[58] F. Gonzalez-Longatt, J. L. Rueda, and E. Vázquez Martínez, *Effect of Fast Acting Power Controller of Battery Energy Storage Systems in the Under-frequency Load Shedding Scheme*. Loughborough University, 2018.

[59] H. R. Chamorro, C. A. Ordonez, J. C.-H. Peng, F. Gonzalez-Longatt, and V. K. Sood, “Coherency Estimation in Power Systems: A Koopman Operator Approach,” in *Computational Intelligence and Optimization Methods for Control Engineering*, J. S. Sáez, Maude, Josée Blondin, Panos M. Pardalos, Ed. Springer, Cham, 2019, pp. 201–225.

[60] A. Peña Asensio, F. Gonzalez-Longatt, S. Arnaltes, and J. L. Rodríguez-Amenedo, “Analysis of the Converter Synchronizing Method for the Contribution of Battery Energy Storage Systems to Inertia Emulation,” *Energies*, vol. 13, no. 6, p. 1478, Mar. 2020, doi: 10.3390/en13061478.

[61] Y. Cao, Y. Li, X. Liu, and C. Rehtanz, *Cyber-Physical Energy and Power Systems*. Singapore: Springer Singapore, 2020.

[62] P. Wall, F. Gonzalez-Longatt, and V. Terzija, "Estimation of generator inertia available during a disturbance," in *2012 IEEE Power and Energy Society General Meeting*, Jul. 2012, pp. 1–8, doi: 10.1109/PESGM.2012.6344755.

[63] P. M. Ashton, G. A. Taylor, A. M. Carter, M. E. Bradley, and W. Hung, "Application of phasor measurement units to estimate power system inertial frequency response," in *2013 IEEE Power & Energy Society General Meeting*, 2013, pp. 1–5, doi: 10.1109/PESMG.2013.6672671.

[64] P. M. Ashton, C. S. Saunders, G. A. Taylor, A. M. Carter, and M. E. Bradley, "Inertia Estimation of the GB Power System Using Synchrophasor Measurements," *IEEE Trans. Power Syst.*, vol. 30, no. 2, pp. 701–709, Mar. 2015, doi: 10.1109/TPWRS.2014.2333776.

[65] D. Zografos and M. Ghandhari, "Power system inertia estimation by approaching load power change after a disturbance," in *2017 IEEE Power & Energy Society General Meeting*, Jul. 2017, pp. 1–5, doi: 10.1109/PESGM.2017.8273824.

[66] D. Zografos, M. Ghandhari, and K. Paridari, "Estimation of power system inertia using particle swarm optimization," in *2017 19th International Conference on Intelligent System Application to Power Systems (ISAP)*, Sep. 2017, pp. 1–6, doi: 10.1109/ISAP.2017.8071383.

[67] D. Zografos, M. Ghandhari, and R. Eriksson, "Power system inertia estimation: Utilization of frequency and voltage response after a disturbance," *Electr. Power Syst. Res.*, vol. 161, pp. 52–60, Aug. 2018, doi: 10.1016/j.epsr.2018.04.008.

[68] P. Wall, P. Regulski, Z. Rusidovic, and V. Terzija, "Inertia estimation using PMUs in a laboratory," in *IEEE PES Innovative Smart Grid Technologies Conference Europe*, Jan. 2015, vol. 2015-January, no. January, doi: 10.1109/ISGTEurope.2014.7028985.

[69] X. Cao, B. Stephen, I. F. Abdulhadi, C. D. Booth, and G. M. Burt, "Switching Markov Gaussian Models for Dynamic Power System Inertia Estimation," *IEEE Trans. Power Syst.*, vol. 31, no. 5, pp. 3394–3403, Sep. 2016, doi: 10.1109/TPWRS.2015.2501458.

[70] J. Zhang and H. Xu, "Online Identification of Power System Equivalent Inertia Constant," *IEEE Trans. Ind. Electron.*, vol. 64, no. 10, pp. 8098–8107, Oct. 2017, doi: 10.1109/TIE.2017.2698414.

[71] S. Aranovskiy, A. Bobtsov, R. Ortega, and A. Pyrkin, "Performance Enhancement of Parameter Estimators via Dynamic Regressor Extension and Mixing," in *IEEE Transactions on Automatic Control*, Jul. 2017, vol. 62, no. 7, pp. 3546–3550, doi: 10.1109/TAC.2016.2614889.

[72] J. Schiffer, P. Aristidou, and R. Ortega, "Online Estimation of Power System Inertia Using Dynamic Regressor Extension and Mixing," *IEEE Trans. Power Syst.*, vol. 34, no.

6, pp. 4993–5001, Nov. 2019, doi: 10.1109/TPWRS.2019.2915249.

[73] J. L. Myers, A. D. Well, and J. Robert F. Lorch, *Research Design and Statistical Analysis*. 2010.

[74] X. Yan and X. G. Su, *Linear Regression Analysis*. WORLD SCIENTIFIC, 2009.

[75] F. Gonzalez-Longatt, J. Rueda, I. Erlich, W. Villa, and D. Bogdanov, "Mean Variance Mapping Optimization for the identification of Gaussian Mixture Model: Test case," in *IS'2012 - 2012 6th IEEE International Conference Intelligent Systems, Proceedings*, 2012, pp. 158–163, doi: 10.1109/IS.2012.6335130.

[76] G. Gan, C. Ma, and J. Wu, "Data Clustering: Theory, Algorithms, and Applications (ASA-SIAM Series on Statistics and Applied Probability)." p. 466, 2007.

[77] P. Kundur, N. J. Balu, and M. G. Lauby, *Power system stability and control*. New York: McGraw-Hill, 1994.

[78] P. M. Anderson and A. A. Fouad, *Power system control and stability*. New York: IEEE Press, 2003.

[79] F. Gonzalez-Longatt, J. Rueda, I. Erlich, W. Villa, and D. Bogdanov, "Mean Variance Mapping Optimization for the identification of Gaussian Mixture Model: Test case," in *2012 6th IEEE INTERNATIONAL CONFERENCE INTELLIGENT SYSTEMS*, Sep. 2012, pp. 158–163, doi: 10.1109/IS.2012.6335130.

[80] L. Ehrlinger, T. Grubinger, B. Varga, M. Pichler, T. Natschlager, and J. Zeindl, "Treating Missing Data in Industrial Data Analytics," in *2018 Thirteenth International Conference on Digital Information Management (ICDIM)*, Sep. 2018, pp. 148–155, doi: 10.1109/ICDIM.2018.8846984.

[81] E. A. Mohammed, C. Naugler, and B. H. Far, "Emerging Business Intelligence Framework for a Clinical Laboratory Through Big Data Analytics," in *Emerging Trends in Computational Biology, Bioinformatics, and Systems Biology*, Elsevier, 2015, pp. 577–602.

[82] "Fingrid." https://www.fingrid.fi/en/ (accessed Sep. 10, 2019).

[83] "Nord Pool." https://www.nordpoolgroup.com/ (accessed Sep. 10, 2019).

[84] "System Separation in the Continental Europe Synchronous Area on 8 January 2021 – update." https://www.entsoe.eu/news/2021/01/15/system-separation-in-the-continental-europe-synchronous-area-on-8-january-2021-update/ (accessed Mar. 29, 2021).

[85] ENTSOE, "Nordic Balancing Philosophy." [Online]. Available: https://docstore.entsoe.eu/Documents/Publications/SOC/Nordic/Nordic_Balancing_Philosophy_160616_Final_external.pdf.

[86] J. Torriti, “Understanding the timing of energy demand through time use data: Time of the day dependence of social practices,” *Energy Res. Soc. Sci.*, vol. 25, pp. 37–47, Mar. 2017, doi: 10.1016/j.erss.2016.12.004.

[87] F. Gonzalez-Longatt, “Effects of Fast Acting Power Controller of BESS in the System Frequency Response of a Multi-Machine System: Probabilistic Approach,” 2018.

[88] L. Saarinen, P. Norrlund, U. Lundin, E. Agneholm, and A. Westberg, “Full-scale test and modelling of the frequency control dynamics of the Nordic power system,” in *2016 IEEE Power and Energy Society General Meeting (PESGM)*, Jul. 2016, vol. 2016-Novem, pp. 1–5, doi: 10.1109/PESGM.2016.7741711.

[89] IEEE Standard Association, *IEEE Std. 1547-2018. Standard for Interconnection and Interoperability of Distributed Energy Resources with Associated Electric Power Systems Interfaces*. 2018.

[90] H. R. Chamorro, A. C. Sanchez, A. Pantoja, I. Zelinka, F. Gonzalez-Longatt, and V. K. Sood, “A network control system for hydro plants to counteract the non-synchronous generation integration,” *Int. J. Electr. Power Energy Syst.*, vol. 105, pp. 404–419, Feb. 2019, doi: 10.1016/j.ijepes.2018.08.020.

[91] A. J. S. J. Veronica, N. S. Kumar, and F. Gonzalez-Longatt, “Robust PI controller design for frequency stabilisation in a hybrid microgrid system considering parameter uncertainties and communication time delay,” *IET Gener. Transm. Distrib.*, vol. 13, no. 14, pp. 3048–3056, Jul. 2019, doi: 10.1049/iet-gtd.2018.5240.

[92] A. J. Veronica, N. S. Kumar, and F. Gonzalez-Longatt, “Design of Load Frequency Control for a Microgrid Using D-partition Method,” *Int. J. Emerg. Electr. Power Syst.*, vol. 21, no. 1, Feb. 2020, doi: 10.1515/ijeeps-2019-0175.

[93] K. Stein, M. Tun, M. Matsuura, and R. Rocheleau, “Characterization of a fast battery energy storage system for primary frequency response,” *Energies*, vol. 11, no. 12, p. 3358, Dec. 2018, doi: 10.3390/en11123358.

[94] F. Sanchez, F. Gonzalez-Longatt, A. Rodriguez, and J. L. Rueda, “Dynamic Data-Driven SoC Control of BESS for Provision of Fast Frequency Response Services,” in *2019 IEEE Power & Energy Society General Meeting (PESGM)*, Aug. 2019, pp. 1–5, doi: 10.1109/PESGM40551.2019.8973551.

[95] G. Delille, B. Francois, and G. Malarange, “Dynamic Frequency Control Support by Energy Storage to Reduce the Impact of Wind and Solar Generation on Isolated Power System’s Inertia,” *IEEE Trans. Sustain. Energy*, vol. 3, no. 4, pp. 931–939, Oct. 2012, doi: 10.1109/TSTE.2012.2205025.

[96] P. Mercier, R. Cherkaoui, and A. Oudalov, “Optimizing a Battery Energy Storage System for Frequency Control Application in an Isolated Power System,” *IEEE Trans. Power Syst.*, vol. 24, no. 3, pp. 1469–1477, Aug. 2009, doi: 10.1109/TPWRS.2009.2022997.

[97] S. Chen, T. Zhang, H. B. Gooi, R. D. Masiello, and W. Katzenstein, “Penetration Rate and Effectiveness Studies of Aggregated BESS for Frequency Regulation,” *IEEE Trans. Smart Grid*, vol. 7, no. 1, pp. 167–177, Jan. 2016, doi: 10.1109/TSG.2015.2426017.

[98] H. Saadat, “Power System Analysis.” p. 718, 1999, doi: 10.1017/CBO9781107415324.004.

[99] P. W. Sauer and M. A. Pai, *Power system dynamics and stability*, vol. 101. Prentice hall Upper Saddle River, NJ, 1998.

[100] A. E. M. Operator, “FAST FREQUENCY RESPONSE IN THE NEM,” Aug. 2017. Accessed: Apr. 30, 2021. [Online]. Available: www.aemo.com.au.

[101] B. Sri Revathi, P. Mahalingam, and F. Gonzalez-Longatt, “Interleaved high gain DC-DC converter for integrating solar PV source to DC bus,” *Sol. Energy*, vol. 188, pp. 924–934, Aug. 2019, doi: 10.1016/j.solener.2019.06.072.

[102] T. Weitzel and C. H. Glock, “Energy management for stationary electric energy storage systems: A systematic literature review,” *Eur. J. Oper. Res.*, vol. 264, no. 2, pp. 582–606, 2018, doi: 10.1016/j.ejor.2017.06.052.

[103] P. Jayamaha, “Energy Storage For Frequency Support In Weak Electrical Grids,” 2015.

[104] F. Milano, F. Dörfler, G. Hug, D. J. Hill, and G. Verbic, “Foundations and Challenges of Low-Inertia Systems,” *20th Power Syst. Comput. Conf.*, p. 25, 2018, doi: 10.23919/PSCC.2018.8450880.

[105] Y. Cho, J. W. Shim, S. J. Kim, S. W. Min, and K. Hur, “Enhanced frequency regulation service using Hybrid Energy Storage System against increasing power-load variability,” 2013, doi: 10.1109/PESMG.2013.6672784.

[106] E. Erlend Løklingholm, “Design and Operation Investigations for large Converter-Fed Synchronous Machines in Hydropower Applications,” Norwegian University of Science and Technology (NTNU), Norway, 2019.

[107] R. J. Kerkman, T. A. Lipo, W. G. Newman, and J. E. Thirkell, “An Inquiry into Adjustable Speed Operation of a Pumped Hydro Plant Part 1 - Machine Design and Performance,” *IEEE Trans. Power Appar. Syst.*, vol. PAS-99, no. 5, pp. 1828–1837, Sep. 1980, doi: 10.1109/TPAS.1980.319773.

[108] M. Valavi and A. Nysveen, “Variable-Speed Operation of Hydropower Plants: A Look at the Past, Present, and Future,” *IEEE Ind. Appl. Mag.*, vol. 24, no. 5, pp. 18–27, Sep. 2018, doi: 10.1109/MIAS.2017.2740467.

[109] “Converting to Variable Speed at a Pumped-Storage Plant - Hydro Review.” https://www.hydroreview.com/2013/09/01/converting-to-variable-speed-at-a-pumped-storage-plant/#gref (accessed Apr. 25, 2020).

[110] “estorage,” 2017. https://www.estorage-project.eu/wp-

content/uploads/2013/06/eStorage-D1.3-Report-on-Le-Cheylas-upgrade-studies.pdf (accessed Apr. 18, 2020).

[111] M. Farhadi and O. Mohammed, "Energy Storage Technologies for High-Power Applications," *IEEE Trans. Ind. Appl.*, vol. 52, no. 3, pp. 1953–1961, May 2016, doi: 10.1109/TIA.2015.2511096.

[112] T. Krechel, F. Sanchez, F. Gonzalez-Longatt, H. Chamorro, and J. L. Rueda, "Transmission system-friendly microgrids: an option to provide ancillary services," in *Distributed Energy Resources in Microgrids*, Elsevier, 2019, pp. 291–321.

[113] J.-K. Lung, Y. Lu, W.-L. Hung, and W.-S. Kao, "Modeling and Dynamic Simulations of Doubly Fed Adjustable-Speed Pumped Storage Units," *IEEE Trans. Energy Convers.*, vol. 22, no. 2, pp. 250–258, Jun. 2007, doi: 10.1109/TEC.2006.875481.

[114] T. Krechel, F. Sanchez, F. Gonzalez-Longatt, H. Chamorro, and J. L. Rueda, "A Transmission System Friendly Micro-grid: Optimising Active Power Losses," 2019.

[115] K. Skytte, C. Bergaentzlé, F. Junqueira Fausto, and P. Andreas Gunkel, "Flexible Nordic Energy System: Summary Report," Nordic Energy Research, 2019. [Online]. Available: www.Flex4RES.org.

[116] F. Sanchez, J. Cayenne, F. Gonzalez-Longatt, and J. L. Rueda, "Controller to Enable the Enhanced Frequency Response Services from a Multi-Electrical Energy Storage System," *IET Gener. Transm. Distrib.*, Nov. 2018, doi: 10.1049/iet-gtd.2018.5931.

[117] H. R. Chamorro, F. R. S. Sevilla, F. Gonzalez-Longatt, K. Rouzbehi, H. Chavez, and V. K. Sood, "Innovative primary frequency control in low-inertia power systems based on wide-area RoCoF sharing," *IET Energy Syst. Integr.*, Feb. 2020, doi: 10.1049/iet-esi.2020.0001.

[118] L. Lia, T. Jensen, K. E. Stensby, G. Holm Midttømme, and A. M. Ruud, "The current status of hydropower development and dam construction in Norway," *Int. J. Hydropower Dams*, vol. 22, no. 3, pp. 37–43, 2015, doi: Retrive from https://www.hydropower-dams.com/.

[119] "Electricity production - Energifakta Norge." https://energifaktanorge.no/en/norsk-energiforsyning/kraftproduksjon/ (accessed Apr. 23, 2020).

[120] kundur, *kundur*. .

[121] T. Steihaug, "The Conjugate Gradient Method and Trust Regions in Large Scale Optimization," *SIAM J. Numer. Anal.*, vol. 20, no. 3, pp. 626–637, Jun. 1983, doi: 10.1137/0720042.

[122] R. H. Byrd, J. C. Gilbert, and J. Nocedal, "A trust region method based on interior point techniques for nonlinear programming," *Math. Program. Ser. B*, vol. 89, no. 1, pp. 149–185, 2000, doi: 10.1007/PL00011391.

[123] G. Hutchison *et al.*, "Frequency Based Emergency Disconnection Policy Review for the Nordic Region," no. June, Brussels, Belgium: ENTSO-E, 2017, pp. 1–75.

[124] D. Kraft and DFVLR-FB, *A software package for sequential quadratic programming*. Koln, Germany: DLR German Aerospace Center – Institute for Flight Mechanics, 1988.

[125] F. M. Gonzalez-Longatt, "Impact of emulated inertia from wind power on under-frequency protection schemes of future power systems," *J. Mod. Power Syst. Clean Energy*, vol. 4, no. 2, 2016, doi: 10.1007/s40565-015-0143-x.

[126] Y. R. Omar, I. Z. Abidin, S. Yusof, H. Hashim, and H. A. Abdul Rashid, "Under Frequency Load Shedding (UFLS): Principles and implementation," in *PECon2010 - 2010 IEEE International Conference on Power and Energy*, 2010, pp. 414–419, doi: 10.1109/PECON.2010.5697619.

[127] R. V. Fernandes, S. A. B. De Almeida, F. P. Maciel Barbosa, and R. Pestana, "Load shedding - Coordination between the Portuguese transmission grid and the distribution grid with minimization of loss of distributed generation," 2009, doi: 10.1109/PTC.2009.5282171.

[128] J. A. Laghari, H. Mokhlis, M. Karimi, A. H. Abu Bakar, and H. Mohamad, "A New Under-Frequency Load Shedding Technique Based on Combination of Fixed and Random Priority of Loads for Smart Grid Applications," *IEEE Trans. Power Syst.*, vol. 30, no. 5, pp. 2507–2515, Sep. 2015, doi: 10.1109/TPWRS.2014.2360520.

[129] K. U. Z. . Mollah, M. . Bahadornejad, and N. . Nair, "Automatic under-frequency load shedding in New Zealand power system — A systematic review - IEEE Conference Publication," 2011, Accessed: Sep. 28, 2020. [Online]. Available: https://ieeexplore.ieee.org/document/6102531.

[130] U. Rudez and R. Mihalic, "Dynamic analysis of transition into island conditions of Slovenian power system applying underfrequency load shedding scheme," 2009, doi: 10.1109/PTC.2009.5282175.

[131] P. Gupta, R. S. Bhatia, and D. K. Jain, "Active ROCOF Relay for Islanding Detection," *IEEE Trans. Power Deliv.*, vol. 32, no. 1, pp. 420–429, Feb. 2017, doi: 10.1109/TPWRD.2016.2540723.

[132] M. Sanaye-Pasand and H. Seyedi, "New centralised adaptive load-shedding algorithms to mitigate power system blackouts," *IET Gener. Transm. Distrib.*, vol. 3, no. 1, pp. 99–114, Jan. 2009, doi: 10.1049/iet-gtd:20080210.

[133] K. Mehrabi, S. Afsharnia, and S. Golshannavaz, "Toward a wide-area load shedding scheme: Adaptive determination of frequency threshold and shed load values," *Int. Trans. Electr. Energy Syst.*, vol. 28, no. 1, pp. 1–14, 2018, doi: 10.1002/etep.2470.

[134] U. Rudez and R. Mihalic, "WAMS-Based Underfrequency Load Shedding With Short-Term Frequency Prediction," *IEEE Trans. Power Deliv.*, vol. 31, no. 4, pp. 1912–1920, Aug. 2016, doi: 10.1109/TPWRD.2015.2503734.

[135] L. Shun, L. Qingfen, and W. Jiali, “Dynamic optimization of adaptive under-frequency load shedding based on WAMS,” in *Proceedings of 2016 IEEE Information Technology, Networking, Electronic and Automation Control Conference, ITNEC 2016*, Sep. 2016, pp. 920–926, doi: 10.1109/ITNEC.2016.7560496.

[136] C. T. Hsu, H. J. Chuang, and C. S. Chen, “Artificial neural network based adaptive load shedding for an industrial cogeneration facility,” 2008, doi: 10.1109/08IAS.2008.137.

[137] J. Yan, C. Li, and Y. Liu, “Adaptive load shedding method based on power imbalance estimated by ANN,” in *IEEE Region 10 Annual International Conference, Proceedings/TENCON*, Dec. 2017, vol. 2017-Decem, pp. 2996–2999, doi: 10.1109/TENCON.2017.8228375.

[138] X. Xu, H. Zhang, Y. Chai, F. Shi, Z. Li, and W. Li, “Trajectory sensitivity-based emergency load shedding optimal algorithm,” in *Proceedings of the 5th IEEE International Conference on Electric Utility Deregulation, Restructuring and Power Technologies, DRPT 2015*, Mar. 2015, pp. 1368–1372, doi: 10.1109/DRPT.2015.7432444.

[139] H. Mohamad, A. I. M. Isa, Z. M. Yasin, N. A. Salim, and N. N. A. M. Rahim, “Optimal load shedding technique for an islanding distribution system by using Particle Swarm Optimization,” in *3rd International Conference on Power Generation Systems and Renewable Energy Technologies, PGSRET 2017*, 2017, vol. 2018-Janua, pp. 154–158, doi: 10.1109/PGSRET.2017.8251819.

[140] X. Zhang, J. Ma, S. Yao, and R. Chen, “Optimization method of under frequency load shedding schemes for systems with high permeability new energy,” in *2019 4th International Conference on Intelligent Green Building and Smart Grid, IGBSG 2019*, 2019, pp. 577–580, doi: 10.1109/IGBSG.2019.8886196.

[141] H. H. Alhelou, M. E. Hamedani-Golshan, T. C. Njenda, and P. Siano, “Wide-area measurement system-based optimal multi-stage under-frequency load-shedding in interconnected smart power systems using evolutionary computing techniques,” *Appl. Sci.*, vol. 9, no. 3, p. 508, Feb. 2019, doi: 10.3390/app9030508.

[142] H. Haes Alhelou, M. E. Hamedani Golshan, T. C. Njenda, and N. D. Hatziargyriou, “An Overview of UFLS in Conventional, Modern, and Future Smart Power Systems: Challenges and Opportunities,” *Electr. Power Syst. Res.*, vol. 179, no. February 2019, p. 106054, 2020, doi: 10.1016/j.epsr.2019.106054.

[143] L. Sigrist, L. Rouco, and F. M. Echavarren, “A review of the state of the art of UFLS schemes for isolated power systems,” *Int. J. Electr. Power Energy Syst.*, vol. 99, no. September 2017, pp. 525–539, 2018, doi: 10.1016/j.ijepes.2018.01.052.

[144] A. A. Hafez, A. Y. Hatata, and A. Y. Abdelaziz, “Multi-Objective Particle Swarm for Optimal Load Shedding Remedy Strategies of Power System,” *Electr. Power Components Syst.*, vol. 47, no. 18, pp. 1651–1666, 2019, doi: 10.1080/15325008.2019.1689454.

[145] IEEE, *IEEE Std C37.117 - IEEE Guide for the Application of Protective Relays Used for*

Abnormal Frequency Load Shedding and Restoration, no. August. Piscataway, NJ, USA, 2007.

[146] Y. R. Omar, I. Z. Abidin, S. Yusof, H. Hashim, and H. A. Abdul Rashid, "Under Frequency Load Shedding (UFLS): Principles and implementation," in *PECon2010 - 2010 IEEE International Conference on Power and Energy*, 2010, pp. 414–419, doi: 10.1109/PECON.2010.5697619.

[147] F. Gonzalez-Longatt, F. Sanchez, and R. Leelaruji, "Unveiling the Character of the Frequency in Power Systems," in *2019 IEEE PES GTD Grand International Conference and Exposition Asia (GTD Asia)*, Mar., pp. 57–62, doi: 10.1109/GTDAsia.2019.8715972.

[148] H. H. Alhelou, M. E. Hamedani-Golshan, T. C. Njenda, and P. Siano, "A survey on power system blackout and cascading events: Research motivations and challenges," *Energies*, vol. 12, no. 4, 2019, doi: 10.3390/en12040682.

[149] S. Profileprojections, C. Generation, R. Energy, and C. Expansion, "Strategy for NAPSI Technical Assistance for Mongolia - RENEWABLE ENERGY CAPACITY EXPANSION PLAN," ADB: Mandaluyong, Philippines, 2018.

[150] Office of Electricity Delivery and Energy Reliability, "United States Electricity Industry Primer," 2015.

[151] P. Zummo, "America's Electricity Generation Capacity," 2021. Accessed: May 16, 2021. [Online]. Available: www.PublicPower.org.

[152] WECC, "Underfrequency Load Shedding Program Assessment Report," Utah, 2018.

[153] "PRC-006-SERC-02:Automatic Underfrequency Load Shedding Requirements - NERCipedia." https://nercipedia.com/active-standards/prc-006-serc-02automatic-underfrequency-load-shedding-requirements/ (accessed Jan. 25, 2020).

[154] "PRC-006-SERC-02:Automatic Underfrequency Load Shedding Requirements - NERCipedia." .

[155] IEEE, *IEEE Std C37.111 IEEE Guide for AC Generator Protection*, vol. 2006, no. February. IEEE: Piscataway, NJ, USA, 2013.

[156] IEEE, "IEEE Std C37.106. Guide for Abnormal Frequency Protection for Power Generating Plants," in *IEEE*, IEEE: Piscataway, NJ, USA, 2004, pp. 1–34.

[157] F. Biscani and D. Izzo, "esa/pagmo2: pagmo 2.14.0," 2019. https://zenodo.org/record/3697219 (accessed Mar. 13, 2020).

[158] M. A. Pai, *Energy Function Analysis for Power System Stability*. Springer US, 1989.

[159] P. Wall, F. Gonzalez-Longatt, and V. Terzija, "Estimation of generator inertia available during a disturbance," in *IEEE Power and Energy Society General Meeting 2012* , 2012,

pp. 1–8, doi: 10.1109/pesgm.2012.6344755.

[160] H. Seyedi and M. Sanaye-Pasand, “Design of New Load Shedding Special Protection Schemes for a Double Area Power System,” *Am. J. Appl. Sci.*, vol. 6, no. 2, pp. 317–327, Feb. 2009, doi: 10.3844/ajassp.2009.317.327.

[161] “Improved Harmony Search (IHS) — pagmo 2.15.0 documentation.” https://esa.github.io/pagmo2/docs/cpp/algorithms/ihs.html#_CPPv4N5pagmo3ihsE (accessed Mar. 13, 2020).

Attachments

Publication 1:

Optimal Frequency Support of Variable-Speed Hydropower Plants at Telemark and Vestfold, Norway: Future Scenarios of Nordic Power System.

M. N. Acosta, D. Pettersen, F. Gonzalez-Longatt, J. Peredo Argos, and M. A. Andrade, "Optimal Frequency Support of Variable-Speed Hydropower Plants at Telemark and Vestfold, Norway: Future Scenarios of Nordic Power System," *Energies*, vol. 13, no. 13, p. 3377, Jul. 2020, doi: 10.3390/en13133377.

energies

MDPI

Article

Optimal Frequency Support of Variable-Speed Hydropower Plants at Telemark and Vestfold, Norway: Future Scenarios of Nordic Power System

Martha N. Acosta [1,2], Daniel Pettersen [2], Francisco Gonzalez-Longatt [2,*], Jaime Peredo Argos [3] and Manuel A. Andrade [1]

[1] School of Mechanical and Electrical Engineering, Universidad Autónoma de Nuevo León, San Nicolás de los Garza 66455, NL, Mexico; martha.acostamnt@uanl.edu.mx (M.N.A.); manuel.andradest@uanl.edu.mx (M.A.A.)
[2] Department of Electrical Engineering, Information Technology and Cybernetics, University of South-Eastern Norway, 3918 Porsgrunn, Norway; 222496@student.usn.no
[3] Gamesa Electric, 39200 Cantabria, Spain; Jaime.peredo@siemensgamesa.com
* Correspondence: fglongatt@fglongatt.org

Received: 20 May 2020; Accepted: 19 June 2020; Published: 1 July 2020

Abstract: The integration of renewable resources is quickly growing in the Nordic power system (NPS), and it has led to increasing challenges for the operation and control of the NPS. Nordic countries require that the first-generation power plants have a more flexible operation regime to overcomes power imbalances coming from fluctuations of the demand and supply. This paper assesses optimal frequency support of variable-speed hydropower plants installed in Telemark and Vestfold, Norway, considering future scenarios of NPS. The total kinetic energy of the NPS is expected to be significantly reduced in the future. This paper looks into the implementation of hydropower units with a variable-speed operation regime and battery energy storage systems (BESS), equipped with fast-active power controller (FAPC) technology, to provide fast frequency response after a system frequency disturbance. The frequency support was formulated as an optimization process; therefore, the parameter of the FAPC was optimally calculated for future scenarios of low inertia in NPS. Three main futures scenarios were developed for technology penetration in the Vestfold and Telemark area in Norway. The simulation results showed that the integration variable-speed hydropower units and BESS technologies improved the frequency response even in low-kinetic energy scenarios.

Keywords: battery energy store system; converter-fed synchronous machine; doubly fed induction machine; fast active power injection controller; frequency control; frequency support; future Nordic power system; kinetic energy; variable-speed hydropower plants

1. Introduction

Close to 80% of the electricity produced the Nordic countries is already emission-free with hydropower alone representing half of all electricity generated in the region [1]. Hydroelectricity is a significant source of energy, mainly in Nordic countries, especially in Norway. The Norwegian hydropower system was developed over a period of more than 100 years; however, the substantial capacity of the hydropower plants was installed from the 1950s until the end of the 1980s [2]. Official figures indicate the installed capacity of the Norwegian power supply system was 33,755 MW(at the beginning of 2018) and normal annual production was 141 TWh [3,4]. In Sweden, most hydropower installations are from the 1950s and 1960s [2,4]. Installed hydropower capacity in Sweden was 16,506 MW in 2018 [3]. Many of those power plants installed in Nordic countries have reached an

age when upgrading and extension are needed, primarily because of the state of the mechanical and electrical equipment.

The modern power system is experiencing many changes. One of them is the increased volume of highly variable power generation coming from renewable resources like wind power and solar. As a consequence, the generation mix must be able to deliver a fast response in order to deal with the high variability of renewable sources. Thus, the pressure is on the traditional generation of power systems to adapt faster to variations in demand; this situation puts extra-stress on the traditional dispatchable resources such as conventional hydropower plants. The secure and economical operation of the modern power system requires the generation power plants to have a more flexible operation regime to keep the balance coming from the fluctuations coming from the demand and supply.

The majority of the hydropower plants in operation today are based in classical damp, and they are equipped with classic fixed-speed synchronous generators directly connected to the grid. They are carefully controlled in order to adapt to the system frequency (e.g., 50 Hz). This approach makes the operation regime as a constant speed operation where the speed of rotation is set by the optimal speed of the hydraulic machine. The traditional hydropower plants are based on generation units equipped with traditional Francis turbines; they are designed for a wide range of heads and flows. The conventional pump and storage power plants are equipped with reversible pump-turbines to have a runner with fixed geometry. In both cases, controlling the rotational speed and efficiency of the generation units at several regimes is not always possible, the hydraulic efficiency is high at the operating design point, but it drops when the operation is changed from this point at the fixed speed.

A more attractive option is to allow the hydraulic turbine to operate at an adjustable speed, as a consequence, enabling high efficiency at load level different to operating design point. From the operational point of view, the variable speed operation of the hydro turbine is very attractive because add the needed flexibility require to tackle the balancing challenges coming from the renewable generation. The variable speed of the hydraulic turbine offers many other benefits such as [4]: extending the life-time of the turbine by reducing the tear and wear of the mechanical elements of the hydraulic turbine. Also, it produces a substantial decrease in the number of starts and stops, yielding less runner fatigue damage. Moreover, it improves efficiency with significant variation in the head, at part load and with large discharge variations. Furthermore, a lower number of generation units are needed to handle substantial variations in discharge and improves the ability to control active power in pumping mode.

The installations of the hydropower plants were forced to change due to the integration of new technologies in the power system, new market requirements, and improved designs and materials. The combination of hydropower plants with a variable speed regime and a renewable resources, like wind power and solar, seem to be a solution to maintain the balance between the generation and the demand in the Nordic power system since it is expected that 90% of the electrical production coming from wind and hydropower in the year 2050. Moreover, there are several projects of exchange energy between Nordic countries and other countries in Europe. For instance, Norway has a plan to import the excess of wind-generation from Denmark and export hydro-generation back when wind power plants have low energy production, allowing Denmark 40% of its total production to come from renewable sources. Like this example, there are projects with Netherlands, Sweden, and Finland, and there are plans for a similar project with Germany and the UK [5].

The purpose of this research paper is evaluating the future of the Nordic power system in terms of frequency stability considering the predicted decrease of the total kinetic energy and the increase of the power demand in the forthcoming 20 years. The imminent dismissing of high inertia power plants (thermal and nuclear power plants) as well as the inclusion of more intermittent sources (wind and solar power plants) raises the need to evaluate the retrofit of the existing hydropower plants. Retrofitting the conventional hydropower plants by including variable speed regime using converter-fed synchronous machines and doubly fed induction machine is the most viable option for the Nordic power system, due to the high dependence on energy production coming from hydropower

plants that it will experience in the upcoming years and in addition to the capability to regulate the frequency and efficiency that these variable speed technologies offer. Furthermore, the installation of the battery energy storage system in the Nordic power system is considered, since it can provide fast frequency support, it can contribute to system inertia, and its costs have been decreasing in recent years. These three technologies are equipped with a frequency sensitive control that determines the amount of active power that will be delivered to face a frequency disturbance. It is of interest to evaluate how those technologies can improve the frequency response facing the decreasing kinetic energy when a disturbance occurs. To carried out this study a portion of the Norwegian power system was modelled in DIgSILENT® PowerFactory™, and a set of future scenarios were defined following the predicted changes on the Nordic power system in the next 20 years. The parameters of the frequency sensitivity control were optimized to provide optimal frequency support to the Nordic power system and enhance the frequency response. The improvement of the frequency response was evaluated by computing several frequency indicators.

The rest of this paper is organized as follows: Section 2 presents a detailed description of the pumped-storage hydropower plants and the variable-speed hydro plants. Section 3 introduces the principle of the battery energy storage system. Section 4 describes the frequency control optimization, its formulation and the frequency indicators. Section 5 is dedicated to present the future scenarios of the Nordic power system for the period 2020–2040. Section 6 presents the result of evaluating the defined future scenarios. Section 7 provides the main conclusions of this research paper.

2. Pumped-Storage Hydro Plants (PSHPs)

Hydropower has been a source of mechanical power since ancient times, used to grind flour but also for many other tasks. One of those tasks is producing electricity, and for this purpose, hydropower is used for four different approaches: conventional (dams), pumped-storage (PS), run-of-the-river (ROR), and tide. The conventional dams are the most widely used approach to hydropower production. Norway has more than 900 hydropower plants, and they provide nearly 96% of its electricity, making it the sixth-largest hydropower producer in the world. On the other hand, an opportunistic approach of using hydropower production is the so-called pumped hydro storage (PHS); it is the oldest technology for large-scale energy storage. Around 1392 MW of the total installed capacity (33,755 MW) in Norway are PHS, and there is more potential by retrofitting or updating the installed hydropower plants. The PHS uses a convenient and straightforward principle with two water reservoirs located at different altitudes; when water is released from the higher reservoir to the lower reservoir the kinetic energy of the water flow released is used by the hydro turbine and generator to produce electricity. There is the possibility of using electricity from the power grid to refill the higher reservoir by using the hydro turbine in pump operation mode.

2.1. Variable-Speed Operation of PSHP

Several types of runners are available for hydropower plant application: Pelton, Francis, and Kaplan. Traditionally, the hydropower units are optimally designed to operate a specific rotational speed, head, and discharge. Thus, a fixed speed operation regime allows only very limited deviations of head and discharge because of its geometry. The hydraulic turbine may reach its maximum efficiency of energy conversion, cavitation and vibration-free operation when working at rated conditions (rotational speed, head, and discharge). The hydraulic efficiency curve for fixed speed operation is designed so that the efficiency is highest at the best point for which the turbine is designed. Therefore, if the operating point is moved away from the best point, the efficiency drops. The Francis turbine type is one of the most flexible runners because it allows a wide variation of the operation discharge. However, changes in the head results in an extreme reduction on hydraulic efficiency and the variable speed operation can be particularly advantageous in Francis turbines with high specific speed (n_{qA}).

The steady-state operation of a hydraulic runner, such as the Francis turbine, is characterized by the rotational speed (n) and the discharge (Q):

$$n_{11} = \frac{nD}{\sqrt{H}} \tag{1}$$

$$Q_{11} = \frac{Q}{D^2\sqrt{H}} \tag{2}$$

where H is the nominal head (m), Q the rated discharge (m^3/sec), n the nominal speed (rpm), and D the runner diameter (m). The above equation can be used to create the topographic curves for a given turbine of pump–turbine working in turbine mode, also known as a Hill diagram (see Figure 1). For a typical Francis turbine, the efficiency hill chart is given in unit values n_{11}– Q_{11} where unit speed (n_{11}) and unit discharge (Q_{11}) are given in (1)–(2) and the unit power (P_{11}) is calculated as:

$$P_{11} = \frac{P}{D_1^2\sqrt{H^3}} \tag{3}$$

where P is the power input of the turbine (typically in MW).

The values n_{11} and Q_{11} lies close to the best point of operation ('bep' in Figure 1) that gives the best efficiency of the runner. Consider a hydraulic turbine working at the 'bep' ① and then the operating is shifted to ② (discharge and speed maintained but the head is reduced) as a consequence the efficiency drops from η_1 to η_2. Recovery to η_3 efficiency (③) is possible by reducing the speed to n_4, with further improvement possible (④,⑤) by decreasing the discharge (from Q_4 to Q_5).

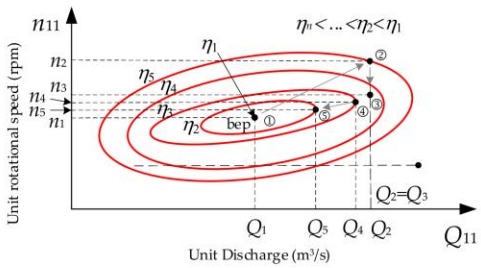

Figure 1. Hill diagram showing the topographic curves of efficiency for a pump–turbine operating in the turbine mode.

From the previous analysis, it is shown that the turbine efficiency is higher for variable speed operation than for fixed speed operation, but that the efficiency gain is smallest at the best point of operation at rated power and head. Some scientific publications have demonstrated that the hydraulic efficiency would be 3–10 percentage points higher for variable speed than for conventional operation [4,6].

Figure 2 shows representative hydraulic turbine efficiency curves over a range of head and power output for both single and adjustable speed units. From this figure, it is clear the hydraulic efficiency gain is most significant at low power outputs and low head [7,8]. There is some additional efficiency gain at operation above rated power and rated head, but the main benefits of variable speed operation are achieved at operation below the best point [4].

There are several advantages of the variable speed of the hydraulic turbines. However, traditional hydropower units are not designed to operate at variable speeds; in fact, they are designed and built to operate at a fixed speed to obtain a constant frequency by using a classical synchronous generator

directly connected to the power networks. The authors in Reference [6] found that by using a DC rather than an AC link, it was no longer necessary to tie the generator synchronously to the system frequency; in fact, the speed of the hydraulic turbine could be adjusted freely to satisfy the load demand at the maximum possible hydraulic efficiency. The results in Reference [6] indicated that in addition to an increased hydraulic turbine efficiency of a partial load, the efficiency of large synchronous machines operated with loads lower than the rated output power had been found to increase with variable speed operation [4,6]. At partial loading, down to 40% of rated power, the efficiency of the synchronous machine was found to increase by up to one percentage point [4].

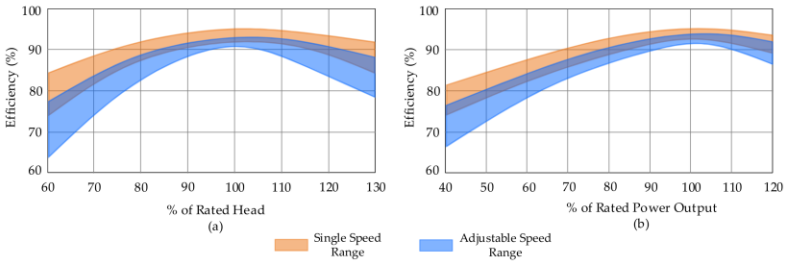

Figure 2. Hydraulic turbine efficiency (%) versus: (**a**) rated head (% of the rated value) and (**b**) rated power output (% of the rated output power), considering fixed-speed and variable-speed operation.

The first implementations of variable-speed technology started during the early 1990s, and it was mainly dedicated for *reversible pump-turbines* (RPTs) installed at pumped-storage power plants in Japan and Europe. Installations of this technology were recently done for pumped-storage projects in India and China [9], Slovenia [10], Japan [11], South Africa [12], and Switzerland [13].

2.2. *Generator Technologies for Variable-Speed Operation of PSHP*

The variable operation of the hydro turbine offers many advantages, and the majority of the generation technologies used to enable variable speed use of power electronics converters. Two technologies are the most used today to achieve the variable-speed operation conditions in hydropower units [14]:

- Doubly fed induction machines (DFIMs);
- Converter-fed synchronous machines (CFSMs).

The CFSM is recognized to have superior performance, but one crucial drawback to this technology is that it requires a fully rated power electronic converter (FRPEC), the use of a FRPEC implies a high-cost, and it is not suitable for high power levels. As a consequence, the DFIM results to be a more attractive option for variable-speed hydro turbines at high power levels applications, because the power electronic converter itself can be considerably smaller (size of converter ~10m^3/MVA [12]), as it is not rated to 100% of the generator capacity as in the CFSM.

2.2.1. Doubly Fed Induction Machines (DFIMs)

Doubly fed induction machines (DFIMs) have been used for many years in variable speed wind turbines, with a successful market share in modern wind farms. The DPIM for variable speed application has been proved, and it is a very mature option for the development of variable-speed hydropower units; in fact, this technology has been applied for pumped storage plants [14] with power ratings up to 400 MVA.

Figure 3 shows a general scheme of a DFIM used for a variable-speed hydro turbine. The DFIM is coupled to the hydro turbine, the DFIM stator is directly connected to the grid, while the rotor windings

are connected via a power electronic converter, using slip rings. The power electronic converter consists of a back-to-back converter, i.e., rotor side converter (RSC) and grid-side converter (GSC), which has a power rating on the partial scale of the DFIM rated power. The DFIM uses the exchange between the wound rotor and the power electronic converter to provide the speed variation. Therefore, the stator needs to be oversized in sub-synchronous mode, due to the additional power transiting from the rotor to the stator. The power electronic converter is rated to a lower than the generator capacity, as power just needed to feed the excitation, which is a function of the expected speed variation. The DFIM rotors typically have two to three times the number of turns of the stator, leading to a higher rotor voltage and lower current [15]. Doubly fed induction machine technology is generally the preferred solution for large unit outputs (>100 MW) [16].

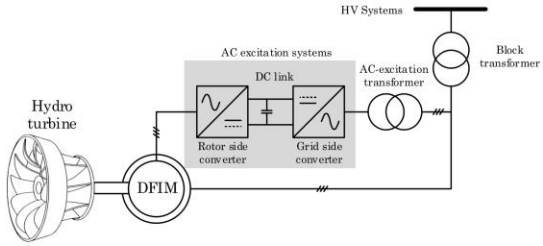

Figure 3. Schematic representation of asynchronous variable speed with doubly fed induction machines (DFIM) technology.

2.2.2. Converter-Fed Synchronous Machines (CFSMs)

Converter-fed synchronous machine (CFSM) technologies use a classical synchronous machine that is connected to the power system via a full-rated power electronic converter.

Figure 4 shows a general scheme of a CFSM used for a variable-speed hydro turbine. Typically, a back-to-back voltage source converter (VSC) is used to connect two AC sides using a DC link. The back-to-back power electronic converter allows decoupling the frequency of the synchronous machine from the AC grid, allowing a wide range of rotor speed and frequency variation. The generated variable frequency is converted into DC power before being inverted to AC power in a desired continuously frequency that is the synchronous frequency of the power system. As all generated power must pass through the power electronic converters, they must be rated to the full power of the generator with a relatively high cost, as a consequence, the application of the CFSM is limited to relatively low power ratings (<100 MW) [17]. Also, another important consideration of the CFSM is the space required to accommodate a new generation unit. Finally, another element to consider in the CFSM is the efficiency drops due to the losses in the back-to-back converter [17].

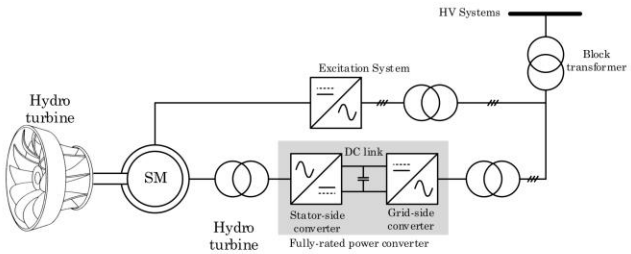

Figure 4. Schematic representation of synchronous variable speed with converter-fed synchronous machine (CFSM) technology.

3. Energy Storage System to Support Hydropower Sources in the NPS

Hydropower units have two main characteristics that have made them take a prominent role in the power system: are categorized as a renewable resource and have higher controllability compared to both wind and solar power. Moreover, hydropower turbines as today provide a natural inertial response. This characteristic is crucial for frequency control purposes, especially as the low inertia scenarios in the NPS, as caused by the decommissioning of high inertia power sources (nuclear, thermal) and the grown replacement by intermittent sources (wind, solar) with low inertia [18]. This paradigm change makes it necessary to introduce new technologies that can be used to give support and help to maintain system frequency. The use of energy storage systems (ESSs) has gotten a much more significant role to keep the balance in the power system by storing energy and converting it back when it is needed [19]. The global database for the Department of Energy (DOE based in USA), which was last updated 18th February 2020, shows that there are over 1600 ESSs projects in the world: 763 of battery energy storage system (BESS), 350 of pumped hydro storage, 53 of the flywheel, 29 of the supercapacitor, and the rest belong to another kind of ESSs [20]. Most of the projects are combined with wind or solar plants, but they could also be combined with hydropower generation units to increase the flexibility of the units. Of the technologies that are currently on the market, BESS seems to be the best suited to increase the stability of the system in cooperation with hydropower units because it offers very high efficiency and energy density, fast response and has long time life [21]. Therefore, in this research paper, BESS technology is integrated into combining with the variable speed technologies as an alternative to facing the dropping of system inertia in the future years.

Battery Energy Storage System

The battery energy storage system (BESS) follows a process of three main stages consisting of converting the electrical energy into another energy form, the storage of the transformed energy during a period of time, and the transformation of the stored energy into electrical energy again. Those three steps are related to three main subsystems [22]:

1. Power conversion system: this subsystem consists of an electrical or an electromechanical device that allows converting electrical energy;
2. Battery energy system: the principal element of this subsystem is an electromechanical energy storage technology (battery) to store/deliver the energy;
3. The controllers associated to the BESS: this subsystem has a set of controllers that can be divided into two categories: (i) fast inner controller is directly connected to the power conversion system and is related to the control of the converter's AC currents of the *dq*-axis, and (ii) slow outer controllers groups three controls *P*-*Q* control, fast active power control, and battery charge control.

4. Frequency Control Optimization

This section is dedicated to describing the frequency control considering the TSO/DSO iterations. Moreover, it is fully explained the fast-active power controller as a control strategy to provide fast frequency response to the power system. Finally, the frequency control optimization is the formulate based on the gain of the FAPC installed at the DFIM, CFSM, and BESS technologies to minimize the maximum frequency deviation following a system frequency disturbance.

4.1. Frequency Control and TSO/DSO Interactions

The increasing integration of intermittent power sources such as wind and solar plants has created an intrinsic uncertainty in the power balance between the production and the consumption of energy in the power system. This issue has limited the transmission systems operators (TSOs) operational capabilities, and the power system security has become dependent on the intermittent power sources available in the distribution network. To counteract the effects of low inertia, TSOs have resorted to the use of ESSs installed in the distribution network to provide fast frequency response (FFR) by absorbing

or injecting active power to the grid. Therefore, the interaction of the TSOs and the distribution system operators (DSOs) can help to balance the power supply and as a consequence has an effective frequency control [23].

The TSO/DSO interactions can be described considering a transmission system equipped with N_{SG} synchronous generators connected to N_{DS} distribution systems through sub-transmission networks which contains power transformers and protection equipment. After a power imbalance, in the primary frequency control period, the dynamic of the automatic voltage regulation and power system stabilizer can be overlooked, and the frequency dynamics can be written using the swing equation [24]:

$$\begin{array}{ll} \frac{2H_k}{\omega_0}\frac{dw_k}{dt} = P_{m,k} - P_{SG,k} - D_k(\omega_k - \omega_0) & \\ \frac{d\delta_k}{dt} = \omega_k - \omega_0 & \forall k = 1, 2, \ldots, N_{SG} \end{array} \tag{4}$$

where ω_k is the angular speed, D_k is the damping coefficient, H_k is the inertia constant, $P_{m,k}$ is the mechanical power, and $P_{SG,k}$ is the electrical power of the k-th synchronous generator. Moreover, ω_0 is the nominal angular speed.

Meanwhile, the FFR support to the TSO from the DSOs consider the contribution of the active power delivered by the ESSs installed in the grid. This paper considers three technologies that can provide FFR support to the power system: DFIM, CFSM, and BESS. The DSO is denoted by the network model of Vestfold and Telemark area in Norway connected to the TSO represented by the Nordic power system (NPS) equivalent. The total active power contributing to FFR (P_{FFRC}) can be written as:

$$P_{FFRC} = \sum_{i=1}^{N_{DFIM}} P_{DFIM,i} + \sum_{j=1}^{N_{CFSM}} P_{CFSM,j} + \sum_{k=1}^{N_{BESS}} P_{BESS,k} \quad \forall \begin{cases} i = 1, 2, \ldots N_{DFIM} \\ j = 1, 2, \ldots N_{CFSM} \\ k = 1, 2, \ldots N_{BESS} \end{cases} \tag{5}$$

where $P_{DFIM,i}$ represent the active power of the i-th DFIM, $P_{CFSM,j}$ is the active power of the j-th CFSM and $P_{BESS,k}$ is the active power of the k-th BESS.

4.2. Fast Active Power Controller (FAPC)

The natural resistance of the synchronous generator to angular acceleration after a disturbance comes from an inherent physical characteristic of its rotor, called inertia. This rotational inertia offers to damp to the frequency. The scientific literature presents several controllers trying to mimic the behavior of the synchronous generator by using power electronic converters (PECs). The main objective of the PECs-based controllers enabling FFR of the PEC by injecting/absorbing active power using the local measured frequency [25].

The fast-active power (FAP) controller is an FFR model that uses the frequency deviation to regulate the injection/absorption of the active power of the PEC. The FAP controller injects active power when the power system has an under-frequency condition, and it absorbs active power when the power system is facing an over frequency condition. Moreover, the energy available in the DC side of the PEC determinates its limits of operation. The FAP controller is able to deliver the fully active power in less than one second typically after measurement of frequency deviation [26]. According to the classical control theory, the FAP controller can be modelled implementing two strategies: proportional control action and derivative control action. The proportional control action approach is used in this paper.

The proportional control action is linear feedback control in which the controlled variable is adjusted by a gain that is proportional to the deviation of the measured value from the desired value. In the proportional FAP (PFAP) controller the controlled variable is the active power, the desired value is the nominal frequency (f_0), and the frequency deviation (Δf) is represented by the difference between f_0 and the local measured frequency (f). Moreover, the gain is the droop coefficient (K_d) of the ESS. Considering a dead band, saturation and that K_d can be varying between a range of values, i.e., $K_d \in [K_{d,min}, K_{d,max}]$, the power–frequency characteristic of the PFAP controller is shown in Figure 5.

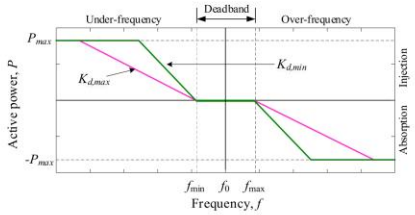

Figure 5. Power–frequency characteristic of the proportional fast active power (PFAP) controller.

Mathematically speaking, the PFAP controller is described as follows:

$$P = \begin{cases} K_p f & \text{absortion if } f > f_{max} \\ 0 & \text{not acting if } f_{\min} \le f \le f_{\max} \\ -K_p f & \text{injection if } f < f_{min} \end{cases} \quad (6)$$

4.3. Optimization of the System Frequency Response

The classical synchronous generator response to a power imbalance is defined by the amount of the kinetic energy stored on the rotating masses and the droop value used in the governors of the synchronous generators. These two variables influence the frequency response of the power system and therefore, the amount of active power provided by the generators to recover the balance between generation power and demand power. The imminent substitution of power plants based on synchronous generators by new technologies such as DFIM, CFSM rise the need to analyze the repercussions that they have on the frequency response. Since the DFIM, CFSM technologies are equipped with fast active power injection controllers, the frequency response of the power system can be substantially improved by the appropriate amount of active power contribution. Therefore, it is of utmost importance defining the correct settings of the droop coefficient (K_d) of the PFAP controller.

This section is dedicated to presenting the main frequency response characteristics and describing the optimization approach used to compute the optimal settings of the droop coefficients.

4.3.1. Frequency Response Indicators

The power system requires several control actions to maintain the balance between the power generation and the power demand, one of them is the primary response or primary frequency control. The primary response typically takes place within the first 10–30 s after a frequency event occurs, and it is very important since it acts to reduce de frequency deviation. The synchronous generators cannot restore a power imbalance instantaneously. Therefore, the KE stored in rotating masses acts in a small-time frame (typically less than 10 s) to arrest the frequency deviation, until the governor is activated. As a consequence, the primary response involves two processes: the inertial response and governor action, as shown in Figure 6. Due to the PFAP controllers are a sensitivity frequency control, the active power is delivered with a very short time-delay, and its rate of change can be proportional to the rate of change of frequency (see Figure 6b).

The main frequency response indicators are illustrated in Figure 6a and are defined following [27]:

- Minimum frequency (f_{min}): denotes the minimum value that the frequency reaches during the transient response after a frequency event. It is computed as the difference between the nominal frequency (f_0) and the maximum frequency deviation (Δf_{max}) during the transient response, i.e., $f_{min} = f_0 - \Delta f_{max}$.
- Minimum time (t_{min}): is the time at which the frequency reaches its minimum value (f_{min}) and its maximum deviation (Δf_{max}). The inertial response begins from the disturbance start (t_s) until the frequency reaches its minimum value at t_{min}; after that, the governor action initiates.

- Rate of Change of Frequency (*ROCOF*): represents the speed at which the frequency changes in one second, i.e., it is the time derivative of the frequency and it is described as $ROCOF = df/dt$ (Hz/s).
- Steady-state frequency (f_{ss}): is the value at which the frequency settle, typically is after the inertia response and the governor action, at this point, the *ROCOF* is zero. This indicator gives a measure of the ability of the power system to recuperate after a frequency event.

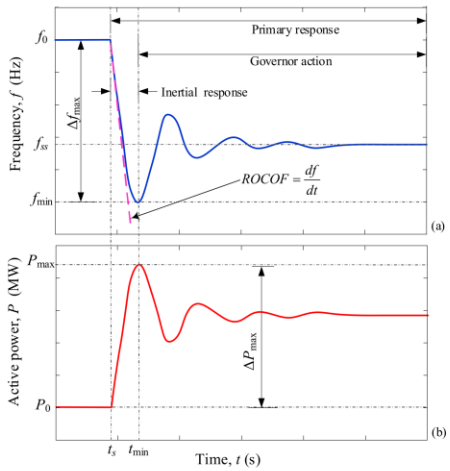

Figure 6. (**a**) frequency response and (**b**) active power contribution by the proportional fast active power (PFAP) controller of a power system after a frequency event.

4.3.2. Optimization Problem

The volume of active power delivered by PFAP controllers, to arrest the frequency decaying, depends on the K_d value. Therefore, the main objective is formulating the problem of determining the settings of K_d as an optimization problem which allows minimizing the maximum frequency deviation (Δf_{max}) by supplying the proper amount of active power.

Decision Variables

The optimization problem is formulated considering the technologies for variable speed operation (i.e., DFIM and CFSM) and the battery energy storage system (BESS). The droop coefficients of these three technologies were used as decision variables. The set of decision variables of each technology were vectorially expressed as:

$$\mathbf{K}_\alpha = \left[\begin{array}{ccccccc} K_{d,\alpha,1} & K_{d,\alpha,2} & \cdots & K_{d,\alpha,i} & \cdots & K_{d,\alpha,N_\alpha} \end{array} \right] \forall\, i = 1,2,\ldots N_\alpha \quad (7)$$

$$\mathbf{K}_\beta = \left[\begin{array}{ccccccc} K_{d,\beta,1} & K_{d,\beta,2} & \cdots & K_{d,\beta,j} & \cdots & K_{d,\beta,N_\beta} \end{array} \right] \forall\, j = 1,2,\ldots N_\beta \quad (8)$$

$$\mathbf{K}_\gamma = \left[\begin{array}{ccccccc} K_{d,\gamma,1} & K_{d,\gamma,2} & \cdots & K_{d,\gamma,k} & \cdots & K_{d,\gamma,N_\gamma} \end{array} \right] \forall\, k = 1,2,\ldots N_\gamma \quad (9)$$

where $K_{d,\alpha,i}$ is the droop coefficient of the i-th DFIM, $K_{d,\beta,j}$ is the droop coefficient of the j-th CFSM and $K_{d,\gamma,k,}$ is the droop coefficient of the k-th BESS. N_α, N_β, and N_γ is the number of DFIM, CFSM and BESS connected to the power system, respectively. Computing the optimal settings of K_d the active power injection by the PFAP controller is defined, and the frequency response can be improved.

Therefore, the decision variable vector ($\mathbf{x}$) is comprised of K_d of all technologies equipped with the PFAP controller (i.e., DFIM, CFSM, and BESS), and it is written as:

$$\mathbf{x} = \begin{bmatrix} \mathbf{K}_\alpha & \mathbf{K}_\beta & \mathbf{K}_\gamma \end{bmatrix}_{1\times(N_\alpha+N_\beta+N_\gamma)} \tag{10}$$

The decision variables were constricted by considering the upper and lower limits to maintain the setting values of the PFAP controllers inside realistic physical values. The upper and lower limits are defined as:

$$\begin{array}{c} \mathbf{K}_\alpha^{\mathrm{L}} < \mathbf{K}_\alpha < \mathbf{K}_\alpha^{\mathrm{U}} \\ \mathbf{K}_\beta^{\mathrm{L}} < \mathbf{K}_\beta < \mathbf{K}_\beta^{\mathrm{U}} \\ \mathbf{K}_\gamma^{\mathrm{L}} < \mathbf{K}_\gamma < \mathbf{K}_\gamma^{\mathrm{U}} \end{array} \tag{11}$$

where the superscripts L and U indicate the lower and upper bounds of the droop coefficients of DFIM ($\mathbf{K}_\alpha$), droop coefficients of CFSM ($\mathbf{K}_\beta$), and droop coefficients of BESS ($\mathbf{K}_\gamma$), respectively.

Objective Function

The constant change in the production of energy or its demand cause second-by-second small variations in the system's frequency. When a power imbalance occurs (generally caused by the sudden increase of demand or an outage of single/multiple generation units) the system frequency decrease. The depth to which the system frequency drops (f_{min}) depends on the amount of the kinetic energy stored on the synchronous generators. If the frequency falls too low, the under-frequency relays may be activated the load shedding to arrest the frequency decaying and recover the frequency. To avoid the activation of the under-frequency protections and, therefore, the unnecessary disconnection of loads, it is essential to limit the drops of the frequency by minimizing the maximum frequency deviation (Δf_{max}).

As it was intended to minimize the maximum frequency deviation regardless of where in the system the disturbance occurs, the frequency of the power system was represented adopting the concept of center of inertia (COI). The frequency of the center of inertia (f_{COI}) was computed as the inertia weighted average of the frequencies of all generators connected to the power system. Mathematically speaking, f_{COI} is written as [22]:

$$f_{COI} = \frac{\sum_{i=1}^{N_G} H_i f_i}{H_{\mathrm{T}}} \tag{12}$$

where H_i and f_i are the inertia constant and frequency of the i-th generator, respectively. H_{T} is the total system inertia computed as $\sum_{i=1}^{N_G} H_i$ and N_G is the number of generators connected to the power system.

The objective function to minimize the maximum frequency deviation of the center of inertia ($\Delta f_{COI,\,max}$) is written as:

$$\min_{\mathbf{x}}[f(\mathbf{x})] = \min_{\mathbf{x}}[\Delta f_{COI,\max}(\mathbf{x})] = \left|f_0 - f_{COI\min}\right| \tag{13}$$

5. Defining of Future Scenarios

This section is dedicated to defining a series of possible scenarios for the integration of DFIM, CFSM, and BESS technologies. The future scenarios were constructed taking into account the technological advances that would have been done in the most recent years, the market/policies of today, and the future Nordic power system.

5.1. Nordic Power System (NPS)

The Nordic power system (NPS) is the synchronous power system that spans the four countries of Denmark, Finland, Norway and Sweden. No significant changes in the installed capacity of hydropower in the NPS were expected, but there was a shift from the use of conventional power sources, such as

thermal power and nuclear power, to more intermittent sources [2]. Table 1 shows an overview of the expected variations in the production of wind, thermal, and nuclear power in the interval from 2020 to 2040.

Table 1. Power generation in the NPS in the period 2020–2040 [2].

Source	2020 (GW)	2030 (GW)	2040 (GW)	Change 2020–2040 (%)
Wind	20	30	45	+125
Thermal	8	5	3.5	−56
Nuclear	12	10.5	2.5	−79

Table 1 shows that the majority of the nuclear power in the NPS will be decommissioned before 2040 and that the reduction in nuclear power will be compensated by an increase in wind power. The wind turbines will not be placed in the same location as the nuclear power plants, and this will change the layout and composition NPS in the future. The NPS will have a more significant percentage of intermittent power sources that is located further from the loads, which will put a more significant strain on the transmission grid.

The load is estimated to increase in the coming years, and they estimate that it will reach a peak load of 79 GW in 2040, the relationship between the estimated production and consumption in the NPS in the coming years is shown in Figure 7.

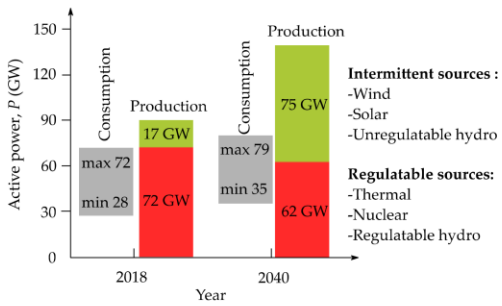

Figure 7. Production and consumption in the NPS (2018) and forecast by 2040 [3].

Figure 7 shows that it is estimated that the peak consumption in the NPS will exceed the installed capacity of regulated power production. This means that the NPS will be reliant on the intermittent power production and imports, to ensure the system stability, and prevent the need for load shedding. This will also make it very important that the regulated power production is flexible so that it can be used to keep the system stability.

A report carried out in 2016 by the Nordic TSOs highlights five key subjects as the main future challenges for the Nordic grid [4]:

- System flexibility;
- Generation adequacy;
- Frequency quality;
- System inertia;
- Transmission adequacy.

The main causes of these issues are the transition to a more electrified society (system flexibility, generation, and transmission adequacy), the decommission of nuclear power and greater penetration of wind and solar (system inertia, generation and transmission adequacy) and the overall decrease in

the system inertia (frequency quality and system inertia). These issues led the Swedish TSO to carry out a survey, which looked on the future market situation until 2040 for the NPS, which included their estimation of the future development of the system inertia, which is shown in Figure 8.

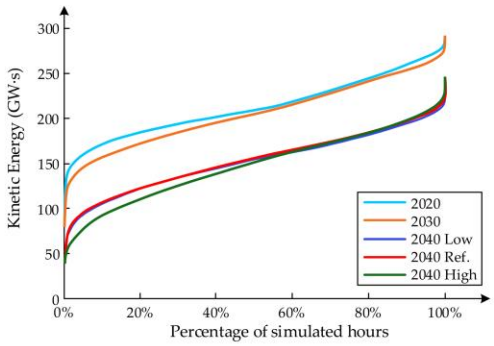

Figure 8. System inertia in the NPS for the period 2020–2040 [5].

Figure 8 shows that the inertia in the NPS will decrease gradually over the next couple of decades. One important factor for the year 2020 is the low inertia situations is presented in periods with a low load in the NPS, in contrast, for the year 2040, a portion of the low inertia condition is produced at hours with a high system load.

This also shows that it is necessary to introduce new sources of system inertia, to replace the high inertia sources that are planned to be decommissioned in the next 20 years. This is required to ensure that the system inertia does not reach a critically low level, which will lower the frequency quality and make the system vulnerable for fault situations. Another major factor that has to be considered is that Sweden is planning to decommission all of its Nuclear power production in the next 20–30 years. This means that the rotational inertia of the NPS is considered to decrease in the same time period, as the nuclear powerplants are getting decommissioned. The estimated rotational inertia that will be used in the simulation is shown in Table 2, and the values are taken from Figure 8.

Table 2. Rotational energy in the NPS (GW·s) for the period 2020–2040.

Level	2020	2030	2040
High	260	255	190
Low	174	159	105

The peak load of the NPS is expected to increase in the simulation period to around 79 GW in 2040. The estimated load for the simulation period 2020–2040 is shown in Table 3, and it is estimated from Figure 7.

Table 3. System load of the NPS (GW) for the period 2020–2040.

Level	2020	2030	2040
High	72.6	75.8	79
Low	28.6	31.8	35

5.2. Future Scenarios

The major waterways in the NPS are already used for hydropower production or are considered as natural reserves, so it is not expected that there will be built out any new big hydropower plants in the

100MW class in the near future. Therefore, the most significant evolution in the hydropower production in the NPS will be the reinvestment or expansion of already existing powerplants. This reinvestment or expansion can vary from a reduction the friction of the shafts to increase the overall efficiency of the plant, to overhauling the complete powerplant, which includes building a new power station with the state-of-the-art control units and turbines. The decrease of rotational energy and the increase of the general load is decreasing the overall system stability, and this means that the system gets more vulnerable for disturbances. The scenarios in this paper will look into the impact of introducing hydropower generation units with a variable speed operation regime and battery energy storage systems on system stability.

The scenarios are built considering ten-year interval at 2020, 2030 and 2040. Each ten-year interval considers three main scenarios:

- Scenario 0: This scenario considers only the maintenance action of the existing hydropower units in the system. Therefore, new types of technologies are not integrated into the system; the purpose of this scenario is observing the performance of the NPS to a disturbance with the existing conventional power plants based on synchronous generators any other technology is assumed to be no frequency sensible.
- Scenario 1: In this scenario, some significant hydropower generation (greater than 100 MW) will be replaced with DFIM units and medium hydropower generation units (less than 100 MW) will be substituted with CFSM units. This will be done in two intervals: three units will be replaced in the year 2030, and an additional four will be replaced in the year 2040. This scenario will mainly focus on looking into how the implementation of variable-speed hydro will impact the overall system frequency stability.
- Scenario 2: This scenario follows the same pattern as Scenario 1, but also it will include the installation of five BESSs, one will be introduced in the year 2030, and the remaining four will be implemented in the year 2040. This scenario investigates the benefits related to the system stability installing BESS in the NPS.

The scenarios defined above will be focused on the case of the low rotational energy since it represents the critical operation of the NPS.

5.2.1. Year 2020

For the year 2020, the model is used as it is, without any changes to the NPS model. This year will be used as a reference point, to see how the future scenarios will compare to the current state of the NPS. Therefore, only Scenario 0 will be performed considering the amount of low rotational energy established for this year in Table 2.

5.2.2. Year 2030

The year 2030 will experience a slight drop in rotational energy, as the most significant drop of rotational energy is expected to happen in the interval 2030–2040, as the Swedish nuclear powerplants will be decommissioned because of old age. Therefore, it is not expected to be any major changes in the stability of the NPS in this year. The DFIM technologies are expected to be the dominant solution with variable-speed hydro for high power applications, so any big powerplants over 100 MW will be built with the use of DFIM, while smaller powerplants under 100 MW will use CFSM technologies as the preferred solution. The battery energy storage system could still be considered as too expensive to be implemented in the NPS, because of the low power prices, but it could be possible that there will be implemented a demo installation of batteries at one of the smaller hydropower plants, to see how it can be implemented in the NPS in the future.

Scenario 0

For this scenario is it only expected to be done maintenance and retrofitting to a level that all the power stations have the same capabilities as they have in today's NPS. The total kinetic energy of the NPS decreases 8.62% concerning the year 2020, taking a value of 159 GW·s.

Scenario 1

In this scenario, the total kinetic energy is the same as Scenario 0, but there will be introduced variable speed capabilities at three of the systems powerplants. Two powerplants over 100 MW, are replaced with DFIM technology and one medium-sized hydropower generation unit will be substituted with CFSM. The total production capacity of variable-speed hydropower plants installed in the NPS is 374 MVA. The location of the different varied speed installations in the model are summarized in Table 4.

Table 4. Varied speed installations in the NPS model in the year 2030.

Power Station	Installed Capacity (MVA)	New Technology
Såheim	189	DFIM
Hjartdøla	130	DFIM
Fjone	55	CFSM

Scenario 2

Scenario 2 will follow the same pattern as Scenario 1 when it comes to the changes on the powerplants, but there will also be installed a BESS at busbar to one of the powerplants, to help with system support. The location and size of the BESS in the NPS model are shown in Table 5.

Table 5. Battery installations in the NPS model in the year 2030.

Power Station	Installed Capacity of the Plant [MVA]	BESS Capacity (MVAh)
Fjone	38	55

5.2.3. Year 2040

The NPS will experience a significant drop in the total kinetic energy in the year 2040 due to the expected decommission of the Swedish nuclear powerplants. In this ten-year interval, the peak consumption will exceed the installed capacity of regulated power in the NPS. As a consequence, the NPS will be more dependent on a more flexible power supply from the regulatable power sources, to keep a stable system frequency and it will also require the introduction of synthetic inertia to ensure a satisfactory level of inertia in the system.

CFSM will become the dominant technology of variable-speed hydropower plants when it comes to power applications less than 100 MW. It is also expected that BESS declining in price, so it could be even more attractive to be used as system support in the NPS.

Scenario 0

Year 2040 will experience a reduction of the total kinetic energy of the NPS around 39.66% regarding the year 2020, taking a value of 105 GW·s. In this scenario, it is only expected to be done maintenance and retrofitting to a level that all the power stations have the same capabilities as they have in today's NPS.

Scenario 1

In the year 2040, in addition to the three powerplants already installed in the year 2030 two DFIM (Såheim and Hjartdøla) and one CFSM (Fjone), it will be retrofitted four powerplants with

varied speed hydro. From the four powerplants retrofitted, one powerplant over 100 MW is replaced with DFIM technology, and three medium-sized hydropower are substituted with CFSM since it is expected that CFSM will be the dominating technology on the market at this time. The total number of variable-speed hydropower plants installed in the NPS is seven, and its total capacity is 794 MVA. Summarization of all the varied speed hydro installations in the NPS model is shown in Table 6.

Table 6. Varied speed installations in the NPS model in the year 2040.

Power Station	Installed Capacity (MVA)	New Technology
Såheim	189	DFIM
Hjartdøla	130	DFIM
Mår	190	DFIM
Fjone	55	CFSM
Mæl	38	CFSM
Skollenborg	99	CFSM
Svelgfoss	93	CFSM

Scenario 2

Scenario 2 considered the same powerplants retrofitted as in Scenario 1, with the same type of technology choice. In this scenario, in addition to the BESS installed in the year 2030 (Fjone), it will also be introduced four BESS in different sizes, providing a total of 275 MVA. The location and capacity of all the installed BESS are shown in Table 7.

Table 7. Battery installation in the NPS model in the year 2040.

Power Station	Installed Capacity of the Plant (MVA)	BESS Capacity (MVAh)
Fjone	38	55
Mæl	38	38
Fritzøe	7	7
Skollenborg	99	99
Svelgfoss	93	93

6. Simulation and Results

6.1. Vestfold and Telemark System

The authors of this research paper developed a network model of the Vestfold and Telemark area in Norway using data publicly available; as a consequence, the model may have discrepancies to the real model. The network model represents the 132 kV network in the geographical area of Vestfold and Telemark interconnected to the Norwegian power system at 420 kV and 300 kV. The network consists of 109 busbars from 11 kV (generation voltage level) up to 420 kV and the total active power demand in the regional system is P_d = 1643 MW divided between 58 different lumped loads in varying sizes, from 16 MW and up to 62 MW. The total installed capacity in the regional network is P_G = 1083 MVA divided between 20 hydropower generation units (from 2.3 MVA up to 190 MVA). The Vestfold and Telemark network imports P_{tie} = 560 MW from the Norwegian power system to cover the total power demand. Figure 9 shows a geographical representation of the Vestfold and Telemark power system, where the green areas represent the loads and the red areas represent the hydropower generation units.

The scenarios defined in the previous section are assessed considering a frequency disturbance applied to the power system at t = 0 s and observing the indicators of the frequency of the centre of inertia (f_{COI}): maximum frequency deviation ($\Delta f_{COI,\,max}$), minimum frequency ($f_{COI,\,min}$), minimum time ($t_{COI,\,min}$), the maximum rate of change of frequency ($ROCOF_{COI,\,max}$), and steady-state frequency ($f_{COI,\,ss}$). The frequency disturbance is defined as the sudden disconnection of a large generation unit ΔP = 1300 MW.

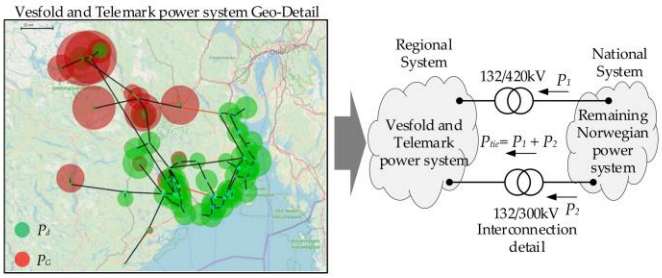

Figure 9. Geographical representation of the Vestfold and Telemark power system.

The under-frequency scheme of the Nordic power system is implemented to operate in a mandatory range, starting at a frequency level of 48.7–48.8 Hz until a final frequency level of 48 Hz [28]. Therefore, the minimum frequency ($f_{COI,\,min}$) should not reach values below 48.7 Hz to avoid the trigger of the under-frequency relay, and it can be done by the implementation of the DFIM, CFSM, and BESS technologies.

The described power is modelled in DIgSILENT®® PowerFactory™ version 2020 to assess the performance of the system frequency response, a closed-loop framework using Python is used to automatize simulation during the optimization purpose. The optimization procedure was performed using the Sequential Least SQuares Programming method [29]. The simulation process consists of time-domain simulations using RMS values from DIgSILENT®® PowerFactory™ to obtain the frequency response of Vestfold and Telemark power system. The total simulation time is 150 s since this timescale is adequate to replicate the phenomenon related to the electromechanical variables. Moreover, Scenario 0, Scenario 1, and Scenario 2 of each ten-year interval were used to assess the performance of the frequency response considering the effect of the DFIM, CFSM and BESS technologies.

6.2. Base Case: Scenario 0

Scenario 0 denotes the outlook at which the NPS does not create any changes on the hydropower plants thought the 2020–2040 period; the only maintenance is carried out on the hydropower plants. However, during the 2020–2040 period, the NPS suffers a decreasing of the total kinetic energy of 8.62% and 39.66% regarding the year 2020, respectively. The decreases in the kinetic energy produce a deterioration in the frequency response after being inserted a frequency disturbance (ΔP = 1300 MW at t = 0 s) as shown in Figure 10.

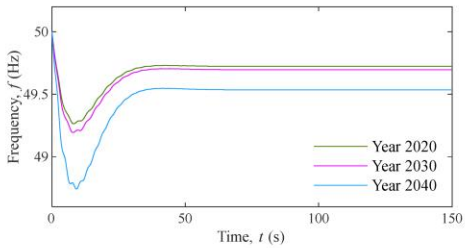

Figure 10. Comparison of the frequency response for decreasing the kinetic energy in the period 2020–2040 on Scenario 0.

Although the frequency is recovered after a few seconds and the power system remains stable on the three ten-year intervals (2020, 2030, and 2040), the frequency indicators are several affected

by the decreasing of the kinetic energy as described in Table 8. As the kinetic energy decreases, the frequency minimum ($f_{COI,\,min}$) reaches its deepest values and, as a consequence, the maximum frequency deviation ($\Delta f_{COI,\,max}$) grows. Moreover, the speed at which the frequency falls in the year 2040 (i.e., the maximum *ROCOF* ($ROCOF_{COI,\,max}$)) increases by approximately 41.5% concerning the year 2020. The deteriorating of these indicators is directly related to the inertial response since the synchronous generators do not have enough energy stored on its rotating masses to try to arrest the frequency drop.

Table 8. Summary of frequency response indicators for Scenario 0: the year 2020, 2030, and 2040.

Year	Total Kinetic Energy (GW·s)	$\Delta f_{COI,\,max}$ (Hz)	$f_{COI,\,min}$ (Hz)	t_{min} (s)	$ROCOF_{COI,\,max}$ (Hz/s)	$f_{COI,\,ss}$ (Hz)
2020	174	0.738	49.265	8.132	−0.186	49.723
2030	159	0.806	49.194	7.912	−0.204	49.697
2040	105	1.258	48.742	9.182	−0.318	49.536

From the results of Table 8, it is necessary to include other technologies that can provide frequency support, especially in the year 2040, where the grates drop of inertia occurs. In the year 2040, $f_{COI,\,min}$ reaches values that are on the under-frequency load shedding operation zone, and it can produce the activation of the under-frequency relays and start an unnecessary load shedding or even worst produce an instability condition.

6.3. Optimized Response: Scenario 1 and Scenario 2

This section is dedicated to assessing the solution of the objective function formulated in (13), which the primary purpose is minimizing the maximum frequency deviation of the frequency of the centre of inertia ($\Delta f_{COI,\,max}$) and compute the optimal settings of the droop coefficients of the DFIM ($K_{d,\alpha}$), CFSM ($K_{d,\beta}$) and BESS ($K_{d,\gamma,k}$) technologies. In this stage, Scenario 1 and Scenario 2 are evaluated, Scenario 1 denotes the perspective of substituting several big and medium hydropower plants by DFIM and CFSM technologies, respectively. Meanwhile, Scenario 2 considers replacing big and medium hydropower plants with DFIM and CFSM technologies and additionally install several BESS at a key point of the NPS.

6.3.1. Year 2030

For this year, the objective function defined in (13) is evaluated to compute the optimal droop coefficients ($K_{d,\alpha}$, $K_{d,\beta}$ and $K_{d,\gamma}$) of Scenario 1 and Scenario 2. The optimization solution is presented in Table 9.

Table 9. Optimal droop coefficients ($K_{d,\alpha}$, $K_{d,\beta}$ and $K_{d,\gamma}$) of Scenario 1 and Scenario 2 in the year 2030.

Power Station	Technology	Scenario 1	Scenario 2
Såheim	DFIM	0.0001	0.0001
Hjartdøla	DFIM	0.0072	0.0001
Fjone	CFSM	0.052	0.0001
Fjone	BESS	-	0.0001

The optimal coefficients obtained from the optimization are used to set the parameters of the PFAP controllers, and system frequency is evaluated by inserting a frequency disturbance of ΔP = 1300 MW at t = 0 s. The frequency response of Scenario 0, Scenario 1, and Scenario 2 is shown in Figure 11.

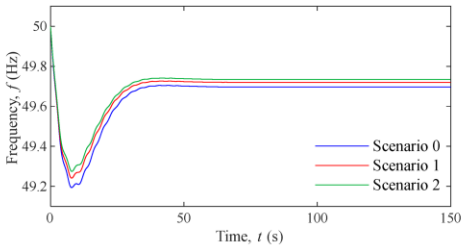

Figure 11. Frequency response after inserting a frequency disturbance of ΔP = 1300 MW at t = 0 s with a total kinetic energy of 159 GW.s.

From Figure 11, it is evident that the frequency response was improved by the inclusion of DFIM and CFSM technologies for Scenario 1 regarding Scenario 0. Moreover, in Scenario 2, the frequency response was enhanced concerning Scenario 1 due to the inclusion of BESS. The improvement of the frequency response in Scenarios 1 and Scenario 2 was mainly related to the fast action of the PFAP controllers, since those controllers deliver the proper amount of active power to stop the frequency deviation. The total active power contribution of the power plants to the disturbance is presented in Figure 12.

The frequency response indicators of the three scenarios assessed in the year 2030 are depicted in Table 10. this table, it is possible to observe that the optimized PFAP controller can improve the frequency response indicators concerning Scenario 0, even when the total kinetic energy decreased regarding the year 2020.

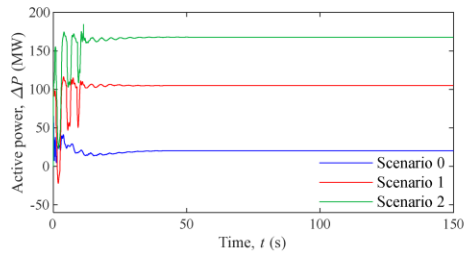

Figure 12. Total active power contribution of synchronous generators (Scenario 0), synchronous generators, DFIM and CFSM (Scenario 1) and synchronous generators, DFIM, CFSM and BESS (Scenario 2) in the year 2030.

Table 10. Frequency response indicators of Scenario 0, Scenario 1 and Scenario 2 in the year 2030.

Scenario	$\Delta f_{COI,\,max}$ (Hz)	$f_{COI,\,min}$ (Hz)	t_{min} (s)	$ROCOF_{COI,\,max}$ (Hz/s)	$f_{COI,\,ss}$ (Hz)
0	0.806	49.194	7.912	−0.204	49.697
1	0.759	49.241	7.912	−0.195	49.720
2	0725	49.275	7.995	−0.196	49.734

Figure 13 presents the minimum frequency ($f_{\min}$) and the maximum ROCOF that the synchronous generator experiences in Scenario 1 and Scenario 2. This figure shows that the inclusion of BESS makes that $f_{\min}$ of all synchronous generators connected to the NPS reduces and the maximum *ROCOF* has a slight decrease.

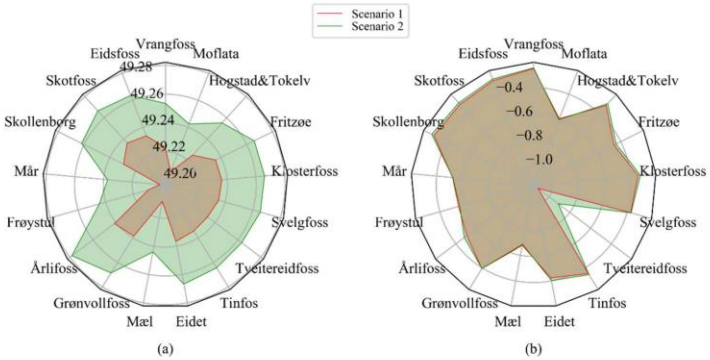

Figure 13. Frequency indicators of the synchronous generators in operation for Scenario 1 and Scenario 2 of the year 2030: (**a**) minimum frequency (f_{min}) and (**b**) Maximum *ROCOF*.

6.3.2. Year 2040

The year 2040 is critical due to the fact that it experience a substantial decrease in total kinetic energy (around 39.66% regarding the year 2020), and it produces that the minimum frequency reaches values inside the operation zone of the under-frequency loads shedding. For this year, the objective function defined in (13) is evaluated to compute the optimal droop coefficients ($K_{d,\alpha}$, $K_{d,\beta}$ and $K_{d,\gamma}$) of Scenario 1 and Scenario 2 and the optimization solution is presented in Table 11.

Table 11. Optimal droop coefficients ($K_{d,\alpha}$, $K_{d,\beta}$ and $K_{d,\gamma}$) of Scenario 1 and Scenario 2 in the year 2040.

Power Station	Technology	Scenario 1	Scenario 2
Såheim	DFIM	0.0001	0.0001
Hjartdøla	DFIM	0.0975	0.0001
Mår	DFIM	0.0001	0.0001
Fjone	CFSM	0.0126	0.0001
Mæl	CFSM	0.0001	0.0001
Skollenborg	CFSM	0.0152	0.0001
Svelgfoss	CFSM	0.0298	0.0001
Fjone	BESS	-	0.0001
Mæl	BESS	-	0.0001
Fritzøe	BESS	-	0.0001
Skollenborg	BESS	-	0.0001
Svelgfoss	BESS	-	0.0001

The optimal coefficients obtained from the optimization were used to set the parameters of the PFAP controllers, and the system frequency was evaluated by inserting a frequency disturbance of ΔP = 1300 MW at t = 0 s. Figure 14 depicts the frequency response of the Scenario 0, Scenario 1 and Scenario 2. In this figure, it can be observed that Scenario 1 and Scenario 2 presents an improvement in the frequency response compared with Scenario 0. Moreover, in Scenario 2, the minimum frequency significantly decreases in comparison with Scenario 1. The slight drop of frequency, around 80 s in Scenario 2, was produced by the discharge of the BESS, they already delivered the active power to arrest the frequency decline and to reduce the minimum frequency, and then start the charging process. This process is clearly shown in Figure 15, where the total contribution of active power is shown.

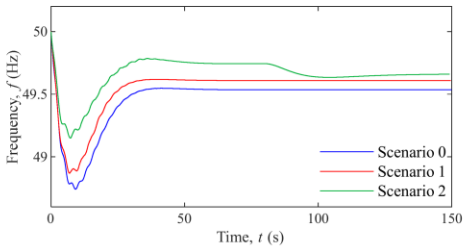

Figure 14. Frequency response after inserting a frequency disturbance of ΔP = 1300MW at t = 0 s, with a total kinetic energy of 105 GW.s.

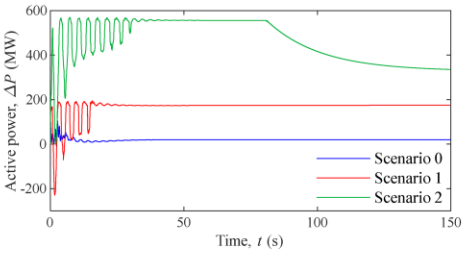

Figure 15. Total active power contribution of synchronous generators (Scenario 0), synchronous generators, DFIM and CFSM (Scenario 1) and synchronous generators, DFIM, CFSM and BESS (Scenario 2) in the year 2040.

Table 12 presents the frequency response indicators of the three scenarios assessed in the year 2040. From this table, the Scenario 1 and Scenario 2 shows that the optimal parameters of PFAP controller can significantly enhance the frequency response indicators concerning to Scenario 0 to face an important decreasing in the total kinetic energy, as considered in the year 2040. The installation of variable-speed hydropower technologies in the NPS allows reducing the minimum frequency of 0.127 Hz and the maximum *ROCOF* 0.036 Hz/s moving the frequency out of the under-frequency load shedding operation zone. However, the minimum frequency value remains near to the under-frequency load shedding operation zone. Scenario 2, which includes the installation of BESS, present a significant diminution of the maximum frequency deviation of 0.408 Hz, which places the minimum frequency outside the zone of the under-frequency load shedding activation. The maximum *ROCOF*, as well as the steady-state frequency, are improved.

Table 12. Frequency response indicators of Scenario 0, Scenario 1 and Scenario 2 in the year 2040.

Scenario	$\Delta f_{COI,\,max}$ (Hz)	$f_{COI,\,min}$ (Hz)	t_{min} (s)	$ROCOF_{COI,\,max}$ (Hz/s)	$f_{COI,\,ss}$ (Hz)
0	1.258	48.742	9.182	−0.318	49.536
1	1.131	48.869	6.905	−0.282	49.609
2	0.850	49.150	7.223	−0.274	49.660

Figure 16 shows that the minimum frequency and the maximum *ROCOF* of the synchronous generators connected to the NPS are substantially improved with the inclusion of BESS as frequency support.

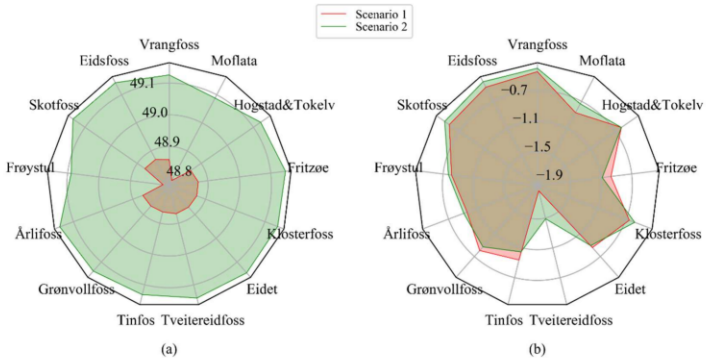

Figure 16. Frequency indicators of the synchronous generator in operation for Scenario 1 and Scenario 2 of the year 2040: (**a**) minimum frequency (f_{min}) and (**b**) Maximum *ROCOF*.

Due to the converter decouples DFIM, CFSM, and BESS technologies from the source (the primary source had enough energy to cope with the frequency support) they were the same in the sense of active power delivery, and the optimal droop coefficients ($K_{d,\alpha}$, $K_{d,\beta}$, and $K_{d,\gamma}$) of the PFAP controller are computed based on the active power available to deliver and the frequency deviation. Therefore, the optimal droop coefficients obtained from the optimization process for Scenario 2 indicates that DFIM, CFSM and BESS have the same rate to deliver the active power, i.e., the droop coefficients forces the source to deliver the active power at the maximum rate (0.001) in order to provide a quick active power response and avoid the frequency drops below 48.7 Hz.

7. Conclusions

The simulation results show that retrofitting the conventional hydropower plants by incorporating variable-speed technologies in the upcoming years will allow dealing with the problem of increasing renewable sources and the decreasing of the system inertia in the NPS. In the future, the hydropower units will require to be more flexible, and this flexibility can be reached by the incorporation of variable speed technologies, which provide more efficient than conventional hydropower units when the generation units are producing outside its rated head/output values.

The approaches presented in this paper demonstrates the positive benefits of incorporating the doubly fed induction machine, converter-fed synchronous machine and battery energy storage system technologies as a reliable tool to ensure the frequency stability of the NPS in the perspective of disconnection of several thermal and nuclear power plants and therefore low levels of kinetic energy. The doubly fed induction machine and converter-fed synchronous machine technologies shown superior performance compared with the synchronous generators since those technologies can modify the active power depending on the speed variation range and therefore, resulting in a high ability to regulate the frequency especially in scenarios of low kinetic energy. Moreover, the incorporation of the battery energy storage system provides frequency support by supplying fast active power, covering the lack of active power, especially in scenarios of great inertia reduction such in the year 2040.

The optimization of the parameters of the PFAP controller allows for providing the optimal amount of active power to recover the frequency deviation. Furthermore, the optimal values of the droop coefficients allow stopping the frequency de decaying and avoid the under-frequency load shedding relays activation. In addition, the formulation to optimize the droop coefficients permit limited the minimum frequency and therefore, substantially improved the frequency response indicators when doubly fed induction machine, converter-fed synchronous machine and battery energy storage system technologies are installed in the NPS.

Author Contributions: Conceptualization, F.G.-L., D.P. and J.P.A.; methodology, M.N.A. and D.P.; software, M.N.A. and D.P.; validation, F.G.-L., J.P.A. and M.A.A.; formal analysis, M.N.A.; investigation, M.N.A. and D.P.; resources, F.G.-L.; data curation, D.P.; writing—original draft preparation, M.N.A.; writing—review and editing, F.G.-L., J.P.A., M.A.A.; visualization, M.N.A. and D.P.; supervision, F.G.-L., J.P.A. and M.A.A. All authors have read and agreed to the published version of the manuscript.

Funding: This research received no external funding.

Acknowledgments: The authors would like to thank the support of University of South-Eastern Norway and Gamesa Electric. Martha N. Acosta would like to acknowledge the support given by CONACYT (México) and Universidad Autónoma de Nuevo León.

Conflicts of Interest: The authors declare no conflict of interest.

References

1. Statista. Available online: https://www.statista.com/statistics/864429/total-hydropower-capacity-in-sweden/ (accessed on 23 April 2020).
2. Lia, L.; Jensen, T.; Stensby, K.E.; Holm Midttømme, G.; Ruud, A.M. The current status of hydropower development and dam construction in Norway. *Int. J. Hydropower Dams.* **2015**, *22*, 37–43.
3. Electricity Production—Energifakta Norge. Available online: https://energifaktanorge.no/en/norsk-energiforsyning/kraftproduksjon/ (accessed on 23 April 2020).
4. Erlend Løklingholm, E. Design and Operation Investigations for Large Converter-Fed Synchronous Machines in Hydropower Applications. Ph.D. Thesis, Norwegian University of Science and Technology (NTNU), Trondheim, Norway, 2019.
5. Skytte, K.; Bergaentzlé, C.; Junqueira Fausto, F.; Andreas Gunkel, P. *Flexible Nordic Energy System: Summary Report*; Nordic Energy Research: Oslo, Norway, 2019; pp. 1–120, ISBN 9788793458659.
6. Kerkman, R.J.; Lipo, T.A.; Newman, W.G.; Thirkell, J.E. An Inquiry into Adjustable Speed Operation of a Pumped Hydro Plant Part 1—Machine Design and Performance. *IEEE Trans. Power Appar. Syst.* **1980**, *PAS-99*, 1828–1837. [CrossRef]
7. U.S. Army Corps of Engineers Division. *Technical Analysis of Pumped Storage and Integration with Wind Power in the Pacific Northwest Final Report*; MWH Americas Inc.: Portland, OR, USA, 2009; pp. 1–166.
8. Raabe, J. *Hydro Power: The Design, Use, and Function of Hydromechanical, Hydraulic, and Electrical Equipment*; VDI-Verlag, Ed.; VDI-Verlag GmbH: Dusseldorf, Germany, 1985; ISBN 3184006166.
9. Tehri Pumped Storage Plant-Power Technology|Energy News and Market Analysis. Available online: https://www.power-technology.com/projects/tehri-pumped-storage-plant/ (accessed on 25 April 2020).
10. AVČE Pumped Storage Power Plant on the Soča river: Rudis. Available online: https://www.rudis.si/en/reference/avce-pumped-storage-power-plant-on-the-soca-river/ (accessed on 25 April 2020).
11. Omarugawa Pumped Storage Power Plant Japan—GEO. Available online: http://globalenergyobservatory.org/geoid/45067 (accessed on 25 April 2020).
12. Snapshots of Pumped-Storage Projects—Hydro Review. Available online: https://www.hydroreview.com/2008/12/01/snapshots-of-pumped-storage-projects/#gref (accessed on 25 April 2020).
13. Limmern Pumped Storage Power Plant. Available online: https://www.axpo.com/ch/en/about-us/energy-knowledge.detail.html/energy-knowledge/limmern-pumped-storage-power-plant.html (accessed on 25 April 2020).
14. Valavi, M.; Nysveen, A. Variable-Speed Operation of Hydropower Plants: A Look at the Past, Present, and Future. *IEEE Ind. Appl. Mag.* **2018**, *24*, 18–27. [CrossRef]
15. Kougias, I.; Aggidis, G.; Avellan, F.; Deniz, S.; Lundin, U.; Moro, A.; Muntean, S.; Novara, D.; Pérez-Díaz, J.I.; Quaranta, E.; et al. Analysis of emerging technologies in the hydropower sector. *Renew. Sustain. Energy Rev.* **2019**, *113*, 109257. [CrossRef]
16. Converting to Variable Speed at a Pumped-Storage Plant—Hydro Review. Available online: https://www.hydroreview.com/2013/09/01/converting-to-variable-speed-at-a-pumped-storage-plant/#gref (accessed on 25 April 2020).
17. Estorage. Available online: https://www.estorage-project.eu/wp-content/uploads/2013/06/eStorage-D1.3-Report-on-Le-Cheylas-upgrade-studies.pdf (accessed on 18 April 2020).
18. Hadjipaschalis, I.; Poullikkas, A.; Efthimiou, V. Overview of current and future energy storage technologies for electric power applications. *Renew. Sustain. Energy Rev.* **2009**, *13*, 1513–1522. [CrossRef]

19. Weitzel, T.; Glock, C.H. Energy management for stationary electric energy storage systems: A systematic literature review. *Eur. J. Oper. Res.* **2018**, *264*, 582–606. [CrossRef]
20. U.S. Department of Energy DOE OE Global Storage Database. Available online: https://www.sandia.gov/ess-ssl/global-energy-storage-database-home/ (accessed on 16 March 2020).
21. Farhadi, M.; Mohammed, O. Energy Storage Technologies for High-Power Applications. *IEEE Trans. Ind. Appl.* **2016**, *52*, 1953–1961. [CrossRef]
22. Gonzalez-Longatt, F.M. Effects of Fast Acting Power Controller of BESS in the System Frequency Response of a Multi-Machine System: Probabilistic Approach. In Proceedings of the 2018 IEEE Innovative Smart Grid Technologies—Asia (ISGT Asia), Perth, Australia, 22–25 May 2018; pp. 804–809.
23. Krechel, T.; Sanchez, F.; Gonzalez-Longatt, F.; Chamorro, H.; Rueda, J.L. Transmission system-friendly microgrids: An option to provide ancillary services. In *Distributed Energy Resources in Microgrids*; Elsevier: Amsterdam, The Netherlands, 2019; pp. 291–321, ISBN 9780128177747.
24. Anderson, P.M.; Fouad, A.A. *Power System Control and Stability*; IEEE Press: New York, NY, USA, 2003; ISBN 8126518189.
25. Gonzalez-Longatt, F.; Rueda, J.L.; Vázquez Martínez, E. *Effect of Fast Acting Power Controller of Battery Energy Storage Systems in the Under-Frequency Load Shedding Scheme*; Loughborough University: Loughborough, UK, 2018; ISBN 9781538642917.
26. Gonzalez-Longatt, F.; Chikuni, E.; Rashayi, E. Effects of the Synthetic Inertia from wind power on the total system inertia after a frequency disturbance. In Proceedings of the IEEE International Conference on Industrial Technology, Antalya, Turkey, 9–12 October 2013; pp. 826–832.
27. Gonzalez-Longatt, F.; Sanchez, F.; Leelaruji, R. Unveiling the Character of the Frequency in Power Systems. In Proceedings of the 2019 IEEE PES GTD Grand International Conference and Exposition Asia (GTD Asia), Bangkok, Thailand, 19–23 March 2019; pp. 57–62.
28. Hutchison, G.; Breidablik, Ø.; Kuisti, H.; Luukkonen, I.; Nielsen, M.; Nielsen, F.B.; Setréus, J.; Sørensen, L.G.; Turunen, J. *Frequency Based Emergency Disconnection Policy Review for the Nordic Region*; ENTSO-E: Brussels, Belgium, 2017; pp. 1–75.
29. Kraft, D.; DFVLR-FB. *A Software Package for Sequential Quadratic Programming*; DLR German Aerospace Center—Intitute for Flight Mechanics: Koln, Germany, 1988.

Publication 2:

Optimal Under-Frequency Load Shedding Setting at Altai-Uliastai Regional Power System, Mongolia.

M. N. Acosta *et al.*, "Optimal Under-Frequency Load Shedding Setting at Altai-Uliastai Regional Power System, Mongolia," *Energies*, vol. 13, no. 20, p. 5390, Oct. 2020, doi: 10.3390/en13205390.

energies

MDPI

Article

Optimal Under-Frequency Load Shedding Setting at Altai-Uliastai Regional Power System, Mongolia

Martha N. Acosta [1,2], Choidorj Adiyabazar [3], Francisco Gonzalez-Longatt [1,*], Manuel A. Andrade [2], José Rueda Torres [4], Ernesto Vazquez [2] and Jesús Manuel Riquelme Santos [5]

1 Department of Electrical Engineering, Information Technology and Cybernetics, University of South-Eastern Norway, 3918 Porsgrunn, Norway; Martha.Acosta@usn.no
2 School of Mechanical and Electrical Engineering, Universidad Autónoma de Nuevo León, San Nicolas de los Garza 66455, NL, Mexico; manuel.andradest@uanl.edu.mx (M.A.A.); evazquezmtz@gmail.com (E.V.)
3 Power System Analysis and Research Department, National Dispatching Center Co. Ltd., Ulaanbaatar 17032, Mongolia; Choidorj.a@ndc.energy.mn
4 Department of Electrical Sustainable Energy, Delft University of Technology (TU Delft), 2628 Delft, The Netherlands; J.L.RuedaTorres@tudelft.nl
5 Department of Electrical Engineering, Universidad de Sevilla, 41004 Seville, Spain; jsantos@us.es
* Correspondence: fglongatt@fglongatt.org

Received: 31 August 2020; Accepted: 10 October 2020; Published: 15 October 2020

Abstract: The Altai-Uliastai regional power system (AURPS) is a regional power system radially interconnected to the power system of Mongolia. The 110 kV interconnection is exceptionally long and susceptible to frequent trips because of weather conditions. The load-rich and low-inertia AURPS must be islanded during interconnection outages, and the under-frequency load shedding (UFLS) scheme must act to ensure secure operation. Traditional UFLS over-sheds local demand, negatively affecting the local population, especially during the cold Mongolian winter season. This research paper proposes a novel methodology to optimally calculate the settings of the UFLS scheme, where each parameter of the scheme is individually adjusted to minimise the total amount of disconnected load. This paper presents a computationally efficient methodology that is illustrated in a specially created co-simulation environment (DIgSILENT® PowerFactory™ + Python). The results demonstrate an outstanding performance of the proposed approach when compared with the traditional one.

Keywords: frequency control; improved harmony search; metaheuristic algorithm; Mongolian power system; optimisation; under-frequency load shedding

1. Introduction

The power system continuously deals with power imbalances coming from fluctuations caused by imbalances between generation and demand. However, when the power system faces a severe power imbalance, such as the one caused by an abrupt increase of demand or a sudden disconnection of single/multiple generation units, several emergency control actions must be taken. One of those emergency control actions is under-frequency load shedding (UFLS) [1]. Its primary purpose is to stop the frequency from declining and to try and re-establish the balance between power demand and power generation by disconnecting an appropriate amount of load [2].

The classical automatic UFLS scheme uses under-frequency relays (UFRs), which are designed to operate any time the frequency drops below a predefined threshold using the instantaneous value of the local frequency [3]. The classical load shedding (LS) is performed at the same location where the frequency is sensed, and it can be done over one or multiple steps. The implementation of the

classical UFLS scheme implies identifying the most severe possible power imbalance and estimating the total amount of load disconnection, ensuring the frequency recovers above a minimum permissible value [4]. Once the total amount of LS is calculated, the parameters of the UFRs (number of load shedding stages, block size of load to be shed, frequency threshold and the time delay for each stage) must be set [5]. Typically, power system operators determine the fixed settings of UFRs using a trial and error procedure based on experience [3].

All parameters of UFRs require careful calculation, but the block size of LS and the number of LS steps require special attention. If these two parameters have inappropriate settings, it can cause undesirable results: (i) over-frequency conditions and/or loss of power service continuity produced by excessive LS at the initial stages of the frequency response and (ii) inability to arrest the frequency drop, leading to further loss of generation units or even system-wide blackout, produced by underestimated load shedding in the initial stages. Therefore, the total amount of LS is an extremely important factor for security and economic operation of a power system [6,7].

The main disadvantage of implementing the UFLS scheme using the traditional method is that errors can easily be made at the time when parameters of the UFRs are set. This is because the number of parameters to compute increases as the number of UFRs connected to the system increases, thereby becoming a complex problem and increasing the risk of inappropriate performance.

Although there are a vast number of methodologies to implement the traditional UFLS scheme that propose several sets of parameters depending on the country/company utility requirements [8–11], recent methods have focused on solving the problem of calculating the UFR parameters using computational algorithms. Authors of [12] used the genetic algorithm to minimise the LS and the dynamic frequency deviation of the power system. In [13], an adaptative UFLS scheme based on an artificial neuronal network (ANN) was proposed to estimate the power imbalance and then define the settings of UFRs. In [14], a methodology that combines UFLS with online fuzzy control strategy was presented to reduce the LS value. The authors of [15] introduced a method to compute the optimal values of load shedding, frequency threshold and time delay considering the high penetration of renewable generation resources. In [16], a technique was presented to assess the optimal load capacity and load disconnection sequence during a power system emergency. The particle swarm optimisation (PSO) algorithm has been implemented to estimate the amount of power imbalance and then calculate the size of LS [17], to solve a multi-objective function and determine the optimal amount of LS [18], and to compute the optimal amount of LS in an islanded operation scenario [19]. The trajectory sensitivity technique has been used to minimise the total LS cost of the power system [20]. Meanwhile, wide-area measurements (WAMs) have been used to create an intelligent UFLS scheme. For instance, the authors of [21] introduced a method based on artificial intelligence (AI) techniques and WAMs to calculate the optimal UFLS settings, [22] proposed an intelligent under-frequency and under-voltage scheme using WAMs to recover the frequency and voltage and the authors of [23] presented an adaptative UFLS model based on WAM information to set up an emergency LS strategy. Furthermore, several techniques are focused on addressing the effect of the measurement time delay on the performance of UFLS schemes [24–26]. A detailed literature review of the UFLS scheme is out of scope of this paper. For further information, the authors of [27] have presented a comprehensive analysis of UFLS schemes available in the literature.

The main drawback of most of the previous methodologies is that they assume the settings are the same for all UFRs as it can be a practical way to simplify the optimisation problem. However, that assumption can overestimate the total amount of load shedding and the frequency recovery because each load has a different active power value. Even if all the UFRs are set with the same block size of load shedding, the resulting load to be disconnected will be different. This fact can produce an over-frequency condition.

Moreover, another drawback of several methodologies, such as [14,18,19,21,22], is that they simplify the optimisation problem by considering only the block size of LS as a control variable and keep the number of load shedding stages, frequency threshold and time delay as fixed values. However,

not considering all parameters of UFRs limits the solution of the optimisation problem and can produce a wrong estimation of the optimal settings because the number of load shedding stages, frequency threshold and time delay have an impact on the frequency response.

The main objective of this research paper was to overcome the disadvantages of existing methodologies by introducing a novel method to optimally calculate the settings of the UFLS scheme. In this new approach, the principal parameters of the UFRs (number of load shedding stages, block size of load shedding, frequency threshold and the time delay for each stage) are considered in order to minimise the total amount of disconnected load. The significant contributions unfolding from this paper are listed below:

- The proposed methodology was formulated to consider and individually adjust each parameter of each UFR (number of load shedding stages, block size of load shedding, frequency threshold and the time delay for each stage) of the UFLS scheme. Thus, it allows all parameters that impact the frequency response to be taken into account, therefore obtaining the optimal settings and avoiding over/under load disconnection.
- A co-simulation framework (DIgSILENT® PowerFactory™ + Python) dedicated to performing optimisation of the UFLS scheme was developed by implementing the improved harmony search metaheuristic algorithm in Python and using time-domain simulations and discrete events from DIgSILENT® PowerFactory™.
- The optimal UFLS scheme was tested in the Altai-Uliastai regional power system of Mongolia. It was modelled in DIgSILENT® PowerFactory™ using the data of the real system. Simulation results showed the optimal UFLS scheme had superior performance compared to the traditional scheme currently installed in the Altai-Uliastai regional power system.
- The optimal settings of the UFLS scheme were assessed by carrying out a sensitivity analysis to ensure the optimisation reached the optimal solution.

The remainder of the paper is organised as follows. Section 2 presents a brief description of the Mongolian power system as well as the Altai-Uliastai regional power system. Section 3 introduces the implementation principles of the traditional UFLS scheme and describes the main characteristics of the Altai-Uliastai regional power system's UFLS scheme. Section 4 gives a detailed description of the formulation of optimal UFLS proposed in this research work. Section 5 depicts the methodology used to implement optimal UFLS, including a brief review of the optimisation method used. Section 6 describes the test system and the case studies used to assess the proposed methodology. Section 7 presents the results and the sensitivity analysis of the optimal setting. Finally, Section 8 presents the principal observations and conclusions.

2. Mongolian Power System

2.1. Overview of the MPS

The Mongolia power system (MPS) is an unbundled grid containing five regional power systems (RPS) as shown in Figure 1: (i) Central (CRPS), (ii) Western (WRPS), (iii) Altai-Uliastai (AURPS), (iv) Eastern (ERPS) and (v) Southern (SRPS). The MPS produces around 85% of its total electricity using coal-fired power plants, and the remaining 15% is supplied by renewable energy sources (RES), including hydro, wind and solar power plants. Furthermore, the MPS is composed of nine thermal power plants, three wind power plants, five solar power plants and three hydropower plants. The interconnection between the five RPS of the MPS is through 220 and 110 kV overhead transmission lines [28,29]. CRPS is the most extensive local energy system and is connected to AURPS, ERPS and SRPS through a 110 kV transmission line. In addition, CRPS has an interconnection with the Russian power system through a 220 kV double-circuit transmission line.

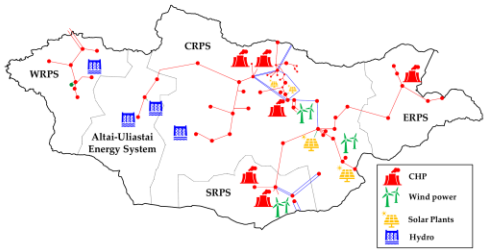

Figure 1. Representation of the Mongolia power system (MPS) indicating the main generation and transmission infrastructure.

The weather of Mongolia strongly influences the power consumption in the MPS, and the grid is operated considering two main seasons: winter and summer. Winter season is considered to start from the second half of September and lasts until the first half of May. In this season, temperatures reach values below −35 °C, and it is necessary to use central heating system. This causes high demand and requires a large number of generation units to be on service; therefore, the total rotational inertia of the MPS is high. On the other hand, the summer season starts in the second half of May and lasts until the first half of September. During this time, the central heating system is stopped, and the power demand reaches its minimum values. As the demand is reduced, several big power plants are scheduled to be out of service for maintenance purposes, and the total rotational inertia significantly decreases.

2.2. *Altai-Uliastai Regional Power System*

AURPS is as one of the five RPS of the MPS; it started to operate in 2009. It consists of six hydropower plants supplying electricity to 31 provinces and two towns. The largest hydropower plant of AURPS is Taishir with an installed capacity of 11 MW. Figure 2 depicts the main power generation and transmission infrastructure (actual model used in this paper).

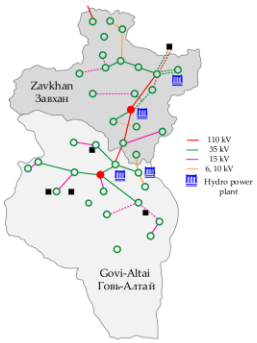

Figure 2. Representation of Altai-Uliastai regional power system (AURPS) indicating the main hydropower plants and transmission infrastructure.

The hydropower production at Altai-Uliastai depends on the water levels, and it operates on an average load of between 3.5 and 4.1 MW. The AURPS generates 49–55% of the total consumption in the region, and the remaining percentage is imported from CRPS through the Murun-Telmen 110 kV transmission line. During the winter season, the small hydropower plants are out of services due to the freezing of rivers; therefore, the power supply in AURPS is critically dependent on power importation

from CRPS. A summary of the power balance at AURPS during summer and winter seasons are shown in Table 1 [29]. It is important to observe that the interconnection between AURPS and CRPS is essential as it provides 38.4% and 83.40% of the total demand for summer and winter seasons, respectively.

Table 1. Winter and summer operational scenarios of AURPS.

Season	Inertia/Demand Level	Production, P_G (MW)	Demand, P_D (MW)	Power Import from CRPS, P_{tie} (MW)
Summer	High/Low	4.6	6.25	2.4
Winter	Low/High	3.0	11.99	10.0

The winter season is a special concern because of low local generation and high demand, making the disconnection of the Murun-Telmen transmission line a critical loss of infeed.

3. Under-Frequency Load Shedding Scheme

3.1. Definition of UFLS Scheme

The implementation of the traditional UFLS scheme is based on setting the values of the parameters of all UFRs installed in the power system. The UFRs are mainly characterised by four parameters (see Figure 3) [4]: (i) the number of stages (N_s) or steps in which the UFR will disconnect the locally connected load, (ii) the block size of LS (ΔP) that will be disconnected at each stage (this value is based on the total load that is locally connected), (iii) the frequency threshold (f_T) at which the load must be shed in each stage and (iv) the time delay (t_d) between activating the consecutive stages.

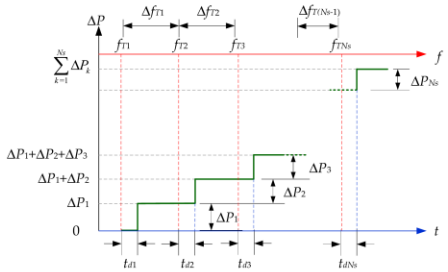

Figure 3. Power–frequency–time (P–f–t) schematic representation of the settings of an under-frequency relay (UFR).

Assuming that the power system has N_{UFR} UFRs installed, the settings of the i-th UFR (i = 1, 2, ... , N_{UFR}) are mathematically described as follows:

$$\mathbf{\Delta P}_i = \left[\begin{array}{cccccc} \Delta P_{1,i} & \Delta P_{2,i} & \dots & \Delta P_{k,i} & \dots & \Delta P_{N_s,i} \end{array} \right]_{1\times N_s} \quad (1)$$

$$\mathbf{F}_i = \left[\begin{array}{cccccc} f_{T1,i} & f_{T2,i} & \dots & f_{Tk,i} & \dots & f_{TN_s,i} \end{array} \right]_{1\times N_s} \quad (2)$$

$$\mathbf{T}_i = \left[\begin{array}{cccccc} t_{d1,i} & t_{d2,i} & \dots & t_{dk,i} & \dots & t_{dN_s,i} \end{array} \right]_{1\times N_s} \quad (3)$$

where $\Delta P_{k,i}$ defines the block size of LS, $f_{Tk,i}$ represent the frequency threshold and $t_{dk,i}$ is the time delay of the k-th stage in the i-th UFR. The process to calculate the four settings of each UFR becomes complex as the number of UFRs installed in the power system increases. This complexity is due to the fact that $3 \times N_s$ parameters must be computed for each UFR, and the total number of parameters to be computed in the power system is $(3N_s + 1) \times N_{UFR}$.

The correct performance of the UFLS scheme relies on the appropriate calculation of a set of settings, and this is dependent on considering (appropriately) the power system dynamic. Therefore, several factors must be considered in the procedure to implement the UFLS scheme. The UFLS must limit the maximum frequency deviation (Δf) as well as the depth of the frequency response (f_{nadir}) to protect the turbine generator units from prolonged under/low-frequency conditions. Consequently, it is essential to coordinate the UFLS scheme with under-frequency protection of the turbine generator units. Moreover, the UFLS must consider a reasonable margin between the nominal frequency (f_0) and the frequency threshold of the first stage (f_{T1}) to avoid activating the UFRs on non-emergency frequency conditions. After the UFRs action, the frequency will settle at a certain value depending on the initial overload and the load reduction per frequency reduction. Thus, UFLS must consider the actions of other controllers and/or the actions of system operators to avoid over-frequency scenarios after UFR activation. All these considerations raise the necessity of adopting techniques that facilitate the computation of UFR parameters and obtaining optimal settings to ensure the security of the power system by avoiding over/under shedding when the UFRs are activated.

3.2. UFLS Scheme in AURPS

The MPS uses a decentralised conventional UFLS scheme based on an automatic static UFR (ANSI number 81) taking measurements at each local placement. The traditional UFLS scheme at AURPS is adjusted to arrest the frequency before 47 Hz by disconnecting a maximum of 55% of the total demand, thus avoiding activation of under-frequency protection of the generation units, which are set at 46 Hz. Typically, the frequency threshold (f_T) is in the interval from 49.4 to 47.2 Hz, the time delay (t_d) is adjusted between 6 and 18 cycles and the number of steps is nine. Table 2 shows the settings used in the existing UFLS scheme in AURPS.

Table 2. Actual traditional UFLS settings of AURPS.

UFR Location	Element	ΔP (%)	f_T (Hz)	t_d (s)
Baynshand	Load	28	48.0	0.15
Baynhairhan	Load	55	47.8	0.15
Jargalant	Load	50	47.8	0.15
Uildwer	Load	87	47.8	0.15
Harzat	Load	55	47.8	0.15
Uliastai	Line	Open	48.8	0.10
Guulin [1]	Line	Open	48.0	0.15
Biger garaa [1]	Line	Open	48.0	0.10

[1] Out of service in the winter season.

4. Optimal UFLS Scheme

The UFLS scheme can be formulated as a mathematical optimisation problem seeking to obtain the optimal settings of the UFRs by considering an objective function. In this research paper, the objective of computing the UFLS settings at AURPS was to minimise the total load disconnection and at the same time ensure the security of the power system by stopping frequency decline after a significant system frequency disturbance. The formulation of the UFLS optimisation problem consisted of defining the mathematical expression for the objective function by considering a set of variables that impacts the frequency response and the operational requirements of the power system.

4.1. Frequency Quality Metrics

The metrics of the frequency during the primary frequency response (typically within the first 10–30 s after a frequency event occurs) are the time (t_{min}) at which the frequency reaches its maximum depth, called minimum instantaneous frequency (f_{min}) or frequency nadir, and the value at which the frequency settles, known as steady-state frequency (f_{ss}) [30,31]. After a system frequency disturbance,

in addition to the amount of rotational inertia available in the power system, the action of the UFRs directly influences the metrics of the frequency response, namely, the total amount of load shedding, the frequency threshold and the time delay impact on the values of f_{min} and t_{min}. Meanwhile, the total amount of load shedding mainly determines the level at which the frequency will settle (f_{ss}). Therefore, in a general approach, the UFLS parameters $N_{s,}$ ΔP, f_T and t_d, the interval between two frequency thresholds (Δf_T) and even the best placement of the UFRs can be taken as frequency control variables at the time to formulate the UFLS as an optimisation problem.

The four main settings of each UFR—number of stages (N_s), block size of load shedding ($\Delta\mathbf{P}$), frequency threshold ($\mathbf{F}$) and time delay ($\mathbf{T}$)—are used as frequency control variables to solve the UFLS optimisation problem. Therefore, the frequency control variables vector ($\mathbf{x}_{\mathrm{FC}}$) is mathematically written as follows:

$$\mathbf{x}_{\mathrm{FC}} = \begin{bmatrix} \mathbf{x}_1 & \mathbf{x}_2 & \dots & \mathbf{x}_i & \dots & \mathbf{x}_{N_{UFR}} \end{bmatrix}_{1\times(N_{UFR}\times 3N_s)} \tag{4}$$

$$\mathbf{x}_i = \begin{bmatrix} \Delta\mathbf{P}_i & \mathbf{F}_i & \mathbf{T}_i \end{bmatrix}_{1\times 3N_s} \forall i = 1, 2, \dots, N_{UFR} \tag{5}$$

and $\Delta\mathbf{P}_i$, $\mathbf{F}_i$ and $\mathbf{T}_i$ are defined in (1)–(3), containing a total number of frequency control variables of $N = 3N_{FR} \times N_s$.

Transmission system operators (TSOs) define several boundaries for UFR parameters according to the operational requirements of the power system. As a consequence, the frequency control variables are bounded as follows:

$$\begin{array}{l} \Delta\mathbf{P}_{\min} < \Delta\mathbf{P}_i < \Delta\mathbf{P}_{\max} \\ \mathbf{F}_{\min} < \mathbf{F}_i < \mathbf{F}_{\max} \qquad \forall i = 1, 2, \dots, N_{UFR} \\ \mathbf{T}_{\min} < \mathbf{T}_i < \mathbf{T}_{\max} \end{array} \tag{6}$$

where $\Delta\mathbf{P}_{\min}$, $\mathbf{F}_{\min}$ and $\mathbf{T}_{\min}$ are the minimum limits of the block size of LS, frequency threshold and the time delay, respectively. Moreover, $\Delta\mathbf{P}_{\max}$, $\mathbf{F}_{\max}$ and $\mathbf{T}_{\max}$ represent the maximum limit of the block size of LS, frequency threshold and the time delay, respectively.

4.2. Objective Function

The main objective of optimising the settings of UFRs is to minimise the total amount of load shedding after an under-frequency disturbance occurs in order to recover the frequency into allowable values and avoid over/under LS conditions produced by wrong settings of the UFLS scheme. The objective function is defined as the sum of all active power disconnected by the UFRs, and it is written as follows:

$$\min_{\mathbf{x}}[f(\mathbf{x}_{\mathrm{FC}})] = \min_{\mathbf{x}}[P_{LS}(\mathbf{x}_{\mathrm{FC}})] = \sum_{i=1}^{N_{UFR}} \sum_{k=1}^{N_{sT}} \Delta P_{k,i} P_{L,i} \tag{7}$$

where $P_{L,i}$ is the total active power of the load controlled by the i-th UFR, $\Delta P_{k,i}$ is the block size of LS (% of $P_{L,i}$) at the k-th activated stage of the i-th UFR and N_{sT} is the number of triggered stages during the under-frequency event. Be aware that N_{sT} can be smaller or equal to N_s.

4.3. Operational Frequency Requirements

Although the main purpose of optimising the settings of the UFRs is to minimise the total amount of load shedding (P_{LS}), the frequency of the power system must fulfil specific operational requirements after the action of the UFLS scheme, i.e., frequency quality metrics being inside certain limits. Therefore, the operational frequency requirements are included in the optimisation problem as a set of inequality constraints based on two frequency quality metrics: minimum frequency (f_{min}) and the steady-state frequency (f_{ss}).

4.3.1. Minimum Frequency

After a disturbance, if the frequency falls too deep, the under-frequency protection (UFP) of the synchronous generator can be activated and premature generator tripping before system load shedding may occur, ultimately leading to unnecessary system collapse. Therefore, it is essential to coordinate the UFLS scheme with the UFP of generators. This can be done by ensuring that the minimum frequency (f_{min}) does not reach the operating zone of the UFP of generators. This condition can be written as follows:

$$\begin{aligned} &\mathbf{g}_{\alpha}(\mathbf{x}_{\mathrm{FC}}) = \left[\begin{array}{cccccc} g_{\alpha,1} & g_{\alpha,2} & \cdots & g_{\alpha,i} & \cdots & g_{\alpha,N_{UFR}} \end{array} \right]_{1\times N_{UFR}} \\ &g_{\alpha,i} = f_{limit} - f_{min,i} \quad \forall\, i = 1,\ldots,N_{UFR} \end{aligned} \tag{8}$$

where f_{limit} represents frequency limit before the operating zone of UFP of the generators.

4.3.2. Steady-State Constraint

Turbine generator units have load operating limitations during abnormal frequency conditions to avoid exposing the turbine blades from stress and increasing their lifetime. For instance, at 50 Hz nominal frequency, turbine generator units must be protected from prolonged operation below 49.2 Hz [32,33]. Consequently, the continuous operation of turbine generator units requires the steady-state frequency (f_{ss}) to be inside specific limits as follows:

$$f_{ss,\min} \leq f_{ss} \leq f_{ss,\max} \tag{9}$$

where $f_{ss,\min}$ and $f_{ss,\max}$ are the minimum and maximum limits of f_{ss}. This restriction is formulated as two inequality constraints as follows:

$$\begin{aligned} &\mathbf{g}_{\beta}(\mathbf{x}_{\mathrm{FC}}) = \left[\begin{array}{cccccc} g_{\beta,1} & g_{\beta,2} & \cdots & g_{\beta,i} & \cdots & g_{\beta,N_{UFR}} \end{array} \right]_{1\times N_{UFR}} \\ &g_{\beta,i} = f_{ss,i} - f_{ss,\max} \quad \forall\, i = 1,\ldots,N_{UFR} \end{aligned} \tag{10}$$

and

$$\begin{aligned} &\mathbf{g}_{\gamma}(\mathbf{x}_{\mathrm{FC}}) = \left[\begin{array}{cccccc} g_{\gamma,1} & g_{\gamma,2} & \cdots & g_{\gamma,i} & \cdots & g_{\gamma,N_{UFR}} \end{array} \right]_{1\times N_{UFR}} \\ &g_{\gamma,i} = f_{ss,\min} - f_{ss,i} \quad \forall\, i = 1,\ldots,N_{UFR} \end{aligned} \tag{11}$$

The vector $\mathbf{G}(x_{\mathrm{FC}})$ contains the inequality constraints defined in (8), (10) and (11), and it is defined as follows:

$$\mathbf{G}(\mathbf{x}_{\mathrm{FC}}) = \left[\begin{array}{ccc} \mathbf{g}_{\alpha}(\mathbf{x}_{\mathrm{FC}}) & \mathbf{g}_{\beta}(\mathbf{x}_{\mathrm{FC}}) & \mathbf{g}_{\gamma}(\mathbf{x}_{\mathrm{FC}}) \end{array} \right]_{1\times(3N_{FR})} \leq 0 \tag{12}$$

where the total number of inequality constraints of the UFLS optimisation problem is $N_{\mathrm{ineq}} = 3N_{FR}$.

5. Optimisation Framework

This section is dedicated to giving a brief description of the improved harmony search metaheuristic algorithm used to solve the UFLS problem. Furthermore, the optimisation framework developed to calculate the optimal UFLS scheme, which mainly consists of the interface of PowerFactory$^{\mathrm{TM}}$ + Python, is presented.

5.1. Optimisation Algorithm: Improved Harmony Search (IHS)

IHS is a metaheuristic algorithm based on the harmony search algorithm proposed by Geem et al. [34]. The IHS algorithm is focused on the musical composition process. It mimics the procedure that musicians follow to improvise new pitches and create harmonies until they find the best harmony. The improvised pitches are represented by the set of variables of the optimisation problem, and the best harmony is the set of variables that produces the optimal solution by evaluating the objective function [34]. First, the IHS algorithm is initialised by randomly creating a harmony

(set of pitches), the harmony is used to evaluate the objective function and it is stored in a memory called harmony memory (HM). Then, a new harmony is improvised using the following criteria: selecting new pitches from the HM or creating them randomly. The new harmony is compared against the worst harmony stored in the HM; the HM is updated if the new harmony is better than the worst harmony in term of objective function evaluation. The IHS algorithm stops until it reaches a predefined number of improvisations (*NI*) [35]. This algorithm requires several parameters to be initialised: (i) the number of improvisations (*NI*), which determines the number of times the objective function will be evaluated; (ii) the harmony memory size (*HMS*), which defines the number of harmonies that will be stored in the HM; (iii) the harmony memory considering rate (*HCMR*), which is the probability of choosing the new pitches from HM; (iv) the pitch adjustment rate (*PAR*), which is the maximum (PAR_{max}) and minimum (PAR_{min}) probability of adjusting the new pith when it is selected from the HM and (v) the maximum (bw_{max}) and the minimum (bw_{min}) bandwidth distance [35].

5.2. Co-Simulation Framework: PowerFactory + Python

The optimal UFLS scheme formulated in Section 4 was solved using the IHS algorithm, and the practical implementation required co-simulation between two subsystems: one dedicated to obtaining the system frequency response of the power system and another dedicated to iteratively solving the numerical optimisation problem (see Figure 4).

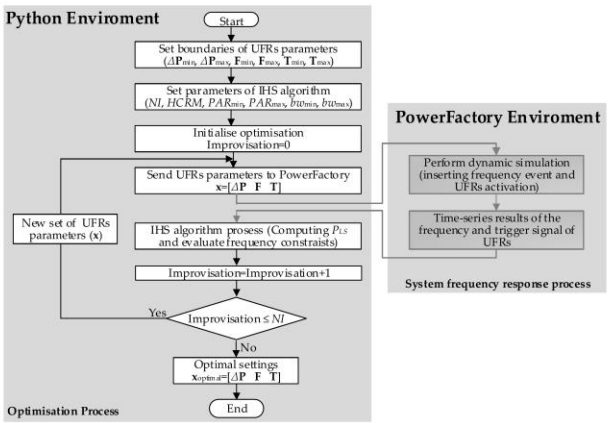

Figure 4. Co-simulation framework for optimal UFLS scheme.

The core of the co-simulation framework for optimal UFLS scheme is the optimisation process inside the python environment. It was implemented in the general-purpose programming language Python, and the IHS algorithm was taken from a scientific Python library (PyGMO), built to bring massive parallel optimisation interface [36]. The framework was complemented using DIgSILENT® PowerFactory™, which performed time-domain simulations and produced time-series of the electrical variables (frequency, active power) and discrete events (insert a disturbance, activation of UFRs).

The optimisation was performed using Python in an automatised close loop with PowerFactory™. For each improvisation, the UFR settings were taken from the optimisation output and placed on the UFRs in the power system model inside PowerFactory™. Then, a time-domain simulation, including the discrete events, was performed by PowerFactory. The dynamic response of the frequency and trigger signal of each stage of UFRs were interpreted at a high level by Python and used to compute the objective function and evaluate the frequency operational requirements. The simulation stopped

when the pre-set number of improvisations (*NI*) was reached. The pseudocode of the IHS algorithm is presented in Algorithm 1.

Algorithm 1. Improved Harmony Search Algorithm.

1: Initialise the IHS parameters: k, NI, HMS, $HMCR$, PAR_{min}, PAR_{max}, bw_{min} and bw_{max}.
2: HM = random(HMS, n) % Initialise the harmony memory
3: **while** ($k < NI$):
4: **for** j **in range**(0, n)
5: **if** rand(0,1) ≤ $HMCR$ %Harmony memory selection
6: j = randint(1, HMS)
7: x_{new} = HM(j,:)
8: $PAR_k = PAR_{min}+(PAR_{max}-PAR_{min}/NI)*k$
9: **if** rand() ≤ PAR_k % pitch adjustment
10: $bw_k = bw_{max}*\exp((\ln(bw_{min}/bw_{max})/NI)*k)$
11: $x_{new} = x_{new}+\text{rand}(-1,1)*bw_k$
12: **else** % Random selection
13: $x_{new} = \text{rand}(x_L, x_U)$
14: x(k,:) = x_{new}
15: **if** f(x) ≤ $f(x_{worst})$ %update the harmony memory
16: x_{worst} = x
17: $k = k+1$ %Stopping criteria
18: **end**

6. Description of the Test System

The real model of the AURPS was implemented in DIgSILENT® PowerFactory™ version 2020, and it was used to obtain the optimal settings of UFRs of the UFLS scheme. The schematic single-line diagram of the AURPS is shown in Figure 5. It consists of 46 loads, 39 lines, 25 two-winding transformers, six three-winding transformers and 13 synchronous generators.

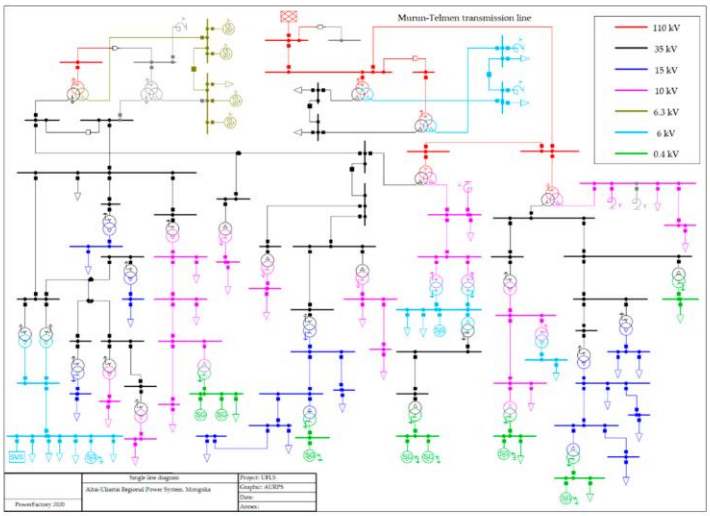

Figure 5. Schematic single-line diagram of Altai-Uliastai regional power system (AURPS).

The AURPS is radially interconnected to CRPS, and its power demand–supply highly depends on the power import from CRPS. Because the interconnector is exceptionally long, it is susceptible to frequent trips due to weather conditions. During interconnection outages, AURPS must be islanded and secure operation tried to be kept by activating the UFLS scheme. At this point, the islanded AURPS has a significant lack of power generation, and depending on the operational season (summer or winter), the inertia/demand levels significantly changes, directly impacting the UFLS performance. Currently, the traditional UFLS scheme of AURPS considers the same settings of UFRs for both operational seasons (summer and winter). However, the system operating conditions change significantly during winter compared to the summer season, as depicted in Table 1. During the winter season, local power production decreases 34.78%, and the power consumption increases 94.84% compared to the summer season. The decrease in power production and the increase in power demand in the winter season creates a significant reduction of system inertia. These operational conditions make the AURPS extremely vulnerable to any system event, and the UFLS scheme must be carefully adjusted to ensure secure operation of the AURPS. Consequently, in this paper, the settings of UFRs were computed for two operational scenarios: (i) high inertia—summer season, characterised by a high inertia level and low demand, and (ii) low inertia—winter season, characterised by a low inertia level and high demand requiring special attention in calculating the setting of UFRs.

The most significant frequency disturbance in the AURPS is the sudden disconnection of the Murun-Telmen 110 kV transmission line, causing a critical operational condition due to significant infeed loss. Therefore, this frequency event was used as the worst possible disturbance in AURPS. The sudden disconnection of the Murun-Telmen 110 kV transmission line was applied at t = 1.00 s.

The UFRs installed in the loads were based on a multi-step UFR, function ANSI 81, and the UFRs installed in the lines used the model SEL-751A provided in the DIgSILENT® PowerFactory™ Global Library. The UFRs of the loads only had one stage as in the real network; therefore, Ns = 1.

The boundaries of the frequency control variables were set following the technical and operational requirements of AURPS. f_{min} must not reach values below 47 Hz to avoid intervention of the UFP of the generators that are pre-set at 46.0 Hz; therefore, f_{limit} = 47 Hz. The continuous operating range of the generation units must be kept between 49.8 and 50.2 Hz; therefore $f_{ss,\min}$ = 49.8 Hz and $f_{ss,\max}$ = 50.2 Hz. The frequency threshold (f_T) should be between 47.6 and 49.4 Hz; therefore, $F_{\min}$ = 47.6 and $F_{\max}$ = 49.4 Hz. t_d should be at least six cycles (0.1 s) and should not exceed 18 cycles (0.3 s); therefore, $T_{\min}$ = 0.1 s and $T_{\max}$ = 0.3 s [29].

The set of parameters of IHS algorithm were set as those reported in the literature [37] as: HMS = 1.0, $HMCR$ = 0.90, $PAR_{\min}$ = 0.35, $PAR_{\max}$ = 0.99, $bw_{\min} = 1 \times 10^{-5}$, $bw_{\max}$ = 1.0 and NI = 500.

7. Results

This section is dedicated to presenting the outcomes of assessing the optimal UFLS for high inertia—summer season and low inertia—winter season scenarios and discussing the results. Furthermore, sensitivity analysis is carried out to evaluate the optimal settings.

7.1. Optimal Settings of UFLS Scheme

7.1.1. High Inertia—Summer Season

The optimal setting of the UFRs for high inertia—summer season scenario obtained by computing the IHS algorithm are depicted in Table 3. Moreover, the objective function defined in (7), evaluated through 500 improvisations, is shown in the convergence curve in Figure 6. The optimal settings of UFRs produced a minimum load shedding of $P_{LS}(x_{\mathrm{FC}})$ = 3.144 MW, which was reached in improvisation 303.

Table 3. Optimal UFLS settings of high inertia—summer season scenario of AURPS.

UFR Location	Element	ΔP (%)	f_T (Hz)	t_d (s)
Baynshand	Load	17.845	48.124	0.248
Baynhairhan	Load	43.595	48.644	0.244
Jargalant	Load	12.477	48.401	0.219
Uildwer	Load	29.740	48.784	0.210
Harzat	Load	9.733	47.986	0.188
Uliastai	Line	Open	49.317	0.220
Guulin	Line	Open	48.720	0.105
Biger garaa	Line	Open	48.661	0.126

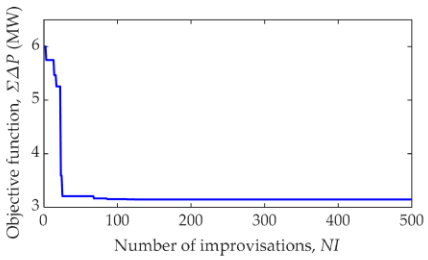

Figure 6. Convergence curve of optimal settings of UFRs for high inertia—summer season.

The dynamic response of the system frequency using the optimal settings of the UFLS scheme was computed and compared with the traditional UFLS scheme in AURPS. Figure 7 shows the frequency response comparison between the optimal UFLS and the traditional UFLS after the disconnection of the Murun-Telmen 110 kV transmission line. Moreover, Figure 8 depicts the active power of the loads and lines and also shows the trigger sequence of the UFRs during the outage.

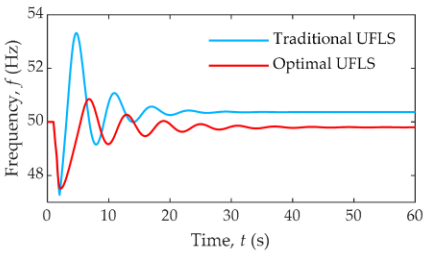

Figure 7. Frequency response in AURPS after disconnection of the Murun-Telmen 110 kV transmission line for high inertia—summer season scenario.

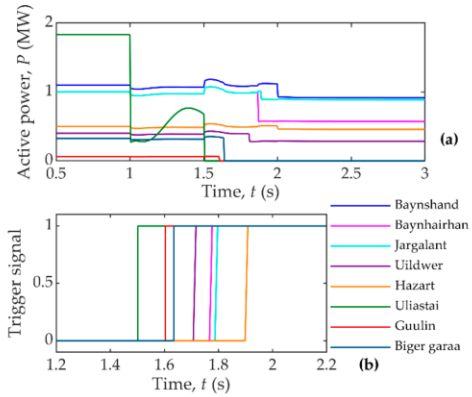

Figure 8. UFRs action in high inertia—summer season scenario: (**a**) active power; (**b**) trigger signal of the UFRs.

From Figure 7, it can be observed that the traditional UFLS scheme produced an over-frequency condition that caused the frequency to reach values above 53 Hz, which could result in activation of the over-frequency protection of the synchronous generators. The frequency quality metrics were computed to verify the positive improvements of the optimal UFLS scheme in the frequency response compared with the traditional UFLS, and the results are presented in Table 4. The optimal UFLS scheme prevented an unnecessary load shedding of 1.056 MW. It improved f_{min} by reducing the frequency depth by 0.232 Hz and avoided an over-frequency of continuing operation by settling the frequency at 49.8 Hz. The optimal setting of UFRs fulfilled the technical and operational constraints defined in (12).

Table 4. Frequency quality metrics of high inertia—summer season scenario.

UFLS Type	P_{LS} (MW)	f_{min} (Hz)	f_{ss} (Hz)	t_{min} (s)
Traditional	4.200	47.279	50.368	1.990
Optimal	3.144	47.511	49.800	2.160

7.1.2. Low Inertia—Winter Season

The disconnection of the Murun-Telmen 110 kV transmission line becomes extremely dangerous for the AURPS in low inertia—winter season scenario because demand is the maximum and small hydropower plants are out of service. Therefore, it is crucial to optimally compute the proper UFR settings.

The convergence curve of the objective function defined in (7) is presented in Figure 9. The IHS algorithm reached the minimum value at improvisation 348, indicating that optimal settings of UFRs depicted in Table 5 produced a minimum load shedding of $P_{LS}(x_{FC})$ = 4.803 MW.

Table 5. Optimal UFLS settings of low inertia—winter season scenario of AURPS.

UFR Location	Element	ΔP (%)	f_T (Hz)	t_d (s)
Baynshand	Load	84.818	49.003	0.264
Baynhairhan	Load	5.049	47.661	0.275
Jargalant	Load	72.712	48.816	0.108
Uildwer	Load	5.001	48.382	0.161
Harzat	Load	74.248	49.108	0.150
Uliastai	Line	Open	49.120	0.187

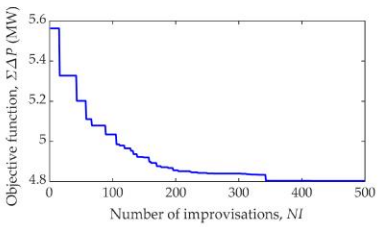

Figure 9. Convergence curve of optimal settings of UFRs for low inertia—winter season.

The optimal settings of the UFRs were evaluated by performing dynamic simulation of the AURPS model, applying a frequency event by disconnecting the Murun-Telmen 110 kV transmission line. Figure 10 shows the frequency response comparison between the traditional UFLS and the optimal UFLS. Using the traditional UFLS caused the minimum frequency to reach values below the frequency limit (f_{limit} = 47 Hz). This condition was caused by the inertia reduction, the increase in the power demand and the UFR parameters having the wrong setting. In contrast, the frequency response was improved by using the optimal settings, thereby avoiding activating UFP of the generators and a possible system collapse.

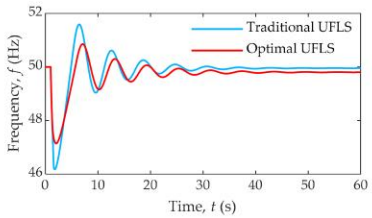

Figure 10. Frequency response in AURPS after disconnection of the Murun-Telmen 110 kV transmission line for low inertia—winter season scenario.

The active power disconnected and the trigger sequence of the UFRs during the outage are depicted in Figure 11. Before the UFR action, the negative value of active power in Uliastai indicates that the power flow direction has changed during the outage.

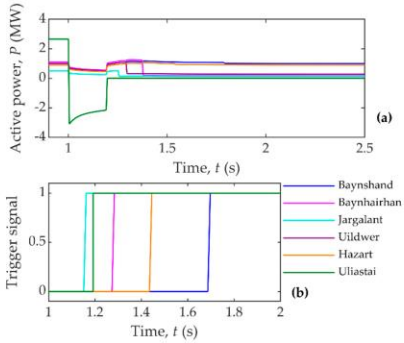

Figure 11. UFR action in low inertia—winter season scenario: (**a**) active power; (**b**) trigger signal of the UFRs.

Table 6 presents the frequency quality metrics of the optimal UFLS and traditional UFLS scheme. The optimal setting of UFRs significantly improved the frequency response by taking f_{min} out of the operating zone of UFP of generators, thus reducing the frequency depth by 0.978 Hz. Moreover, it prevented the unnecessary disconnection of 0.29 MW, and the frequency constraints defined in (12) were fulfilled.

Table 6. Frequency quality metrics of low inertia—winter season scenario.

UFLS Type	P_{LS} (MW)	f_{min} (Hz)	f_{ss} (Hz)	t_{min} (s)
Traditional	5.093	46.164	49.955	1.775
Optimal	4.803	47.142	49.804	2.038

7.2. Sensitivity Analysis

The optimal UFLS scheme formulation was focused on obtaining a set of optimal parameters (N_s, ΔP, f_T, t_d) for the UFRs that produce the minimum load disconnection during a frequency event and at the same time satisfy some frequency requirements. A sensitivity analysis was carried out to ensure that the resulting settings were optimal. This was done by decreasing the optimal block size of load shedding (ΔP) in all UFRs to demonstrate that another set of parameters (N_s, ΔP, f_T, t_d) did not exist for the UFRs that would cause minimum total load disconnection (calculated using (7)) and would satisfy the operational frequency requirements defined in (12).

The sensitivity analysis consisted of decreasing ΔP from 1% to 5% of its optimal values and observing the frequency quality metrics to ensure the set of parameters would meet the mentioned frequency constraints. The results of the sensitivity analysis are presented in Figure 12.

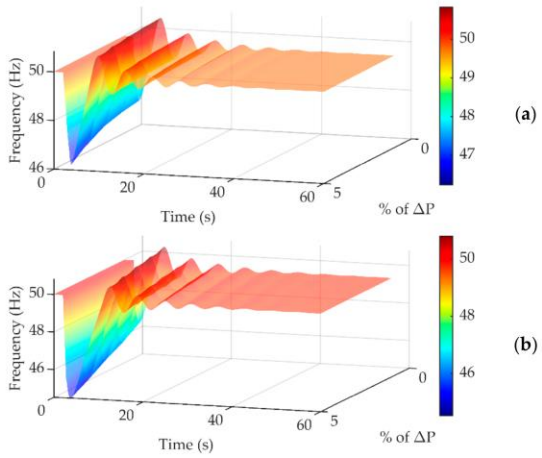

Figure 12. Frequency response by decreasing ΔP from 1% to 5%: (**a**) high inertia—summer season; (**b**) low inertia—winter season.

The sensitivity analysis for high inertia—summer season scenario, presented in Figure 12a, showed the steady-state frequency settled between 49.795 and 49.774 Hz for 1% and 5% of ΔP reduction, respectively, violating the constraints defined in (10), which determines that $f_{ss,\min}$ must be greater or equal to 49.8 Hz. Moreover, the minimum frequency was between 47.384 and 46.222 Hz for 1 and 5% of ΔP reduction, respectively. Even though, for 1% of ΔP reduction f_{min} satisfied (10) and (11), the constraint of steady-state was not fulfilled. Meanwhile, for low inertia—winter season scenario,

neither of the constraints defined in (12) were satisfied due to the minimum frequency falling below the frequency limit (f_{limit} = 47 Hz) and the steady-state frequency being lower than $f_{ss,\min}$ for all percentages of ΔP reduction (see Figure 12b). Therefore, it has been proved that the UFLS parameters of high inertia—summer season and low inertia—winter season scenarios are optimal.

8. Conclusions

The optimal UFLS scheme developed in this paper allows computation of the optimal settings of UFRs and minimisation of the total amount of load shedding. Moreover, the set of frequency constraints that are defined to ensure the operational frequency requirements are satisfied, and the sensitivity analysis demonstrates that the calculated parameters of UFRs are globally optimal. This methodology can be used to calculate optimal settings of the UFLS scheme of any power system and allows the user to choose which variables they want to include in the optimisation process.

The computation of the UFR parameters of the UFLS scheme is carried out by applying a new approach that calculates the parameters of each UFR instead of assuming that UFRs have the same parameters. In this new methodology, the IHS metaheuristic algorithm is used; the set of frequency constraints defined in the optimal UFLS scheme allowing the minimum frequency as well as the steady-state frequency to be limited into desired values, even in significantly deteriorated operational scenarios, such as the ones with low inertia and high demand. This represents the main advantage as an unnecessary load shedding is prevented, and it is ensured that the frequency will be within the operational requirements of the power system.

The proposed optimal UFLS scheme was tested on the model of one regional power system belonging to the Mongolian power system, obtaining satisfactory results. The optimal UFLS scheme is suitable for replacement of the traditional UFLS scheme of AURPS as it was calculated using real data to model AURPS in DIgSILENT® PowerFactory™ and to perform the optimisation. Moreover, the optimal UFLS scheme overcomes the current UFLS scheme of AURPS, providing optimal settings for two operational scenarios: high and low inertia.

Author Contributions: Conceptualisation, F.G.-L., M.A.A., J.R.T., C.A. and M.N.A.; methodology, F.G.-L., M.N.A. and C.A.; software, M.N.A.; validation, F.G.-L., M.A.A., J.R.T., J.M.R.S. and E.V.; formal analysis, M.N.A., F.G.-L., M.A.A. and J.R.T.; investigation, M.N.A. and C.A.; resources, F.G.-L.; data curation, M.N.A. and C.A.; writing—original draft preparation, M.N.A.; writing—review and editing, F.G.-L., C.A., M.A.A., J.R.T., J.M.R.S. and E.V.; visualisation, M.N.A. and C.A.; supervision, F.G.-L., M.A.A., J.R.T., J.M.R.S. and E.V. All authors have read and agreed to the published version of the manuscript.

Funding: This research received no external funding.

Acknowledgments: Martha N. Acosta acknowledges the financial support given by CONACYT (Mexico) and would like to thank the support of the University of South-Eastern Norway and Universidad Autónoma de Nuevo León. Choidorj Adiyabazar wants to acknowledge the financial support given by National Dispatching Centre of Mongolia Co., Ltd. and the University of South-Eastern Norway. F. Gonzalez-Longatt would like to express his gratitude to DIgSILENT GmbH for supporting his research.

Conflicts of Interest: The authors declare no conflict of interest.

References

1. Gonzalez-Longatt, F.M. Impact of emulated inertia from wind power on under-frequency protection schemes of future power systems. *J. Mod. Power Syst. Clean Energy* **2016**, *4*. [CrossRef]
2. Omar, Y.R.; Abidin, I.Z.; Yusof, S.; Hashim, H.; Abdul Rashid, H.A. Under Frequency Load Shedding (UFLS): Principles and implementation. In Proceedings of the PECon2010—2010 IEEE International Conference on Power and Energy, Kuala Lumpur, Malaysia, 29 November–1 December 2010; pp. 414–419.
3. Sigrist, L.; Rouco, L.; Echavarren, F.M. A review of the state of the art of UFLS schemes for isolated power systems. *Int. J. Electr. Power Energy Syst.* **2018**, *99*, 525–539. [CrossRef]

4. Acosta, M.N.; Andrade, M.A.; Vazquez, E.; Adiyabazar, C.; Gonzalez-Longatt, F.; Rueda, J.; Palensky, P. Improvement of the Frequency Response Indicators by Optimal UFLS Scheme Settings. In Proceedings of the 2020 IEEE 29th International Symposium on Industrial Electronics (ISIE), Hague, The Netherlands, 17–19 June 2020; IEEE: Hague, The Netherlands; pp. 1250–1255.
5. Hafez, A.A.; Hatata, A.Y.; Abdelaziz, A.Y. Multi-Objective Particle Swarm for Optimal Load Shedding Remedy Strategies of Power System. *Electr. Power Components Syst.* **2019**, *47*, 1651–1666. [CrossRef]
6. IEEE. *IEEE Std C37.117—IEEE Guide for the Application of Protective Relays Used for Abnormal Frequency Load Shedding and Restoration*; IEEE: Piscataway, NJ, USA, 2007; ISBN 073815539X.
7. Ketabi, A.; Hajiakbari Fini, M. Adaptive underfrequency load shedding using particle swarm optimization algorithm. *J. Appl. Res. Technol.* **2017**, *15*, 54–60. [CrossRef]
8. Laghari, J.A.; Mokhlis, H.; Karimi, M.; Abu Bakar, A.H.; Mohamad, H. A New Under-Frequency Load Shedding Technique Based on Combination of Fixed and Random Priority of Loads for Smart Grid Applications. *IEEE Trans. Power Syst.* **2015**, *30*, 2507–2515. [CrossRef]
9. Fernandes, R.V.; De Almeida, S.A.B.; Maciel Barbosa, F.P.; Pestana, R. Load shedding—Coordination between the Portuguese transmission grid and the distribution grid with minimization of loss of distributed generation. In Proceedings of the 2009 IEEE Bucharest PowerTech: Innovative Ideas Toward the Electrical Grid of the Future, Bucharest, Romania, 28 June–2 July 2009.
10. Mollah, K.U.Z.; Bahadornejad, M.; Nair, N.K. *Automatic under-Frequency Load Shedding in New Zealand Power System—A Systematic Review*; IEEE Conference Publication: Piscataway, NJ, USA, 2011.
11. Rudez, U.; Mihalic, R. Dynamic analysis of transition into island conditions of Slovenian power system applying underfrequency load shedding scheme. In Proceedings of the 2009 IEEE Bucharest PowerTech: Innovative Ideas Toward the Electrical Grid of the Future, Bucharest, Romania, 28 June–2 July 2009.
12. Hong, Y.Y.; Chen, P.H. Genetic-based underfrequency load shedding in a stand-alone power system considering fuzzy loads. *IEEE Trans. Power Deliv.* **2012**, *27*, 87–95. [CrossRef]
13. Yan, J.; Li, C.; Liu, Y. Adaptive load shedding method based on power imbalance estimated by ANN. In Proceedings of the TENCON 2017—2017 IEEE Region 10 Conference, Penang, Malaysia, 5–8 November 2017; Volume 2017-Decem, pp. 2996–2999.
14. Huang, B.; Du, Z.; Liu, Y.; Zhao, F. Study on online under-frequency load shedding strategy with virtual inertia control of wind turbines. *J. Eng.* **2017**, *2017*, 1819–1823. [CrossRef]
15. Drabandsari, A.; Amraee, T. Optimal Setting of Under Frequency Load Shedding Relays in Low Inertia Networks. In Proceedings of the 2018 Smart Grid Conference (SGC), Kurdistan, Iran, 28–29 November 2018; pp. 1–6.
16. Lytvynchuk, V.A.; Kaplin, M.I.; Bolotnyi, N.P. The Method of Design an Optimal Under-Frequency Load Shedding Scheme. In Proceedings of the 2019 IEEE 6th International Conference on Energy Smart Systems, ESS 2019—Proceedings, Kyiv, Ukraine, 17–19 April 2019; Volume 1, pp. 14–17. [CrossRef]
17. Abedini, M.; Sanaye-Pasand, M.; Azizi, S. Adaptive load shedding scheme to preserve the power system stability following large disturbances. *IET Gener. Transm. Distrib.* **2014**, *8*, 2124–2133. [CrossRef]
18. Zhang, X.; Ma, J.; Yao, S.; Chen, R. Optimization method of under frequency load shedding schemes for systems with high permeability new energy. In Proceedings of the 2019 4th International Conference on Intelligent Green Building and Smart Grid, IGBSG 2019, Yichang, China, 6–9 September 2019; pp. 577–580. [CrossRef]
19. Mohamad, H.; Isa, A.I.M.; Yasin, Z.M.; Salim, N.A.; Rahim, N.N.A.M. Optimal load shedding technique for an islanding distribution system by using Particle Swarm Optimization. In Proceedings of the 3rd International Conference on Power Generation Systems and Renewable Energy Technologies, PGSRET 2017, Johor Bahru, Malaysia, 4–6 April 2017; pp. 154–158. [CrossRef]
20. Xu, X.; Zhang, H.; Chai, Y.; Shi, F.; Li, Z.; Li, W. Trajectory sensitivity-based emergency load shedding optimal algorithm. In Proceedings of the 5th IEEE International Conference on Electric Utility Deregulation, Restructuring and Power Technologies, DRPT 2015, Changsha, China, 26–29 November 2015; pp. 1368–1372. [CrossRef]
21. Shun, L.; Qingfen, L.; Jiali, W. Dynamic optimization of adaptive under-frequency load shedding based on WAMS. In Proceedings of the 2016 IEEE Information Technology, Networking, Electronic and Automation Control Conference, ITNEC 2016, Chongqing, China, 20–22 May 2016; pp. 920–926.

22. Wang, J.; Zhang, H.; Zhou, Y. Intelligent under Frequency and under Voltage Load Shedding Method Based on the Active Participation of Smart Appliances. *IEEE Trans. Smart Grid* **2017**, *8*, 353–361. [CrossRef]
23. Jianjun, Z.; Dongyu, S.; Dong, Z.; Yang, G. Load Shedding Control Strategy for Power System Based on the System Frequency and Voltage Stability. In Proceedings of the 2018 China International Conference on Electricity Distribution (CICED), Tianjin, China, 17–19 September 2018; pp. 1352–1355.
24. Alhelou, H.H.; Golshan, M.E.H.; Zamani, R.; Moghaddam, M.P.; Njenda, T.C.; Siano, P.; Marzband, M. An improved UFLS scheme based on estimated minimum frequency and power deficit. In Proceedings of the 2019 IEEE Milan PowerTech, PowerTech 2019, Milano, Italy, 23–27 June 2019.
25. Haes Alhelou, H.; Hamedani Golshan, M.; Njenda, T.; Siano, P. WAMS-Based Online Disturbance Estimation in Interconnected Power Systems Using Disturbance Observer. *Appl. Sci.* **2019**, *9*, 990. [CrossRef]
26. Alhelou, H.; Hamedani-Golshan, M.; Njenda, T.; Siano, P. Wide-Area Measurement System-Based Optimal Multi-Stage Under-Frequency Load-Shedding in Interconnected Smart Power Systems Using Evolutionary Computing Techniques. *Appl. Sci.* **2019**, *9*, 508. [CrossRef]
27. Haes Alhelou, H.; Hamedani Golshan, M.E.; Njenda, T.C.; Hatziargyriou, N.D. An Overview of UFLS in Conventional, Modern, and Future Smart Power Systems: Challenges and Opportunities. *Electr. Power Syst. Res.* **2020**, *179*, 106054. [CrossRef]
28. Adiyabazar, C.; Acosta, M.N.; Gonzalez-Longatt, F.; Rueda, J.L.; Palensky, P. Under-Frequency Load Shedding in Mongolia: Simulation Assessment Considering Inertia Scenarios. In Proceedings of the 2020 IEEE 29th International Symposium on Industrial Electronics (ISIE), Delft, The Netherlands, 17–19 June 2020; IEEE: Delft, The Netherlands; pp. 1256–1261.
29. Profileprojections, S.; Generation, C.; Energy, R.; Expansion, C. *Strategy for NAPSI Technical Assistance for Mongolia—Renewable Energy Capacity Expansion Plan*; ADB: Mandaluyong, Philippines, 2018.
30. Gonzalez-Longatt, F.; Sanchez, F.; Leelaruji, R. Unveiling the Character of the Frequency in Power Systems. In Proceedings of the 2019 IEEE PES GTD Grand International Conference and Exposition Asia (GTD Asia), Bangkok, Thailand, 20–23 March 2019; pp. 57–62.
31. Acosta, M.N.; Pettersen, D.; Gonzalez-Longatt, F.; Peredo Argos, J.; Andrade, M.A. Optimal Frequency Support of Variable-Speed Hydropower Plants at Telemark and Vestfold, Norway: Future Scenarios of Nordic Power System. *Energies* **2020**, *13*, 3377. [CrossRef]
32. IEEE. *IEEE Std C37.111 IEEE Guide for AC Generator Protection*; IEEE: Piscataway, NJ, USA, 2013; Volume 2006, ISBN 9782832207666.
33. IEEE IEEE Std C37.106. *Guide for Abnormal Frequency Protection for Power Generating Plants*; IEEE: Piscataway, NJ, USA, 2004; pp. 1–34. [CrossRef]
34. Geem, Z.W.; Kim, J.H.; Loganathan, G.V. A New Heuristic Optimization Algorithm: Harmony Search. *Simulation* **2001**, *76*, 60–68. [CrossRef]
35. Lee, K.S.; Geem, Z.W. A new meta-heuristic algorithm for continuous engineering optimization: Harmony search theory and practice. *Comput. Methods Appl. Mech. Eng.* **2005**, *194*, 3902–3933. [CrossRef]
36. Biscani, F.; Izzo, D. esa/pagmo2: Pagmo 2.14.0. Available online: https://zenodo.org/record/3697219 (accessed on 13 March 2020).
37. Improved Harmony Search (IHS)—Pagmo 2.15.0 Documentation. Available online: https://esa.github.io/pagmo2/docs/cpp/algorithms/ihs.html#_CPPv4N5pagmo3ihsE (accessed on 13 March 2020).

Publication 3:

Optimal UFLS Settings: An Assessment of Frequency System Response Indicators.

M. N. Acosta, C. Adiyabazar, F. Gonzalez-Longatt, J. L. Rueda, and P. Palensky, "Optimal UFLS Settings: An Assessment of Frequency System Response Indicators," in *2020 IEEE PES Innovative Smart Grid Technologies Europe (ISGT-Europe)*, Oct. 2020, pp. 1141–1145, doi: 10.1109/ISGT-Europe47291.2020.9248760.

Optimal UFLS Settings: An Assessment of Frequency System Response Indicators

Martha N. Acosta
School of Mechanical and Electrical Engineering
Universidad Autónoma de Nuevo León
Nuevo León, México
martha.acostamnt@uanl.edu.mx

Choidorj Adiyabazar
Power System Analysis and Research Department
National Dispatching Center Co.,Ltd
Ulaanbaatar, Mongolia
choidorj.a@ndc.energy.mn

F. Gonzalez-Longatt
Martha N. Acosta
Department of Electrical engineering, Information Technology and Cybernetics
University of South-Eastern Norway
Porsgrunn, Norway
fglongatt@fglongatt.org

J.L. Rueda
Department of Electrical Sustainable Energy
Delft University of Technology (TU Delft)
Delft, Netherlands
J.L.RuedaTorres@tudelft.nl

P. Palenski
Department of Electrical Sustainable Energy
Delft University of Technology (TU Delft)
Delft, Netherlands

***Abstract*— This paper investigates the positive changes in the system frequency response indicators caused by the implementation of a set of optimal settings of an under-frequency load shedding (UFLS) scheme. The optimal UFLS scheme is optimised by minimising the total amount of load shedding and considering the recovery process of the system frequency into its operational values after several losses of generation and satisfies the requirements of the UFLS standard (PRC-006-SERC-02). The idea of implementing the optimal UFLS scheme is to identify how changes the minimum frequency, minimum time, rate of change of frequency and steady-state frequency when the amount of load shedding change. The optimal UFLS scheme formulation starts with identifying the variables to control with the optimisation and its respective bounds. Then, the objective function is formulated in terms of the total load shedding, and finally, the restrictions and requirements of the systems are written as inequality constraints. The optimal UFLS is evaluated in the IEEE 39-bus system. The simulations results demonstrate the suitability of the optimal UFLS to improve the frequency response indicators.**

Keywords— frequency control, frequency response indicators, optimisation, under-frequency load shedding.

I. Introduction

The frequency stability is concerned with the ability of a power system to supply its load after a disturbance involving a generation-load imbalance at a frequency within an acceptable range [1]. The sudden disconnection of large generation units causes a significant power imbalance between the power generation and the load demand. This active power imbalance produces a fast drop in the system frequency generated by the deficit of power supply [2]. If the control actions are not appropriately designed, the frequency can drop to values considered unacceptable or even trip a cascade event putting the power system in risk of instability and subsequent blackout. Moreover, if the system frequency reaches unacceptably low values, there is a small-time window to implement emergency actions. If the size of the system frequency disturbance is large, the scheduled power reserve may not be enough to restore the frequency and the power system operators may use emergency control and protection schemes to maintain power system frequency [3]. An emergency control plan used by years is the well-known *under-frequency load shedding* (UFLS). The UFLS strategy is designed to balance the demand for electricity with the supply rapidly and to avoid cascading power system failure [4]. It is essential to coordinate the UFLS with under-frequency protection of the generator. Premature generator tripping, before system load shedding is complete, can lead to unnecessary system collapse [5]. The situation of frequency control and stability and the problem of adequate settings of UFLS is becoming more complicated with the increased penetration of renewables generation sources [6].

The primary objective of UFLS schemes is to arrest frequency dropping in due time by shedding an appropriate amount of load, in order to recover the frequency into its nominal values [7]. Ideally, the UFLS must act as the primary option and by doing so, preventing the action of generation-side under-frequency protections, which would finally lead to a cascading power outage [8]. In the traditional UFLS schemes, the settings of the UFLS relays are mainly based on the power system operator's knowledge of the power system performance during major frequency events. However, although the frequency is recovered into its nominal values, the UFLS settings are not optimal, and they end up disconnecting more load than necessary.

The UFLS is becoming a very attractive research topic in recent time to deal with several problems related to extremally reduced inertia scenarios, the market pressure to minimise the reserve margins and the operating the tie-line near to the limit of capacities. Many different approaches are reported in the scientific literature. [9] combines UFLS with online fuzzy control strategy to reduce the load shedding value, [10] uses wide are measurements system (WAMS) in combination with under-frequency and under-voltage schemes to recover the frequency and voltage. Furthermore, [11] proposed an artificial neuronal network for estimating the amount of power imbalance in the grid. [12] recommend a method to compute the optimal values of load shedding, frequency threshold and time delay considering the high penetration of renewable generation resources. [13] proposes an adaptative UFLS model based on WAMS information to set up an emergency load shedding strategy and [14] depict a method for assess the optimal load capacity and load disconnection sequence during a power system emergency. The limitation of previous optimization applications is that it assumes all UFLS relay has the same parameters and is no clear in which load is implemented the UFLS.

The limitation of most of the previous methodologies is that it assumes the settings are the same for all relays. This assumption can affect the total amount of load shedding since the amount of load shedding that each relay active depend on

the load value even when all relays have the same settings. The propose of this paper is to investigate the positive changes in the system frequency response indicators caused by the implementation of an optimal setting of a UFLS scheme. An optimal calculation process of the settings of the UFLS improves the power system reliability by minimising the unnecessary excessive load shedding and prevent the operation of under-frequency protections of the synchronous generator. However, this research paper introduces the problem of optimal settings of UFLS relayed using mathematical optimisation. Then, the methodology is used to set the UFLS parameters on a test system, and the principal motive is to determinate how the optimal settings impact the frequency response indicators: minimum frequency, minimum time, rate of change of frequency and steady-state frequency. This paper is organised as follows: in Section II, the methodology to calculate the optimal UFLS scheme is described. Section III presents a description of the test system and the cases defined for assessing the UFLS scheme. Section IV describes the results obtained and present the main observations of the results. Finally, Section V presents the conclusion.

II. Optimal UFLS scheme formulation

The UFLS is explicitly dedicated to deal with under frequency events where there is a lack of generation or an excess of power demand. This section is dedicated to formulating the UFLS scheme as an optimization problem.

A. Metrics: Frequency response

The frequency response of a power system is typically analysed by using time-domain plots of the system frequency when the major event is applied, and its indicators are (see Fig. 1): the minimum frequency (f_{min}) is the resulting value of the difference between nominal frequency (f_0) and the maximum frequency deviation (Δf_{max}), i.e., $f_{min} = f_0 - \Delta f_{max}$. The minimum time ($t_{min}$) is the time at which the frequency reaches its minimum value and its maximum deviation. Moreover, the Rate of Change of Frequency (*RoCoF*) represents the speed at which the frequency changes, i.e., the amount of frequency change in one second, $RoCoF = df/dt \ \left[\mathrm{Hz/s}\right]$. Finally, the steady-state frequency (f_{ss}) denotes the frequency value at which the *RoCoF* is zero. This value is typically reached after the inertia response and the governor action [4]-[12-13].

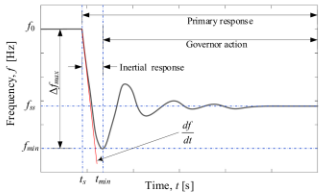

Fig. 1. Frequency response metrics (f_{min}, t_{min}, $RoCoF_{max}$ and f_{ss}).

B. UFLS Settings

UFLS relays are used to protect the system and keep the frequency of the system close to the nominal value shedding some of the system load. UFLS relays can be classified into two categories[15]: (i) Fixed number of stages and time delays and (ii) Adaptative number of stages and variable shed demands. The traditional UFLS relay (such as ANSI 81L) falls in the first category and is extensively used in power systems. In this research paper, the UFLS relays are considered to have a fixed number of stages, but the setting will be optimised in the next subsections. Traditional UFLS scheme relies basically on four main settings: (i) block size of the dropped load (ΔP) defines the amount of load to be dropped at all stages, (ii) the number of stages (N_S) is an integer value that denotes the number of steps in which the load will be dropped, (iii) the frequency setpoint (f_{sp}) is a pre-set frequency value at which the load must be shed in each stage and (iv) the time delay (t_d) between activating the consecutive stages.

C. Optimisation Problem Definition

The process to formulate the optimal settings of UFLS scheme in this paper is based in the following steps: First, the appropriate set of control variables are identified, those variables are selected to control the frequency response following a system frequency disturbance at the time the optimisation considered the main aspects of the UFLS relay features and respective bounds are defined for the relay settings. Then, the objective function to be minimised was written in terms of the control variables, and finally, the restrictions and requirements of the systems are written as inequality constraints. The full procedure of each step is described below.

1) Variables

The control vector ($\mathbf{x}$) is a vector used to specify the control variables to be used in the optimisation process:

$$\mathbf{x} = \left[\Delta P_{ij} \quad f^1_{sp,j} \quad \Delta f_{sp,kj}\right]^{\mathrm{T}}, \begin{cases} i = 1,\ldots,N_S \\ j = 1,\ldots,N_R \\ k = 1,\ldots,N_S - 1 \end{cases} \tag{1}$$

where ΔP_{ij} is the percentage load shedding of the i-th stage in the j-th UFLS relay, $f^1_{sp,ij}$ is the first frequency setpoint of the j-th UFLS relay and $\Delta f_{sp,kj}$ represents the interval between two subsequent frequency setpoints. Moreover, N_R is the number of UFLS relays installed in the power system, and N_S is the number of load shedding stages in each relay.

The control variables are bounded by its upper (u) and lower (l) allowable values as follows:

$$\begin{aligned} \Delta P_l &\le \Delta P_{ij} \le \Delta P_u \\ f^1_{sp,l} &\le f^1_{sp,j} \le f^1_{sp,u} \\ \Delta f_{sp,l} &\le \Delta f_{sp,kj} \le \Delta f_{sp,u} \end{aligned} \tag{2}$$

where ΔP_l and ΔP_u, represents the minimum and maximum permissible percentage of load shedding, respectively. $f^1_{sp,l}$ and $f^1_{sp,u}$ are the minimum and maximum limit frequency setpoint in the first stage, respectively. Moreover, $f^1_{sp,l}$ and $f^1_{sp,u}$ are the minimum and maximum values allowed for Δf_{sp}.

2) Objective function

The idea of optimising the settings of the UFLS relays is to reduce, as much as possible, the amount of load shedding during the under-frequency event. Consequently, the purpose of the UFLS optimisation is determinate the minimum amount of load shedding required to recovers the steady-state frequency into its operating values. Therefore, the objective function is formulated as the sum of all active stages in each UFLS relay multiplied by active power in its respective load. The objective function is defined as follows:

$$f(\mathbf{x}) = \min\left(\sum_{j=1}^{N_R}\sum_{i=1}^{n_S}\Delta P_{ij} P_j\right) \tag{3}$$

where P_j is the active power of the j-th load with UFLS relay and n_S is the number of activated stages. n_s is different from N_s ($n_s \leq N_s$).

3) Constraints

The objective function defined in (3) is subject to certain restrictions to ensure the security of the power system and fulfil the technical requirements of the utility companies:

a) Steady-state frequency (f_{ss}): after a massive loss of generation, the f_{ss} must remain inside the operating range of the synchronous generators, i.e., $f_{ss}^{\min} \leq f_{ss} \leq f_{ss}^{\max}$. This restriction is formulated as two inequality constraints as follow

$$g_1(\mathbf{x}) = f_{ss} - f_{ss}^{\max} \leq 0$$
$$g_2(\mathbf{x}) = f_{ss}^{\min} - f_{ss} \leq 0 \quad (4)$$

b) Frequency setpoint (f_{sp}): the f_{sp} in each stage of the UFLS relays shall be inside the limits defined by the technical requirements of the utility companies, i.e., $f_{sp}^{\min} \leq f_{sp} \leq f_{sp}^{\max}$. Since the optimisation gives the first f_{sp} of each relay and it is already bounded, it is necessary to define the inequality constraint for the minimum limit as follows:

$$g_3(\mathbf{x}) = f_{sp}^{\min} - f_{sp,ij} \leq 0 \quad (5)$$

III. CASE STUDY DEFINITION

To investigates the positive changes in the system frequency response indicators caused by the implementation of an optimal setting of a UFLS scheme, the classical IEEE 39-bus system is used. In this test system, generator G1 represents the aggregation of several. The original model data come from the book titled "Energy Function Analysis for Power System Stability" [16]. The test system has been implemented in DIgSILENT® PowerFactory™ 2020. The schematic single line diagram of the test system is shown in Fig. 2. The test system consists of ten generators, 19 loads, 34 transmission lines, 12 transformers and 39 buses. The total active power generation is 6,140.81 MW, and the total power demand is 6097.10 MW [17]. The frequency response of the test system is excited by a frequency event, in this case, the sudden disconnection of generators G1 and G9 at t = 1.0s, these generators represent a loss of a generation of 29.8% of the total generation, $\Delta P = P_{G1}+P_{G9}$. The UFLS relays are installed in all loads. In this paper, the 19 UFLS relays (N_R = 19) has four load shedding stages (N_S=4). The time delay was set as t_d = 0.20s. The generators causing the disturbance (G1 and G6) are highlighted with red colour, and the loads where the UFLS relays are installed are marked with blue colour in Fig. 2.

Three cases are defined: *Case I* refers to the natural frequency response of the IEEE-39 bus system without any UFLS scheme. *Case II* study the frequency response of the test system considering the UFLS but using a traditional setting. Finally, *Case III* represents the frequency response of the test system, considering the optimal settings of the UFLS scheme defined in Section II. For all cases, it is observed the indicators of the frequency response: (i) f_{min}, (ii) t_{min}, (iii) $RoCoF_{max}$ and (iv) f_{ss}.

Due to the IEEE-39 bus system is representative of the North American system, the parameters of the UFLS relays must satisfy the SERC (South-eastern Electric Reliability Council) UFLS Standard: PRC-006-SERC-02 [18]: (i) f_{ss} shall be between 59.5 Hz and 60.5 Hz, (ii) f_{sp} shall be no lower than 58.4 Hz and not higher than 59.5 Hz, (iii) Δf_{sp} shall be at least 0.2 Hz but no greater than 0.5 Hz and (iv) t_d shall be at least six cycles (0.1sec).

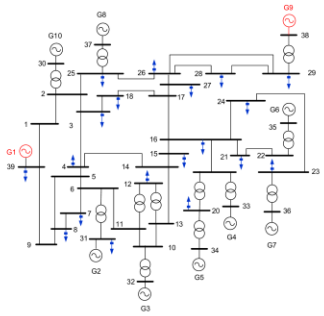

Fig. 2. Descriptive single-line diagram of the IEEE-39 bus system.

Case I (No UFLS scheme): In this case, it is presented the dynamic response of the frequency when the disturbance occurs by disconnecting the generators G1 and G9, and there is not a UFLS scheme installed.

Fig. 3 shows the frequency response measured in all buses. The inertia response acts to try to stop the frequency drop since there is not installed a UFLS scheme in the IEEE-39 bus system. Despite the action of the inertia response, the frequency drop cannot be arrested and continues dropping reaching values below the minimum allowable frequency and causing that the system becomes unstable. The minimum permissible frequency in 60 Hz nominal frequency, is defined by the under-frequency relays settings of the synchronous generators that typically operates if the frequency reach vales from 58.4 Hz to 57.9 and the frequency does not recover within 30 seconds [19].

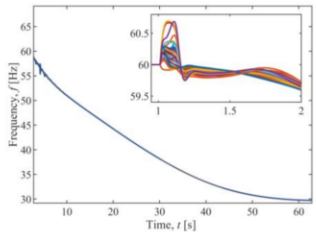

Fig. 3. *Case I (No UFLS scheme)*: Frequency response measured in the 39 buses after the disconnection of generators G1 and G9.

Meanwhile, Fig. 4 shows the *RoCoF* of all buses, the maximum *RoCoF* produced by the disconnection of generators G1 and G9 is presented in bus 29, and its value is $RoCoF_{max}$ =32.885Hz/s at 1.012s. The high amount of the *RoCoF* is due to significant generation deficiency, i.e., the disconnection of generators G1 and G9 represents almost 30% of the total generation, and this size of the loss of generation causes that the total system inertia decreases. From the results in *Case I*, it is evident that the power system requires a UFLS scheme to arrest the frequency drop and avoid the activation of the under-frequency relays that protect the synchronous generators. Moreover, a UFLS scheme is needed to recover

the frequency into the established f_{ss} limits, i.e., $59.5 \leq f_{ss} \leq 60.5$.

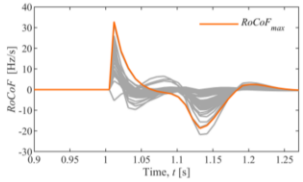

Fig. 4. *Case I (No UFLS scheme)*: *RoCoF* measured in the 39 buses after the disconnection of generators G1 and G9.

Case II (Traditional UFLS scheme): This case presents the frequency response when a traditional UFLS scheme is implemented on all loads installed on the IEEE-39 bus system. The settings of the installed UFLS relays are selected to fulfil the requirements of the SERC UFLS Standard. The settings are presented in Table I. The block size of the dropped load (ΔP) of each *Stage* are chosen such that the total load shedding covers the loss of generation, i.e., $\Delta P = P_{G1}+P_{G9}$. Moreover, the minimum frequency does not take values below 58.4 Hz.

TABLE I. UFLS RELAYS SETTINGS USING CASE II (TRADITIONAL UFLS SCHEME)

Stage	ΔP (%)	f_{sp} (Hz)	Δf_{sp} (Hz)	t_d (s)
1	15	59.3	0.3	0.2
2	10	59.0	0.3	0.2
3	10	58.7	0.3	0.2
4	5	58.4	0.3	0.2

Case III (Optimal UFLS scheme): shows the frequency response when the optimal UFLS scheme is used to obtain the parameters of the UFLS relays previously installed in the 19 loads. The settings obtained from the optimal UFLS scheme are described in Table II.

The convergence curve of the objective function defined in (3) after being evaluated 3,000 times is presented in Fig. 5. It is observed from iteration 2,351 the value of the objective function remains constant at ΔP=1,768.79MW; this indicates that the objective function reaches its minimum value and fulfil the constraints defined in Section II.C.3).

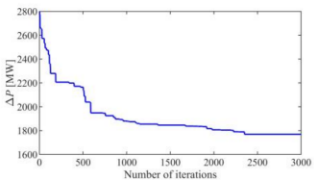

Fig. 5. Convergence curve of the optimal UFLS scheme. *Case III*.

From Table II, it can be observed that the settings are for the first and second stage of all relays, except relay in Load 24 that also has settings for third stage and relay in Load 29 has settings only for the first stage. These results mean that it is only required to activate those stages to ensure the frequency recovering and fulfil the inequality constrains defined in (4). Furthermore, it is given the frequency setpoint of each stage, and those values satisfy the inequality constraint defined in (5) which determine that frequency setpoint must be $58.4 \leq f_{sp} \leq$ (59.5-59.3).

TABLE II. UFLS RELAYS SETTINGS USING CASE III (OPTIMAL UFLS SCHEME)

Relays Location	ΔP (%)			f_{sp} (Hz)		
	Stage 1	*Stage 2*	*Stage 3*	*Stage 1*	*Stage 2*	*Stage 3*
Load 03	22.02	3.35	—	59.40	58.93	—
Load 04	0.19	11.78	—	59.43	59.10	—
Load 07	4.68	4.75	—	59.31	58.91	—
Load 08	6.40	0.09	—	59.44	59.06	—
Load 12	13.23	2.27	—	59.31	58.89	—
Load 15	19.69	11.25	—	59.44	59.00	—
Load 16	53.51	11.25	—	59.38	59.01	—
Load 18	48.85	5.38	—	59.45	59.01	—
Load 20	32.56	0.05	—	59.34	59.02	—
Load 21	16.02	19.09	—	59.49	59.13	—
Load 23	18.81	1.69	—	59.41	59.15	—
Load 24	48.72	46.60	4.68	59.42	59.20	58.99
Load 25	44.51	48.25	—	59.47	59.06	—
Load 26	36.82	48.59	—	59.45	59.07	—
Load 27	15.94	2.38	—	59.39	58.90	—
Load 28	26.05	3.20	—	59.46	59.01	—
Load 29	17.21	—	—	59.37	59.02	—
Load 31	36.81	18.87	—	59.35	59.00	—
Load 39	0.01	0.29	—	59.45	59.04	—

IV. RESULTS AND DISCUSSION

The dynamic simulation of the IEEE-39 bus system to evaluate the three cases defined above are presented in this section. The frequency response of *Case I*, *Case II* and *Case III* is shown in Fig. 6.

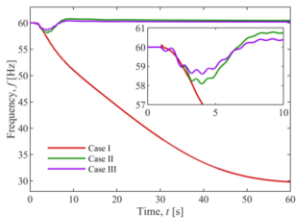

Fig. 6. Frequency response for *Case I, Case II* and *Case III* after the disconnection of generators G1 and G9.

The changes in the frequency depending on whether there is installed a UFLS scheme. *Case I* represent the worst case since there is not installed a UFLS scheme in the IEEE-39 bus system and therefore only the inertia response tries to stop the frequency drop. Despite the action of the inertia response, the frequency drop cannot be arrested, and the system becomes unstable. On the other hand, *Case II* improve the frequency response by reducing the f_{min}, t_{min} and recovering f_{ss} inside the established operating values. Moreover, it showed how it is

improved the frequency response when it is optimised the total load shedding in *Case III*. The frequency response indicators and the total load shedding are summarised in Table III.

TABLE III. FREQUENCY RESPONSE INDICATORS AND TOTAL LOAD SHEDDING FOR CASE I, CASE II AND CASE III

Case	f_{min} (Hz)	t_{min} (s)	$RoCoF_{max}$ (Hz/s)	f_{ss} (Hz)	ΔP (MW)
I	values below 58.4 Hz at 3.062s		−32.885	Frequency instability	—
II	58.092	3.995	−32.885	60.365	2438.84
III	58.602	4.020	−32.885	60.157	1768.79

In *Case I*, the frequency cannot be recovered by the inertia response and governor action taking values below the 58.4 Hz at 3.062s. This frequency value is outside of the f_{ss} limits and reaches the frequency setpoint of the under-frequency protection of generators. Therefore, low-frequency values cause the system to become unstable. In contrast, when the UFLS scheme is implemented, the frequency responds indicators depend on the UFLS relays settings. In *Case II*, the minimum frequency and minimum time are reached at f_{min}=58.092Hz and t_{min}=3.995s, respectively. Furthermore, the four stages were activated for all UFLS relays, and the load shedding is ΔP=2438.84MW which represents 40% of the total load. Thus, the steady-state frequency is improved and is f_{ss}=60.365 Hz. Meanwhile, using the settings obtained from *Case III,* the values of the minimum frequency and minimum time is at f_{min}=58.602Hz and t_{min}=4.020s, respectively. In this case, f_{min} is improved by 0.88% concerning *Case II*. In this case, *Stage 1* is activated in all UFLS relays, *Stage 2* is not activated only the UFLS relay installed in Load 29, and *Stage 3* is just activated in the relay installed in Load 24. Moreover, the load shedding is ΔP =1768.79MW, which represents 29% of the total load, and it decreases 11% whit respect *Case II*. Furthermore, the steady-state frequency remains inside the established limits, and its value is f_{ss}=60.157 Hz.

V. CONCLUSIONS

The main observations obtained from this research paper are the implementation of UFLS scheme in the power system is essential since it can avoid a possible frequency instability due to significant loss of generation event. Besides, the optimal settings in the UFLS scheme prevent an unnecessary load shedding since the total load shedding amount decrease significantly concerning the traditional UFLS scheme. Moreover, it is demonstrated that the impact of minimising the total amount of load shedding is directly reflected in the frequency response indicators. Thus, these indicators were improved by using the optimal UFLS scheme. The minimum frequency value as well as the maximum frequency deviation value decrease when the optimal UFLS scheme is implemented in contrast with the traditional UFLS scheme. Furthermore, the steady-state frequency in both cases is recovered inside predefined values, and the amount of load shedding does not impact the maximum *RoCoF*. However, its value increases depending on the size of the loss of generation since the total system inertia diminish.

ACKNOWLEDGMENT

Ms Martha N. Acosta would like to acknowledge the financial support given by CONACYT (México), and the support of University of South-Eastern Norway and Universidad Autónoma de Nuevo León. Mr Choidorj Adiyabazar wants to acknowledge the financial support given by National Dispatching Centre of Mongolia Co., Ltd. and the University of South-Eastern Norway. Prof F. Gonzalez-Longatt would like to express his gratitude to DIgSILENT GmbH for supporting his research.

REFERENCES

[1] P. Kundur *et al.*, "Definition and Classification of Power System Stability IEEE/CIGRE Joint Task Force on Stability Terms and Definitions," *IEEE Trans. Power Syst.*, vol. 19, no. 3, pp. 1387–1401, Aug. 2004.

[2] F. Gonzalez-Longatt, "Impact of synthetic inertia from wind power on the protection/control schemes of future power systems: Simulation study," in *IET Conference Publications*, 2012, vol. 2012, no. 593 CP.

[3] H. Bevrani, *Robust Power System Frequency Control*, Second Edi. Springer International Publishing, 2014.

[4] F. Gonzalez-Longatt;, F. Sanchez;, and Rujiroj Leelaruji, "Unveiling the Character of the Frequency in Power Systems," in *IEEE-PES GTD Grand International Conference & Exposition Asia 2019 (IEEE-PES GTD Asia 2019)*, 2019.

[5] IEEE, *IEEE Std C37.117 - IEEE Guide for the Application of Protective Relays Used for Abnormal Frequency Load Shedding and Restoration*, no. August. 2007.

[6] F. Sanchez and F. Gonzalez-Longatt, "Optimization of Frequency Controller Parameters of a BESS by considering Rate of Change Constraints," in *2019 IEEE Milano PowerTech, Powertech 2019*, 2019.

[7] Y. R. Omar, I. Z. Abidin, S. Yusof, H. Hashim, and H. A. Abdul Rashid, "Under Frequency Load Shedding (UFLS): Principles and implementation," in *PECon2010 - 2010 IEEE International Conference on Power and Energy*, 2010, pp. 414–419.

[8] L. Sigrist, L. Rouco, and F. M. Echavarren, "A review of the state of the art of UFLS schemes for isolated power systems," *Int. J. Electr. Power Energy Syst.*, vol. 99, no. September 2017, pp. 525–539, 2018.

[9] B. Huang, Z. Du, Y. Liu, and F. Zhao, "Study on online under-frequency load shedding strategy with virtual inertia control of wind turbines," *J. Eng.*, vol. 2017, no. 13, pp. 1819–1823, 2017.

[10] J. Wang, H. Zhang, and Y. Zhou, "Intelligent under Frequency and under Voltage Load Shedding Method Based on the Active Participation of Smart Appliances," *IEEE Trans. Smart Grid*, vol. 8, no. 1, pp. 353–361, 2017.

[11] J. Yan, C. Li, and Y. Liu, "Adaptive load shedding method based on power imbalance estimated by ANN," in *TENCON 2017 - 2017 IEEE Region 10 Conference*, 2017, vol. 2017-Decem, pp. 2996–2999.

[12] A. Drabandsari and T. Amraee, "Optimal Setting of Under Frequency Load Shedding Relays in Low Inertia Networks," in *2018 Smart Grid Conference (SGC)*, 2018, pp. 1–6.

[13] Z. Jianjun, S. Dongyu, Z. Dong, and G. Yang, "Load Shedding Control Strategy for Power System Based on the System Frequency and Voltage Stability(Apr 2018)," in *2018 China International Conference on Electricity Distribution (CICED)*, 2018, no. 201804230000057, pp. 1352–1355.

[14] V. A. Lytvynchuk, M. I. Kaplin, and N. P. Bolotnyi, "The Method of Design an Optimal Under-Frequency Load Shedding Scheme," *2019 IEEE 6th Int. Conf. Energy Smart Syst. ESS 2019 - Proc.*, vol. 1, pp. 14–17, 2019.

[15] Y. Y. Hong and P. H. Chen, "Genetic-based underfrequency load shedding in a stand-alone power system considering fuzzy loads," *IEEE Trans. Power Deliv.*, vol. 27, no. 1, pp. 87–95, Jan. 2012.

[16] M. A. Pai, *Energy Function Analysis for Power System Stability*. Springer US, 1989.

[17] P. Wall, F. Gonzalez-Longatt, and V. Terzija, "Estimation of generator inertia available during a disturbance," in *IEEE Power and Energy Society General Meeting 2012* , 2012, pp. 1–8.

[18] "PRC-006-SERC-02:Automatic Underfrequency Load Shedding Requirements - NERCipedia." [Online]. Available: https://nercipedia.com/active-standards/prc-006-serc-02automatic-underfrequency-load-shedding-requirements/. [Accessed: 25-Jan-2020].

[19] H. Seyedi and M. Sanaye-Pasand, "Design of New Load Shedding Special Protection Schemes for a Double Area Power System," *Am. J. Appl. Sci.*, vol. 6, no. 2, pp. 317–327, Feb. 2009.

Publication 4:

Descriptive Statistical Analysis of Frequency control-related variables of Nordic Power System.

M. N. Acosta, M. A. Andrade, E. Vazquez, F. Sanchez, F. Gonzalez-Longatt, and J. L. Rueda, "Descriptive Statistical Analysis of Frequency control-related variables of Nordic Power System," in *2020 IEEE Power & Energy Society General Meeting (PESGM)*, Aug. 2020, pp. 1–5, doi: 10.1109/PESGM41954.2020.9282021.

Descriptive Statistical Analysis of Frequency control-related variables of Nordic Power System

Martha N. Acosta
Manuel A. Andrade
Ernesto Vazquez
School of Mechanical and Electrical Engineering
Universidad Autónoma de Nuevo León
Nuevo León, México
martha.acostamnt@uanl.edu.mx

Francisco Sanchez
Centre for Renewable Energy Systems Technology (CREST)
Loughborough University
Loughborough, United Kingdom
F.Sanchez@lboro.ac.uk

F. Gonzalez-Longatt
Institutt for elektro, IT og kybernetikk
Universitetet I Sørøst-Norge
Prosgrunn, Norway
fglongatt@fglongatt.org

Jose Luis Rueda
Department of Electrical Sustainable Energy
Delft University of Technology
(TU Delft)
Delft, Netherlands
J.L.RuedaTorres@tudelft.nl

***Abstract*—This paper presents a descriptive statistical analysis (DSA) of time-series of electro-mechanical quantities related to the frequency control (e.g. kinetic energy (KE), electrical frequency and power demand) of the Nordic power system (NPS). The idea of the DSA is to identify main observables features and patterns between these variables. Historical data publicly available has been used in this research paper; pre-processing included evaluating and identify missing data, and it filled by using the linear interpolation. The DSA uses descriptive statistical indicators to obtaining observable features. The dispersion analysis is used to observes how affects the KE to the electrical frequency. The data is grouped by weeks, days and hours, and its correlation coefficient was calculated. A correlation analysis between the KE and the power demand was computed, and the linear regression was used to construct a prediction model.**

***Index Terms*—Correlation coefficients, dispersion analysis, statistical analysis, patterns, power system.**

I. INTRODUCTION

The increasing connection of renewable generation sources (RES) in the power system has raised concerns to the transmission systems operators (TSOs) since the rotational inertia contribution of these kinds of generation sources are smaller (or even non-existent) than those of synchronous generators [1]. The low amount of inertia in the power system affects the electrical frequency response, and the power system becomes weak and less tolerant of disturbances. Therefore, the capability to estimate and track the inertia available in the power system in real-time would allow TSOs taking control actions as well as have more precise operational planning scenarios[2]. This research paper presents a descriptive statistical analysis (DSA) of time-series of electro-mechanical quantities related to the frequency control, specifically is looking for obtaining observable features (mean, standard deviation, correlation coefficients and dispersion of the data) and identifying patterns of three electro-mechanical variables of the Nordic power system (NPS): kinetic energy (KE), electrical frequency and power demand. If the observable features and patterns of these variables are identified, a model could be constructed that allows estimating and predicting the KE of the system using the electrical frequency measurements and the power demand forecast [2]. The main contributions of this research paper are: (i) it presents a statistical analysis of the three electro-mechanical variables (see Section II), (ii) the use of the presented DSA allowed obtaining observable features time-series of electro-mechanical quantities related to the frequency control in the NPS: kinetic energy (KE), electrical frequency and power demand. Getting the main observable features and patterns that will allow constructing a prediction model to estimate the KE. This paper is organised as follows: in Section II, a description of the historical data used for the DSA is given. Moreover, the pre-processing of the time-series data and the missing data filling is presented. Furthermore, the methods applied to realise the DSA described. Section III presents the results of the DSA of the KE, power frequency and power demand frequency. Finally, Section IV presents the conclusions.

II. DESCRIPTIVE STATISTICAL ANALYSIS (DSA)

This section is dedicated to introducing the implemented DSA together with the data used in this paper.

A. Historic data

The historical data, publicly available of the NPS, is used in this paper. Essentially, three main electro-mechanical variables related to the frequency control are collected and analysed in this paper: the KE, the power demand (P_d) and the electrical frequency (f). Although a massive amount of data is available for illustrative purposes, this paper focuses on the data during the month of August 2019. Only one-month time series data was used for the DSA to determinate if the features and patterns that will be found give relevant information that indicates that an extensive data set is worth analysing. The historical time-series of the KE and the electrical frequency were obtained from Finland´s TSO company (Fingrid) database [3]. The KE raw data resolution is one sample per minute, while the

electrical frequency data resolution is one sample every three minutes. Fingrid has no data about the power demand of the NPS; it is obtained from Nord Pool company database[4]. The power demand time-series has a resolution of one sample per hour. There is a clear problem with the granularity of the data.

B. Pre-processing data

Raw time-series has been collected and then imported from a .csv file into MATLAB®. The data structure selected was a matrix that contains seven columns: year (YY), month (MM), day (dd), day of the week (weekday or weekend), hour (hh), minute (mm), and variable values. Then, the matrix data structure was evaluated to identify potential missing data. The KE has 44,640 samples, of which 1.16% are missing samples. Meanwhile, the electrical frequency has 14,880, of which 0.14% are missing samples. The power demand has 744 samples, and it has no missing samples. Since the missing data rate, a simple process of filling the missing data was performed using the simplest principle, linear interpolation [5]. Due to the granularity of the data, time-series with different sample frequency, and to avoid adding noise or losing information, the time series were not resampled. The process used in this paper is: samples were taken from the variable with the highest sampling frequency corresponding to the time of the variable with lower sampling frequency. For instance, to perform the analysis between KE and the power demand, only the KE samples corresponding to each hour were taken to have the same resolution as the power demand, one sample per hour.

C. Methods

The techniques used to perform the DSA from the electrical frequency, KE and P_d of the NPS are presented [6]. Following subsections show the main statistical methods used in this paper. For the sake of simplicity, let consider a set of observed values of a random variable in the form of $\mathbf{x} = \{x_1, x_2, \ldots, x_N\}$.

The *standard deviation* (σ) is used to measure the time series data dispersion and is calculated as follows:

$$\sigma = \sqrt{\frac{1}{N}\sum_{i=1}^{N}(x_i - \bar{\mathbf{x}})^2} \tag{1}$$

where x_i is the i-th observation of $\mathbf{x}$ and $\bar{\mathbf{x}}$ represents the mean value. The coefficient of variation (v) is used as a relative measure of the dispersion of the data concerning $(\bar{\mathbf{x}})$, and it is calculated as:

$$v = \frac{\sigma}{\bar{\mathbf{x}}} \times 100\% \tag{2}$$

The *correlation coefficient* (ρ): is a measure of the linear dependence between $\mathbf{x}$ and $\mathbf{y}$, and it is computed as follows:

$$\rho(\mathbf{x},\mathbf{y}) = \frac{1}{N-1}\sum_{i=1}^{N}\left(\frac{x_i - \bar{\mathbf{x}}}{\sigma_{\mathbf{x}}}\right)\left(\frac{y_i - \bar{\mathbf{y}}}{\sigma_{\mathbf{y}}}\right) \tag{3}$$

where x_i is the i-th observed value, $\bar{\mathbf{x}}$ is the mean and σ_X is the standard deviation of $\mathbf{x}$. Meanwhile, y_i is the i-th observed value, $\bar{\mathbf{y}}$ is the mean and σ_Y is the standard deviation of $\mathbf{y}$.

The linear regression is a statistical technique for investigating and modelling the relationship between $\mathbf{x}$ and $\mathbf{y}$ and its model is:

$$\hat{y} = \beta_0 + \beta_1 x \tag{4}$$

where $\hat{y}$ is the predicted value from the fit, $\beta_0 = \bar{\mathbf{y}} - \beta_1 \bar{\mathbf{x}}$ is the y-intercept and $\beta_1 = \sum_{i=1}^{N}(x_i - \bar{\mathbf{x}})(y_i - \bar{\mathbf{y}}) \Big/ \sum_{i=1}^{N}(x_i - \bar{\mathbf{x}})^2$ is the slope. The suitability of the regression model can be expressed by computing the *goodness of fit* indicators: (i) the *sum of square due to error* (*SSE*) is a measure of the total deviation of $\hat{y}$ from the fit to the response values, (ii) the R^2 is the measure of how effective is the fit to explain the variations of the data, the adjusted R^2 is computed based on the residual degree of freedom and (iv) the *root mean square error* (RMSE) is an estimation of the standard deviation of the random components in the data.

D. Relationship between KE, electrical frequency and power demand

The variability of the electrical frequency in a power system depends mainly on two aspects: (i) the amount of KE stored in the rotating masses of the power system and (ii) the imbalance between the generation and the power demand. This relation can be represented with the swing equation [7]:

$$\frac{df}{dt} = \frac{f_0}{2H}P_m - P_e \tag{5}$$

where f_0 is the rated electrical frequency in p.u., H is the inertia constant in seconds. P_m and P_e are the mechanical power and electrical power in p.u., respectively. Since it is in terms of H, now the relationship between H and the KE most be defined. The inertia constant is commonly used as a measure of the stored energy in the rotating masses of the system and is calculated as follows [8]:

$$H = \frac{E_{kin}}{S_B} = \frac{1}{2}J\omega_0^2\left(\frac{1}{S_B}\right) \tag{6}$$

where E_{kin} is the KE stored in a rotating mass in W·s. J is the moment of inertia expressed in kg·m^2, ω_0 is the rated speed in rad/s, and S_B is the rated apparent power in MVA. Substituting (6) in (5) the swing equation can be written in terms of KE as [9]:

$$\frac{df}{dt} = \frac{f_0}{2E_{kin}}(P_m - P_e)S_B \tag{7}$$

From (7), to maintain the electrical frequency into its nominal value, P_m and P_e must always be equal. Following an imbalance, df/dt will depend on the amount of KE stored in the rotating masses. If the KE is low, the electrical frequency variation will be higher. Otherwise, if the KE is significant, the electrical frequency variations will be small. In the NPS, to maintain the electrical frequency into its nominal range (49.9 - 50.1 Hz) the active power reserves available are used. If the power demand is higher or lower than expected, an imbalance occurs between the power demand and the scheduled production a frequency deviation is produced and the *frequency-controlled reserves* (FCR) are activated to regulate up, and a new balance is reached. If the frequency deviation remains, the TSOs manually activated *the frequency restoration reserves* (FRR) within 15 minutes [10].

III. Numerical Results

This section is dedicated to present the DSA that was realised to the KE, electrical frequency and power demand. It is performed a data dispersion analysis from KE and electrical frequency. Then, the correlation and the correlation coefficients of KE and power demand are computed for data grouped weekly, daily and hourly.

A. Dispersion analysis

The objective of carrying out the dispersion analysis of the KE and electrical frequency data is to verify if the time-series data of these variables follows the behaviour described by (12). If it is assumed that when existing a power imbalance produced by the power demand variation, this imbalance will be corrected in the next 15 minutes by the activation of FFR. Therefore, within 15 minutes periods, the generators power dispatch remains constant, and the deviation of the electrical frequency will depend on the KE stored in the generators. For this analysis, it is taken from KE data set only the samples that correspond whit the observations of the electrical frequency every 3 minutes. Therefore, KE has the same number of samples as the electrical frequency, which are 14,880 samples. Once the data has the same resolution, it is grouped every 15 minutes, i.e., each group of data have five observations, and then mean, standard deviation and coefficient of variation are calculated. Table I presents the summary of the dispersion analysis results for the KE and electrical frequency of the NPS for August 2019.

TABLE I. Dispersion analysis of the *KE* and electrical frequency for August 2019.

Variable	Mean		Standard deviation (σ)		Coefficient of variation (v)	
	Max	***Min***	***Max***	***Min***	***Max***	***Min***
KE [GW·s]	206.600	127.600	3.130	0.000	1.854%	0.000%
f [Hz]	50.115	49.876	0.071	0.002	0.140%	0.004%

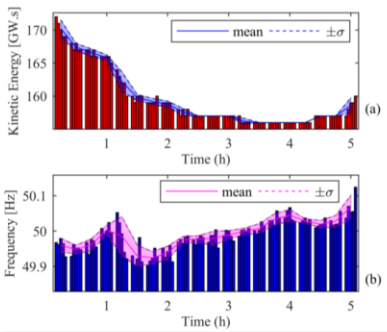

Figure 1. The mean and standard deviation of (a) KE and (b) electrical frequency for the first five hours of August 2019.

In Table I, the maximum standard deviation of KE is 3.130 GW·s and its maximum deviation concerning to the mean is 1.854%. These two indicators remain low within 15 minutes periods. Therefore, the KE tend to be close to the mean, and it can be concluded that the KE remains constant within 15 minutes periods and its variations depend on the change of power setpoint in the generators. Meanwhile, mean values of the electrical frequency are not into its nominal range, and this means that the among of KE is not enough to maintain the electrical frequency into its nominal values. Fig. 1 represents the standard deviation of KE and the electrical frequency in 15 minutes periods for the first five hours of August 2019.

The variation of the electrical frequency for 15 minutes periods does not depend exclusively on the variation of the KE. Observing hours 2:30, 2:45, 3:00, 3:30, 3:45, 4:00, 4:15, 4:30and 4:45, in Fig. 1 (a) the standard deviation is zero, i.e., the KE values remain constant within these periods, while the standard deviation of the electrical frequency for the same time periods is different from zero (see Fig. 1 (b)), which indicates that other factors like load-self regulation and the change in the power demand are causing these deviations.

B. Correlation analysis

The correlation analysis was used to determinate the degree of dependency of KE and the power demand of the NPS. Besides, the regression coefficients were computed to investigate whether it is possible to obtain a reliable prediction model. The time-series data of KE must be in the same resolution of the power demand to perform the correlation analysis, and since the power demand times-series data has a resolution of one sample per hour, to having the KE in the same resolution, it is taken the KE samples that correspond for each hour. Therefore, KE has 744 samples, equal to P_d.

All month considering weekends and without weekends: In this analysis, the measurements of all month were taken. Fig. 2 presents the time-series data grouped by weeks; it can be observed that KE and P_d follow two kinds of patter depending if it is weekdays or weekend days. P_d and KE present its lowest values between 0:00 to 5:00 hours; then they start to increase until reaching their maximum values around 10:00 hours and remains around these values until 21:00 hours when they begin to decrease to the minimum amount, each weekday follow this behaviour. On the other hand, on weekend days P_d and KE present its lowest values between 0:00 to 5:00 hours, then they start to increase until they reach their maximum value. However, the hours of the maximum values are different on Saturday and Sunday. These difference in the patterns are expected since the human activities are differents during the weekdays and weekend days, i.e., on weekdays the P_d consumption is defined by scheduled activities such as work hours, school hours, business opening and closing hours. Meanwhile, on weekends there are no specific activities planned [11].

Fig. 3 shows the correlation between KE and P_d of the NPS and the slopes of the linear regression for August 2019. The correlation coefficient, ρ, for this data set considering weekends is 0.8438 and without weekend days is 0.8536. ρ is higher when weekend days are despised than when they are admitted. The increase ρ when weekends are not considering indicates that the KE and P_d on weekends have no defined patterns, unlike weekdays, where the power demand follows the same pattern every 24 hours.

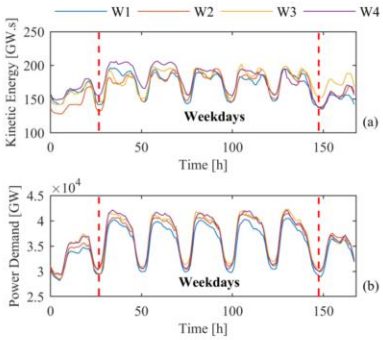

Figure 2. (a) KE and (b) P_d grouped by weeks.

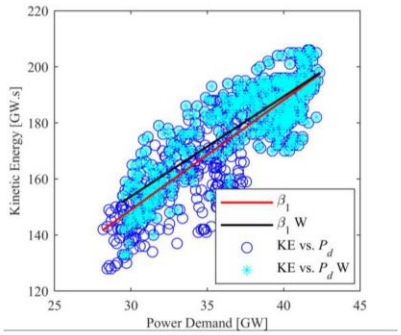

Figure 3. Correlation between KE and P_d: considering weekends (dark blue marks and red line) and without weekends (blue marks and dark line) of August 2019.

Since this value of correlation shows that exist a dependency between the P_d and KE, now it is essential to investigate whether this dependency allows making a reliable prediction model. It is known that the RMSE value is related to the degree of complexity of the model, i.e., to the degree of the linear regression model [12]. The degree of the linear regression model was chosen as one since the RMSE reduction between one and nine degrees is 3.5% and it is not worth adding complexity to the model if the decrease of RMSE is not significant. The results of performing the linear regression for KE and power demand data are summarised in Table II.

TABLE II. INDICATORS OF THE LINEAR REGRESSION OF KE AND POWER DEMAND FOR AUGUST 2019.

Indicator	***Values considering weekends***	***Values without weekends***
SSE	7.206×10^4	3.838×10^4
R^2	0.712	0.729
Adjusted R^2	0.711	0.728
RMSE	9.855	8.543

From Table II, the values of *SSE* indicate that the linear regression model has a high error component due to the fit only can represent 72.9% of the total variation in the data about the average. Moreover, when it is not considered the weekend measurements in the prediction model, the *SSE* and *RMSE* indicators decrease 46.7% and 13.3%, respectively. These results lead to conclude that it is advisable to consider creating two separate prediction models, one to represent the behaviour of the weekend days and another to describe the weekdays.

1) Data grouped by week: In this study, the data were grouped by weeks, and its correlation coefficients were computed. From Fig. 2, in each week, both KE and Pd have the same periodic variations over 24 hours, and graphically it can be concluded that both follow the same pattern every 24 hours. The correlation coefficient calculation was carried out to validate the above conclusion. The correlation coefficients without weekends have values between 0.85 and 0.92, as shown in Fig. 4. These coefficients show a strong correlation between KE and power demand, and it can be concluded that the four weeks of August follows the same pattern. Meanwhile, the correlation coefficients considering weekends have values between 0.84 and 0.89. The correlation decreases around 3% when weekends are included, and it indicates that weekday and weekend days have not the same patter.

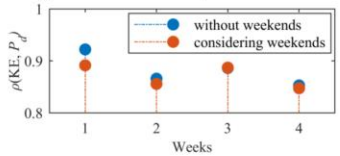

Figure 4. The correlation coefficients $\rho(KE, P_d)$ of the four weeks.

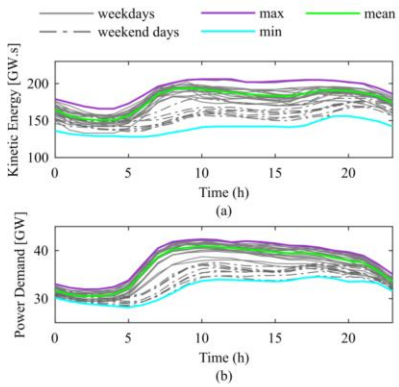

Figure 5. (a) KE and (b) P_d grouped by days considering weekends.

2) Data grouped by day: in this study, the data were grouped by days, and its correlation coefficients were computed. Fig. 5 presents the data of KE and the P_d of August 2019, including the measurements of weekends. In this figure, it is shown that two groups of data are formed: (i) weekdays around the mean and (ii) weekend days below the mean. Graphically it could be concluded that these two variables follow different patterns, a pattern representing weekdays and another pattern describing the weekend days.

The correlation coefficient between KE and P_d are presented in Fig. 6. The lowest values of the correlation coefficients, around 0.6, are those that correspond to the weekend days and it is expected since on weekends there are not defined patterns. Otherwise, weekdays have the highest correlation coefficient values, around 0.9. Therefore, these variables follow the same pattern in weekdays.

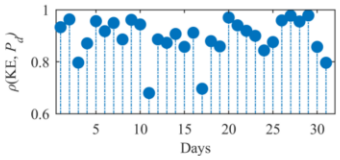

Figure 6. The correlation coefficient $\rho(KE, P_d)$ of days of August 2019.

3) Data grouped by hours: The correlation coefficient for the data grouped by hours is shown in Fig. 7. The range of values of the correlation coefficients that were considered with strong correlation is between 0.76 and 0.91, which correspond to the time range between 5:00 and 18:00 hours. The KE and power demand follow the same pattern and between 5:00 and 18:00 hours the hours are the same for all the month without considering the measures of weekend days.

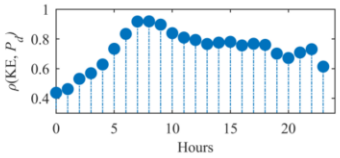

Figure 7. The correlation coefficient $\rho(KE, P_d)$ per hour without weekends.

IV. Conclusion

Based on the methods applied for the DSA, it is concluded that the KE values remain constant within 15 minutes periods since the maximum coefficient of variation does not exceed 2%, which means that the data are close to the mean. Besides, for the same 15 minutes periods, when the KE remains constant, i.e., the standard deviation is zero, the electrical frequency continues to vary. These variations manifest that the electrical frequency variation not only depends on the KE change; it also depends on load self-regulation and the difference in the power demand. The power demand and the KE have a strong correlation and follow the same pattern over 24 hours in weekdays. Otherwise, on weekend days, these variables do not follow the same pattern over 24 hours and therefore have a weak correlation. It suggests that it is necessary to create two separate models to represent the data: weekdays model and weekend days model. Although in this paper, it just analysed the electromechanical variables of one month, it is obtained relevant information about the behaviour of the variables between, minutes, hours, days and weeks. It was found that depends on the time scale it can be extracted specific information of the power system and hence create a particular model that related these variables.

Acknowledgement

Ms Martha N. Acosta wants to acknowledge the financial support given by CONACYT (Mexico) and the support of the University of South-Eastern Norway.

References

[1] F. Sanchez and F. Gonzalez-Longatt, "Optimization of Frequency Controller Parameters of a BESS by considering Rate of Change Constraints," in *2019 IEEE Milano PowerTech, Powertech 2019*, 2019.

[2] H. R. Chamorro, C. A. Ordonez, J. C.-H. Peng, Francisco Gonzalez-Longatt, and V. K. Sood, "Coherency Estimation in Power Systems: A Koopman Operator Approach," in *Computational Intelligence and Optimization Methods for Control Engineering*, J. S. Sáez, Maude, Josée Blondin, Panos M. Pardalos, Ed. Springer, Cham, 2019, pp. 201–225.

[3] "Fingrid." [Online]. Available: https://www.fingrid.fi/en/. [Accessed: 10-Sep-2019].

[4] "Nord Pool." [Online]. Available: https://www.nordpoolgroup.com/. [Accessed: 09-Oct-2019].

[5] L. Ehrlinger, T. Grubinger, B. Varga, M. Pichler, T. Natschlager, and J. Zeindl, "Treating Missing Data in Industrial Data Analytics," in *2018 Thirteenth International Conference on Digital Information Management (ICDIM)*, 2018, pp. 148–155.

[6] J. Han, M. Kamber, and J. Pei, *Data Mining: Concepts and Techniques*. Elsevier, 2012.

[7] P. Kundur, N. J. Balu, and M. G. Lauby, *Power system stability and control*. New York: McGraw-Hill, 1994.

[8] P. M. Anderson and A. A. Fouad, *Power system control and stability*. New York: IEEE Press, 2003.

[9] H. R. Chamorro, A. C. Sanchez, A. Pantoja, I. Zelinka, F. Gonzalez-Longatt, and V. K. Sood, "A network control system for hydro plants to counteract the non-synchronous generation integration," *Int. J. Electr. Power Energy Syst.*, vol. 105, pp. 404–419, Feb. 2019.

[10] ENTSOE, "Nordic Balancing Philosophy."

[11] J. Torriti, "Understanding the timing of energy demand through time use data: Time of the day dependence of social practices," *Energy Res. Soc. Sci.*, vol. 25, pp. 37–47, Mar. 2017.

[12] T. Hastie, R. Tibshirani, and J. Friedman, *The Elements of Statistical Learning: Data Mining, Inference, and Prediction*, 2nd ed., vol. 27, no. 2. New York: Springer New York, 2009.

Publication 5:

Improvement of the Frequency Response Indicators by Optimal UFLS Scheme Settings.

M. N. Acosta *et al.*, "Improvement of the Frequency Response Indicators by Optimal UFLS Scheme Settings," in *2020 IEEE 29th International Symposium on Industrial Electronics (ISIE)*, Jun. 2020, vol. 2020-June, pp. 1250–1255, doi: 10.1109/ISIE45063.2020.9152466.

Improvement of the Frequency Response Indicators by Optimal UFLS Scheme Settings

Martha N. Acosta
Manuel A. Andrade
Ernesto Vázquez
School of Mechanical and Electrical Engineering
Universidad Autónoma de Nuevo León
Nuevo León, México
martha.acostamnt@uanl.edu.mx

Choidorj Adiyabazar
Power System Analysis and Research Department
National Dispatching Center Co.,Ltd
Ulaanbaatar, Mongolia
choidorj.a@ndc.energy.mn

F. Gonzalez-Longatt
Institutt for elektro, IT og kybernetikk
Universitetet I Sørøst-Norge
Porsgrunn, Norway
fglongatt@fglongatt.org

J.L Rueda and P. Palensky
Department of Electrical Sustainable Energy
Delft University of Technology (TU Delft)
Delft, Netherlands
J.L.RuedaTorres@tudelft.nl

***Abstract*—This research investigates the positive changes in the system frequency response indicators caused by the implementation of a set of optimal settings of an under-frequency load shedding (UFLS) scheme. The optimal under-frequency load shedding (UFLS) scheme is optimised by minimising the total amount of load shedding and taking into account the recovery process of the system frequency into its operational values after several losses of generation and satisfies the requirements of the under-frequency load shedding standard (PRC-006-SERC-02). The idea of implementing the optimal UFLS scheme is to identify how changes the minimum frequency, minimum time, rate of change of frequency and steady-state frequency when the amount of load shedding change. The optimal UFLS scheme formulation starts with identifying the variables to control with the optimisation and its respective bounds. Then, the objective function is formulated in terms of the total load shedding, and finally, the restrictions and requirements of the systems are written as inequality constraints. The optimal UFLS is evaluated in the IEEE 39-bus system. The simulations results demonstrate the suitability of the optimal UFLS to improve the frequency response indicators.**

Keywords—frequency stability, optimisation, under-frequency load shedding

I. INTRODUCTION

The frequency stability is concerned with the ability of a power system to supply its load after a disturbance involving a generation-load imbalance at a frequency within an acceptable range [1]. The sudden disconnection of large generation units producing a considerable percentage of the total demand in a power system might cause an important power imbalance between the power generation and the load demand. This active power imbalance produces a fast drop in the system frequency generated by the deficit of power supply [2]. If the appropriate control actions are in place, the system frequency must reach an acceptable value after a few seconds. However, if the power imbalance is larger than the designed specification, the frequency can drop to values considered unacceptable or even trip a cascade event putting the power system in risk of instability and subsequent blackout.

To avoid any potential damage of generation units and load-side equipment, it is crucial to precisely control the system frequency within an established, acceptable frequency range or at least, to prevent longer frequency excursions out of this established range. However, if the system frequency reaches unacceptably low values (predefined security threshold), there is a small-time window to implement restorative or emergency actions. If the size of the system frequency disturbance is large, the scheduled power reserve may not be enough to restore the system frequency and the power system operators may use emergency control and protection schemes to maintain power system frequency [3]. An emergency control plan used by years is the well-known *under-frequency load shedding* (UFLS).

The UFLS strategy is designed so as to balance the demand for electricity with the supply rapidly and to avoid a rapidly cascading power system failure [4]. In simple terms, the UFLS is designed to prevent the system frequency from staying too low for too long by disconnecting the right amount of power loads to regain frequency control. Under-frequency operation is usually more problematic with regard to possible equipment damages than over-frequency operation due to the limited amount of spinning reserves.

The schemes are system protection schemes; it means the scheme objective is the integrity of the system frequency as a whole, in contrast to equipment protections, trying to minimise equipment damages [5]. It is essential to coordinate system under-frequency load shedding with under-frequency protection of the generator. Premature generator tripping, before system load shedding is complete, can lead to unnecessary system collapse.

A real example of frequency stability problems and the actions of UFLS is the famous Italian blackout of 28 September 2003 (see Fig. 1). During the frequency event, the frequency dropped down to 49 Hz, due to the loss of power infeed coming from the central interconnected European power system. The frequency continued dropping until it reaches the under-frequency threshold of 47.5 Hz in the next 150 seconds [6], all generation units were tripped according to the predefined UFLS scheme. However, the main reason for the blackout was that during this terminal phase of the frequency collapse the under-voltage load shedding (UVLS) did not appropriately compensate the additional loss of generation coming from around 7.5 GW of distributed power plants tripped during under-frequency operation [7]. The Italian blackout of 28 September

2003 made clear the need to redefine the load shedding plan in Italy in order to appropriately handle the loss of imported power or the power plants operating on the distribution grid.

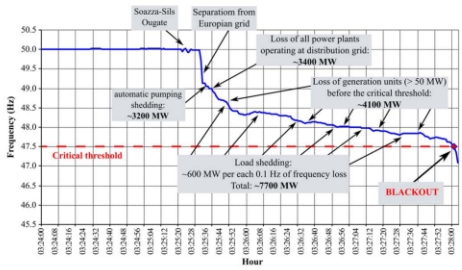

Fig. 1. Plot of the frequency behaviour during the transitory frequency event in Italy 28 September 2003 [6].

The major frequency event in Italy of 28 September 2003 made evident the importance of an appropriate UFLS. However, the situation of frequency control and stability and the problem of adequate settings of UFLS is becoming more and more complicated with the increased penetration levels of power converted based generation technologies (reducing the total system rotational inertia) [8].

The primary objective of UFLS schemes is to arrest frequency dropping in due time by shedding an appropriate amount of load, in order to recover the frequency into its nominal values [9]. Ideally, the UFLS must act as the primary option and by doing so, preventing the action of generation-side under-frequency protections, which would finally lead to a cascading power outage [10]. In the traditional UFLS schemes, the settings of the UFLS relays are mainly based on the power system operator's knowledge of the power system performance during major frequency events. However, although the frequency is recovered into its nominal values, the UFLS settings are not optimal, and they end up disconnecting more load than necessary.

The main propose of this research paper is to investigate the positive changes in the system frequency response indicators caused by the implementation of an optimal setting of a UFLS scheme. An optimal calculation process of the settings of the UFLS improves the power system reliability by minimising the unnecessary excessive load shedding and prevent the operation of under-frequency protections of the synchronous generator. However, this research paper introduces the problem of optimal settings of UFLS relayed using mathematical optimisation. Then, the methodology is used to set the UFLS on a test system, and the ulterior motive is to determinate how the optimal stings impact the frequency response indicators: minimum frequency, minimum time, rate of change of frequency and steady-state frequency.

This paper is organised as follows: in Section II, it is described the methodology to calculate the optimal UFLS scheme such as the selected variables to be controlled by the optimisation, the objective function formulation, and the constraints. Section III presents a description of the test system that is used to evaluate the optimal UFLS scheme. Moreover, three cases are presented for assessing the UFLS scheme. Section IV describes the results obtained and present the main observations of the results. Finally, Section V presents the conclusion.

II. Optimal UFLS scheme formulation

The frequency load shedding (FLS) is an emergency control strategy dedicated to mitigating substantial mismatch between the generation and the loads. The UFLS is dedicated specifically to deal with under frequency events where there is a lack of generation or an excess of power demand. Load shedding is becoming a very attractive research topic in recent time to deal with several problems related to extremally reduced inertia scenarios, the market pressure to minimise the reserve margins and the operating the tie-line near to the limit of capacities.

Many different approaches are reported for implementing UFLS settings are detailed in the scientific literature: traditional schemes, artificial intelligence techniques, and more recently, meta-heuristic optimisation algorithms. A summary of those methods is beyond the scope of this paper but [10] provides a compressive and relative new overview.

A. Frequency Response indicators

The system frequency response (SFR) of a power system is typically analysed by using time-domain plots of the system frequency when the major event is applied (typically a sudden generation disconnection). The principal frequency response indicators are represented in Fig. 2, and they are defined as follows [4]-[12-13]:

- The minimum frequency (f_{min}) denotes the minimum value that the frequency reaches during the transient response when the major event is applied.
- The minimum time (t_{min}) is the time required from the instant where a disturbance is started until the frequency reaches its minimum value.
- The Rate of Change of Frequency (*RoCoF)* represents the speed of change of frequency (*df*) concerning with the time change (*dt*), i.e. $RoCoF = df/dt \ [\mathrm{Hz/s}]$.
- The steady-state frequency (f_{ss}) refers to the value at which the frequency is positioned after the transient response and at which the *RoCoF* is zero. This value can be interpreted as the capability of the power system of recovering after a disturbance.

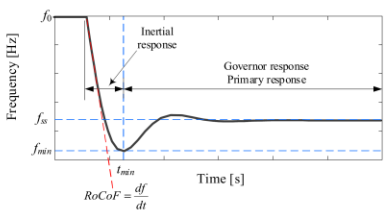

Fig. 2. Representation of the principal frequency response indicators in a classical SFR signal.

B. UFLS Settings

UFLS relays are adopted to protect the system by shedding some of the system load to keep the frequency of the system close to the nominal value.

UFLS relays can be classified into two categories[11]: (i) Fixed number of stages and time delays and (ii) Adaptative number of stages and variable shed demands. The traditional UFLS relay (such as ANSI 81L) falls in the first category and is extensively used in power systems. In this research paper, the UFLS relays are considered to have a fixed number of stages, but the setting will be optimised in the next subsections. Traditional UFLS scheme relies basically on four main settings:

- *Block size of dropped load*: (percentage or power unit) It defines the block size of load shedding is the size of load to be dropped at all stages.
- *Number of load shedding stages*: (integer) Load shedding is usually implemented on stages. It defines the number of steps to be used to shed the load.
- *Frequency threshold*: (typically in Hertz) It defines a pre-set frequency level at each stage in which load must be shed.
- *Time delay for each stage.* (seconds or cycles) It defines the time delay between activating the consecutive stages.

C. Optimisation Problem Definition

The process to formulate the optimal UFLS scheme followed in this paper is based in the following steps: First, the appropriate set of control variables are identified, those variables are selected in order to control the frequency response following a system frequency disturbance at the time the optimisation considered the main aspects of the UFLS relay features and respective bounds are defined for the relay settings. Then, the objective function to be minimised was written in terms of the control variables. Finally, the restrictions and requirements of the systems are written as inequality constraints. The full procedure of each step is described below.

1) Variables

The control vector (**x**) is a vector used to specify the control variables to be used in the optimisation process:

$$\mathbf{x} = \left[\Delta P_{ij} \quad f^{1}_{sp,j} \quad \Delta f_{sp,kj}\right]^{\mathrm{T}}, \quad \begin{cases} i = 1,\ldots,N_S \\ j = 1,\ldots,N_R \\ k = 1,\ldots,N_S - 1 \end{cases} \tag{1}$$

where ΔP_{ij} is the percentage load shedding of the i-th stage in the j-th UFLS relay, $f^{1}_{sp,ij}$ is the first frequency set-point of the j-th UFLS relay and $\Delta f_{sp,kj}$ represents the interval between two subsequent frequency set-points. Moreover, N_R is the number of UFLS relays installed in the power system, and N_S is the number of load shedding stages in each relay.

The control variables are bounded by its upper (u) and lower (l) allowable values as follows:

$$\begin{aligned} &\Delta P_l \le \Delta P_{ij} \le \Delta P_u \\ &f^{1}_{sp,l} \le f^{1}_{sp,j} \le f^{1}_{sp,u} \\ &\Delta f_{sp,l} \le \Delta f_{sp,kj} \le \Delta f_{sp,u} \end{aligned} \tag{2}$$

where ΔP_l and ΔP_u, represents the maximum and minimum permissible percentage of load shedding, respectively. $f^{1}_{sp,l}$ and $f^{1}_{sp,u}$ are the maximum and minimum limit frequency set-point in the first stage, respectively. Moreover, $\Delta f_{sp,l}$ and $\Delta f_{sp,u}$ are the maximum and minimum values that can take Δf_{sp}.

2) Objective function

In this paper, the idea of optimising the settings of the UFLS relay is to reduce as much as possible the power demand interrupted during the under-frequency event. As a consequence, the purpose of the UFLS optimisation is determinate the minimum amount of load shed required to recovers the steady-state frequency into its operating values. Therefore, the objective function is formulated as the sum of all active stages in each UFLS relay multiplied by active power in its respective load. The objective function is:

$$\min\left(\sum_{j=1}^{N_R}\sum_{i=1}^{n_S}\Delta P_{ij}P_j\right) \tag{3}$$

where P_j is the active power of the j-th load with UFLS relay and n_S is the number of activated stages. n_s is different from N_s ($n_s \le N_s$).

3) Constraints

The objective function defined in (3) is subject to certain restrictions to ensure the security of the power system and fulfil the technical requirements of the utility companies:

a) Steady-state frequency (f_{ss}): after a massive loss of generation, the f_{ss} must remain inside the operating range of the synchronous generators, i.e., $f_{ss}^{\min} \le f_{ss} \le f_{ss}^{\max}$. This restriction is formulated as two inequality constraints as follow

$$f_{ss} - f_{ss}^{\max} \le 0 \tag{4}$$

and

$$f_{ss}^{\min} - f_{ss} \le 0 \tag{5}$$

b) Frequency set-point (f_{sp}): the f_{sp} in each stage of the UFLS relays shall be inside the limits defined by the technical requirements of the utility companies, i.e., $f_{sp}^{\min} \le f_{sp} \le f_{sp}^{\max}$. Since the optimisation gives the first f_{sp} of each relay and it is already bounded, it is necessary to define the inequality constraint for the minimum limit as follows:

$$f_{sp}^{\min} - f_{sp,ij} \le 0 \tag{6}$$

III. STUDY CASE

To investigates the positive changes in the system frequency response indicators caused by the implementation of an optimal setting of a UFLS scheme, a classical and well-known tests system is used: the IEEE 39-bus system. The IEEE 39 bus system is well known as ten machines New-England Power

System. Generator 1 represents the aggregation of a large number of generators. The original model data come from the book titled "Energy Function Analysis for Power System Stability" [12]. The test system has been implemented in DIgSILENT® PowerFactory™ 2020. The schematic single line diagram of the test system is shown in Fig. 3. The test system consists of ten generators, 19 loads, 34 transmission lines, 12 transformers and 39 buses. The total active power generation is 6,140.81 MW, and the total power demand is 6097.10 MW [13].

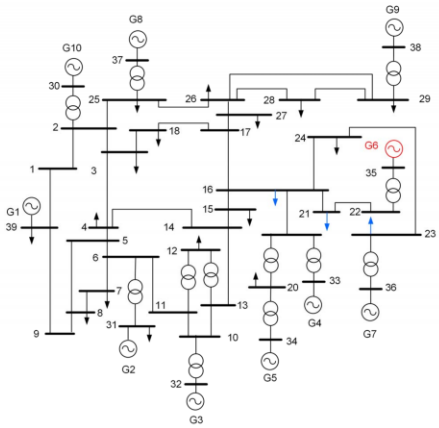

Fig. 3. Illustrative single-line diagram of the IEEE-39 bus system. UFLS relays have been installed in buses 16, 21 and 22 (noted in the diagram). Frequency disturbance is the sudden disconnection of G6 (highlighted).

The SFR of the test system is excited by a system frequency event, in this very specific case, the sudden disconnection of G6 at $t = 1.0$ second, which represents a loss of 10.585% of the total generation, $\Delta P = P_{G6}$. The UFLS relays are installed near to generator G6 in Load 16, Load 21 and Load 23. In this paper, the three UFLS relays ($N_R = 3$) has four load shedding stages (N_S=4). The time delay was set as $t_d = 0.20$ s. The generator causing the disturbance (G6) is highlighted with red colour, and the loads where the UFLS relays are installed are marked with blue colour in Fig. 3.

In this paper, three simulation cases are considered: *Case I* refers to the natural SFR of the test system without any UFLS scheme. *Case II* study the SFR of the test system considering the UFLS but using a traditional setting. Finally, Case III represents the SFR of the tests system but considering the optimal settings of the UFLS is presented in Section II. The three defined cases considering the time delay as $t_d = 0.20$ s, four load shedding stages (N_S=4) and the same disturbance, $\Delta P = 650$MW.

The Improved Harmony Search (IHS) metaheuristic algorithm is applied to solve the UFLS optimisation problem. Details of the IHS algorithm are described in [14]. For all cases, it is observed the indicators of the frequency response: (i) minimum frequency (f_{min}), (ii) minimum time (t_{min}), (iii) the maximum *RoCoF* and (iv) steady-state frequency (f_{ss}).

As the test system is representative of the North American system, the parameters of the UFLS relays must satisfy the SERC (South-eastern Electric Reliability Council) UFLS Standard: PRC-006-SERC-02 [15]:

- f_{ss} shall be kept within the continuous operating range of the generating units between 59.5 Hz and 60.5 Hz. Therefore, f_{ss} is bounded as $59.5 \leq f_{ss} \leq 60.5$.
- The highest value of f_{sp} shall be no lower than 59.3 Hz and not higher than 59.5 Hz. Moreover, the lowest value of f_{sp} shall be no lower than 58.4 Hz. Therefore, f_{sp} is bounded as $58.4 \leq f_{sp} \leq (59.5\text{-}59.3)$.
- Δf_{sp} shall be at least 0.2 Hz but no greater than 0.5 Hz, i.e., $0.2 \leq \Delta f_{sp} \leq 0.5$.
- The time delay (t_d) for the high-speed trip shall be at least six cycles, i.e., $0.1\text{s} \leq t_d$.

Case I (Case Base): In this case, it is presented the dynamic response of the frequency when the disturbance occurs by outage the generator G6, and there is not a UFLS scheme installed. Fig. 4 shows the frequency response measured in all buses. The minimum frequency is f_{min} = 57.923Hz at t_{min} = 29.582s, and it is presented in bus 39.

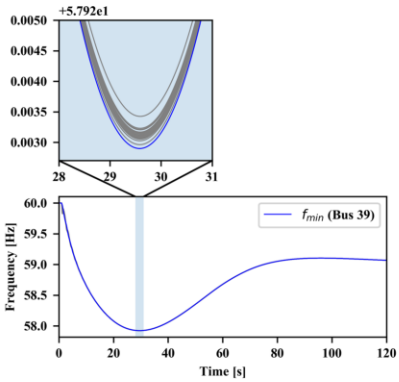

Fig. 4. Frequency response in the 39 buses after the outage of generator G6: *Case I.*

Fig. 5 shows the *RoCoF* of all buses, the maximum *RoCoF* produced by the disconnection of G6 is presented in bus 36 and its value is $RoCoF_{max} = -2.565$Hz/s at 1.012s.

The steady-state frequency for Case I is f_{ss}= 59.024 Hz, and it is evident that the power system requires a UFLS scheme to recover the frequency into the established f_{ss} limits, i.e., $59.5 \leq f_{ss} \leq 60.5$. Moreover, the under-frequency relays of the synchronous generators, in 60 Hz nominal frequency, typically operates if the frequency reach vales from 58.4 Hz to 57.9 and the frequency does not recover within 30 seconds [16]. Therefore, another reason to install the UFLS scheme is to avoid the activation of the under-frequency relays that protect the synchronous generators since, in this case, f_{min} reaches values below 58Hz.

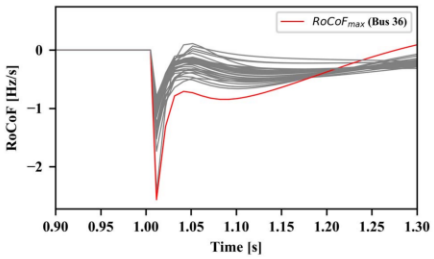

Fig. 5. *RoCoF* response in the 39 buses after the outage of generator G6: *Case I.*

Case II (Traditional UFLS scheme): This case presents the frequency response when a traditional UFLS scheme is implemented on the IEEE-39 bus system in Load 16, Load 21 and Load 23. The settings of the installed UFLS relays are chosen in order to fulfil the requirements of the SERC UFLS Standard. The settings are presented in Table I.

TABLE I. UFLS RELAYS SETTINGS USING THE TRADITIONAL UFLS SCHEME

Stage	ΔP (%)	f_{sp} (Hz)	Δf_{sp} (Hz)	t_d (s)
1	30	59.3	0.3	0.2
2	25	59	0.3	0.2
3	25	58.7	0.3	0.2
4	20	58.4	0.3	0.2

Case III (Optimal UFLS scheme): shows the frequency response when the optimal UFLS scheme is used to obtain the parameters of the UFLS relays previously installed in Load 16, Load 21 and Load 23.

The settings obtained from the optimal UFLS scheme are described in Table II, it can be observed that the settings are for the first stage of all relays and only the second stage of the relay in Load 23. These results mean that it is only required to activate those stages in order to ensure the frequency recovering. Furthermore, it is given the frequency set-point of each stage and those values satisfy the constraint defined in (6).

TABLE II. UFLS RELAYS SETTINGS USING THE OPTIMAL UFLS SCHEME

Stage	*Load 16*		*Load 21*		*Load 23*	
	ΔP (%)	f_{sp} (Hz)	ΔP (%)	f_{sp} (Hz)	ΔP (%)	f_{sp} (Hz)
1	32.690	59.339	22.566	59.311	46.868	59.416
2	---	---	---	---	8.225	59.146
3	---	---	---	---	---	---
4	---	---	---	---	---	---

The convergence curve of the objective function defined in (3) after being evaluated 300 times is presented in Fig. 6. It is observed from generation 230 the value of the objective function remains constant; this indicates that the objective function reaches its minimum value and fulfil the constraints defined in Section II.C.3) by (4), (5) and (6) .

IV. RESULTS AND DISCUSSION

The dynamic simulation of the IEEE-39 bus system to evaluate the three cases defined above are presented in this section. The frequency response of *Case I*, *Case II* and *Case III* is shown in Fig. 7. In this figure, it can be observed the changes in the frequency response depending on whether or not there is installed a UFLS scheme.

Case II improve the frequency response by reducing the f_{min}, t_{min} and recovering the steady-state frequency inside the established operating values. Moreover, it showed how it is improved the frequency response when it is optimised the total load shedding in *Case III*, the minimum frequency and minimum time is minimised and the steady-state frequency remains inside the established operating values.

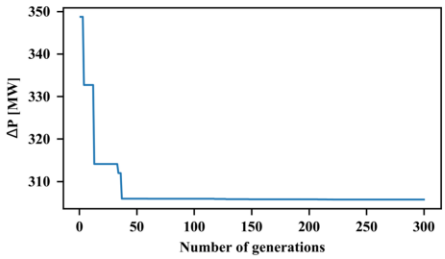

Fig. 6. Convergence curve of the optimal UFLS scheme. *Case III.*

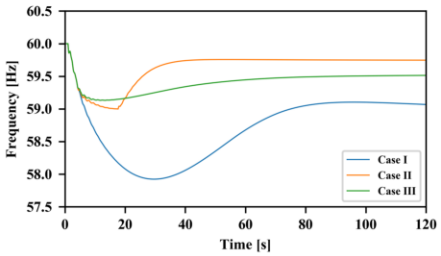

Fig. 7. Frequency response for *Case I, Case II* and *Case III* after the outage of generator G6.

The frequency response indicators and the total load shedding are summarised in Table III.

TABLE III. FREQUENCY RESPONSE INDICATORS AND TOTAL LOAD SHEDDING FOR THE THREE CASES

Case	f_{min} (Hz)	t_{min} (s)	$RoCoF_{max}$ (Hz/s)	f_{ss} (Hz)	ΔP (MW)
I	57.923	29.582	−2.565	59.024	----
II	58.999	17.665	−2.565	59.746	463.925
III	59.130	11.618	−2.565	59.521	305.736

From Table III, the frequency response indicators after the disconnection of generator G6 are discussed. In Case I, the frequency reaches its minimum value at 29.582s, and its steady-

state operation value is 59.024 Hz, this frequency value is outside of the established f_{ss} limits. The maximum *RoCoF* after the disturbance is -2.565 Hz/s. Since in this case there is not installed a UFLS scheme, there are no actions to arrest the frequency decaying. In contrast, when the UFLS scheme is implemented, the frequency responds indicators depend on the UFLS relays settings. In Case II, the minimum frequency and minimum time are reduced 1.85% and 40.28 %, respectively concerning Case I. Furthermore, the stages activated for all UFLS relays are Stage 1 and Stage 2, and the load shedding is 463.925 MW which represents 7.61% of the total load. Thus, the steady-state frequency is improved and is 59.746 Hz.

Meanwhile, the settings for the UFLS relays obtained from Case III decreases the values of the minimum frequency and minimum time in 2.08% and 60.72 %, respectively in contrast to Case I. In this case, Stage 1 activated for all UFLS relays, and Stage 2 is just activated in the relay installed in Load 23. Moreover, the load shedding is 305.736 MW, which represents 5.01% of the total load, and it decreases 34.01 % whit respect Case II. Furthermore, the steady-state frequency remains inside the established limits, and its value is 59.521 Hz.

V. Conclusions

The principal conclusion in this research paper is that the optimal settings in the UFLS scheme prevent an unnecessary load shedding since it is observed a decreeing in the total load shedding concerning with the traditional UFLS scheme. Moreover, it is identified that the impact of minimising the total amount of load shedding is directly reflected in the frequency response indicators, and thus these indicators were improved.

The minimum frequency value as well as the minimum time value decrease when the optimal UFLS scheme is implemented in contrast with the traditional UFLS scheme. Moreover, the steady-state frequency in both cases is recovered inside predefined values. Furthermore, the maximum *RoCoF* is not modified by the presence of UFLS scheme and is not impacted by the amount of load shedding.

Acknowledgement

Ms Martha N. Acosta would like to acknowledge the financial support given by CONACYT (México), and the support of University of South-Eastern Norway and Universidad Autónoma de Nuevo León. Prof F. Gonzalez-Longatt would like to express his gratitude to DIgSILENT GmbH for supporting his research.

References

[1] P. Kundur *et al.*, "Definition and Classification of Power System Stability IEEE/CIGRE Joint Task Force on Stability Terms and Definitions," *IEEE Trans. Power Syst.*, vol. 19, no. 3, pp. 1387–1401, Aug. 2004.

[2] F. Gonzalez-Longatt, "Impact of synthetic inertia from wind power on the protection/control schemes of future power systems: Simulation study," in *IET Conference Publications*, 2012, vol. 2012, no. 593 CP.

[3] H. Bevrani, *Robust Power System Frequency Control*, Second Edi. Cham: Springer International Publishing, 2014.

[4] F. Gonzalez-Longatt;, F. Sanchez;, and Rujiroj Leelaruji, "Unveiling the Character of the Frequency in Power Systems," in *IEEE-PES GTD Grand International Conference & Exposition Asia 2019 (IEEE-PES GTD Asia 2019)*, 2019.

[5] IEEE, *IEEE Std C37.117 - IEEE Guide for the Application of Protective Relays Used for Abnormal Frequency Load Shedding and Restoration*, no. August. 2007.

[6] UCTE, *Final Report of the Investigation Committee on the 28 September 2003 Blackout in Italy*, no. 1. 2004.

[7] S. Corsi and C. Sabelli, "General blackout in Italy sunday September 28, 2003, h. 03:28:00," in *2004 IEEE Power Engineering Society General Meeting*, 2004, vol. 2, pp. 1691–1701.

[8] F. Sanchez and F. Gonzalez-Longatt, "Optimization of Frequency Controller Parameters of a BESS by considering Rate of Change Constraints," in *2019 IEEE Milano PowerTech, Powertech 2019*, 2019.

[9] Y. R. Omar, I. Z. Abidin, S. Yusof, H. Hashim, and H. A. Abdul Rashid, "Under Frequency Load Shedding (UFLS): Principles and implementation," in *PECon2010 - 2010 IEEE International Conference on Power and Energy*, 2010, pp. 414–419.

[10] L. Sigrist, L. Rouco, and F. M. Echavarren, "A review of the state of the art of UFLS schemes for isolated power systems," *Int. J. Electr. Power Energy Syst.*, vol. 99, no. September 2017, pp. 525–539, 2018.

[11] Y. Y. Hong and P. H. Chen, "Genetic-based underfrequency load shedding in a stand-alone power system considering fuzzy loads," *IEEE Trans. Power Deliv.*, vol. 27, no. 1, pp. 87–95, Jan. 2012.

[12] M. A. Pai, *Energy Function Analysis for Power System Stability*. Springer US, 1989.

[13] P. Wall, F. Gonzalez-Longatt, and V. Terzija, "Estimation of generator inertia available during a disturbance," in *IEEE Power and Energy Society General Meeting 2012* , 2012, pp. 1–8.

[14] M. Mahdavi, M. Fesanghary, and E. Damangir, "An improved harmony search algorithm for solving optimization problems," *Appl. Math. Comput.*, vol. 188, no. 2, pp. 1567–1579, May 2007.

[15] "PRC-006-SERC-02:Automatic Underfrequency Load Shedding Requirements - NERCipedia." [Online]. Available: https://nercipedia.com/active-standards/prc-006-serc-02automatic-underfrequency-load-shedding-requirements/. [Accessed: 25-Jan-2020].

[16] H. Seyedi and M. Sanaye-Pasand, "Design of New Load Shedding Special Protection Schemes for a Double Area Power System," *Am. J. Appl. Sci.*, vol. 6, no. 2, pp. 317–327, Feb. 2009.

Publication 6:

Optimal Settings of Fast Active Power Controller: Nordic Case.

M. N. Acosta, F. Gonzalez-Longatt, S. Denysiuk, and H. Strelkova, "Optimal Settings of Fast Active Power Controller: Nordic Case," in *2020 IEEE 7th International Conference on Energy Smart Systems (ESS)*, May 2020, pp. 63–67, doi: 10.1109/ESS50319.2020.9160281.

Optimal Settings of Fast Active Power Controller: Nordic Case

M. N. Acosta
School of Mechanical and Electrical Engineering
Universidad Autónoma de Nuevo León
Nuevo León México
martha.acostamnt@uanl.edu.mx

F. Gonzalez-Longatt
M. N. Acosta
Department of Electrical Engineering, Information Technology and Cybernetics
University of South-Eastern Norway
Porsgrunn, Norway
flongatt@flongatt.org

S. Denysiuk, H. Strelkova
Power Supply Department
IEE Igor Sikorsky Kyiv Polytechnic Institute
Kyiv, Ukraine
spdens@ukr.net

***Abstract*— The Nordic power system is continuously changing, and it has been experiencing a growing replacing of conventional power plants with renewable power plants, this together with other factors are causing reduction of the total inertia of the Nordic power system. The application of technologies that emulates the dynamic response of the synchronous generators has been a feasible solution. This paper focuses on finding the bests control adjustment of the fast-active power injection/absorption (FAPIA) model by using an optimization algorithm. The FAPIA model has two frequency sensible control actions: a proportional control (*K-f*) and a derivative control (*K-df/dt*). The optimization problem is defined using the gains of the proportional and derivative control together with the volume of FAPIA model contribution as decision variables. Two objective functions are determined based on two system frequency response indicators: minimum frequency, the and steady-state frequency. A simplified version of the Nordic power system is implemented for system frequency response studies.**

Keywords*— Fast active power injection/absorption, frequency control, frequency response indicators, low inertia, optimization.

I. Introduction

The constant evolving of the Nordic Power System (NPS) has raised several challenges related to frequency control. Particularly, one of the challenges that are facing the NPS is the reduction of the total system inertia [1], [2]. The total system inertia has been decreased due to the increase of the wind power plants installed in the NPS, closure of thermal power plants, closure of Swedish nuclear power plants and more than 50% increase of the capacity of the interconnector between the NPS and other power systems [3], [4]. It has been estimated that the total kinetic energy of the NPS will be below 120–145 GW·s around 1–19% of the time, this value will be depending on the clime year [5], [6]. Therefore, it is essential to develop a simple and robust methodology that allows facing a low inertia problem.

An alternative to deal with the low inertia in the NPS is to insert synthetic inertia (SI) to the system by using SI controllers [7]. The SI controller family uses a derivative function as its main controller; however, it has several disadvantages in wind turbine implementations and other forms of power converter interfaced technologies [8], [9].

Consequently, an efficient procedure to deal with the low inertia and improve the system frequency is the fast-active power injection/absorption (FAPIA) controller. It is a frequency sensitive controller that imitate the inertia response of the synchronous generators by using a proportional (*K-f*) and derivative (*K-df/dt*) control actions [4]. The extremely fast response within 1 second and the very short time-delay related to measurement are two advantages that highlight the FAPI controller performance.

This paper presents the concept of FAPIA controller and an intensive-search methodology to quantify the volume of FAPIA require to fulfil the future low inertia scenario of the Nordic Power System. However, finding the correct settings of FAPIA controllers and the total FAPIA volume represent a challenge. The principal objective of this research paper is finding the proper settings of FAPIA controllers in the low inertia scenario by using the interior-point optimization algorithm. Moreover, carried out an assessment of the frequency response indicator when the total system inertia decreases.

The paper is organized as follows: A full description of the FAPI controller is presented in Section II. Section III presented a methodology applied to optimize the FAPI controller parameters. Two objective functions are defined base of two frequency response indicators: steady-state frequency and minimum frequency. Section IV describes the simplified model of the NPS used to evaluate the proposed objective functions and assed the frequency response indicators. Section V presents a discussion of the results obtained by assessing the frequency response indicators in low inertia he scenario. Furthermore, the optimization solution for the FAPIA controller parameters is described and evaluated. Section VI presents the main conclusion of this research paper.

II. Fast Active Power Injection/Absorption

The modern power converters (MPCs) based on voltage source converters can modify the active power production in a limited spectrum defined by the availability of energy in the DC side of the MPC [3][10], this MPC power converter is distinguished by its fast response [1]. The fast-active power injection/absorption (FAPIA) is a frequency response model that is activated by the controller in the MPC [11], [5]. The main purpose of using the FAPIA controller is to fast compensate the frequency deviation by (i) injecting active power when the system has an under-frequency condition and (ii) absorbing active power when the system has an over-frequency condition. In general, the FAPIA controller uses the frequency deviation as an input, and the output is the active power to be delivered. The FAPIA controller follows the classic linear control theory and implement two control actions: (i) proportional control action and (ii) derivative control action.

A. *Proportional control action (K-f control)*

The proportional control action (*K-f* control) is linear feedback control in which the active power injection is controlled by a correction factor (gain). The gain is proportional to the frequency deviation (Δf), i.e., the difference between the nominal frequency (f_0) and the current measured frequency (f). The classical power-frequency (*P-f*) characteristic, considering a dead band and saturation, of the *K-f* control used in FAPI controller is shown in Fig. 1.

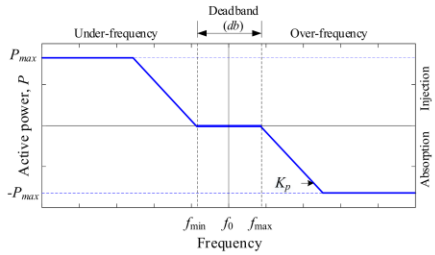

Fig. 1. Classical power-frequency (*P-f*) characteristic of the *K-f* control implanted un the FAPI controller.

The *K-f* control action considering the deadband, shown in Fig. 1, can be mathematically described as:

$$P = \begin{cases} 0 & \text{if } f_{\min} \le f \le f_{\max} \\ K_p f & \text{if } f > f_{\max} \\ -K_p f & \text{if } f < f_{\min} \end{cases} \quad (1)$$

The physical limitations of the MPCs are included by writing two physical restrictions as follows

$$P = \begin{cases} P_{\max} & \text{if } P \ge P_{\max} \\ -P_{\max} & \text{if } P \le -P_{\max} \end{cases} \quad (2)$$

The isolated effect of variating the K_p values in a range $[K_{p,\min}, K_{p,\max}]$ is reflected on the *P-f* characteristic, in which the slope changes, this change is illustrated in Fig. 2. Moreover, Fig. 3 presents the power-time (*P-t*) characteristic considering K_p variations in the range $[K_{p,\min}, K_{p,\max}]$.

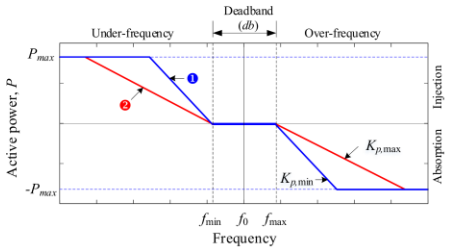

Fig. 2. Classical *P-f* characteristics of the *K-f* control considering K_p variations, i.e., $K_p \in [K_{p,\min}, K_{p,\max}]$.

From Fig. 3, it can be observed that as the values of K_p increases the active power (*P*) delivered by the FAPIA controller also increases during frequency events outside the deadband. Moreover, high values of K_p tend to increase the speed at which *P* reaches its maximum limit, i.e., the FAPIA controller reaches its active power production limits faster than low values of K_p. Meanwhile, low values of K_p make the frequency response slower and lower.

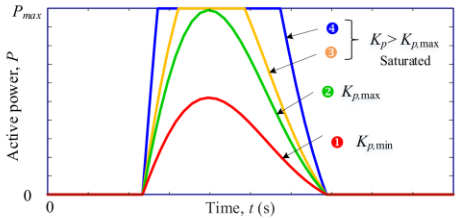

Fig. 3. Power-time (*P-t*) characteristics of the *K-f* control K_p variations, i.e., $K_p \in [K_{p,\min}, K_{p,\max}]$.

B. *Derivative control action (K-df/dt control)*

The derivative control action (*K-df/dt* control) refers to the rate of change of the error concerning the time. The *K-df/dt* control is used to overcome the drawbacks presented in the *K-f* control. The *K-df/dt* control is mainly related to the rate of change of frequency (*ROCOF*), i.e., *ROCOF= df/dt.* Using this control action on the FAPIA controller allows that the FAPIA controller behavior emulates the dynamic of the synchronous generator.

The active power injected/absorbed by the FAPIA controller during the system frequency disturbance is calculated using a mathematical expression analogous to the swing equation of a synchronous generator:

$$\Delta P = K_d \frac{df(t)}{dt} \quad (3)$$

where K_d represents the gain of the derivative controller, sometimes called synthetic inertia (seconds) and f is locally measured frequency (p.u) and ΔP represents injected/absorbed active power by the FAPIA controller.

C. *Combining control actions*

A combination of the *K-f* control and *K-df/dt* control would take advantage of the dynamic performance of both functions; it is mathematically formulated as:

$$\Delta P = K_p \Delta f - K_d \frac{d\Delta f}{dt} \quad (4)$$

where term K_p represents the gain of the *K-f* control of the FAPIA controller without considering saturation and deadband, and the term K_d represents the inertial contribution of active power which is proportional to the *ROCOF* of the system.

The frequency responsive term K_p has a strong influence on the steady-state frequency, and the ROCOF mainly influences the K_d term after the disturbance. The effect of K_d term is equivalent to an increase in the system's kinetic energy, and therefore it reduces the initial *ROCOF*.

III. Optimization of the FAPIA

The frequency response of a power system can be significatively modified by the appropriate volume of frequency response. However, defining the appropriate settings of FAPIA controllers and the total FAPIA contribution can be represented as an optimization problem. In this section, an optimization approach is used to define the optimal values of the FAPI controllers: K_p and K_d and the total

volume of FAPI contribution α_{FAPI}. The next section presents the system frequency response indicators, and then the optimization problem is presented.

A. System Frequency Response

The system frequency response of a power system is mainly evaluated by employing the dynamic response (time-domain plots) of the system frequency caused by a disturbance in the power system. The system frequency response is evaluated by three main indicators[12], [13]:

(i) *Minimum frequency* (f_{min}): The minimum value that the frequency reaches in the dynamical response after a disturbance.

(ii) *Steady-state frequency* (f_{ss}): is the value in which the frequency settles (final value) after the dynamical response.

(iii) The rate of change of frequency (*ROCOF*) represents the speed at which the frequency changes concerning the time, *ROCOF* = *df*/*dt* [Hz/s].

B. Optimization approach

The optimization problem in this paper is formulated as a continuous optimization problem because the decision variables are continuous. The decision vector **x** has three main decision variables, the K_d the gain of the derivative control action, K_p represents the proportional control action of the FAPIA controller, and the volume of FAPIA controller contribution is α_{FAPIA}.

$$\mathbf{x} = \begin{bmatrix} K_p & K_d & \alpha_{FAPIA} \end{bmatrix}^T \tag{5}$$

Acting on the three decision variables, the active power contribution of the FAPI is defined, and the frequency response can be modified.

The decision variables (x_i) are restricted in order to fulfil two main conditions: (i) reduce the searching space and (ii) more important to keep the parameters inside realistic physical values. Therefore, the bound are defined as:

$$\mathbf{x}_{\mathbf{lower}} \leq \mathbf{x} \leq \mathbf{x}_{\mathbf{upper}} \tag{6}$$

where $x_{lower,i}$ and $x_{upper,i}$ define the upper and lower bounds of the *i*-th decision variable.

The previous sections defined the main indicators to consider in the system frequency response. Now, those indicators are used to define the objective function. In this paper, two objective functions are examined:

1) Minimizing steady-state frequency deviation

The steady-state frequency (f_{ss}) is a very important indicator as it is defined by the droop used in the governors of the synchronous generators and the size of the system frequency disturbance (ΔP). In this paper, the steady-state frequency deviation (Δf_{ss}) is minimized using the difference between the nominal frequency and the steady-state frequency. The objective function is written as:

$$\min\left(\Delta f_{ss}\right) = \min\left[\left\| f_0 - f_{ss} \right\|\right] \tag{7}$$

However, using the equation above the steady-state frequency will ideally back to the rated frequency, f_0, and that is an unsatisfactory solution because the FAPIA controller will be used for frequency control not to overlap the Automatic Generation Control (AGC). The AGC is responsible for modified the active power injections of the synchronous machines at post-contingency to recover the steady-state frequency to the nominal frequency, f_0. Consequently, this paper considers the FAPIA contribution to recover the steady-state frequency into a pre-defined frequency f_{set}, and the objective function expressed in (7) now is written as:

$$\min\left(\Delta f_{ss}\right) = \min\left[\left\| f_{set} - f_{ss} \right\|\right] \tag{8}$$

2) Minimizing the deviation of the minimum frequency

The minimum frequency (f_{min}) is an important indicator of the frequency response. This indicator represents the minimum frequency that the power system reaches after a disturbance. In general, the synchronous generators maintain a continues operation when the frequency is inside its operative limits, i.e., $f_L \leq f_0 \leq f_U$ where f_0 is the nominal frequency, f_L and f_U represent the lower and upper limit of frequency. If the frequency reaches values below f_L, the under-frequency protection of the synchronous generator can be activated.

Therefore, minimizing the deviation of the minimum frequency (the difference between f_{min} and the f_L), Δf_{min}, ensures that f_{min} will not take values below f_L and therefore avoiding the activation of the under-frequency protection of the synchronous generators. The objective function to minimize the deviation of the minimum frequency is written as:

$$\min\left(\Delta f_{min}\right) = \min\left[\left\| f_L - f_{min} \right\|\right] \tag{9}$$

IV. System Frequency Response Model

The Nordic power system is composed of four countries: Norway, Sweden, Denmark and Finland. Typically, the NPS has a simplified model represented by three control areas (i) Area 1: Sweden, (ii) Area 2: Norway and (iii) Area 3: Finland. An illustrative diagram of the simplified NPS is presented in Fig. 4. Each control area is considered to have local generation and load, and interconnection transmission lines are included between Norway-Sweden and Sweden-Finland.

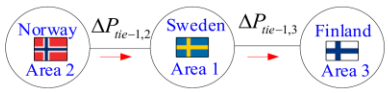

Fig. 4. Simplified model of the NPS. ΔP_{tie} is used to represents the incremental active power change during a system frequency event

The details of the block diagram of a single control area are presented in Fig. 5.

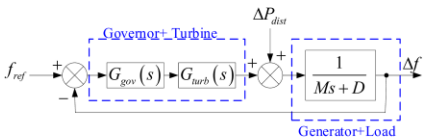

Fig. 5. Block diagram of a single control area: The main controllers involved in the frequency response are represented in the control area. ΔP_{dist} represents the system frequency disturbance.

Form Fig. 5, $G_{gov}(s)$ is the transfer function of the governor, $G_{turb}(s)$ is the transfer function of the hydro turbine and the term 1/Ms+D (where *M* is the equivalent moment of

inertia and D represents the power demand of the frequency-dependent loads) represent the transfer function of the generator and load.

In this paper, the equivalent model of Area 1, Area 2 and Area 3 have been implemented using MATLAB® R2019b for the proposes of assessing the frequency response indicators and evaluate the two objective functions proposed in Section III. The full details of the model and the parameters are described in [6].

V. Simulations and Results

The implemented equivalent model of the Nordic Power system is used to assess the sensitivity analysis of the frequency response indicator in the scenario of low inertia. Moreover, the optimal settings for the FAPIA controller are obtained by using the two objective function defined in Section III.B.

A. Sensitivity analysis of the frequency response indicators

The frequency response indicators are affected by the decreasing of the total system inertia in the NPS. Therefore, this section is dedicated to carrying on a sensitivity analysis of the frequency response indicators. For this study, a sudden step increases in the load demand (ΔP) is considered as a frequency disturbance.

The frequency response is assessed by observing its indicators: (i) minimum frequency (f_{min}), (ii) steady-state frequency (f_{ss}) and (iii) maximum *ROCOF*. The load demand increase is ΔP= 0.0280 p.u. and the nominal inertia is H_0=4.84 seconds. The nominal inertia is gradually decreased until the frequency response cannot be recovered and the NPS is unstable.

Fig. 6 show the behavior of f_{min} when the system inertia of the NPS is progressively reduced. From this figure, it can be concluded that as long as the system inertia is smaller, the frequency deviation increases and therefore f_{min} reaches lower values for the same frequency disturbance.

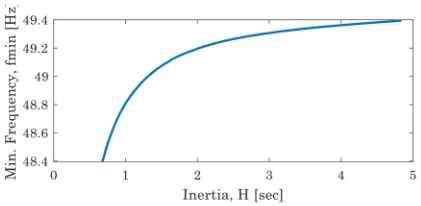

Fig. 6. Minimum frequency (f_{min}) behavior by gradually decreasing the system inertia of the NPS.

Meanwhile, if the system inertia is smaller, the maximum *ROCOF* increases for the same step increases in the load demand, it is shown in Fig. 7. Finally, the frequency response of the NPS is gradually deteriorated when the system inertia is decreasing. The unstable frequency response means that the kinetic energy stored in the rotating masses of the NPS is not enough to recover the frequency as it is presented in Fig. 8.

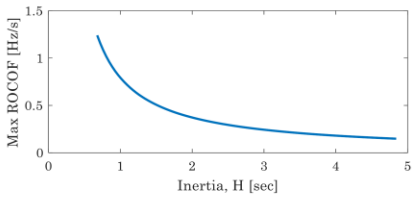

Fig. 7. Maximum *ROCOF* behavior by gradually decreasing the system inertia of the NPS.

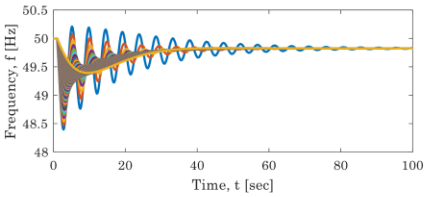

Fig. 8. Frequency response by gradually decreasing the system inertia of the NPS.

The sensitivity analysis highlights the downsides of having a low level of inertia in the power system and how it deteriorates the power system security in case of a disturbance. Moreover, for the test system, the minimum inertia that the NPS can tolerate is H_{min}=0.6776 seconds which represent 14% of the nominal inertia (H_0).

B. Optimization solution of the two objective functions proposed

This section is dedicated to evaluating the solution of the two objective functions proposed in Section III.B. The objective of evaluating the proposed objective functions is to obtain optimal setting of the FAPIA controller parameters (K_p, K_d and α_{FAPIA}) for a given disturbance. The interior-point optimization algorithm given in the MATLAB® R2019b is applied to solve the optimization problem. Details of the interior-point optimization algorithm are described in [14], [15]. The frequency disturbance is ΔP= ΔP= 0.0280 p.u., representing a sudden step, increases in the load demand. Moreover, the total system inertia is set 50% of the nominal inertia; therefore, $H = 0.5H_0$=2.42 seconds.

1) Minimizing steady-state frequency deviation

The objective function defined in (8) to minimize the steady-state frequency deviation is evaluated. For illustrative purposes in this paper, the pre-defined steady-state frequency is f_{set}=49.9 Hz.

The optimization solution provides a decision variable vector as $\mathbf{x}$ = [2.5172 2.2628 2.5173] which represent the optimal settings of the FAPIA controller. The first element of the vector is the gain of the *K-f* control, K_p=2.5172. The second element represents the gain of the *K-df/dt* control, i.e., K_d=2.2628. The third element of the vector is the volume of FAPIA controller, and it is α_{FAPIA}=2.5173.

The FAPIA controller parameters are set using the results of the optimization, and a frequency disturbance is inserted in the NPS. The frequency response is shown in Fig. 9. The minimum frequency that the NPS reaches is f_{min}= 49.836 Hz,

the maximum *ROCOF* is -0.144 Hz/sec, and the steady-state frequency is f_{ss} = 49.9 Hz demonstrating that the optimal settings of the FAPIA controller parameters are fulfilling the minimization equation describe in (8) and the steady-state deviation is Δf_{ss} =0 Hz.

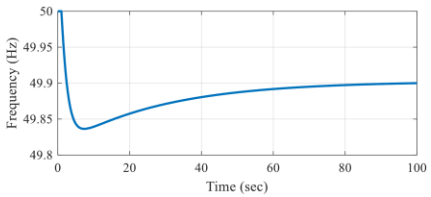

Fig. 9. Frequency response using the optimal settings for minimizing the steady-state frequency deviation (Δf_{ss}).

2) Minimizing the deviation of the minimum frequency

The minimization of the minimum frequency deviation of the NPS is performed using the equation defined in (9). For this study, the lower limit of frequency is selected as f_L=49.5 Hz; this value is chosen for illustrative proposes.

The decision variable vector for the objective function defined in (9) that contains the optimal settings of the FAPIA controller is **x** = [0.7166 0.6927 0.7133]. The gain of the *K-f* control is K_p=0.7166, the gain of the *K-df/dt* control is K_d=0.6927, and the volume of FAPIA controller is α_{FAPIA}=0.7133.

Fig. 10 present the frequency response for a frequency disturbance using the optimal settings for the FAPIA controller parameters. It is observed that the minimum frequency does not exceed the lower limit of frequency (f_L) demonstrating that the optimal setting of the FAPIA controller are fulfilling the minimization equation describe in (9), in fact, the f_{min} that the NPS reaches is f_{min}= 49.5 Hz and Δf_{min} =0 Hz. The maximum *ROCOF* is -0.144 Hz/sec and the steady-state frequency is f_{ss} = 49.836 Hz.

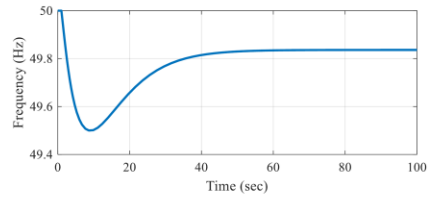

Fig. 10. Frequency response using the optimal settings for minimizing the minimum frequency deviation (Δf_{min}).

VI. Conclusions

The frequency response indicators are deteriorating in low inertia scenarios. Creating a sensitivity analysis of those indicators can help to prevent the minimum inertia in the power system in order to ensure frequency stability when a disturbance occurred. The optimal setting of FAPIA controller parameters obtained from the optimization solution fulfils the requirements of the pre-set frequency values for the two objective functions. The optimal setting of the FAPIA controller depends only on the pre-defended steady-state value and the pre-defended frequency limits in the dynamic response. Furthermore, using the two objective function allows ensuring that the two frequency response indicators (steady-state frequency and minimum frequency) do no exceeds certain pre-set values.

Acknowledgment

Ms Martha N. Acosta would like to acknowledge the financial support given by CONACYT (México) as well as the support of Universidad Autónoma de Nuevo León, Mexico, and the University of South-Eastern Norway, Norway.

References

[1] F. Sanchez, J. Cayenne, F. Gonzalez-Longatt, and J. L. Rueda, "Controller to Enable the Enhanced Frequency Response Services from a Multi-Electrical Energy Storage System," *IET Gener. Transm. Distrib.*, Nov. 2018.

[2] H. Chamorro, F. Gonzalez, K. Rouzbehi, R. Sevilla, H. Chavez, and V. Sood, "Innovative Primary Frequency Control in Low-Inertia Power Systems Based on Wide-Area RoCoF Sharing," *IET Energy Syst. Integr.*, Feb. 2020.

[3] T. Krechel, F. Sanchez, F. Gonzalez-Longatt, H. Chamorro, and J. L. Rueda, "A Transmission System Friendly Micro-grid: Optimising Active Power Losses," in *13th IEEE PES PowerTech Conference*, 2019.

[4] A. J. Veronica, N. S. Kumar, and F. Gonzalez-Longatt, "Design of Load Frequency Control for a Microgrid Using D-partition Method," *Int. J. Emerg. Electr. Power Syst.*, vol. 21, no. 1, Feb. 2020.

[5] F. Gonzalez-Longatt, "Effects of Fast Acting Power Controller of BESS in the System Frequency Response of a Multi-Machine System: Probabilistic Approach," in *International Conference on Innovative Smart Grid Technologies (ISGT Asia 2018)*, 2018.

[6] L. Saarinen, P. Norrlund, U. Lundin, E. Agneholm, and A. Westberg, "Full-scale test and modelling of the frequency control dynamics of the Nordic power system," in *2016 IEEE Power and Energy Society General Meeting (PESGM)*, 2016, vol. 2016-Novem, pp. 1–5.

[7] H. R. Chamorro, I. Riaño, R. Gerndt, I. Zelinka, F. Gonzalez-Longatt, and V. K. Sood, "Synthetic inertia control based on fuzzy adaptive differential evolution," *Int. J. Electr. Power Energy Syst.*, vol. 105, pp. 803–813, Feb. 2019.

[8] H. R. Chamorro, A. C. Sanchez, A. Pantoja, I. Zelinka, F. Gonzalez-Longatt, and V. K. Sood, "A network control system for hydro plants to counteract the non-synchronous generation integration," *Int. J. Electr. Power Energy Syst.*, vol. 105, pp. 404–419, Feb. 2019.

[9] A. J. S. J. Veronica, N. S. Kumar, and F. Gonzalez-Longatt, "Robust PI controller design for frequency stabilisation in a hybrid microgrid system considering parameter uncertainties and communication time delay," *IET Gener. Transm. Distrib.*, vol. 13, no. 14, pp. 3048–3056, Jul. 2019.

[10] B. Sri Revathi, P. Mahalingam, and F. Gonzalez-Longatt, "Interleaved high gain DC-DC converter for integrating solar PV source to DC bus," *Sol. Energy*, vol. 188, pp. 924–934, Aug. 2019.

[11] F. Gonzalez-Longatt, J. Rueda, and E. Vázquez Martínez, "Effect of Fast Acting Power Controller of Battery Energy Storage Systems in the Under-frequency Load Shedding Scheme," in *International Conference on Innovative Smart Grid Technologies (ISGT Asia 2018)*, 2018.

[12] F. Gonzalez-Longatt;, F. Sanchez;, and Rujiroj Leelaruji, "Unveiling the Character of the Frequency in Power Systems," in *IEEE-PES GTD Grand International Conference & Exposition Asia 2019 (IEEE-PES GTD Asia 2019)*, 2019.

[13] F. Gonzalez-Longatt, J. L. Rueda, and E. Vázquez Martínez, *Effect of Fast Acting Power Controller of Battery Energy Storage Systems in the Under-frequency Load Shedding Scheme*. Loughborough University, 2018.

[14] T. Steihaug, "The Conjugate Gradient Method and Trust Regions in Large Scale Optimization," *SIAM J. Numer. Anal.*, vol. 20, no. 3, pp. 626–637, Jun. 1983.

[15] R. H. Byrd, J. C. Gilbert, and J. Nocedal, "A trust region method based on interior point techniques for nonlinear programming," *Math. Program. Ser. B*, vol. 89, no. 1, pp. 149–185, 2000.

Errata

Page/Line	*Original text*	*Corrected text*
10/12	"...are focussing..."	"...are focused..."
21/16	"...Britan..."	"...Britain..."
22/1	"Amprior"	"...Amprion..."
43/16; 59/6	"...staticts..."	"...statistics..."
59/6	"...whit..."	"...with..."
62/2	"...are have implemented..."	"...have implemented..."
113/16	"...defined in (5.9) and (5.9) ..."	"...defined in (5.8) and (5.9) ..."
131/19	"...instaled..."	"...installed..."

Doctoral dissertation no. 103
2021
—

Intelligent frequency control for the secure operation of modern power system

Dissertation for the degree of Ph.D
—

Martha Nohemi Acosta Montalvo—
ISBN: 978-82-7206-621-4 (print)
ISBN: 978-82-7206-622-1 (online)

usn.no